

## **Adaptive Characteristics of Fiber-Reinforced Elastomeric Isolators**

**ADAPTIVE CHARACTERISTICS OF FIBER-REINFORCED  
ELASTOMERIC ISOLATORS**

By  
NIEL C. VAN ENGELEN, B. ENG. & MGT.

Faculty of Engineering  
Department of Civil Engineering

A Thesis Submitted to the School of Graduate Studies in Partial Fulfilment of the  
Requirements for the Degree of Doctor of Philosophy

McMaster University

© Copyright by Niel C. Van Engelen, December 2015

Doctor of Philosophy (2015)  
(Civil Engineering)

McMaster University  
Hamilton, Ontario, Canada

TITLE: Adaptive Characteristics of Fiber-Reinforced Elastomeric  
Isolators

AUTHOR: Niel C. Van Engelen, B.Eng. & Mgt. (McMaster  
University)

SUPERVISORS: Dr. Michael J. Tait & Dr. Dimitrios Konstantinidis

NUMBER OF PAGES: xviii, 202

## **Lay Abstract**

Earthquakes remain a significant and potentially devastating threat to both developed and developing countries. Structural elements within a building, such as beams and columns, must deform considerably to accommodate the relative floor displacements that develop due to ground motion. Conventional construction materials are not capable of undergoing these large deformations without irreversible and potentially catastrophic damage. The introduction of a flexible layer at the foundation level of a structure, using elements known as isolators, can dramatically reduce damage. The deformation is concentrated at the flexible layer, which can undergo large displacements without any damage. This concept, known as base isolation, protects both the structure and its contents. Traditional isolators are expensive, thus far hindering the application of base isolation systems. A novel isolator design has been proposed that has the potential for widespread economical application. To increase the application, building codes need to be developed, requiring substantial research on the isolator properties. A key component of the novel isolator is the ability to alter the isolator geometry to further enhance the response. This is validated through experimental testing and complex computer models.

## Abstract

Seismic base isolation has become an increasingly common approach to reduce earthquake induced losses. Base isolation aims to decouple structures, such as buildings or bridges, from strong ground motions through the introduction of a flexible layer, typically located at the foundation. Base isolation is a well-established concept and accepted as an effective method of protecting both the structure and its contents from damage due to earthquakes.

Elastomers are ideal for base isolation due to their soft material properties and ability to undergo large recoverable strains. Steel-reinforced elastomeric isolators (SREIs) have been widely applied as base isolators; however, the weight and cost of SREIs have been perceived as barriers to the widespread application of base isolation. In order to alleviate these concerns, it has been proposed that the steel reinforcement could be replaced with lighter fiber reinforcement with similar tensile properties as steel. Recent investigations have demonstrated that fiber-reinforced elastomeric isolators (FREIs) are viable and have desirable characteristics.

An additional proposed cost saving measure was to place the FREI unbonded between the upper and lower supports. The combination of the flexible fiber reinforcement and the unbonded application resulted in a unique *rollover* deformation under horizontal displacement. Rollover causes a nonlinear force-displacement relationship characterized by a softening and stiffening phase. This nonlinear relationship is believed to be advantageous and to allow the performance of the device to be tailored to the earthquake hazard level.

This work investigates the adaptive characteristics of unbonded FREIs. It is demonstrated that the softening and stiffening characteristics of the isolator can be altered through modifications to the isolator or to the surrounding support geometry. Equations are developed to predict the horizontal force-displacement relationship. Furthermore, simple expressions appropriate for use in building and bridge design codes are proposed for critical isolator properties. Potential limitations introduced due to the unbonded application are identified and addressed through the development of a new partially bonded hybrid isolator. It is demonstrated that unbonded FREIs are highly versatile and a potentially competitive device appropriate for widespread application in developed and developing countries.

## **Acknowledgements**

This work would not have been possible without the support and guidance of my family, friends, supervisors and the assistance of many colleagues throughout my undergraduate and graduate studies at McMaster University and my short time at the University of California, Berkeley. I would like to extend my most sincere thanks to those who have read, questioned, and expanded upon my work.

The support of the Natural Sciences and Engineering Research Council of Canada (NSERC), an Ontario Graduate Scholarship and a Vanier Canada Graduate Scholarship is greatly appreciated.

## Table of Contents

Lay Abstract .....	iii
Abstract .....	iv
Acknowledgements .....	v
Table of Contents .....	vi
List of Tables .....	x
List of Figures .....	xi
Co-Authorship .....	xvii
1 Introduction.....	1
1.1 Basic Concept of Base Isolation.....	2
1.2 Main Design Considerations .....	3
1.3 Economics and Application .....	3
1.4 Types of Isolators .....	4
1.4.1 Steel-Reinforced Elastomeric Isolators .....	5
1.4.2 Fiber-Reinforced Elastomeric Isolators.....	5
1.4.3 Unbonded Fiber-Reinforced Elastomeric Isolators .....	5
1.5 Impetus and Research Objectives.....	6
1.6 Structure of Thesis .....	7
References .....	8
2 Literature Review of Elastomeric Isolators .....	12
2.1 Elastomeric Materials.....	12
2.1.1 Main Considerations.....	12
2.1.2 Long-term Performance .....	12
2.2 Reinforcement .....	13
2.3 Vertical Stiffness .....	15
2.3.1 SREIs.....	15
2.3.2 FREIs.....	16
2.3.3 Boundary Conditions.....	17
2.4 Horizontal Stiffness.....	17
2.4.1 Bonded SREIs and FREIs .....	17
2.4.2 Unbonded FREIs .....	17
2.5 Stability .....	19
References .....	20
3 Model of the Shear Behavior of Unbonded Fiber-Reinforced Elastomeric Isolators	26
Abstract.....	26
3.1 Introduction .....	26
3.2 Background .....	28
3.2.1 Full Rollover Prediction .....	28
3.2.2 Horizontal Force-Displacement Relationships.....	28

3.3	Model Description .....	29
3.3.1	Displacement Prior to Full Rollover .....	29
3.3.2	Deformed Shape and Full Rollover Prediction .....	33
3.3.3	Displacement Exceeding Full Rollover.....	33
3.4	Model Evaluation .....	34
3.4.1	Horizontal Force-Displacement Relationship .....	34
3.4.2	$F_I$ Contribution.....	35
3.4.3	Vertical Compressive Load .....	35
3.4.4	Full Rollover Prediction and Deformed Shape .....	36
3.5	Parametric Study .....	36
3.5.1	Influence of Aspect Ratio.....	36
3.5.2	Influence of $E_m$ .....	37
3.6	Conclusions .....	38
	Nomenclature.....	39
	Acknowledgements .....	40
	References .....	40
4	Development of Design Code Orientated Formulas for Elastomeric Bearings Including Bulk Compressibility and Reinforcement Extensibility.....	51
	Abstract.....	51
4.1	Introduction .....	51
4.2	Accounting for Compressibility .....	53
4.2.1	Compression Modulus and Bending Modulus .....	53
4.2.2	Maximum Shear Strain due to Compression.....	54
4.3	Analytical Solutions .....	55
4.4	Proposed Approximation Derivation .....	57
4.4.1	Material and Geometric Properties.....	57
4.4.2	Infinite Strip Pad .....	58
4.4.3	Circular Pad.....	61
4.4.4	Square Pad.....	62
4.4.5	Annular Pad.....	64
4.5	Discussion .....	68
4.5.1	Compression and Bending Modulus .....	68
4.5.2	Shear Strain due to Compression .....	69
4.5.3	Example.....	70
4.6	Conclusion.....	71
	Acknowledgements .....	71
	References .....	71
5	Shear Strain Demands in Elastomeric Bearings Subjected to Rotation .....	86
	Abstract.....	86

5.1	Introduction .....	86
5.2	Rotations in Elastomeric Bearings .....	87
5.2.1	Code Considerations.....	87
5.2.2	Analytical Solutions .....	89
5.3	Generalized Approximations.....	90
5.3.1	Material and Geometric Properties.....	90
5.3.2	Infinite Strip Pad .....	91
5.3.3	Circular Pad.....	93
5.3.4	Square Pad.....	94
5.3.5	Rectangular Pad.....	94
5.3.6	Annular Pad.....	95
5.4	Discussion .....	98
5.4.1	Generalized Approximation .....	98
5.4.2	Example: Square Pad ( $\rho = 1$ ).....	99
5.4.3	Example: Circular Pad.....	100
5.5	Conclusion.....	100
	Acknowledgements .....	100
	References .....	101
6	Experimental and Finite Element Study on the Compression Properties of Modified Rectangular Fiber-Reinforced Elastomeric Isolators (MR-FREIs).....	109
	Abstract.....	109
6.1	Introduction .....	109
6.2	Background .....	111
6.2.1	MR-FREIs .....	111
6.2.2	Annular Isolators .....	113
6.3	Experimental Testing .....	113
6.3.1	Isolator Design .....	113
6.3.2	Experimental Setup and Vertical Test Procedure.....	114
6.3.3	Experimental Results.....	115
6.4	Finite Element Modeling.....	116
6.4.1	Model Development .....	116
6.4.2	Model Evaluation .....	116
6.5	Parametric Study .....	117
6.5.1	Vertical Stiffness .....	117
6.5.2	Compression Modulus.....	118
6.5.3	Vertical Strain.....	118
6.5.4	Vertical Stress.....	119
6.5.5	Shear Stress .....	120
6.5.6	Fiber Reinforcement Von Mises Stress.....	121

	6.6 Conclusions .....	121
	Acknowledgements .....	121
	References .....	122
7	Structural and non-structural performance of a seismically isolated building using stable unbonded fiber-reinforced elastomeric isolators.....	139
	Summary.....	139
	7.1 Introduction .....	139
	7.2 SU-FREIS and MSG .....	141
	7.3 Predicting Full Rollover .....	142
	7.4 Experimental Program.....	143
	7.5 Model and Methodology .....	145
	7.5.1 Structure and Equipment.....	145
	7.5.2 SU-FREIs .....	145
	7.5.3 Earthquakes and Scaling .....	146
	7.6 Results .....	147
	7.6.1 Structure .....	147
	7.6.2 Light Equipment.....	148
	7.7 Effect of Stiffening.....	149
	7.7.1 Structure .....	149
	7.7.2 Light Equipment.....	150
	7.8 Discussion .....	151
	7.9 Conclusions .....	152
	Acknowledgements .....	153
	References .....	153
8	Partially Bonded Fiber-Reinforced Elastomeric Isolators (PB-FREIs).....	167
	Summary.....	167
	Key Words.....	167
	8.1 Introduction .....	167
	8.2 Background .....	169
	8.2.1 Isolation Systems in Tension.....	169
	8.2.2 Friction and Slip .....	169
	8.2.3 Partially Bonded Region .....	171
	8.3 Experimental testing.....	172
	8.3.1 Isolator Design .....	172
	8.3.2 Experimental Setup and Horizontal Test Procedure .....	172
	8.3.3 Experimental Results.....	173
	8.4 Finite element analysis .....	174
	8.4.1 Model Description.....	174
	8.4.2 Vertical Modulus.....	175

8.4.3 Horizontal Behaviour (Under Compression): $B < B_{max}$ .....	176
8.4.4 Horizontal Behaviour (Under Compression): $B > B_{max}$ .....	176
8.4.5 Horizontal Behaviour (Under Tension): $B > B_{max}$ .....	178
8.4.6 Influence of Vertical Load .....	179
8.5 Conclusion.....	180
Acknowledgements .....	181
References .....	181
9 Conclusions and Recommendations .....	193
9.1 Summary .....	193
9.1.1 Model of the Shear Behavior of Unbonded Fiber-Reinforced Elastomeric Isolators .....	193
9.1.2 Development of Design Orientated Formulas for Elastomeric Bearings.....	194
9.1.3 Experimental and Finite Element Study on the Compression Properties of Modified Rectangular Fiber-Reinforced Elastomeric Isolators .....	194
9.1.4 Structural and Non-structural Performance of a Seismically Isolated Building using Stable Unbonded Fiber-Reinforced Elastomeric Isolators ....	195
9.1.5 Partially Bonded Fiber-Reinforced Elastomeric Isolators.....	195
9.2 Recommendations for Future Study.....	196
Appendix A: Generalized Approximations for a Rectangular Pad.....	198
Preamble .....	198
Compression Modulus.....	198
Maximum Shear Strain due to Compression.....	199
Bending Modulus .....	199
References .....	200

## List of Tables

Table 3-1: Material and Geometric Properties of Selected Isolators .....	42
Table 3-2: Full Rollover and Extension of the Initially Vertical Face Predictions.....	42
Table 4-1: Compression and bending modulus for an incompressible elastomeric pad and correction factors to take into account elastomer compressibility and reinforcement extensibility .....	74
Table 4-2: Factors for the proposed approximations for the maximum shear strain due to compression, Eq. (4-66).....	74
Table 5-1: Summary of the proposed approximate formulas for maximum shear strain due to rotation .....	103
Table 6-1: Specimen geometric characteristics.....	124
Table 6-2: Experimental results. ....	124

Table 6-3:	Material properties.....	124
Table 6-4:	Comparison of the experimental and FE analysis ratios of modified to unmodified vertical stiffness.....	124
Table 7-1:	Experimentally determined effective horizontal stiffness and equivalent viscous damping. ....	157
Table 7-2:	Ratio of the model to experimental effective horizontal stiffness and equivalent viscous damping.....	157
Table 7-3:	Selected broadband fault normal records and scale factors.....	158
Table 7-4:	Effective period at $u/t_r = 2.50$ .....	158
Table 7-5:	Mean peak displacement.....	158
Table 8-1:	Comparison of the ratio of partially bonded to unbonded experimental results.....	183

## List of Figures

Figure 1-1:	Mode shapes of a discretized three storey structure .....	10
Figure 1-2:	Idealized acceleration response spectra showing the decrease in response acceleration caused by a base isolation system .....	10
Figure 1-3:	Friction Pendulum System.....	10
Figure 1-4:	Lateral bulging of an (a) unreinforced and (b) reinforced elastomeric isolator under vertical load .....	10
Figure 1-5:	Profile view of a bonded (a) an undeformed and (b) deformed SREI.....	11
Figure 1-6:	Profile view of an unbonded FREI showing (a) rollover and (b) full rollover .....	11
Figure 1-7:	Idealized horizontal force-displacement relationship for a bonded FREI and SU-FREI .....	11
Figure 2-1:	Bulging of the exterior layers with zero slip and zero friction .....	25
Figure 2-2:	Division of an unbonded FREI into sections .....	25
Figure 3-1:	Profile view of (a) a bonded SREI and (b) an unbonded FREI.....	43
Figure 3-2:	Generalized horizontal force-displacement relationship for bonded isolator and SU-FREIs.....	43
Figure 3-3:	Deformed unreinforced elastomeric isolator as described by Kelly and Konstantinidis (2007) .....	43
Figure 3-4:	(a) Plan view and (b) elevation view of a FREI .....	44
Figure 3-5:	Division of the isolator into sections at a horizontal displacement, $s$ .....	44
Figure 3-6:	Definition of $d_b$ , $h$ and $\theta$ .....	44
Figure 3-7:	Relationship between the assumed equivalent follower point load, $V$ , and $F_2$ .....	45
Figure 3-8:	Deformed and undeformed cantilever with an applied follower point load, $V$ .....	45
Figure 3-9:	Local stresses initially parallel to the fiber reinforcement in the rollover section at $1.50 t_r$ with zero vertical load .....	45

Figure 3-10: Procedure for displacement prior to full rollover .....	46
Figure 3-11: Example of the normalized relationship between the angle of deflection and horizontal displacement for isolator B2.....	47
Figure 3-12: Deformed shape after full rollover showing the influence of additional horizontal displacement.....	47
Figure 3-13: Idealized representation of the isolator after full rollover .....	47
Figure 3-14: Normalized horizontal force as a function of displacement compared with experimental values with 15 % error bars .....	48
Figure 3-15: Comparison of the proposed model and theoretical full rollover deformed shape for isolators B1 .....	48
Figure 3-16: Normalized horizontal force as a function of displacement with various aspect ratios for isolator B1 .....	49
Figure 3-17: Normalized horizontal force as a function of displacement with various values of $\alpha$ for isolator B1 .....	49
Figure 3-18: Deformed shape of the rollover sections with various values of $\alpha$ at $2.00 t_r$ for isolator B1 .....	50
Figure 3-19: Normalized (a) shear displacement and (b) bending displacement of the rollover section as a function of horizontal displacement and various values of $\alpha$ for isolator B1.....	50
Figure 4-1: Compression modulus assuming a compressible elastomer normalized by the compression modulus assuming an incompressible elastomer as a function of shape factor for an infinite strip pad. ....	75
Figure 4-2: Arbitrarily shaped elastomeric pad with a Cartesian coordinate system and displacement field ( $u, v, w$ ).....	75
Figure 4-3: Lateral bulging of a constrained elastomeric pad under compression identifying the locations of the maximum shear strain due to compression.75	75
Figure 4-4: Normalized compression modulus as a function of $\alpha$ and $\beta$ for an infinite strip pad. ....	76
Figure 4-5: Percent error of $E_c$ for an infinite strip pad.....	76
Figure 4-6: Example relationship of the maximum shear strain due to compression normalized by the compression strain of an infinite strip pad as a function of the shape factor for the i) analytical solution and ii) proposed approximation. ....	77
Figure 4-7: Percent error of $\gamma_c/\varepsilon_c$ for an infinite strip pad.....	77
Figure 4-8: Percent error of $E_b$ for an infinite strip pad.....	78
Figure 4-9: Percent error of $E_c$ for a circular pad. ....	78
Figure 4-10: Percent error of $\gamma_c/\varepsilon_c$ for a circular pad. ....	79
Figure 4-11: Percent error of $E_c$ for a square pad. ....	79
Figure 4-12: Percent error of $\gamma_c/\varepsilon_c$ for a square pad. ....	80
Figure 4-13: Percent error of $E_b$ for a square pad.....	80
Figure 4-14: Percent error of $E_c$ for an annular pad ( $\eta = 0.1$ ). ....	81
Figure 4-15: Sensitivity of the percent error for $E_c$ of an annular pad to $\eta$ ( $K/G = 2000, E_{\#}/tG 20000$ ).....	81
Figure 4-16: Percent error of $\gamma_c/\varepsilon_c$ for the outer surface of an annular pad ( $\eta = 0.1$ ). ....	82

Figure 4-17: Example of $\gamma_c/\varepsilon_c$ as a function of $S$ for the inner surface of an annular pad ( $\eta = 0.1$ , $K/G = 2000$ , $E_{ft}/tG = 20000$ ). .....	82
Figure 4-18: Percent error of $\gamma_c/\varepsilon_c$ for the outer surface of an annular pad ( $\eta = 0.1$ ). .....	83
Figure 4-19: Sensitivity of the percent error for $\gamma_c/\varepsilon_c$ at the inner surface of an annular pad to $\eta$ ( $K/G = 2000$ , $E_{ft}/tG = 20000$ ). .....	83
Figure 4-20: Maximum shear strain due to compression as a function of $S$ for selected values of $G$ and $K_{e=2}$ ( $\sigma_c = 7.0$ MPa). .....	84
Figure 4-21: Percent error of (a) CSA (2014), (b) AASHTO (2014a,b) including compressibility and (c) the proposed approximation for a square pad with $G = 0.5$ MPa (left) and $G = 1.0$ MPa (right). .....	85
Figure 5-1: Location of the maximum shear strain due to (a) compression and (b) rotation. ....	104
Figure 5-2: Normalized maximum shear strain due to rotation as a function of the shape factor for an infinite strip pad. ....	104
Figure 5-3: Example of the divergence of the analytical solution and proposed approximation for an infinite strip pad with $K_{e=1}/G = 1000$ . ....	104
Figure 5-4: Comparison of the analytical solution and proposed approximation and percent error as a function of $\lambda$ for an infinite strip pad. ....	105
Figure 5-5: Percent error of $\gamma_r/\theta$ for an infinite strip pad. ....	105
Figure 5-6: Comparison of the analytical solution and proposed approximation and percent error as a function of $\lambda$ for a circular pad. ....	105
Figure 5-7: Comparison of the analytical solution and proposed approximation and percent error as a function of $\lambda$ for a square pad. ....	106
Figure 5-8: Comparison of the analytical solution and proposed approximation and percent error as a function of $\lambda$ for a rectangular pad. ....	106
Figure 5-9: Comparison of the analytical solution and proposed approximation and percent error as a function of $\lambda$ for the outer surface of an annular pad. ....	106
Figure 5-10: Normalized maximum shear strain due to rotation as a function of the shape factor for the inner surface of an annular pad ( $\eta = 0.1$ ). ....	107
Figure 5-11: Comparison of the analytical solution and proposed approximation and percent error as a function of $\lambda$ for the inner surface of an annular pad. ....	107
Figure 5-12: Comparison of the CSA (2014), AASHTO (2014b), and proposed approximations to the analytical solution. ....	107
Figure 5-13: Percent error of (a) AASHTO (2014b) and (b) the proposed approximation. ....	108
Figure 5-14: Comparison of the CSA (2014), AASHTO (2014a,b), and proposed approximations to the analytical solution. ....	108
Figure 6-1: Isolation system supporting a masonry wall with (a) localized square or circular isolators and (b) large rectangular isolators that provide uniform support. ....	125
Figure 6-2: Plan view of potential MR-FREI designs. ....	125
Figure 6-3: Profile view of the lateral bulging of (a) a circular isolator and (b) an annular isolator. ....	125
Figure 6-4: (a) Plan and (b) profile view of a FREI. ....	126

Figure 6-5:	(a) Photograph and (b) plan view of the specimens. ....	126
Figure 6-6:	(a) Photograph of the test apparatus and (b) schematic. ....	126
Figure 6-7:	Compression test time history for an unmodified isolator.....	127
Figure 6-8:	Unmodified specimen C2 experimental results showing the compression modulus determined from the third cycle. ....	127
Figure 6-9:	FE model of C4-46E. ....	127
Figure 6-10:	Deformed shape cross section of C2-35C at the design load. ....	128
Figure 6-11:	Normalized vertical stiffness as a function of (a) diameter and (b) shape factor. ....	128
Figure 6-12:	Normalized compression modulus as a function of (a) normalized diameter and (b) normalized shape factor. ....	129
Figure 6-13:	Normalized shape factor as a function of normalized diameter. ....	129
Figure 6-14:	Vertical strain distribution along the respective segments at the center of the mid-height elastomer layer. ....	130
Figure 6-15:	Average vertical strain as a function of area removed. ....	131
Figure 6-16:	Normalized vertical stress distribution along the respective segments at the center of the mid-height elastomer layer. ....	132
Figure 6-17:	Normalized $S_{xz}$ shear stress contours at the interface of the center elastomeric layer and fiber reinforcement for isolators with interior modification diameter $d/2b =$ a) 0 , b) 0.23, c) 0.35 and d) 0.58. ....	133
Figure 6-18:	Normalized $S_{xz}$ shear stress contours at the interface of the center elastomeric layer and fiber reinforcement for isolators with exterior modification diameter $d/2b =$ a) 0 , b) 0.23, c) 0.35 and d) 0.58. ....	134
Figure 6-19:	Normalized $S_{yz}$ shear stress contours at the interface of the center elastomeric layer and fiber reinforcement for isolators with interior modification diameter $d/2b =$ a) 0 , b) 0.23, c) 0.35 and d) 0.58. ....	135
Figure 6-20:	Normalized $S_{yz}$ shear stress contours at the interface of the center elastomeric layer and fiber reinforcement for isolators with exterior modification diameter $d/2b =$ a) 0 , b) 0.23, c) 0.35 and d) 0.58. ....	136
Figure 6-21:	Normalized Von Mises stress contours in center fiber reinforcement layers for isolators with interior modification diameter of $d/2b =$ a) 0 , b) 0.23, c) 0.35 and d) 0.58. ....	137
Figure 6-22:	Normalized Von Mises stress contours in center fiber reinforcement layers for isolators with exterior modification diameter of $d/2b =$ a) 0 , b) 0.23, c) 0.35 and d) 0.58. ....	138
Figure 7-1:	Idealized division of a (a) bonded and (b) unbonded FREI.....	159
Figure 7-2:	MSG that (a) accelerates full rollover, and (b) delays full rollover.....	159
Figure 7-3:	Cartesian coordinate system and deformed shape of the isolator with A-MSG at full rollover.....	159
Figure 7-4:	(a) Full rollover displacement and (b) corresponding parameters $a$ and $a_o$ for an isolator with unit height, neglecting the thickness of the reinforcement. ....	159
Figure 7-5:	Schematic of the experimental setup. ....	160

Figure 7-6:	Normalized force-displacement experimental hysteresis loops for different levels of MSG.....	160
Figure 7-7:	Isolator deformed shape at $u/t_r = 1.50$ (left), 2.00 (center) and 2.50 (right). .....	161
Figure 7-8:	Idealized prototype structure and light equipment. ....	161
Figure 7-9:	Comparison of the normalized experimental and model hysteresis loops. ....	161
Figure 7-10:	Scaled displacement and pseudo-acceleration response spectra showing the mean spectrum of the 14 ground motions and the design spectrum at Victoria City Hall, Canada. ....	162
Figure 7-11:	Normalized mean peak isolator displacement and normalized base shear as a function of the earthquake hazard level. ....	162
Figure 7-12:	Mean peak IDR as a function of the earthquake hazard level. ....	162
Figure 7-13:	Mean peak floor absolute acceleration at level 3 of the structure as a function of the earthquake hazard level. ....	163
Figure 7-14:	Mean floor pseudo-acceleration response spectra (Level 3). ....	163
Figure 7-15:	Mean displacement of sliding equipment as a function of hazard level (Level 3). ....	164
Figure 7-16:	Fifth order polynomials used in the parametric study displaying the three stiffening levels for each MSG. ....	164
Figure 7-17:	Mean response of key performance indicators as a function of earthquake hazard level. ....	165
Figure 7-18:	Mean floor pseudo-acceleration response spectra ( $k-1$ ). ....	166
Figure 7-19:	Sliding equipment mean displacement demand. ....	166
Figure 8-1:	Deformed shape of (a) an unbonded FREI and (b) a bonded isolator .....	184
Figure 8-2:	Deformed shape of an isolator with $R = 2.5$ and $R = 4.0$ at full rollover, showing the portion of the width that remains in contact with the supports .....	184
Figure 8-3:	Exaggerated delayed loss of contact due to vertical deflection, $d_v$ .....	184
Figure 8-4:	Profile view identifying bonded and unbonded regions of (a) isolator E1-2 ( $B = 50\%$ ) and (b) isolator E2-2, ( $B = 33\%$ ).....	185
Figure 8-5:	Horizontal experimental displacement history .....	185
Figure 8-6:	Normalized experimental force-displacement hysteresis loops for (a) isolator E1-1 and E1-2, and (b) isolator E2-1 and E2-2 .....	186
Figure 8-7:	Comparison of the deformed shape of the rollover of E1-1 and E1-2.....	186
Figure 8-8:	FEA model of isolator E1 .....	187
Figure 8-9:	Comparison of FEA and experimental results with 15 % error bars for (a) E1-1 and (b) E2-1 .....	187
Figure 8-10:	Vertical stress strain relationship for isolator type E1 from FEA under tension and compression.....	187
Figure 8-11:	Normalized local stress $S_{33}$ contours for isolator type E1 with $B = 50\%$ under (a) 1.0 MPa compressive and (b) 0.4 MPa tensile stress.....	188
Figure 8-12:	Comparison of $B = 0\%$ and $B = B_{max} = 5\%$ results for isolator type E1 showing negligible difference between the bonded and unbonded case ....	188

Figure 8-13: Normalized local stress $S_{33}$ contours for isolator type E1 with (a) $B = 0 \%$ and (b) $B = B_{max}$ at $2.00 t_r$ .....	189
Figure 8-14: Normalized force-displacement relationship with $B > B_{max}$ for (a) isolator type E1 and (b) isolator type E2 .....	189
Figure 8-15: Normalized local stress $S_{33}$ of isolator type E1 with $B = 50 \%$ at $2.00 t_r$ ...	190
Figure 8-16: Idealized division of a PB-FREI into five sections. ....	190
Figure 8-17: Normalized local stress $S_{33}$ of isolator type E1 with $B = 75 \%$ at $2.00 t_r$ ...	190
Figure 8-18: Normalized local stress $S_{33}$ of isolator type E2 with $B = 75 \%$ at $2.00 t_r$ ...	190
Figure 8-19: Normalized (a) force and (b) stiffness as a function of displacement for isolator type E1 with $B = 0 \%$ and a 2.0 MPa average vertical compressive stress and $B = 50 \%$ with a 0.2 MPa average vertical tensile stress .....	191
Figure 8-20: Normalized local stress $S_{33}$ of isolator type E2 with $B = 50 \%$ and 0.2 MPa average vertical tensile stress at (a) $1.00 t_r$ , (b) $1.50 t_r$ , and (c) $2.00 t_r$ .....	192

## **Co-Authorship**

This thesis has been prepared in accordance with the regulations for a “sandwich” thesis format as stipulated by the School of Graduate Studies at McMaster University. The thesis has been co-authored as:

### **Chapter 3: Model of the Shear Behavior of Unbonded Fiber-Reinforced Elastomeric Isolators**

Authors: N.C. Van Engelen, M.J. Tait and D. Konstantinidis

The analytical model was developed by N.C. Van Engelen under the supervision of M.J. Tait and D. Konstantinidis. The manuscript was prepared by N.C. Van Engelen under the supervision of M.J. Tait and D. Konstantinidis. This chapter has been published in the Journal of Structural Engineering (ASCE).

### **Chapter 4: Development of Design Code Orientated Formulas for Elastomeric Bearings Including Bulk Compressibility and Reinforcement Extensibility**

Authors: N.C. Van Engelen, M.J. Tait and D. Konstantinidis

The proposed generalized formulas and corrections factors were derived by N.C. Van Engelen under the supervision of M.J. Tait and D. Konstantinidis. The manuscript was prepared by N.C. Van Engelen under the supervision of M.J. Tait and D. Konstantinidis. This chapter has been published in the Journal of Engineering Mechanics (ASCE).

### **Chapter 5: Shear Strain Demands in Elastomeric Bearings Subjected to Rotations**

Authors: N.C. Van Engelen, D. Konstantinidis and M.J. Tait

The proposed generalized formulas and corrections factors were derived by N.C. Van Engelen under the supervision of D. Konstantinidis and M.J. Tait. The manuscript was prepared by N.C. Van Engelen under the supervision of D. Konstantinidis and M.J. Tait. This chapter has been prepared for the Journal of Bridge Engineering (ASCE).

### **Chapter 6: Experimental and Finite Element Study on the Compression Properties of Modified Rectangular Fiber-Reinforced Elastomeric Isolators (MR-FREIs)**

Authors: N.C. Van Engelen, P.M. Osgooei, M.J. Tait and D. Konstantinidis

The experimental testing was conducted by N.C. Van Engelen under the supervision of M.J. Tait. The finite element analysis was conducted by P.M. Osgooei under the supervision of M.J. Tait and D. Konstantinidis. The manuscript was prepared under the

supervision of M.J. Tait and D. Konstantinidis. P.M. Osgooei wrote the finite element model description and related figures. N.C. Van Engelen wrote the remaining sections of the manuscript and prepared the remaining figures. Modifications and revisions were made by all contributing authors. This chapter has been published in Engineering Structures.

### Chapter 7: Structural and Non-structural Performance of a Seismically Isolated Building using Stable Unbonded Fiber-Reinforced Elastomeric Isolators

Authors: N.C. Van Engelen, D. Konstantinidis and M.J. Tait

The experimental testing, OpenSees element development, OpenSees modelling, and analysis was conducted by N.C. Van Engelen under the supervision of D. Konstantinidis and M.J. Tait. The manuscript was prepared by N.C. Van Engelen under the supervision of D. Konstantinidis and M.J. Tait. This chapter has been published in Earthquake Engineering and Structural Dynamics.

### Chapter 8: Partially Bonded Fiber-Reinforced Elastomeric Isolators (PB-FREIs)

Authors: N.C. Van Engelen, P.M. Osgooei, M.J. Tait and D. Konstantinidis

The experimental testing was conducted by N.C. Van Engelen under the supervision of M.J. Tait. The finite element analysis was conducted by P.M. Osgooei under the supervision of M.J. Tait and D. Konstantinidis. The manuscript was prepared under the supervision of M.J. Tait and D. Konstantinidis. P.M. Osgooei wrote the finite element model description and N.C. Van Engelen wrote the remaining sections of the manuscript and prepared the figures. Modifications and revisions were made by all contributing authors. This chapter has been published in Structural Control and Health Monitoring.

## 1 Introduction

Current building codes around the globe, including the National Building Code of Canada (NBCC) [1], use a force-based design approach that predicts the performance of the structure based on the elastic stiffness. It is anticipated and accepted that some level of damage will occur within the structure during a strong earthquake event. In order to accommodate this, the structure is designed such that plastic hinges form in strategic locations to utilize ductility and allow deformations to occur without compromising the structural integrity. Although plastic hinges aid to protect the structure from catastrophic failure, the cost of repairing localized damage remains high [2], and the economic consequences of the loss of functionality of the structure during repairs cannot be overlooked.

In addition to the tragic loss of thousands of lives, 2011 saw the largest economic losses ever recorded worldwide due to earthquake related damages [3]. Included in these losses are the Canterbury earthquakes, a series of earthquakes that were larger than anticipated and occurred in an unexpected area. Although relatively small in a global and historical perspective, this series of earthquakes devastated the downtown core of Christchurch, New Zealand, and resulted in the deaths of nearly 200 people [3]. While the scale of this devastation was intolerable, losses from earthquake events are also inevitable. Large areas of Canada are relatively seismically inactive; however, large portions of the population reside along the west coast and the St. Lawrence River valley, two of the most seismically active areas in Canada. Scenarios portraying moderate seismic events in these areas project losses exceeding 60 billion [4], in addition to a large number of potential injuries and fatalities.

For conventional structures, the issue of repair or replacement requirements after a significant earthquake event will always remain to some degree. Furthermore, the value of an average office building is dominated by the contents and non-structural components contained within it, which can account for 80 % of the total value, far surpassing the worth of the structure [5]. Conventional seismic design approaches offer little protection to equipment within the structure which may be damaged due to the high floor accelerations induced by an earthquake event. In this way, it is possible to compromise the functionality of a facility without necessarily damaging the structure itself.

The inherent large uncertainties associated with earthquake events and the probabilistic nature of design procedures make it imperative to investigate and appreciate the consequences of making an error. These uncertainties present unique challenges to designers when considering earthquake loading on a structure. The long return periods of large seismic events, which can be hundreds or thousands of years, allow past events to fade from memory as the general public becomes complacent and less concerned of the

looming hazard. Designing a structure to withstand earthquakes is a delicate balancing act between perceived hazard, actual hazard, the cost of the structure, insurance premiums, and potential repairs or replacements.

Substantial improvements to earthquake engineering practices often come after a major seismic event. The drive to develop effective methods of mitigating the potential for damage or the loss of functionality of the structure or the contents has seen many new and innovative approaches proposed as the knowledge of the response of structures to strong ground motions increases. Amongst these innovative technologies is seismic base isolation, a passive approach to earthquake engineering that seeks to prevent the development of large seismic forces within the structure, simultaneously protecting the structure, the contents, and most importantly the people within the structure.

### *1.1 Basic Concept of Base Isolation*

Conventional buildings and bridges are constructed directly on top of a foundation that transfers the loads from the structure to the ground. In the case of strong ground motions, the reverse is also true, and the foundation can be viewed as an avenue for loads to be transferred to the superstructure, causing the structure to experience large accelerations and related inertial forces. In lieu of constructing the structure directly on top of the foundation, a soft horizontal layer can be introduced. The soft horizontal layer decouples the structure from ground motions in the horizontal direction, resulting in concentrated large displacements at the isolation layer that dominate the response of the structure, as demonstrated in Figure 1-1. The resulting fundamental frequency of the base isolated structure is in a range where the energy content of a typical earthquake is much less severe, causing lower response accelerations, as illustrated in Figure 1-2. The new low frequency mode shape introduced by the isolation layer experiences minor inter-storey displacements; consequently, the structure ideally responds as a near-rigid block on top of the isolation layer. The overall result is a significant reduction of accelerations and associated forces and other key performance indicators within the structure.

The benefits of a base isolation system are closely related to the shift in the fundamental frequency with secondary benefits and further reductions in accelerations obtained due to superior damping characteristics within the isolation system. The amount of damping introduced by the isolation system varies significantly depending on the type of isolator [6]. It is also not uncommon to include a supplementary damping system (e.g. steel U-shaped dampers or lead dampers) as an addition to the isolation system to improve the overall damping characteristics of the system.

## *1.2 Main Design Considerations*

There are three main design considerations associated with base isolated structures: a high vertical stiffness, low horizontal stiffness and sufficient damping [7]. Intuitively, the isolation layer must be capable of supporting the vertical load of the structure. The vertical accelerations of an earthquake event are often considered to be of lesser concern than the horizontal accelerations, or simply neglected by designers. Isolation elements with a high vertical stiffness are necessary to suppress potential rocking modes introduced by the isolation system [6]. The high vertical stiffness minimizes the vertical movement of the structure, suppressing potential vertical motions and ideally resulting in similar vertical performance as a conventional fixed base structure.

The effectiveness of a base isolation system is primarily associated with horizontal flexibility; therefore, the horizontal stiffness must be sufficiently low to ensure that the fundamental frequency is displaced out of the critical high energy range of a typical earthquake. Despite the shift in fundamental frequency, some energy will always occur at the isolation frequency. A lower fundamental frequency is associated with large displacements, which are responsible for an increase in cost and loss of real estate value as the size of the seismic gap, or area around the structure that the building displaces into, must be increased. It is necessary to ensure that the displacements of the structure do not exceed the seismic gap to prevent the structure from impacting the moat walls. Sufficient damping is required at the isolation level to restrict the displacements to an acceptable level. Some level of initial stiffness is also required to prevent excessive movement under small earthquakes and service wind loading.

## *1.3 Economics and Application*

There are many obstacles to overcome before base isolation becomes common worldwide. One of the most significant obstacles is the additional cost associated with the isolation system. There are four principle cost considerations as a consequence of earthquakes for the construction of new facilities [8]: the initial cost of construction; annual earthquake insurance premium; physical damage that must be repaired after an earthquake; and damage to building contents, injury to occupants, and loss of building use during repairs. Although a base isolation system increases the initial cost of construction, it has the potential to significantly reduce the costs associated with the other three considerations.

The cost of implementing a base isolation system has thus far largely restricted the application to high importance structures, primarily those of historical significance such as city halls and government buildings [6]. New construction projects can be viewed as having an advantage over the retrofit of existing structures simply due to increased access to the isolation layer, resulting in reduced labour in the installation process. It is important

to compare the performance of the seismically isolated structure with a traditional fixed base structure designed to provide the same degree of protection [6]. In this scenario, the base isolated structure is always more cost effective since stiffening a structure to prevent damage typically also results in increased force demand.

Existing structures, constructed according to older building codes based on limited knowledge of structural response to earthquakes, pose a greater risk of catastrophic failure or significant damage. Ultimately, the cost of the isolation system would be substantially less than the costs associated with replacing the structure, including economic losses. In some cases, such as for historical structures, the building is simply irreplaceable. When considering the loss of life that can be prevented by widespread base isolation practice, the initial cost is well justified. Despite this, developing a cost-effective and practical method to apply base isolation in developing countries, where loss of life from seismic events is generally more severe due to poor construction practices, remains a primary focus within the research community.

The acceptance of base isolation within the engineering community is primarily dependant on code requirements and appreciation of the benefits. Current code requirements are generally complicated and conservative, not allowing the full benefits of a base isolated structure to be realized [6]. Full scale data on base isolated structures and performance reviews are generally restricted to the occurrence of a significant earthquake event. Furthermore, although the concept has been recognized for over 100 years, it has only gained significant recognition in the academic community in the last few decades. As the engineering community becomes more familiar with the concept and application, and as earthquake events occur and clearly emphasize the benefits of base isolation, it is anticipated that base isolation will become common practice in high seismicity zones around the world.

#### *1.4 Types of Isolators*

Seismic base isolators generally fall into two broad categories: sliding and elastomeric. The former is characterized by sliding between two or more surfaces with a low coefficient of friction. Variations of the friction pendulum system, shown in Figure 1-3, use a spherical sliding surface to provide a restoring force. If the curvature is constant, the system will have a linear restoring force. Non-linear adaptive responses (i.e. the properties of the device change depending on the loading level) can be obtained by introducing multiple sliding surfaces, such as the triple friction pendulum (TFP) [9] or sliding systems with variable curvature [10].

Elastomers have been used in base isolation since 1969 and are ideal for base isolation due to the soft material properties and near incompressibility [11]. The near incompressibility of the elastomer causes it to bulge laterally when compressed under the

weight of the structure as shown in Figure 1-4. Without reinforcement, the vertical and horizontal stiffness values of a solid elastomeric pad are comparable. In order to suppress potential rocking modes, alternating horizontal layers of elastomer and reinforcement are used. The reinforcement restrains the lateral bulging which develops a high vertical stiffness with little change to the horizontal stiffness.

#### **1.4.1 Steel-Reinforced Elastomeric Isolators**

Steel shims were originally selected as the reinforcement of choice to reduce lateral bulging and vertically stiffen the isolator. A steel-reinforced elastomeric isolator (SREI) typically contains two large steel end plates and many thin reinforcing plates. After an extensive preparation process, the steel is bonded to the elastomeric layers during vulcanization [11]. The large steel end plates are used to mechanically fasten the isolator to the structure and the foundation. A profile view of a bonded SREI is illustrated in Figure 1-5. SREIs are inherently heavy and expensive, weighing one ton or more and costing as much as \$10,000 for a single isolator [12, 13]. The cost and weight of this type of isolator have been perceived to act as barriers to its widespread application.

#### **1.4.2 Fiber-Reinforced Elastomeric Isolators**

Fiber-reinforced elastomeric isolators (FREIs) were proposed as an alternative to conventional SREIs [13]. The fiber reinforcement is substantially lighter than steel but has similar mechanical properties in tension. In this preliminary study [13], advantageous damping characteristics were identified and attributed to the inter-fiber movements. Furthermore, it was suggested that FREIs could be manufactured in larger pads and subsequently cut to the desired size. Isolators cut from a larger pad were evaluated by Toopchi-Nezhad et al. [14] in an experimental study and shown to perform well in the vertical and horizontal direction, thus validating the concept.

#### **1.4.3 Unbonded Fiber-Reinforced Elastomeric Isolators**

The installation costs could be further reduced by positioning the isolator unbonded between the supports, thereby eliminating the need for large steel end plates to mechanically fasten the isolator to the supports. Finite element analysis has identified that the unbonded application also prevents the development of large tensile stresses that occur within the elastomeric layers of bonded isolators [15]. Due to the lower tensile stress demand, the bond requirements between the elastomer and reinforcement are also reduced. Note that the unbonded application determines that this device is unable to resist tensile forces and is also susceptible to slip and residual displacements in extreme loading conditions.

As a consequence of the unbonded application and the lack of flexural rigidity of the fiber reinforcement, unbonded FREIs undergo a unique *rollover* deformation.

Rollover occurs as the initially horizontal surfaces of the isolator rotate and lose contact with the supports, illustrated in Figure 1-6a. Rollover will continue until the initially vertical faces of the isolator become horizontal and contact the supports, denoted as *full rollover*, illustrated in Figure 1-6b. Rollover is the characteristic feature of unbonded FREIs and is associated with several potentially advantageous performance characteristics.

The size of the rollover section is proportional to the horizontal displacement [16]. The resistance to horizontal displacement is greater in pure shear than an equivalent rollover section. Therefore, as rollover occurs the isolator softens. This softening continues until full rollover occurs, restricting further rollover, stiffening the isolator. The magnitude of the softening is proportional to the aspect ratio, defined as the ratio of the width-to-total height in the direction of horizontal displacement. Isolators with low aspect ratios are highly sensitive to rollover. Originally observed by Toopchi-Nezhad et al. [17], as the aspect ratio increases, the size of the rollover section, which remains constant, becomes small in comparison to the size of the isolator, reducing the sensitivity to the rollover and the softening. If the tangential horizontal stiffness remains positive at all levels of imposed horizontal displacement, the isolator is defined as being horizontally *stable* and to have undergone *stable rollover*. Isolators exhibiting this type of stable behaviour were denoted as stable unbonded fiber-reinforced elastomeric isolators (SU-FREIs) [14]. In Toopchi-Nezhad et al. [17] stable rollover was observed in unbonded FREIs with an aspect ratio of 2.5.

The softening and stiffening regimes of SU-FREIs are believed to be ideal to meet the multiple performance objectives, implying that SU-FREIs can serve as adaptive devices. At very low displacements the horizontal stiffness is initially large, which reduces excessive movement due to smaller service loads. If a substantial seismic event occurs, the isolator will operate in the softening regime, maximizing the efficiency of the system. During extreme events, the stiffening regime caused by full rollover is believed to serve as a self-restraint mechanism to restrict excessive displacements. An idealized force-displacement relationship of a SU-FREI and bonded isolator is compared in Figure 1-7.

### 1.5 *Impetus and Research Objectives*

Though the concept of base isolation is well established, the application of this technology has varied significantly globally and is limited in Canada. Initially proposed as potentially low-cost isolators, the development of FREIs has greatly increased the practicality and potential application of elastomeric isolators. While some of the benefits of FREIs have been identified in experimental and finite element studies, understanding and predicting the performance of this type of isolator is largely unexplored. The

characteristic softening and stiffening of SU-FREIs are believed to be ideal for SU-FREIs to function as an adaptive device, enabling the device to meet multiple performance objectives at different hazard levels. To fully appreciate and utilize the identified benefits, a detailed understanding of the factors influencing the characteristics is required, thus enabling designers to obtain the desired hysteretic response for the specific case being considered.

This study demonstrates that the horizontal force-displacement relationship of unbonded FREIs can be predicted, and that critical properties, such as the compression modulus and bending modulus, can be determined from simple expressions appropriate for use in design codes. The versatility and adaptability of unbonded FREIs is established through experimental testing and numerical modelling investigating changes to the geometry of the isolator and the supports to tailor the hysteresis to the desired response. Potential limitations are identified and addressed by proposing a new device: a hybrid isolator merging the beneficial characteristics of an unbonded and fully bonded isolator. This study generates original knowledge aimed at increasing base isolation practice with fiber-reinforced elastomeric isolators by transitioning fiber-reinforcement from being viewed as an unknown variable, to a known variable that offers beneficial features.

### *1.6 Structure of Thesis*

This thesis contains previously published and prepared materials. Chapter 3 to Chapter 8 were designed to become stand-alone documents and, as such, each chapter contains references. Due to the structure of the thesis, it is likely that overlap will occur between chapters, mainly in the introduction and background of each.

Chapter 2 provides a brief literature review with focus on FREIs. The chapter discusses material considerations and fundamental concepts relating to the vertical and horizontal stiffness. Other considerations, such as stability, are also discussed. Many of these concepts are discussed in greater detail in the literature reviews contained within subsequent chapters.

Chapter 3 develops an analytical model for the shear behaviour of unbonded FREIs that includes the contributions of the rollover sections. Large deflection theory is used to model the deformed shape of the rollover section and predict full rollover. The model is used to conduct a parametric study on the width-to-total height aspect ratio and reinforcement stiffness.

Chapter 4 proposes generalized expressions for the compression modulus, bending modulus and maximum shear strain due to compression for use in design codes. The expressions are obtained through a procedure involving Taylor series expansions and truncations. The generalized expressions include bulk compressibility and reinforcement

extensibility and can be adapted to different pad geometries by selecting coefficients from a table.

Chapter 5 expands on Chapter 4, developing generalized expressions for the maximum shear strain due to rotation. Generalized expressions for the compression modulus, bending modulus, and maximum shear strain due to compression for a rectangular pad are also derived. Together, Chapter 4 and 5 present a full suite of generalized equations appropriate for use in design. It is demonstrated that both the compressibility of the elastomer and reinforcement extensibility can be accounted for in simple expressions that are often more accurate than expressions used in existing codes and standards.

Chapter 6 and 7 investigate methods of modifying the hysteretic characteristics of FREIs. Chapter 6 proposes that rectangular isolators can be modified with the introduction of holes to soften the horizontal response. The paper includes an experimental and numerical study on the sensitivity of the vertical properties of modified rectangular FREIs to the size and geometry of the hole. Chapter 7 numerically models a structure subjected to increasing earthquake hazard levels. The study investigates the effect of the softening and stiffening characteristics on the structure based on selected key performance indicators. The stiffening characteristics are altered using modified support geometry to accelerate or delay full rollover.

Chapter 8 proposes the concept of partially bonding FREIs to form a hybrid between bonded and unbonded isolators. An experimental program is conducted with two different isolator layer designs and bond lengths. The experimental results are used to develop a finite element model that investigates the sensitivity of the horizontal properties to bond length and the possibility of vertical tensile loading.

Chapter 9 concludes the thesis. It summarizes the primary findings from each chapter. It also provides recommendations and sets a direction for future research into FREIs.

### *References*

- [1] National Building Code of Canada. 2010. National Building Code of Canada. Canada: Institute for Research in Construction, National Research Council of Canada.
- [2] Priestly MJN. 2000. Performance Based Seismic Design. *12<sup>th</sup> World Conference on Earthquake Engineering*, New Zealand.
- [3] Swiss Re. 2012. *Lessons from Recent Major Earthquakes*. Retrieved from [www.swissre.com](http://www.swissre.com).
- [4] AIR Worldwide. 2013. Study of impact and the insurance and economic cost of a major earthquake in British Columbia and Ontario/Québec. Boston, USA: AIR Worldwide.

- [5] Taghavi S, Miranda E. 2003. Response Assessment of Nonstructural Building Elements, Pacific Earthquake Engineering Research Center Report 2003/05. Berkeley, California: University of California, Berkeley.
- [6] Naeim F, Kelly JM. 1999. *Design of Seismic Isolated Structures: From Theory to Practice*. USA: John Wiley & Sons.
- [7] Derham CJ, Kelly JM, Thomas AG. 1985. Nonlinear Natural Rubber Bearings for Seismic Isolation. *Nuclear Engineering and Design*, 84(3): 417-428.
- [8] Mayes RL, Jones LR, Buckle IG. 1990. Impediments to the Implementation of Seismic Isolation. *Earthquake Spectra*, 6(2): 283-296.
- [9] Fenz D, Constantinou MC. 2008. Spherical Sliding Isolation Bearings with Adaptive Behaviour: Theory. *Earthquake Engineering and Structural Dynamics*, 37(2): 163-183.
- [10] Lu LY, Lee TY, Yeh SW. 2011. Theory and Experimental Study for Sliding Isolators with Variable Curvature. *Earthquake Engineering and Structural Dynamics*, 40(14): 1609-1627.
- [11] Kelly JM, Konstantinidis D. 2011. *Mechanics of Rubber Bearings for Seismic and Vibration Isolation*. Chichester UK: John Wiley & Sons.
- [12] Kelly JM, Marsico MR. 2010. Stability and Post-buckling Behavior in Nonbolted Elastomeric Isolators. *Seismic Isolation and Protection Systems*. 1(1):41-54.
- [13] Kelly JM. 1999. Analysis of Fiber-reinforced Elastomeric Isolators. *Journal of Seismology and Earthquake Engineering*, 2(1): 19-34.
- [14] Toopchi-Nezhad H, Tait MJ, Drysdale, RG. 2008. Lateral Response Evaluation of Fiber-Reinforced Neoprene Seismic Isolators Utilized in an Unbonded Application. *Journal of Structural Engineering*, 134(10): 1627-1637.
- [15] Toopchi-Nezhad H, Tait MJ, Drysdale RG. 2011. Bonded versus Unbonded Strip Fiber Reinforced Elastomeric Isolators: Finite Element Analysis. *Composite Structures*, 93(2): 850-859.
- [16] Kelly JM, Konstantinidis D. 2007. Low-cost Seismic Isolators for Housing in Highly-seismic Developing Countries. *10th World Conference on Seismic Isolation, Energy Dissipation and Active Vibrations Control of Structures*, Istanbul, Turkey.
- [17] Toopchi-Nezhad H, Tait MJ, Drysdale RG. 2008. Testing and Modeling of Square Carbon Fiber-reinforced Elastomeric Seismic Isolators. *Structural Control and Health Monitoring*, 15(6): 876-900.

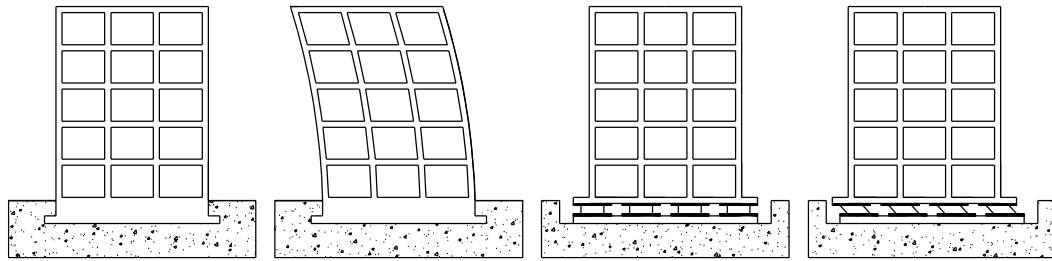


Figure 1-1: Mode shapes of a discretized three storey structure

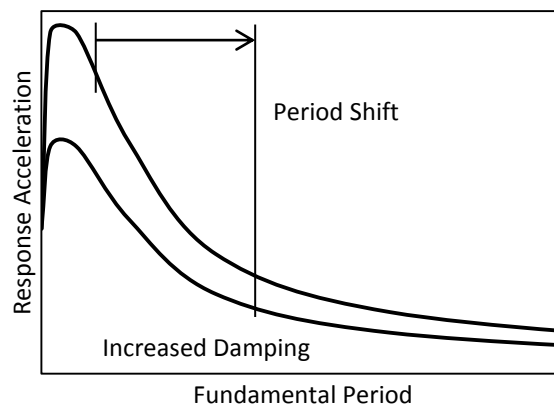


Figure 1-2: Idealized acceleration response spectra showing the decrease in response acceleration caused by a base isolation system



Figure 1-3: Friction Pendulum System

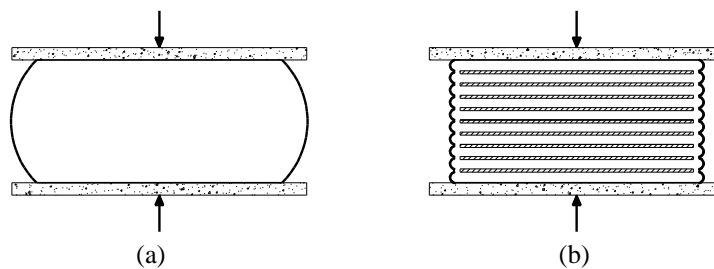


Figure 1-4: Lateral bulging of an (a) unreinforced and (b) reinforced elastomeric isolator under vertical load

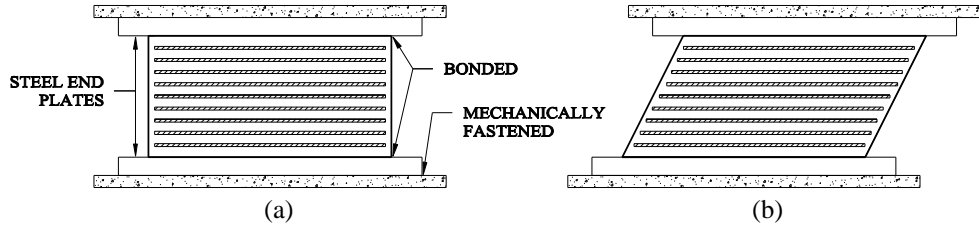


Figure 1-5: Profile view of a bonded (a) undeformed and (b) deformed SREI

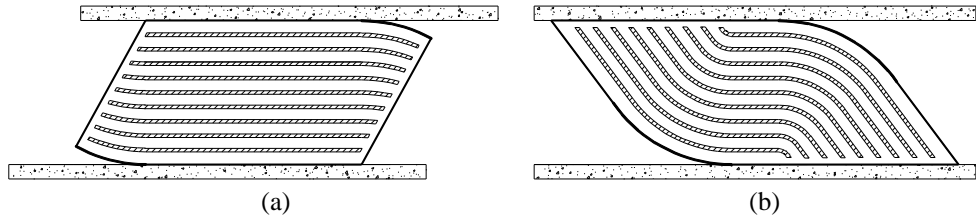


Figure 1-6: Profile view of an unbonded FREI showing (a) rollover and (b) full rollover

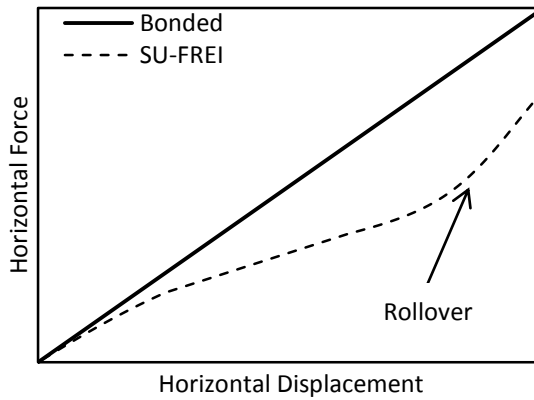


Figure 1-7: Idealized horizontal force-displacement relationship for a bonded FREI and SU-FREI

## **2 Literature Review of Elastomeric Isolators**

### *2.1 Elastomeric Materials*

#### **2.1.1 Main Considerations**

Elastomers are materials that can undergo large recoverable strains at relatively low stress levels [1]. The near incompressibility and soft material properties of elastomers make them ideal for application as base isolators. Elastomeric base isolators are typically manufactured using natural rubber, although Neoprene has also been used [2]. The stress strain relationships of elastomeric materials are inherently non-linear due to the cross-linked molecular chains that are highly twisted, kinked, and coiled [1]. This non-linear behaviour is characterized by three main phenomena: non-linear elastic response under static load; rate-dependent hysteretic behaviour under cyclic loading; and the Mullins effect [3]. The Mullins effect is a strain-induced stress softening during loading cycles. The Mullins effect can be observed in tension, compression, or shear loading. The stress variation over successive cycles is largest between the first and second cycle and decreases over each subsequent cycle. After six to ten cycles, the stress variation often becomes negligible [4]. In light of the Mullins effect, design codes often indicate which cycle the isolator properties should be determined from or stipulate the maximum decrease in horizontal stiffness allowed between successive cycles [5, 6].

Despite the non-linear properties of the elastomer, elastomeric bearings are often studied analytically assuming the elastomer to be linear elastic [7-18]. Material properties, such as the shear modulus, are often selected depending on the magnitude of the expected strain, if possible, or selected from a standardized test at a suggested strain. Numerous FEA investigations have modelled the elastomer using simple material models based on one or two material parameters and obtained good agreement with experimental results [19-23]. Other investigations (e.g. [24]) have selected material models requiring more terms to better capture the non-linear characteristics. Despite the commonly assumed linear elastic behaviour in analytical investigations and simplified material models in FEA, it should be appreciated that the material and load conditions may have considerable influence on the performance of the elastomeric isolator.

#### **2.1.2 Long-Term Performance**

The inherent long design life of structures requires the consideration of the long-term performance: notably, the evolution of the elastomeric properties due to aging, creep due to sustained loads, and fatigue due to repeated cycles. Seismic isolation with elastomeric bearings remains in the early stages of its application and development, consequently research in these areas can be limited.

Aging refers to exposure of the elastomer to environmental factors (e.g. ozone, heat, oxygen, sunlight, humidity, etc.). The aging process of elastomers notably causes stiffening, decrease in ductility before failure and decreased tensile strength. An accurate understanding of the aging characteristics of the elastomeric material is necessary to prevent additional financial burdens due to the premature replacement of a functioning system; or having a system perform otherwise than intended by design due to an increase in the stiffness and decrease in the ductility; which could have significant consequences.

Smaller isolators are more sensitive to aging due to the larger ratio of exposed surface area to total volume of elastomer [25]. The permeability of the elastomer decreases significantly with oxidation, subsequently acting as a mechanism to prevent further oxidation of the interior volume of elastomer. This was demonstrated experimentally on Neoprene and natural rubber by Yura et al. [26]. The investigation used accelerated aging to compare three sizes of square Shore A 50 and 70 Durometer specimens with lengths of 25 mm, 51 mm and 76 mm.

Aging of elastomers has been studied extensively using the Arrhenius approach, which aims to accelerate the natural aging process by heating the elastomer and translating the change in properties into aging at ambient temperatures. This approach has been adapted in numerous design codes; however, it is often difficult to quantify what time period the accelerated approach represents at ambient temperatures. Experimental investigations on the aging of natural rubber using accelerated methods [25-29]; and Neoprene with natural aging [2, 30] and accelerated methods [26, 30-32] have all concluded that the aging of the elastomer may be significant and should be included in the design process; however, the magnitude of the aging varies significantly between the studies and time periods considered.

## 2.2 Reinforcement

The primary function of the reinforcement is to restrain the lateral bulging of the elastomeric layers when vertically compressed under the weight of the structure. Due to the near incompressibility of the elastomer, the restraint of lateral bulging vertically stiffens the isolator while leaving the horizontal stiffness relatively unchanged. As the lateral bulging is increasingly restrained, the bulk compressibility can play an important role in the properties of the isolator. The reinforcement generates shear stresses in the elastomer as lateral bulging develops. The reaction to the shear stress in the elastomer is a horizontal tensile stress in the reinforcement. The analytical solution for tensile stresses in the steel reinforcement of a circular pad was presented in Kelly and Konstantinidis [8, 33] assuming a compressible or incompressible elastomer. The solution showed that the stress in the circular steel plates is often considerably less than the yield stress, with the maximum stress occurring at the center.

Unlike steel reinforcement, the mechanical properties of fiber reinforcement can vary considerably by type of fiber, weave, and density of fibers. For example, Russo et al. [31] compared FREIs with bi-directional and quadri-directional carbon fiber weaves. It was found that the quadri-directional weave increased the vertical stiffness and the energy dissipation during horizontal cyclic tests. Note that the fabric density in the quadri-directional weave was larger than the bi-directional weave. An increase in fabric density (i.e. more fibers are present) is expected to allow for increased inter-fiber movements and consequently increased energy dissipation [10].

In an earlier study on FREIs, Kevlar fiber was used [7]. The experimental portion of the study identified that the use of fiber reinforcement was able to substantially increase the equivalent viscous damping from 8 % associated with the elastomeric compound to between 14 % and 19 % depending on the shear strain. It was postulated that the increased energy dissipation characteristics originate from slip between the individual fibers of the reinforcement [7]. A subsequent study compared the use of Polyester, FIBP, Nylon, carbon and glass fibers as reinforcement [34]. The study confirmed, through experimental testing, that fiber reinforcement was able to provide substantial vertical stiffness and increased damping in comparison to steel reinforcement.

More recently, two experimental programs have compared FREIs and SREIs that either observed no appreciable difference in equivalent viscous damping [35] or that the equivalent viscous damping improved with fiber reinforcement [36]. Naghshineh et al. [35] experimentally compared bonded circular and annular SREI and FREI specimens with different thicknesses of elastomer and reinforcement. The bearings were compared by matching the shape factor, but the total height of the specimens varied. The fiber reinforcement was a bi-direction carbon fiber mesh, which was selected to accommodate better bonding between the elastomeric layers. Based on horizontal cyclic experiments, Naghshineh et al. [35] found that the equivalent viscous damping of the SREI was between 90 % and 128 % of the FREI depending on the specimen and cycle amplitude. Naghshineh et al. [35] concluded that since the equivalent viscous damping was comparable, that the elastomer provides most of the energy dissipation.

Strauss et al. [36] experimentally investigated square bonded and unbonded FREIs and bonded SREIs. The fiber reinforcement was plain weave bi-directional carbon fiber. Three layer designs were considered with the shape factor held consistent between specimens of the same layer design, allowing the total height to vary. Strauss et al. [36] observed that FREIs achieved higher values of equivalent viscous damping than SREIs over a range of vertical stress. By comparing bonded and unbonded FREIs, it was found that the unbonded FREIs generally had lower equivalent viscous damping than the bonded FREIs.

These studies suggest that the energy dissipation of the fiber reinforcement in FREIs is not yet quantifiable. It should be noted that the fundamental differences between a SREI and FREI make a direct comparison difficult to achieve (e.g., the thickness of the reinforcement, and consequently the height and vertical stiffness, amongst other parameters are not necessarily identical).

In general, SREIs and FREIs are analyzed in a similar fashion. Assumptions relating to the elastomer apply to both isolator types with the analysis varying only on assumptions related to the mechanical properties of the reinforcement. Steel reinforcement is often assumed to be rigid in flexure and inextensible, whereas fiber reinforcement is conversely assumed to be extensible and to provide no appreciable resistance in bending. Methods of analyzing elastomeric isolators are further investigated in the subsequent sections.

### 2.3 Vertical Stiffness

The volumetric strain and volume of lateral bulging, and consequently the vertical stiffness, is dependent on the elastomeric layer geometry and thickness. This dependency is often represented by the shape factor of the elastomeric layer, defined as the ratio of loaded area to unloaded area. The assumption of incompressibility is convenient for simplifying the analysis, although it can lead to unconservatively high estimates of the vertical stiffness for moderate and high shape factors [37]. The vertical deformation is accommodated either by lateral bulging, related to the shape factor, or by volumetric strain, related to the bulk modulus. For very small shape factors (i.e. very thick pads) the vertical deformation is accommodated almost entirely by lateral bulging; thus the isolator can be assumed to be incompressible. The reinforcement restrains the elastomeric layers, reducing the volume of elastomer that bulges laterally, which, for equal vertical strain, increases the volumetric strain and dependency on the bulk modulus, thus stiffening the isolator.

#### 2.3.1 SREIs

Closed form solutions for the compression modulus of SREIs have been developed using the *pressure solution*. The basic assumptions of the pressure solution used to simplify the analysis are [38]:

- the elastomer is perfectly bonded to the steel shims
- horizontal planes remain plane and parallel
- lateral bulging follows a parabolic vertical profile
- that the elastomer is linear elastic
- the normal stresses within the elastomer are dominated by the internal pressure
- the shear stresses in the horizontal plane are negligible

- all normal stresses are zero at the free lateral surfaces

The pressure solution is considered valid for elastomeric pads with a shape factor of about 5 or higher [38]. The pressure solution has been used to develop closed form solutions for the compression modulus,  $E_c$ , assuming an incompressible and compressible elastomer for infinite strip [39], circular [37], rectangular [8, 38], and annular [17, 8] pads, respectively. Analytical solutions derived using the pressure solution have been validated numerically with finite element analysis [40]. The vertical stiffness,  $k_v$ , is related to  $E_c$  by:

$$k_v = \frac{E_c A}{t_r} \quad (2-1)$$

where  $A$  is the plan area of the pad, and  $t_r$  is the total thickness of the elastomeric layers in the isolator. Other studies, such as Pinarbasi et al. [41, 42] and Qiao and Lu [43], reduced the number of simplifying assumptions made by the pressure solution, but showed that the solution converged to the pressure solution for pads with large shape factors.

It is interesting to note the high sensitivity of the compression modulus of an annular isolator to the presence of a small hole. The purpose of the hole varies depending on the application and often is a result of the manufacturing procedure; in some situations the hole is intended to contain a lead plug to introduce additional damping, in other situations the hole may be used as a method to reduce horizontal stiffness. In the case of a lead plug, it may be acceptable to assume that the lead plug prevents lateral bulging and thus the influence of the hole is negligible. Otherwise, introducing a small hole can significantly reduce the compression modulus [17], quickly converging to the solution for an infinite strip isolator. Due to this rapid convergence, Kelly and Konstantinidis [8] recommended that the compression modulus of annular isolators conservatively be taken as identical to an infinite strip isolator.

### 2.3.2 FREIs

Using the pressure solution, the vertical compression modulus of a FREI can be determined similar to a SREI with the inclusion of an additional term to the assumed horizontal displacements of the elastomeric layers to account for the extension of the fiber reinforcement [10]. Following the pressure solution, closed form solutions for  $E_c$  assuming incompressible and compressible elastomers and including the extensibility of the fiber have been developed for infinite strip [10, 44], circular [45, 46], rectangular [11, 47], and annular [8, 18] pads, respectively.

All of the analytical solutions for FREIs referenced above indicate that a decrease of the in-plane stiffness of the fiber reinforcement will decrease the compression modulus due to a reduction in restraint of the lateral bulging. This can also be observed in a phenomenon known as *run-in*, where a certain level of vertical load is required before the vertical stiffness develops. The run-in effect is believed to occur as the fiber

reinforcement is pulled taut and aligned. Initially, the lack of straightness may have a large effect on the vertical stiffness due to reduced restraint of the elastomeric layers; however, the stiffness is recovered as the fibers straighten [48].

### **2.3.3 Boundary Conditions**

The analytical solutions for SREIs and FREIs were derived considering only a single elastomeric pad. The solutions can be extended to consider multiple layers by treating the pads as springs in series. In this case, the boundary conditions of the two exterior layers of elastomer, either bonded or unbonded, may be influential over the vertical stiffness. The possibility of slip between the exterior elastomeric layers and the upper and lower supports is illustrated in Figure 2-1. The effect of friction on unbonded SREIs was investigated by Kelly and Konstantinidis [12]. In this study, the isolators considered had unbonded exterior elastomeric layers with half the thickness of the interior layers. If the isolator was fully bonded, the two outer layers would have a stiffness that was four times the stiffness of the interior layers. In the opposing limit, if no friction developed at the upper and lower supports, the two layers combined would have an equal stiffness to a single interior layer. Therefore, the coefficient of friction in unbonded FREIs can also play a critical role in the vertical properties, especially in isolators with a low number of elastomeric layers.

## *2.4 Horizontal Stiffness*

### **2.4.1 Bonded SREIs and FREIs**

The shear modulus of the steel reinforcement is several orders of magnitude greater than the shear modulus of the elastomer, as such, the shear deformation is assumed to occur entirely within the elastomeric layers. Although the steel reinforcement restrains lateral bulging, the elastomer can still deform freely in horizontal shear [8]. Consequently, overlooking non-linearity associated with the elastomer and other effects such as coupling between horizontal and vertical loading, the horizontal stiffness of a bonded SREI can be assumed constant. The assumed concentrated deformation in the elastomeric layers has also been applied to FREIs. Therefore, the basic expression for horizontal stiffness of a bonded FREI is identical to a bonded SREI.

### **2.4.2 Unbonded FREIs**

It is often assumed that the length of the rollover surface that has lost contact with the supports is equal to the horizontal displacement [13, 31, 49]. By also assuming that the elastomer is incompressible and that the rollover follows a parabolic deformed shape, Kelly and Konstantinidis [49] determined that full rollover would theoretically occur at a shear strain,  $\gamma$ , of:

$$\gamma = \frac{5}{3} \frac{h}{t_r} \quad (2-2)$$

where  $h$  is the total height of the isolator.

It is convenient to consider an unbonded FREI in sections; a central section that is in contact with the upper and lower supports and two rollover sections as illustrated in Figure 3-1. The lower bound approximation on the horizontal force-displacement relationship obtained by ignoring the contribution of the rollover sections was proposed by Kelly and Konstantinidis [49]. The lower bound approximation of the horizontal force,  $F$ , is:

$$F = \frac{2bG(2a - s)s}{t_r} \quad (2-3)$$

where  $G$  is the shear modulus of the elastomer,  $2a$  and  $2b$  are the width and length of the isolator and  $s$  is the horizontal displacement. The expression gives a parabolic force-displacement relationship that reaches a maximum as the tangential stiffness becomes negative and the isolator becomes unstable.

Russo et al. [31] compared Eq. (2-3) with available experimental data and showed that the prediction could be improved by including the vertical deflection of the isolator. Including the vertical deflection delays the loss of contact between the upper and lower supports and the isolator; thereby increasing the size of the central section and decreasing the size of the rollover section. Russo et al. [31] averaged the area of the central section at zero horizontal displacement and at the full rollover displacement to determine a constant horizontal stiffness. Note that the approach presented in Russo et al. [31] required the experimentally obtained vertical deflection and full rollover displacement for the model.

The models by Kelly and Konstantinidis [49] and Russo et al. [31] both neglect the benefits of the rollover section and full rollover, which has been shown experimentally to prevent horizontal instability [50]. The model proposed by Toopchi-Nezhad [51] includes the contributions of the rollover sections by assuming the shear strain in the rollover sections is between zero and half of the shear strain in the central section. Toopchi-Nezhad [51] proposed the use of an effective area to equivalently represent the assumed lower shear strains in the rollover sections. Based on an assumed equivalent area of 25 % of the rollover section, and with the full rollover prediction from Kelly and Konstantinidis [49], it was shown by Toopchi-Nezhad [51] that stability could be achieved with aspect ratios of at least 2.5. This result was in good agreement with the experimental observations of Toopchi-Nezhad et al. [50], which showed that an isolator with an aspect ratio of 1.9 was unstable, but that stability could be achieved at an aspect ratio of 2.5. These analytical models are simplified representations of a complex problem but have significant shortcomings, such as not predicting or including full rollover or accounting for the influence of the bending rigidity of the reinforcement.

SU-FREIs are believed to be beneficial over traditional bonded elastomeric isolators due to the adaptive softening and stiffening that occurs with increasing horizontal displacement; however, secondary benefits have been identified. A comparison between a bonded and unbonded FREI using finite element analysis showed that the unbonded application significantly reduces the stress demand on the elastomer and the reinforcement; notably, a significant reduction in tensile and peeling stresses was observed. Although experimental studies on unbonded FREIs are limited, with fewer yet investigating full rollover, existing studies have all observed desirable performance characteristics and properties [31, 35, 36, 50-56].

## 2.5 *Stability*

Elastomeric isolators can be viewed as short columns supporting the weight of the structure and are therefore also susceptible to buckling instability. The isolator is often idealized as a continuous composite system that acts as a beam. In this case, plane sections normal to the undeformed axis are assumed to remain plane, but not necessarily normal to the deformed axis [8]. The current buckling theory extends from work conducted by Haringx [57] and later Gent [58, 59]. A critical load can be determined according to the theory and it is necessary to ensure that the applied load does not exceed the critical buckling load. The bending modulus of an elastomeric pad, which differs from the compression modulus, is required in the derivation of the critical load. The bending modulus has been derived following the pressure solution for an infinite strip [39, 8], circular [37, 8], rectangular [8] and annular [38, 8] SREI assuming an incompressible and compressible elastomer, respectively and an infinite strip [60], and rectangular FREI [47] assuming a compressible elastomer. Note that the bending modulus for a circular and annular pad including reinforcement extensibility and elastomer compressibility has not been derived.

Buckle et al. [61] showed that the critical buckling load decreases with increasing horizontal displacement and that the horizontal stiffness decreases with increasing axial load and increasing horizontal displacement; however, elastomeric isolators may retain significant critical load carrying capacity as the horizontal displacement approaches the diameter of the bearing [62]. If the applied load approaches the critical load, it may also be necessary to reduce the horizontal stiffness accordingly since an interaction exists between the horizontal load and the applied vertical load [8].

The analytical solutions developed by Tsai and Kelly [15, 16] for the buckling load of SREIs at zero horizontal displacement assumed that the steel reinforcement was flexible and extensible, thus making it appropriate for FREIs as well. The solution determined the horizontal stiffness accounting for stability, shear and warping effects and established the buckling load by equating the horizontal stiffness to zero. This analytical

solution represents the most comprehensive solution available for SREIs or FREIs, but it is limited to zero horizontal displacement.

The analytical investigation by Kelly and Marsico [9] for unbonded FREIs ignored the rollover sections, which is believed to provide a lower estimate of the actual buckling characteristics of the isolator. An experimental investigation on the dynamic buckling of SU-FREIs concluded that the buckling load, defined as the load that resulted in a zero tangential stiffness during cyclic sinusoidal testing, was significantly larger than the expected design load of SU-FREIs [54].

### *References*

- [1] Callister WD. 2007. *Materials Science and Engineering an Introduction*. United States of America: John Wiley & Sons.
- [2] Van Engelen NC, Kelly JM. 2015. Retest of Neoprene Seismic Isolation Bearings after 30 Years. *Structural Control and Health Monitoring*, 22(1): 139-151.
- [3] Marckmann G, Verron E, Gornet L, Chagnon G, Charrier P, Fort P. 2002. A Theory of Network Alteration for the Mullins Effect. *Journal of the Mechanics and Physics of Solids*, 50(9): 2011-2028.
- [4] Dorfmann A, Ogden RW. 2004. A Constitutive Model for the Mullins Effect with Permanent set in Particle-Reinforced Rubber. *International Journal of Solids and Structures*, 41(7):1855-1878.
- [5] International Organization for Standardization. 2010. *Elastomeric Seismic-protection Isolators, ISO 22762*. Switzerland: International Organization for Standardization.
- [6] American Society of Civil Engineers. 2010. *Minimum Design Loads for Buildings and other Structures, ASCE/SEI 7-10*. New York: American Society of Civil Engineers.
- [7] Naeim F, Kelly JM. 1999. *Design of Seismic Isolated Structures: From Theory to Practice*. USA: John Wiley & Sons.
- [8] Kelly JM, Konstantinidis D. 2011. *Mechanics of Rubber Bearings for Seismic and Vibration Isolation*. Chichester UK: John Wiley & Sons.
- [9] Kelly JM, Marsico MR. 2010. Stability and Post-buckling Behavior in Nonbolted Elastomeric Isolators. *Seismic Isolation and Protection Systems*. 1(1):41-54.
- [10] Kelly JM. 1999. Analysis of Fiber-reinforced Elastomeric Isolators. *Journal of Seismology and Earthquake Engineering*, 2(1): 19-34.
- [11] Tsai HC, Kelly JM. 2002. Stiffness Analysis of Fiber-Reinforced Rectangular Seismic Isolators. *Journal of Engineering Mechanics*, 128(4): 462-470.
- [12] Kelly JM, Konstantinidis, D. 2009. Effect of Friction on Unbonded Elastomeric Bearings. *Journal of Engineering Mechanics*, 125(9):953-960.
- [13] Konstantinidis D, Kelly JM, Makris N. 2008. Experimental Investigations on the Seismic Response of Bridge Bearings. Earthquake Engineering Research Center Report 2008-02. Berkeley, California: University of California, Berkeley.

- [14] Peng TB, Zhang H, Li JZ, Li WX. 2009. Pilot Study on the Horizontal Shear Behaviour of FRP Rubber Isolators. *Journal of Vibration and Shock*, 28(1): 127-130. [in Chinese]
- [15] Tsai HC, Kelly JM. 2005. Buckling of Short Beams with Warping Effect Included. *International Journal of Solids and Structures*, 42(1): 239-253.
- [16] Tsai HC, Kelly JM. 2005. Buckling Load of Seismic Isolators Affected by Flexibility of Reinforcement. *International Journal of Solids and Structures*; 42(1): 255-269.
- [17] Constantinou MC, Kartoum A, Kelly JM. 1992. Analysis of Compression of Hollow Circular Elastomeric Bearings. *Engineering Structures*, 14(2): 103-111.
- [18] Pinarbasi S, Okay F. 2011. Compression of Hollow-circular Fiber-reinforced Rubber Bearings. *Structural Engineering and Mechanics*, 38(3): 361-384.
- [19] Toopchi-Nezhad H, Tait MJ, Drysdale RG. 2011. Bonded versus Unbonded Strip Fiber Reinforced Elastomeric Isolators: Finite Element Analysis. *Composite Structures*, 93(2): 850-859.
- [20] Toopchi-Nezhad H, Tait MJ, Drysdale RG. 2013. Influence of Thickness of Individual Elastomer Layers (First Shape Factor) on the Response of Unbonded Fiber-Reinforced Elastomeric Bearings. *Journal of Composite Materials*, 47(27): 3433-3450.
- [21] Mordini A, Strauss A. 2008. An Innovative Earthquake Isolation System using Fibre Reinforced Rubber Bearings. *Engineering Structures*, 30(10): 2739-2751.
- [22] Osgooei PM, Tait MJ, Konstantinidis D. 2014. Three-Dimensional Finite Element Analysis of Circular Fiber Reinforced Elastomeric Bearings under Compression. *Composite Structures*, 108: 191-204.
- [23] Osgooei PM, Van Engelen NC, Tait MJ, and Konstantinidis D. Experimental and Finite Element Study on the Lateral Response of Modified Rectangular Fiber-Reinforced Elastomeric Isolators (MR-FREIs). *Engineering Structures*, 85: 293-303.
- [24] Dezfuli FH, Alam MS. 2013. Multi-Criteria Optimization and Seismic Performance Assessment of Carbon FRP-based Elastomeric Isolators. *Engineering Structures*, 49: 525-540.
- [25] Itoh Y, Gu HS. 2009. Prediction of Aging Characteristics in Natural Rubber Bearings Used in Bridges. *Journal of Bridge Engineering*, 14(2): 122-128.
- [26] Yura J, Kumar A, Yakut A, Topkaya C, Becker E, Collingwood J. 2001. Elastomeric Bridge Bearings: Recommended Test Methods, National Cooperative Highway Research Program Report No. 449. Washington D.C.: National Academy Press.
- [27] Gu HS, Itoh Y. 2010. Ageing Behaviour of Natural Rubber and High Damping Rubber Materials Used in Bridge Rubber Bearings. *Advances in Structural Engineering*, 13(6): 1105-1113.
- [28] Coladant C. 1992. Base isolation and aseismic bearings. In *Recent Advances in Earthquake Engineering and Structural Dynamics*, Davidovici V (ed). Ouest Editions: Nantes, 587–624.

- [29] Casciati F, Faravelli L. 2012. Experimental Investigation on the Aging of the Base Isolator Elastomeric Component. *Acta Mechanica*, 223(8): 1633-1643.
- [30] Coladant C. 1993. Durability and Ageing of Elastomeric Bearings in France. *International Post-SMiRT Conference Seminar on Isolation, Energy Dissipation and Control of Vibrations of Structures*, Italy.
- [31] Russo G, Pauletta M, Cortesia A. 2013. A Study on Experimental Shear Behavior of Fiber-Reinforced Elastomeric Isolators with Various Fiber Layouts, Elastomers and Aging Conditions. *Engineering Structures*, 52:422–433.
- [32] Cho H-W, Huang J-S. 2008. Effects of Cyclic Compression and Thermal Aging on Dynamic Properties of Neoprene Rubber Bearings. *Journal of Applied Polymer Science*, 107: 1635-1641.
- [33] Kelly JM, Konstantinidis D. 2009. Steel Shim Stresses in Multilayer Bearings under Compression and Bending. *Journal of Mechanics of Materials and Structures*, 4(6): 1109-1125.
- [34] Moon BY, Kang GJ, Kang BS, Kelly JM. 2002. Design and Manufacturing of Fiber Reinforced Elastomeric Isolator for Seismic Isolation. *Journal of Materials Processing Technology*; 130-131:145-150.
- [35] Naghshineh AK, Akyuz U, Caner A. 2014. Comparison of Fundamental Properties of New Types of Fiber-mesh-reinforced Seismic Isolators with Conventional Isolators. *Earthquake Engineering and Structural Dynamics*, 43(2):301-316.
- [36] Strauss A, Apostolidi E, Zimmermann T, Gerhaher U, Dritsos S. 2014. Experimental Investigations of Fiber and Steel Reinforced Elastomeric Bearings: Shear Modulus and Damping Coefficient. *Engineering Structures*, 75:402-413.
- [37] Chalhoub MS, Kelly JM. 1990. Effect of Bulk Compressibility on the Stiffness of Cylindrical Base Isolation Bearings. *International Journal of Solids and Structures*, 26(7): 743-760.
- [38] Kelly JM. 1993. *Earthquake-resistant design with rubber*. London: Springer.
- [39] Chalhoub MS, Kelly JM. 1991. Analysis of Infinite-Strip-Shaped Base Isolator with Elastomer Bulk Compression. *Journal of Engineering Mechanics*, 117(8): 1791-1805.
- [40] Constantinou MC, Kalpakidis I, Filiatrault A, Ecker Lay RA. 2011. LRFD-Based Analysis and Design Procedures for Bridge Bearings and Seismic Isolators. Rept. No, MCEER-11-0004.
- [41] Pinarbasi S, Akyuz U, Mengi Y. 2006. A New Formulation for the Analysis of Elastic Layers Bonded to Rigid Surfaces. *International Journal of Solids and Structures*, 43: 4271-4296.
- [42] Pinarbasi S, Mengi Y, Akyuz U. 2008. Compression of Solid Annular Circular Discs Bonded to Rigid Surfaces. *International Journal of Solids and Structures*, 45(16): 4543-4561.
- [43] Qiao S, Lu N. 2015. Analytical Solutions for Bonded Elastically Compressible Layers. *International Journal of Solids and Structures*, 58: 353-365.
- [44] Kelly JM. 2002. Seismic Isolation Systems for Developing Countries. *Earthquake Spectra*, 18(3): 385-406.

- [45] Tsai HC, Kelly JM. 2001. Stiffness Analysis of Fiber-Reinforced Elastomeric Isolators, Pacific Earthquake Engineering Research Center Report No. 2001/05. Berkeley, California: University of California, Berkeley.
- [46] Kelly JM, Calabrese A. 2013. Analysis of Fiber-Reinforced Elastomeric Isolators Including Stretching of Reinforcement and Compressibility of Elastomer. *Ingegneria Sismica*, 30(3): 5-16.
- [47] Angeli P, Russo G, Paschini A. 2013. Carbon Fiber-Reinforced Rectangular Isolators with Compressible Elastomer: Analytical Solution for Compression and Bending. *International Journal of Solids and Structures*, 50(22): 3519-3527.
- [48] Kelly, JM. 2008. Analysis of the Run-in Effect in Fiber-Reinforced Isolators under Vertical Load. *Journal of Mechanics of Materials and Structures*, 3(7): 1383-1401.
- [49] Kelly JM, Konstantinidis D. 2007. Low-cost Seismic Isolators for Housing in Highly-seismic Developing Countries. *10th World Conference on Seismic Isolation, Energy Dissipation and Active Vibrations Control of Structures*, Istanbul, Turkey.
- [50] Toopchi-Nezhad H, Tait MJ, Drysdale RG. 2008. Testing and Modeling of Square Carbon Fiber-reinforced Elastomeric Seismic Isolators. *Structural Control and Health Monitoring*, 15(6): 876-900.
- [51] Toopchi-Nezhad H. 2014. Horizontal Stiffness Solutions for Unbonded Fiber Reinforced Elastomeric Bearings. *Structural Engineering and Mechanics*, 49(3): 395-410.
- [52] Toopchi-Nezhad H, Drysdale RG, Tait MJ. 2009. Parametric Study on the Response of Stable Unbonded-Fiber Reinforced Elastomeric Isolators (SU-FREIs). *Journal of Composite Materials*, 43(15): 1569-1587.
- [53] Toopchi-Nezhad H, Tait MJ, Drysdale RG. 2009. Shake Table Study on an Ordinary Low-Rise Building Seismically Isolated With SU-FREIs (Stable Unbonded-Fiber Reinforced Elastomeric Isolators). *Earthquake Engineering and Structural Dynamics*, 38(11): 1335-1357.
- [54] De Raaf MGP, Tait MJ, Toopchi-Nezhad H. 2011. Stability of Fiber-Reinforced Elastomeric Bearings in an Unbonded Application. *Journal of Composite Materials*, 45(18): 1873-1884.
- [55] Russo G, Pauletta M. 2013. Sliding Instability of Fiber-Reinforced Elastomeric Isolators in Unbonded Applications. *Engineering Structures*, 48:70-80.
- [56] Das A, Dutta A, Deb SK. 2015. Performance of Fiber-Reinforced Elastomeric Base Isolators under Cyclic Excitation. *Structural Control and Health Monitoring*, 22(2): 197-220.
- [57] Haringx JA. 1949. Elastic Stability of Helical Springs at a Compression Larger than Original Length. *Applied Scientific Research*, 1(1): 417-434.
- [58] Gent AN. 1964. Elastic Stability of Rubber Compression Springs. *Journal of Mechanical Engineering and Science*, 6(4): 318-326.
- [59] Gent AN, Meinecke EA. 1970. Compression, Bending, and Shear of Bonded Rubber Blocks. *Polymer Engineering and Science*, 10(1): 48-53.
- [60] Kelly JM, Takhirov SM. 2002. Analytical and Experimental Study of Fiber-Reinforced Bearings, Pacific Earthquake Engineering Research Center Report No. 2002/11. Berkeley, California: University of California, Berkeley.

- [61] Buckle I, Nagarajaiah S, Ferrell K. 2002. Stability of Elastomeric Isolation Bearings: Experimental Study. *Journal of Structural Engineering*, 128(1): 3-11.
- [62] Nagarajaiah S, Ferrell K. 1999. Stability of Elastomeric Seismic Isolation Bearings. *Journal of Structural Engineering*, 125(9): 946-954.

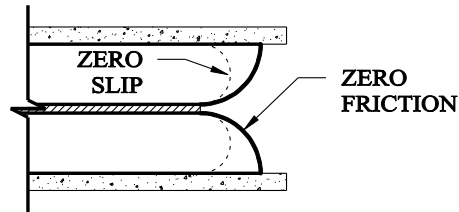


Figure 2-1: Bulging of the exterior layers with zero slip and zero friction

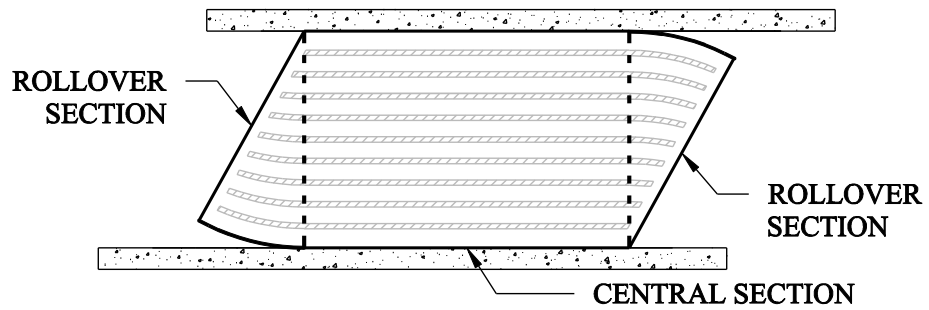


Figure 2-2: Division of an unbonded FREI into sections

### **3 Model of the Shear Behavior of Unbonded Fiber-Reinforced Elastomeric Isolators**

Reproduced with permission from ASCE.

Van Engelen NC, Tait MJ, Konstantinidis D. 2014. Model of the Shear Behavior of Unbonded Fiber-Reinforced Elastomeric Isolators. *Journal of Structural Engineering (ASCE)*, 141(7): 04014169, DOI: 10.1061/(ASCE)ST.1943-541X.0001120.

#### *Abstract*

In this paper, an analytical model is developed and used to predict the horizontal behaviour of unbonded Fiber Reinforced Elastomeric Isolators (FREIs). An advantageous feature of unbonded FREIs is the ability to undergo rollover due to the lack of flexural rigidity of the reinforcement, and the unbonded support conditions of the isolator. The rollover causes a characteristic softening, followed by stiffening, as the initially vertical faces of the isolator come into contact with the upper and lower supports; defined as *full rollover*. The force-displacement relationship is modelled by dividing the isolator into three sections: a central section, which experiences pure shear, and two rollover sections which experience combined shear and bending. The displacements of the rollover section are used to establish the curved deformed profile and predict full rollover. The model is evaluated with experimental data from four unbonded FREI designs. A parametric study is conducted to determine the influence of the aspect ratio and bending stiffness of the composite fiber reinforcement matrix on the horizontal force-displacement relationship.

#### *3.1 Introduction*

The seismic demand on a structure can be significantly reduced by introducing a flexible horizontal layer between the foundation and the structure. This concept, known as base isolation, causes a shift in the fundamental period of the structure, increasing it out of the critical high energy range of an earthquake. The displacements of the structure are concentrated at the isolation level, where specially designed isolators are capable of undergoing large deformations, while the structure essentially displaces as a rigid body.

Elastomers function as a unique engineering material due to their near incompressibility and low shear modulus. The application of elastomeric materials as base isolators can be divided into two categories: conventional Steel Reinforced Elastomeric Isolators (SREIs); and, more recently, Fiber Reinforced Elastomeric Isolators (FREIs). The reinforcement, which is positioned in alternating horizontal layers with the elastomer, enhances the vertical behaviour by restraining the lateral bulging of the elastomer caused by the vertical compressive load (Kelly and Konstantinidis 2011). Due to the steel shims and thick steel end plates, SREIs are inherently heavy and expensive, and require an intensive manufacturing process to bond the elastomer to the steel. By

replacing the steel reinforcement with lighter fiber layers of similar tensile behaviour to that of steel, FREIs may be used to address these concerns (Kelly 1999). Initial investigations of FREIs identified advantages in the manufacturing process and performance of the isolator (Kelly 1999; Toopchi-Nezhad et al. 2008).

An additional method of reducing the costs associated with a base isolation system is to position the isolators in an unbonded application, i.e., with no bonding or mechanical fastening between the contact surfaces of the isolators and the upper and lower supports. The unbonded application eliminates the need for heavy steel end plates, as shown in Figure 3-1. A unique result of unbonded FREIs is the possibility of *rollover* at the ends of the isolator due to relative horizontal displacement of the upper and lower supports. Rollover occurs when a portion of the horizontal surface of the isolator loses contact with the upper and lower supports and is a consequence of the lack of flexural rigidity in the fiber reinforcement and the unbonded application. As rollover occurs, the horizontal stiffness of the isolator decreases. The rollover deformation continues until the initially vertical faces of the isolator become horizontal and come into contact with the upper and lower supports, referred to as *full rollover* (Toopchi-Nezhad et al. 2008). The occurrence of full rollover begins to increase the horizontal stiffness of the isolator. If the tangential horizontal stiffness remains positive, the isolator is considered stable and is denoted as a Stable Unbonded Fiber Reinforced Elastomeric Isolator (SU-FREI) (Toopchi-Nezhad et al. 2009). This variable stiffness, observed with certain width-to-total height aspect ratios, is the characteristic feature of SU-FREIs. This differs from the near constant stiffness of a traditional bonded isolator, illustrated in Figure 3-2. The softening at intermediate displacements increases the efficiency of the isolation system, represented by a larger shift in the fundamental period during design-basis events, while the stiffening at full rollover acts as a self-restraint against the maximum considered earthquake displacement demands (Toopchi-Nezhad et al. 2008). Provisions in design codes define the amount of allowable softening to ensure the retention of a horizontal restoring force and stability (ASCE 2010). In a study utilizing finite element analysis, unbonded FREIs were shown to have several advantages over similar bonded FREIs, such as increased seismic isolation efficiency caused by the softening, reduced stress demand on the elastomeric layers, and negligible peeling stress demand on the bond between layers (Toopchi-Nezhad et al. 2011).

Current methods of evaluating the horizontal stiffness of unbonded FREIs are generally conducted through experimental testing or complex finite element analysis (Mordini and Strauss 2008, Osgoeei et al. 2014). This paper presents an approach for predicting the horizontal force-displacement relationship of unbonded FREIs. The proposed model, which formulates the deformed shape of the rollover and predicts full rollover, is evaluated using experimental data from previous studies (Toopchi-Nezhad

2008; Foster 2011; Van Engelen et al. 2012; de Raaf 2009). The model is expanded to predict the horizontal force-displacement relationship for displacements exceeding full rollover and is subsequently used to conduct a parametric study on the effect of the aspect ratio and bending stiffness of the reinforcement. These are important factors in determining the horizontal stability of an unbonded isolator.

## 3.2 Background

### 3.2.1 Full Rollover Prediction

Kelly and Konstantinidis (2007) developed a model to predict the limiting shear strain of an unbonded elastomeric bridge bearings with thin steel reinforcing plates. The limiting strain was defined as the strain at which full rollover occurs. Based on experimental observations, it was noted that, for the unbonded bearings investigated, displacement beyond full rollover may result in sliding between the bearing and the supports and possible damage to the bearing itself. The model was developed assuming incompressibility, completely flexible reinforcement, and that the free surfaces of the rollover sections are completely stress free. The deformed edge of a rollover section of the bearing, neglecting the thickness of the reinforcement, was assumed to follow a parabolic curve described by:

$$y = \frac{x^2}{d^2} \quad (3-1)$$

where  $d$  is the extension of the initially vertical face of the bearing at full rollover, and  $x$  and  $y$  describe the horizontal and vertical components of the deformed edge, as shown in Figure 3-3. All parameters are normalized by the total height of the isolator. The limiting shear strain was found to be  $c = 5/3$ . To account for the thickness of the reinforcement, which does not deform in shear, the value of  $c$  was increased by the ratio of the total height of the bearing to the total thickness of the elastomeric layers. For a typical steel-reinforced bridge bearing, this increase is approximately 15 %. The extension of the initially vertical face of the bearing was determined to be  $d = 1.25$ , implying that significant extension occurs during rollover. Although the model was developed for thin steel reinforcing plates, the assumption of completely flexible reinforcement lends itself to FREIs, and this model can be used to describe the deformed shape of unbonded FREIs at full rollover.

### 3.2.2 Horizontal Force-Displacement Relationships

Peng et al. (2009) conducted a preliminary theoretical study on the horizontal shear behaviour of unbonded FREIs. A model was developed to relate the horizontal displacement and associated force by dividing the isolator into three sections: a central section, which undergoes pure shear; and two curved shear coupling sections on either end of the central section, which are the rollover sections of the isolator. The deformation

of the two rollover sections was described by two components: shear and bending. When combined, the deformations create the curved profile exhibited by the rollover sections of unbonded FREIs. The shear and bending deformations were related to each other through the horizontal displacement of the isolator and the flexural-to-shear stiffness ratio. The interpretation of the shear and bending deformation involved numerous approximations and assumptions. A relationship between the angle of deflection of the rollover sections and the horizontal displacement was developed and used to calculate the forces for each of the assumed sections. Although it was indicated that the shear and bending displacement could be added together to create the curved profile of the rollover section, the model did not include how these displacements should be combined.

Konstantinidis et al. (2008) proposed a lower-bound force-displacement relationship by assuming that the rollover sections are stress free and contribute no resistance to the horizontal displacement. Therefore, the horizontal force for an unbonded FREI is considered to be only a function of the central section of the isolator. This lower-bound solution is identical to the central pure shear section in the model by Peng et al. (2009). By differentiating the force-displacement relationship, Konstantinidis et al. (2008) identified that the tangential horizontal stiffness would become zero at a horizontal displacement equal to half of the width of the bearing and negative, or unstable, beyond that displacement. Maintaining a positive tangential horizontal stiffness is a requirement to prevent residual displacement. Russo et al. (2013) proposed a modified version of the Konstantinidis et al. (2008) model that used the experimentally obtained vertical deflection of the isolator to increase the area of the central section based on when contact is lost. The models by Peng et al. (2009) and Konstantinidis et al. (2008) are discussed in detail in the following section.

### 3.3 *Model Description*

In the proposed model, the elastomeric material is assumed to be linearly elastic, and to be incompressible. The influence of the vertical compressive load on the horizontal response will be neglected, assuming that the load is small and does not approach the critical buckling load of the isolator. However, the compressive load is assumed to provide sufficient friction between the FREI and the upper and lower supports to prevent slip at all levels of displacement. These assumptions are common for analytical models involving elastomeric isolators, including those by Kelly and Konstantinidis (2007), Peng et al. (2009), and Konstantinidis et al. (2008).

#### 3.3.1 **Displacement Prior to Full Rollover**

It is appropriate to analyze the isolator in sections that act independently of one another but are subjected to an identical horizontal displacement,  $s$ . The dimensions of the isolator considered are  $2a$ ,  $2b$ ,  $h$ , and  $t_r$ , for the width, length, total height, and total

thickness of the elastomeric layers, respectively. Figure 3-4 shows plan and profile views of a FREI, where horizontal displacement is in the  $x$  direction. Following Peng et al. (2009), the division of the isolator into sections can be determined by the deformed shape. Thus, the size of each section is displacement dependent, although the definition of the sections remains unchanged at all levels of displacement. The isolator is divided into a central section, which experiences pure shear deformation, and two rollover sections, which experience a combination of shear and bending deformation. The division between these sections is considered to be a vertical line located at the point where the isolator first loses contact with the horizontal supports, vertically in line with the opposing edge of the isolator, shown in Figure 3-5. The point where the isolator loses contacts with the supports is held fixed, although, as discussed by Russo et al. (2013), the vertical deflection of the isolator will shift this point.

The total horizontal force,  $F$ , is given by:

$$F = F_1 + 2F_2 \quad (3-2)$$

where  $F_1$  and  $F_2$  are the force contributions from the central and rollover sections, respectively. Since the shear deformation is limited to the elastomeric layers, the horizontal displacement is related to the shear strain,  $\gamma$ , by:

$$\gamma = \frac{s}{t_r} \quad (3-3)$$

The length of the free surface of the rollover section is assumed to be equal to  $s$  (Kelly and Konstantinidis 2007), thus, the effective length of the pure shear section is also reduced by  $s$  as horizontal displacement occurs (Figure 3-5). The force contribution from the central pure shear section is:

$$F_1 = G_e \gamma A_r \quad (3-4)$$

where  $G_e$  is the shear modulus of the elastomer and  $A_r$  is the reduced shear area of the central section defined as:

$$A_r = (2b)(2a - s) \quad (3-5)$$

Equation (3-4) can alternatively be expressed as:

$$F_1 = G_e \frac{s}{t_r} (2b)(2a - s) \quad (3-6)$$

Equation (3-6) is the lower-bound solution proposed by Konstantinidis et al. (2008). As  $s$  increases,  $A_r$  decreases, resulting in a parabolic force-displacement relationship that reaches a maximum when the horizontal displacement is equal to half the width of the isolator. If the maximum is reached at a horizontal displacement before significant resistance is provided by the rollover sections, the isolator will exhibit unstable behaviour. This type of horizontal instability is common to isolators with lower width-to-total height aspect ratios, where  $A_r$  reduces rapidly in comparison to the initial loaded area. The sensitivity to  $A_r$  decreases as the aspect ratio increases, allowing the isolator to retain stability.

The curve length of the free edge of the rollover sections is due to contributions from both shear and bending displacements,  $d_s$  and  $d_b$ , respectively. Therefore, the horizontal displacement, which is also the arc length of the stress-free surface that has rolled over (Figure 3-5), can be expressed as the sum of the shear and bending displacements of the rollover sections:

$$s = d_s + d_b \quad (3-7)$$

The force causing these displacements is identical for both components and is the horizontal force contribution from the rollover section,  $F_2$ . The total shear area of a single rollover section is half the rollover area of the free edge due to the wedge-shaped geometry of the rollover portion. The shear displacement contribution can be related to  $F_2$  by:

$$d_s = \frac{2F_2 t_r}{G_e (2b) s} \quad (3-8)$$

Contrary to Peng et al. (2009), the bending displacement is assumed to follow an arc with constant radius equal to the total height of the isolator. Following this simplification, the bending displacement can be approximated as an arc length:

$$d_b = h\theta \quad (3-9)$$

where  $\theta$  is the angle of deflection, defined in Figure 3-6.

The rollover section is treated as a cantilever with a length  $s$  and an equivalent follower point load,  $V$ , applied to the free-edge. The cantilever representation was proposed in Peng et al. (2009), although the interpretation of how the cantilever relates to the horizontal force and displacement of the isolator vary. The equivalent follower point load is representative of the force required to create the rollover deformation and remains perpendicular to the free-edge of the rollover section. The horizontal component is  $F_2$ , which is related to  $V$  by  $\theta$ , as shown in Figure 3-7:

$$F_2 = V \sin \theta \quad (3-10)$$

The magnitude of  $V$  is determined using an iterative process and large deflection theory for a cantilever subjected to a follower force as described by Shvartsman (2007). The nonlinear differential equation governing the Euler-Bernoulli beam is:

$$EI_{eff} \varphi'' + V \sin \left( \varphi + \frac{\pi}{2} - \varphi(0) \right) = 0 \quad (3-11)$$

with the boundary conditions:

$$\begin{aligned} \varphi'(0) &= 0 \\ \varphi(s) &= 0 \end{aligned}$$

where  $EI_{eff}$  is the effective bending stiffness of the rollover section and  $\varphi(l)$  is the rotation of the beam as a function of the arc length,  $l$ , beginning from the free end, as represented in Figure 3-8, with  $\theta = \varphi(0)$ . In Shvartsman (2007), it was shown that Eq. (3-11) could be reduced to a system of nonlinear differential equations in lieu of the elliptic-function solution, thereby simplifying the calculation.

The assumed cantilever and equivalent follower point load is a simplified representation of a complex problem. Finite element analysis, as described in Osgoee et al. (2013), was utilized to obtain the local stress initially parallel to the fiber reinforcement in the rollover section, as shown in Figure 3-9. The layer design of the model is identical to isolator B2 and B3, described later in Table 3-1. The isolator was initially loaded to an average vertical compressive stress of 2.0 MPa and displaced horizontally to  $1.50 t_r$  before being vertically unloaded. Unloading the isolator reduced the influence of the vertical compressive load on the internal stresses and provided a more accurate representation of the stresses associated with the rollover deformation. Lateral bulging is observed at the initially vertical face of the isolator and a band of localized tensile and compressive stresses occur along the composite fiber reinforcement matrix. The level of compressive stress increases towards the point of rotation. Although no external force is applied on the rollover section, significant internal stresses develop. Figure 3-9 shows that the local stress of the interior elastomeric layers at the interface of the central and rollover sections are dominated by tension. The magnitude of the tensile stress increases along the height of the isolator when taken at the interface of the rollover and central section. Based on these observations, the effective bending stiffness of the rollover section is simplified as a composite section with bending about the base of the rollover section. Selecting a value of the elastic modulus of the composite fiber reinforcement matrix in bending,  $E_m$ , based on the fiber reinforcement tensile properties will significantly over-estimate the bending resistance of the rollover section. The value of  $E_m$  should reflect the low flexural rigidity of the composite fiber reinforcement matrix layer. For the isolators investigated in this study, it was considered reasonable to assume  $E_m$  to be of the same order as the elastic modulus of the elastomer,  $E_e$ , and as such a value of  $E_m = E_e$  was used. The sensitivity of the response to  $E_m$  is investigated in this study.

The procedure used in the proposed model for displacement prior to full rollover is outlined in Figure 3-10. The level of  $V$  is increased until the total displacement from Eq. (3-7) converges to the current level of assumed horizontal displacement within a predefined error,  $\epsilon$ . Once  $\theta$  has been determined for a level of  $V$ , the shear displacement can be determined from Eq. (3-8) as a function of  $F_2$ , which is determined from Eq. (3-10). The bending displacement can be solved from Eq. (3-9) and the total displacement is the sum of the bending displacement and shear displacement, as indicated in Eq. (3-7). Figure 3-11 shows an example of the relationship between  $\theta$  and  $s$ . Table 3-1 offers details on the design of the particular isolator. Initially no rotation occurs due to the high bending stiffness of the rollover section. As the size and length of the rollover section increases, an increasing amount of rotation occurs at an increasing rate.

### 3.3.2 Deformed Shape and Full Rollover Prediction

Full rollover of the initially vertical face of the isolator can be predicted using the deformed shape of the assumed cantilever. The surface of the rollover section is assumed to follow the deformed edge of the rollover section. From Shvartsman (2007), the location of the free edge at any level of horizontal displacement can be obtained from:

$$d_v(l) = \int_l^s \sin \varphi d\tilde{l} \quad (3-12)$$

$$d_h(l) = \int_l^s \cos \varphi d\tilde{l} \quad (3-13)$$

for the vertical,  $d_v$ , and horizontal,  $d_h$ , displacement.

When  $d_v = h$  the free edge has contacted the supports and full rollover has occurred. The horizontal displacement corresponding to full rollover is denoted as  $s_r$ . When full rollover occurs, the magnitude of  $d_h$  is representative of the extension of the initially vertical face of the isolator and is denoted as  $d_{hr}$ .

### 3.3.3 Displacement Exceeding Full Rollover

Toopchi-Nezhad et al. (2008) showed that SU-FREIs have desirable characteristics after full rollover occurs; most notable is a significant increase in effective horizontal stiffness. This increase in effective horizontal stiffness acts as a self-restraining mechanism for beyond design-basis displacements. The ability of the isolator to reach strains past full rollover is dependent on the geometry and quality of the isolator; specifically its capacity to resist sliding between the supports and internal delamination between the layers of reinforcement and elastomer. For the purposes of this model, it is assumed that the integrity of the isolator is not compromised. Thus, any additional displacement will cause the curved profile to deform as shown in Figure 3-12. Due to the restriction caused by the contact of the vertical faces, it is assumed that the entire isolator reverts back to pure shear deformation. Any additional horizontal displacement adds shear deformation to the curved profile, resulting in an overall similar curved profile.

The division of the isolator previously defined remains unaltered, with the exception that the rollover sections are now in contact with the upper and lower supports. The total horizontal force after full rollover can be described by the individual contributions of these sections:

$$F = F_{1r} + 2F_{2r} + 2F_{3r} \quad (3-14)$$

where  $F_{1r}$  is the contribution of the central pure shear section after full rollover,  $F_{2r}$  is the force which caused full rollover, and  $F_{3r}$  is the additional contribution from the rollover section, now in shear.

As the rollover sections are no longer increasing, the area of the central section is constant:

$$F_{1r} = G_e \gamma A_{rr} \quad (3-15)$$

where:

$$A_{rr} = (2b)(2a - s_r) \quad (3-16)$$

Therefore, Eq. (3-15) can be expressed as:

$$F_{1r} = G_e \frac{S}{t_r} (2b)(2a - s_r) \quad (3-17)$$

The rollover sections are assumed to only undergo shear deformation. Any further rollover is restricted by the supports and the approach previously used to describe the force contribution is no longer valid. However, the applied force  $F_2$  required to incur full rollover is still present and remains constant for horizontal displacements exceeding full rollover, denoted as  $F_{2r}$ .

Due to the rollover behaviour, the shear area of the rollover sections is now the initially vertical face which has been extended during the rollover deformation. By ignoring the now curved fiber reinforcement, and assuming that the shear area has a length approximately equal to half the extension of the initially vertical face at full rollover,  $d_{hr}$ , as shown in

Figure 3-13, the horizontal force for  $F_{3r}$ , can be determined as:

$$F_{3r} = \frac{G_e(s - s_r)(2b)d_{hr}}{2t_r} \quad (3-18)$$

### 3.4 Model Evaluation

The model is evaluated against four different unbonded FREI designs from previous studies. The properties of the isolators considered are shown in Table 3-1. B1 is based on one isolator from Toopchi-Nezhad (2008); B2 is based on the average of seven isolators from Foster (2011); B3 is from Van Engelen et al. (2012); and B4 is the average of three isolators from de Raaf (2009). All experimental data is based on the effective horizontal stiffness from the unscragged cycles from cyclic tests performed in the respective study. All mechanical and geometric properties were selected as indicated in the respective study. The isolators were tested under an applied average vertical compressive stress of 1.6 MPa or 2.0 MPa which corresponds to a vertical compressive load of approximately 8 kN. These experiments were conducted under vertical load control and horizontal displacement control. The maximum considered displacement was  $2.00 t_r$  and  $2.50 t_r$  for B1, B4, and B2, B3, respectively; only three specimens of B2 were cycled up to  $2.50 t_r$ . All of the isolators exhibited stable rollover behaviour.

#### 3.4.1 Horizontal Force-Displacement Relationship

The normalized experimental and theoretical horizontal force displacement curves are shown graphically in Figure 3-14. It can be observed that in all cases the model demonstrates the characteristic softening and stiffening associated with SU-FREIs. A variable amount of error exists between the different isolators and the different

displacements. Isolators B1, B3, and B4 show good agreement at  $2.00 t_r$  and also  $2.50 t_r$  for isolator B3, with a maximum error of 10.6 %. The under-prediction of the experimental force observed at low displacements is attributed to the assumed linear elasticity of the elastomer.

The model over-predicts the horizontal forces for isolator B2 and B3 at the intermediate displacement range,  $0.75 t_r$  to  $1.50 t_r$ . In general, this range represents the primary operating range of a SU-FREI system as it provides the lowest effective horizontal stiffness; maximizing the efficiency of the isolator. For these isolators, B2 and B3, the model provides a higher stiffness, which would result in a lower prediction of the isolator's potential period shift, but also a lower displacement demand. Full rollover is represented as an instantaneous change in tangential stiffness, visible at approximately  $2.00 t_r$  in the isolators considered. It was identified in de Raaf (2009) that the initially vertical face does not instantaneously contact the supports. The contact increases from the point of rotation along the height of the isolator, stiffening gradually prior to full rollover.

### **3.4.2 $F_I$ Contribution**

The contribution of the central section, identical to the lower-bound approach proposed by Konstantinidis et al. (2008), is also shown in Figure 3-14 without including full rollover. Note that the model proposed by Konstantinidis et al. (2008) was not intended to predict the performance of the isolator past the point of instability. The model is extended beyond instability and full rollover herein for comparative purposes. The lower-bound approach is almost identical to the proposed model at low displacements. As the horizontal displacement increases, the size and force contribution of the rollover sections increases, and the two approaches begin to diverge. Overall, an improved prediction occurs for isolators B1 and B4 in the intermediate displacement range. The approach in Konstantinidis et al. (2008), which predicts that instability occurs in every isolator, neglects the advantages associated with SU-FREIs and provides no indication of the performance after full rollover. It is also important to note that, with the exception of B3, the instability is predicted before full rollover occurs, reducing the available displacement range of the isolator.

### **3.4.3 Vertical Compressive Load**

The proposed model was developed by assuming that the influence of the vertical compressive load was negligible. In a study conducted by de Raaf et al. (2011), it was shown the effective horizontal stiffness of unbonded FREIs decreases with increasing compressive load. Tsai and Kelly (2005a,b) presented a solution for the buckling capacity of bonded SREIs with extensible and flexible reinforcement at zero horizontal displacement. Currently no such solution for describing the influence of vertical compressive load on unbonded FREIs at horizontal displacements exists in the literature.

The complexity of the problem is increased due to the rollover sections, and again at full rollover, as the stress distribution changes when the rollover sections contact the supports.

The solution by Tsai and Kelly (2005a,b) is applied to provide an indication of the sensitivity of the isolators considered to the vertical compressive load. Including the vertical compressive load reduces the horizontal stiffness at zero horizontal displacement by approximately 21 % and 13 % for B2 and B3, respectively, while B1 and B4 are relatively unaffected due to the larger shape factor. It is postulated that the magnitude of the reduction would increase as  $A_r$  decreases, and then decrease at full rollover as the rollover sections increase the area in contact with the supports; reducing the overall vertical stress. The accuracy of the proposed model could be improved by including the influence of vertical compressive load. Furthermore, note that the representation of the experimental data provided by the lower-bound approach,  $F_1$ , for B2 and B3 (see Figure 3-14), would be considerably reduced if the influence of the vertical compressive load were included.

#### **3.4.4 Full Rollover Prediction and Deformed Shape**

Table 3-2 shows the full rollover and extension of the initially vertical face predictions determined according to the Kelly and Konstantinidis (2007) approach and from the proposed model, normalized by the total height of the isolator. Since isolators B2 and B3 had identical designs in terms of the thickness and number of elastomeric and reinforcement layers the predicted values are identical for both models.

For the three isolator designs considered, the displacement at which full rollover occurs is predicted within a 0.7 % error. The extension of the initially vertical face of the isolator predicted by the proposed model is less than the Kelly and Konstantinidis (2007) estimates for all designs, with a maximum error of 2.5 %. The two approaches are compared in Figure 3-15 for isolator B1. The deformed shape is consistent between the two models. The proposed model encloses approximately equal area as the Kelly and Konstantinidis (2007) approach, which was developed assuming incompressibility. A similar deformed shape can be obtained for the other isolators considered in this study.

### *3.5 Parametric Study*

#### **3.5.1 Influence of Aspect Ratio**

Stable rollover is dependent on the aspect ratio,  $R$ , of the isolator (Toopchi-Nezhad et al. 2008). The full rollover prediction and  $F_2$  is independent of  $R$  in the proposed model. Therefore, as  $R$  increases, the relative contribution of the rollover sections,  $F_2$ , decreases in comparison to the central section contribution,  $F_1$ . As a consequence, the desirable softening at intermediate displacements observed in SU-FREIs will become less apparent.

Figure 3-16 shows the normalized horizontal force as a function of displacement for values of  $R$  ranging between 2.0 and infinity for isolator B2. At low displacements, less than  $0.50 t_r$ , the normalized horizontal force is almost identical for all aspect ratios since the amount of rollover is small. At intermediate displacements, the characteristic softening of SU-FREIs is observed, and in the case of  $R = 2.0$ , the softening leads to instability. The amount of softening quickly reduces with increasing  $R$ , and by  $R = 2.5$  the isolator approaches stability over the displacement range. At full rollover, substantial stiffening is observed for lower values of  $R$ . Similar to the softening, the stiffening becomes less substantial with increasing  $R$ .

It was observed in a study conducted by Toopchi-Nezhad et al. (2008) that an unbonded FREI with  $R = 1.9$  was unstable, but that stable rollover could be obtained with  $R = 2.5$ . It is postulated that the transition to stability occurs near  $R = 2.5$ , depending on the isolator's design, as indicated by the proposed model. By  $R = 10.0$ , the overall influence of the rollover sections becomes negligible. It is recommended that isolators with  $R < 2.5$  be treated as unstable FREIs, where the contribution of the rollover sections should not be included, and SU-FREIs with  $R > 10.0$  can satisfactorily be modeled as strip FREIs with a constant effective horizontal stiffness. Unbonded FREIs within  $2.5 \leq R \leq 10.0$  should be treated as SU-FREIs, and the contributions of the rollover sections should be considered.

### 3.5.2 Influence of $E_m$

In the evaluation of the proposed model, it was assumed that the composite fiber reinforcement matrix had an identical elastic modulus in bending as the elastomer,  $E_m = E_e$ . Figure 3-17 shows the influence of  $E_m$  on the horizontal force-displacement relationship of isolator B1, where  $E_m = \alpha E_e$ . A similar trend can be observed as with the aspect ratio, where increasing  $E_m$ , represented by an increase in  $\alpha$ , reduces the softening of the isolator in the intermediate displacements. Unlike the aspect ratio,  $E_m$  also influences  $s_r$ . As  $E_m$  increases the isolator stiffens in bending and the amount of bending deformation decreases, resulting in an increased horizontal force for an identical angle of deflection. The increased horizontal force also causes an increase in the amount of shear displacement. Thus, as  $E_m$  approaches infinity, the amount of bending displacement becomes negligible, and the isolator deforms in pure shear, identical to an isolator with rigid reinforcement, as indicated in Figure 3-18. This shows that full rollover may not occur within the displacement range of interest, depending on the value of  $E_m$ .

The influence of  $E_m$  on the shear and bending displacement of the rollover sections is shown in Figure 3-19. In all cases, the total displacement is initially dominated by shear. At small displacements, the effective length of the rollover section is small, creating a substantial bending stiffness. As a result, the isolator will initially deform in nearly pure shear. As the length of the rollover section increases, the bending stiffness

quickly reduces, and the amount of bending displacement increases. For  $\alpha = 1$ , the amount of shear displacement remains relatively constant at displacements exceeding  $1.00 t_r$ . Note that although the shear displacement remains constant, the force contribution from the rollover sections is increasing because the shear area also increases. As  $E_m$  increases, the shear displacement increases, approaching pure shear deformation as  $E_m$  approaches infinity.

### 3.6 Conclusions

A method of analyzing and predicting the horizontal force-displacement relationship for unbonded FREIs has been presented. The proposed model employs large deflection theory to predict the deformed shape of an unbonded FREI. The deformed shape was used to determine the occurrence of full rollover, and the model was modified to account for the changing boundary conditions after full rollover.

The proposed model was evaluated against experimental data from previous studies. Overall, good agreement was found between the proposed model and the experimental data. It was observed that in some instances the proposed model over-predicted the horizontal force at intermediate displacements. This over-prediction was attributed in part to the fact that the model does not take into account the vertical compressive load, which is known to reduce the effective horizontal stiffness. An existing lower-bound approximation, which ignores the influence of the rollover sections, was shown to incorrectly predict instability, neglecting significant advantages associated with SU-FREIs. The horizontal force contribution of the rollover sections retains the stability of the isolator up to full rollover where the isolator returns to pure shear deformation.

A parametric study using the proposed model was conducted on the aspect ratio and the elastic modulus of the composite fiber reinforcement matrix in bending. Based on the parametric study, the following observations were made:

- 1) An unbonded FREI becomes stable at an aspect ratio of about 2.5, depending on the layer design. At this aspect ratio, the isolator exhibits the characteristic softening and stiffening associated with SU-FREIs. As the aspect ratio increases, the observed softening and stiffening become less significant. It is recommended that unbonded FREIs be treated as SU-FREIs if the aspect ratio is between 2.5 and 10.0, implying that the influence of the rollover sections cannot be ignored. At lower aspect ratios, the unbonded FREI should be considered unstable, while at higher aspect ratios the unbonded FREI can satisfactorily be modeled in pure shear.
- 2) By assuming the elastic modulus of the composite fiber reinforcement matrix in bending is equal to the elastic modulus of the elastomer, satisfactory predictions were obtained for the force-displacement relationship and the full rollover prediction for the unbonded FREIs considered. Increasing  $E_m$  results in an increased force response, and an increased displacement at full rollover.

As  $E_m$  approaches infinity, the unbonded FREI undergoes pure shear and has no rollover, exhibiting a linear force-displacement relationship.

The proposed model serves as a method to predict the horizontal force-displacement relationship of SU-FREIs based on the isolator's geometry and design. The model also aids to predict potential instability and the occurrence of full rollover. Further investigation is required to include the influence of the vertical compressive load on the FREI at horizontal displacement.

### *Nomenclature*

$a$	half width of the isolator
$A_r$	reduced area of the central section
$A_{rr}$	reduced area of the central section at full rollover
$b$	half length of the isolator
$c$	limiting shear strain
$d$	horizontal extension of the initially vertical face normalized by $h$
$d_b$	rollover section bending displacement
$d_h$	free-edge horizontal displacement
$d_{hr}$	extension of the initially vertical face at full rollover
$d_s$	rollover section shear displacement
$d_v$	free-edge vertical displacement
$E_e$	elastic modulus of the elastomer
$EI_{eff}$	effective stiffness of the rollover section
$E_m$	elastic modulus of the composite reinforcement matrix in bending
$F$	total horizontal force
$F_1$	central section horizontal force
$F_{1r}$	full rollover central section horizontal force
$F_2$	rollover section horizontal force
$F_{2r}$	rollover section horizontal force at full rollover
$F_{3r}$	additional full rollover section horizontal force after full rollover
$G_e$	shear modulus of the elastomer
$h$	total height of the isolator
$l$	arc length
$R$	aspect ratio
$s$	horizontal displacement
$s_r$	horizontal displacement at full rollover
$t_r$	total thickness of the elastomeric layers
$V$	equivalent follower point load
$\alpha$	ratio of $E_m/E_e$
$\epsilon$	displacement error tolerance

$\gamma$	shear strain
$\theta$	rollover section maximum angle of deflection
$\varphi$	angle of a deflection as a function of the arc length

### *Acknowledgements*

Financial support for this study was provided by the McMaster University Centre for Effective Design of Structures (CEDS) funded through the Ontario Research and Development Challenge Fund (ORDCF) as well as an Early Researcher Award (ERA) grant, both are programs of the Ministry of Research and Innovation (MRI). Support was also provided through the Natural Sciences and Engineering Research Council (NSERC) of Canada. The support of a Vanier Canada Graduate Scholarship is also gratefully acknowledged.

### *References*

- ASCE. (2010). “Minimum design loads for buildings and other structures.” *ASCE/SEI 7-10*, New York.
- de Raaf, M. (2009). “Experimental study of unbonded fiber reinforced elastomeric bearings.” M.A.Sc. thesis, McMaster Univ., Hamilton, Canada.
- de Raaf, M. G. P., Tait, M. J., and Toopchi-Nezhad, H. (2011). “Stability of fiber-reinforced elastomeric bearings in an unbonded application.” *J. Compos. Mater.*, 45(18), 1873-1884.
- Foster, B. A. D. (2011). “Base isolation using Stable Unbonded Fibre Reinforced Elastomeric Isolators (SU-FREI).” M.A.Sc. thesis, McMaster Univ., Hamilton, Canada.
- Kelly, J. M. (1999). “Analysis of fiber-reinforced elastomeric isolators.” *J. Seismol. Earthq. Eng.*, 2(1), 19-34.
- Kelly, J.M., and Konstantinidis, D. (2007). “Low-cost seismic isolators for housing in highly-seismic developing countries.” *Proc., 10<sup>th</sup> World Conf. on Seismic Isolation, Energy Dissipation and Active Vibrations Control of Structures*, Anti-Seismic Systems International Society (ASSISi), Bologna, Italy.
- Kelly, J. M., and Konstantinidis, D. (2011). *Mechanics of rubber bearings for seismic and vibration isolation*. John Wiley & Sons, Chichester UK.
- Konstantinidis, D., Kelly, J. M., and Makris, N. (2008). “Experimental investigation on the seismic response of bridge bearings.” *Technical Rep. No. EERC 2008-02*, Earthquake Engineering Research Center, University of California, Berkeley, CA.
- Mordini, A., and Strauss, A. (2008). “An innovative earthquake isolation system using fibre reinforced rubber bearings.” *Eng. Struct.*, 30(10), 2739-2751.
- Osgooei, P.M., Tait, M.J., and Konstantinidis, D. (2013). “Three-dimensional finite element analysis of square fiber-reinforced elastomeric isolators (FREIs) under lateral loads.” *Proc., 2013 Canadian Society for Civil Engineering Annual Conf.*, Canadian Society for Civil Engineering, Montreal, Canada.
- Osgooei, P.M., Tait, M.J., and Konstantinidis, D. (2014). “Three-dimensional finite

- element analysis of circular fiber-reinforced elastomeric bearings under compression.” *Compos. Struct.*, 108(1): 191-204.
- Peng, T.B., Zhang, H., Li J.Z., and Li, W.X. (2009). “Pilot study on the horizontal shear behaviour of FRP rubber isolators.” *J. Vib. Shock*, 28(5), 127-130 (in Chinese).
- Russo, G., Pauletta, M., & Cortesia, A. (2013). “A study on experimental shear behavior of fiber-reinforced elastomeric isolators with various fiber layouts, elastomers and aging conditions.” *Eng. Struct.*, 52(1), 422-433.
- Shvartsman, B. S. (2007). “Large deflections of a cantilever beam subjected to a follower force.” *J. Sound Vib.*, 304(3), 969-973.
- Toopchi-Nezhad, H. (2008). “The performance of SU-FREIs (stable unbonded-fiber reinforced elastomeric isolators).” Doctoral dissertation. McMaster Univ., Hamilton, Canada.
- Toopchi-Nezhad, H., Drysdale, R. G., and Tait, M. J. (2009). “Parametric study on the response of stable unbonded-fiber reinforced elastomeric isolators (SU-FREIs).” *J. Compos. Mater.*, 43(15), 1569-1587.
- Toopchi-Nezhad, H., Tait, M. J., and Drysdale, R. G. (2008). “Testing and modeling of square carbon fiber-reinforced elastomeric seismic isolators.” *Struct. Contr. Health Monit.*, 15(6), 876-900.
- Toopchi-Nezhad, H., Tait, M. J., and Drysdale, R. G. (2011). “Bonded versus unbonded strip fiber reinforced elastomeric isolators: Finite element analysis.” *Compos. Struct.*, 93(2), 850-859.
- Tsai, H. C., & Kelly, J. M. (2005a). “Buckling of short beams with warping effect included.” *Int. J. Solids Struct.*, 42(1), 239-253.
- Tsai, H. C., & Kelly, J. M. (2005b). “Buckling load of seismic isolators affected by flexibility of reinforcement.” *Int. J. Solids Struct.*, 42(1), 255-269.
- Van Engelen, N. C., Tait, M. J., & Konstantinidis, D. (2012). “Horizontal behaviour of stable unbonded fiber reinforced elastomeric isolators (SU-FREIs) with holes.” *Proc., 15th World Conference on Earthquake Engineering*, International Association for Earthquake Engineering, Tokyo, Japan.

Table 3-1: Material and Geometric Properties of Selected Isolators

Property	B1	B2*	B3*	B4
Material				
$G_e$ (MPa)	0.40	0.35	0.35	0.40
$E_e$ (MPa)	1.20	1.05	1.05	1.20
Geometric				
$2b$ (mm)	70	63	52	70
$2a$ (mm)	70	63	76	70
$t_r$ (mm)	19	19	19	19
$h$ (mm)	25	22	22	24
$R$	2.8	2.8	3.5	2.9
Average Stress (MPa)	1.6	2.0	2.0	1.6

\* The two exterior layers of elastomer were half the thickness of the interior layers, all values given pertain to the interior layers

Table 3-2: Full Rollover and Extension of the Initially Vertical Face Predictions

Approach	$C$			$D$		
	B1	B2 and B3	B4	B1	B2 and B3	B4
Kelly and Konstantinidis (2007)	1.67	1.67	1.67	1.25	1.25	1.25
Proposed Model	1.65	1.67	1.66	1.22	1.24	1.23

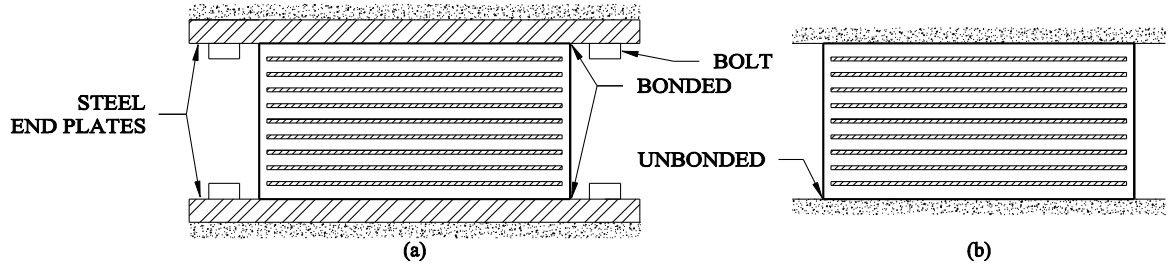


Figure 3-1: Profile view of (a) a bonded SREI and (b) an unbonded FREI

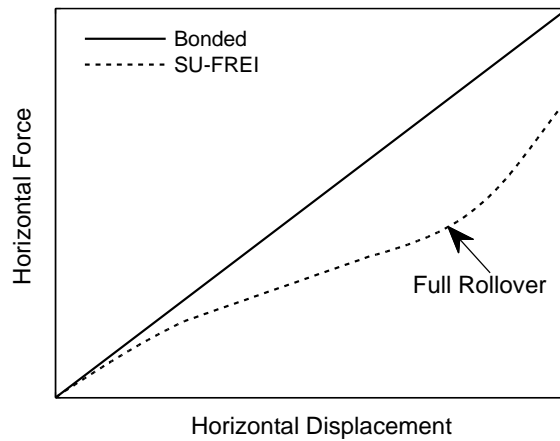


Figure 3-2: Generalized horizontal force-displacement relationship for bonded isolator and SU-FREIs

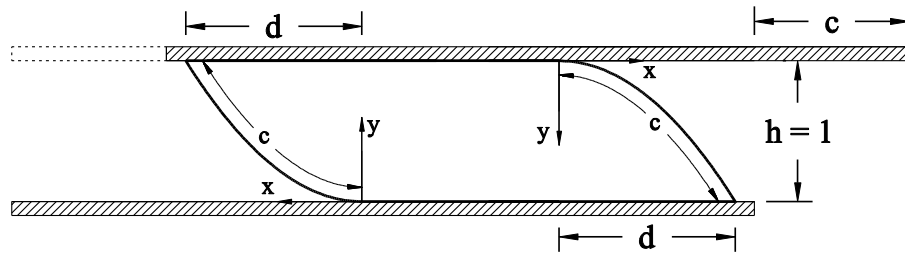


Figure 3-3: Deformed unreinforced elastomeric isolator as described by Kelly and Konstantinidis (2007)

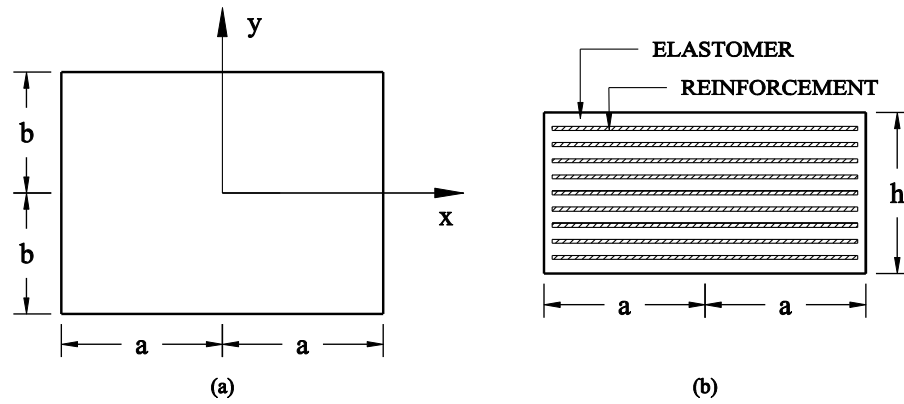


Figure 3-4: (a) Plan view and (b) elevation view of a FREI

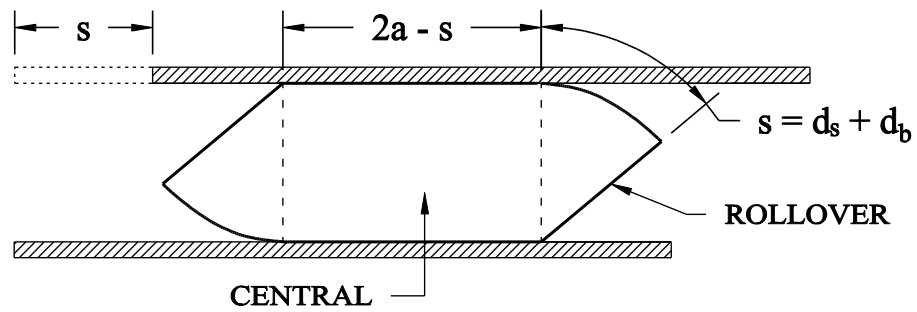


Figure 3-5: Division of the isolator into sections at a horizontal displacement,  $s$

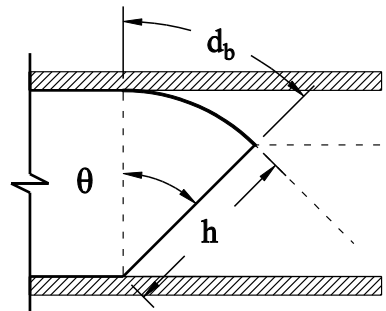


Figure 3-6: Definition of  $d_b$ ,  $h$  and  $\theta$

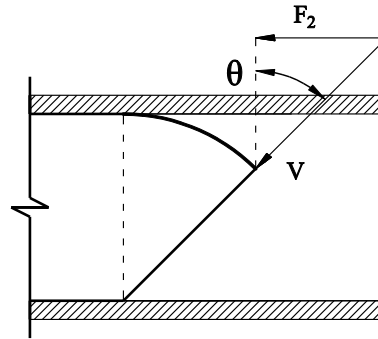


Figure 3-7: Relationship between the assumed equivalent follower point load,  $V$ , and  $F_2$

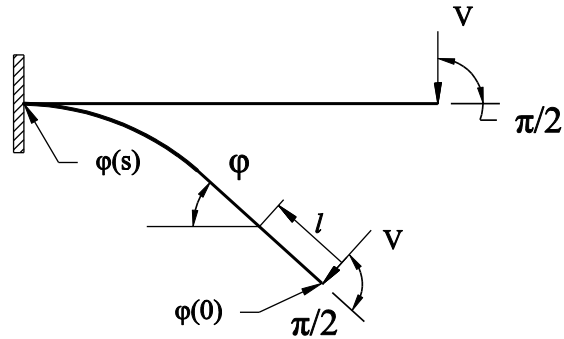


Figure 3-8: Deformed and undeformed cantilever with an applied follower point load,  $V$

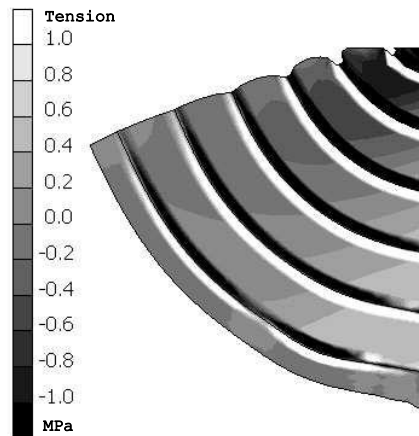


Figure 3-9: Local stresses initially parallel to the fiber reinforcement in the rollover section at  $1.50 t_r$  with zero vertical load

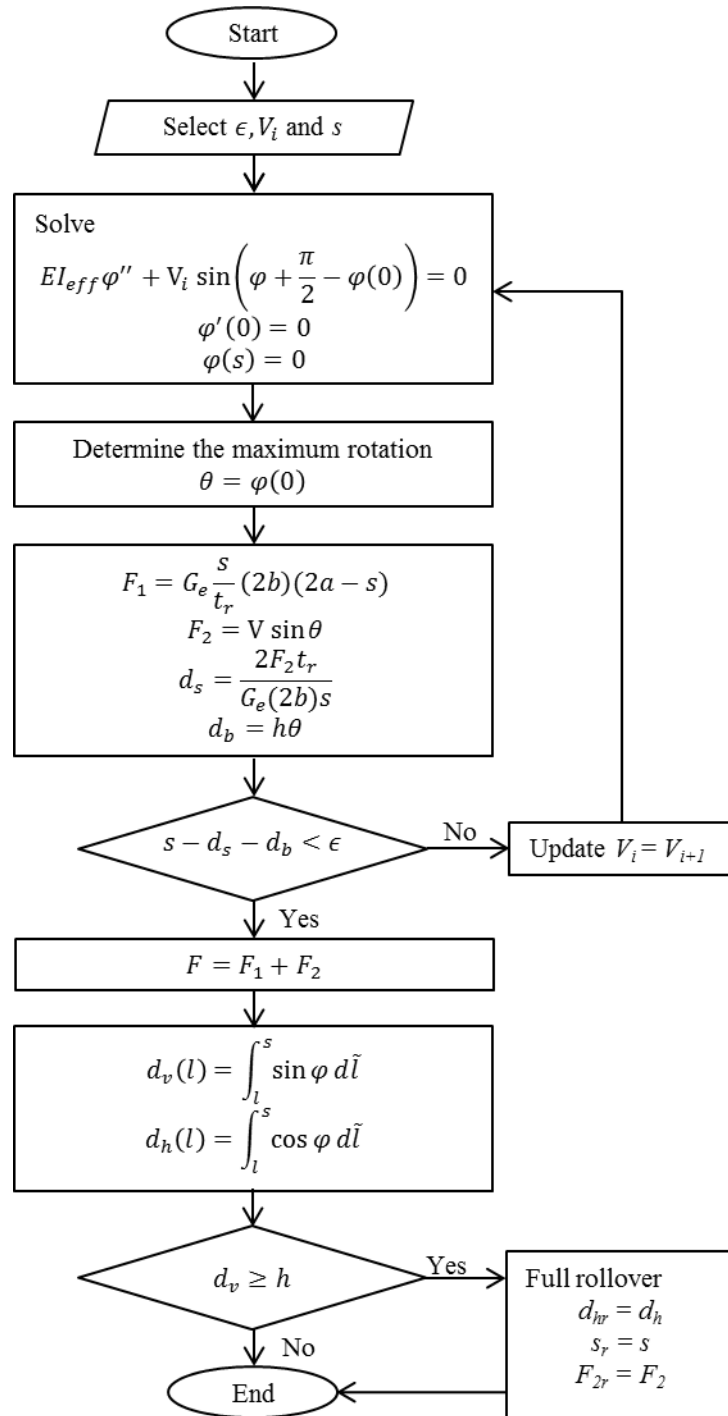


Figure 3-10: Procedure for displacement prior to full rollover

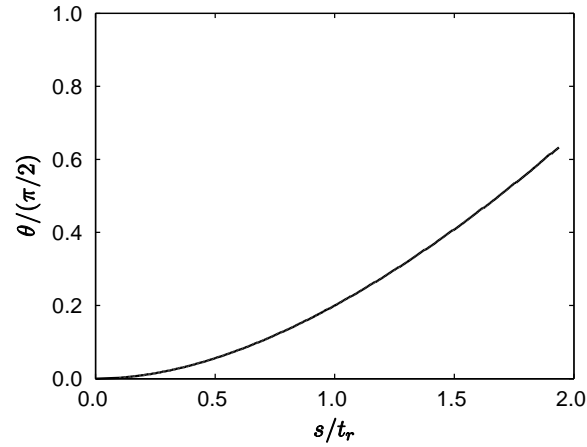


Figure 3-11: Example of the normalized relationship between the angle of deflection and horizontal displacement for isolator B2

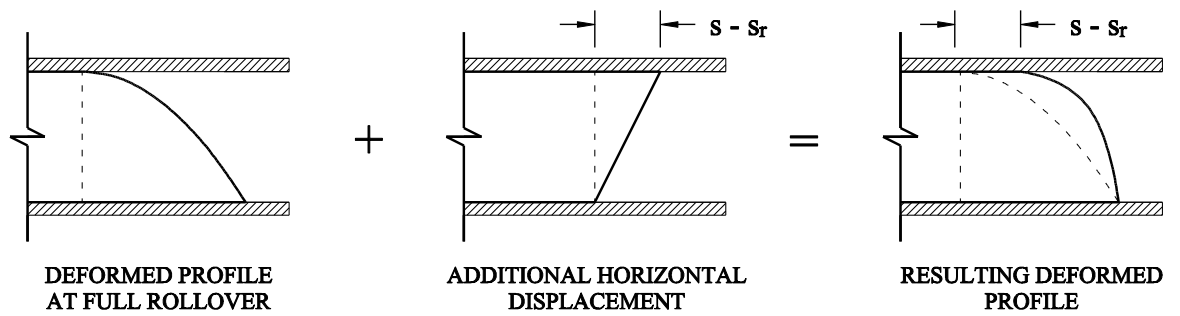


Figure 3-12: Deformed shape after full rollover showing the influence of additional horizontal displacement

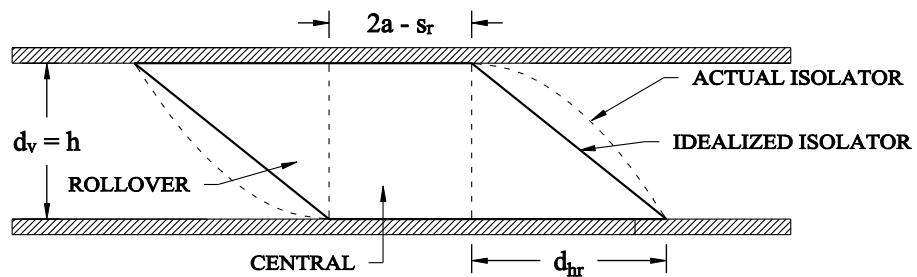


Figure 3-13: Idealized representation of the isolator after full rollover

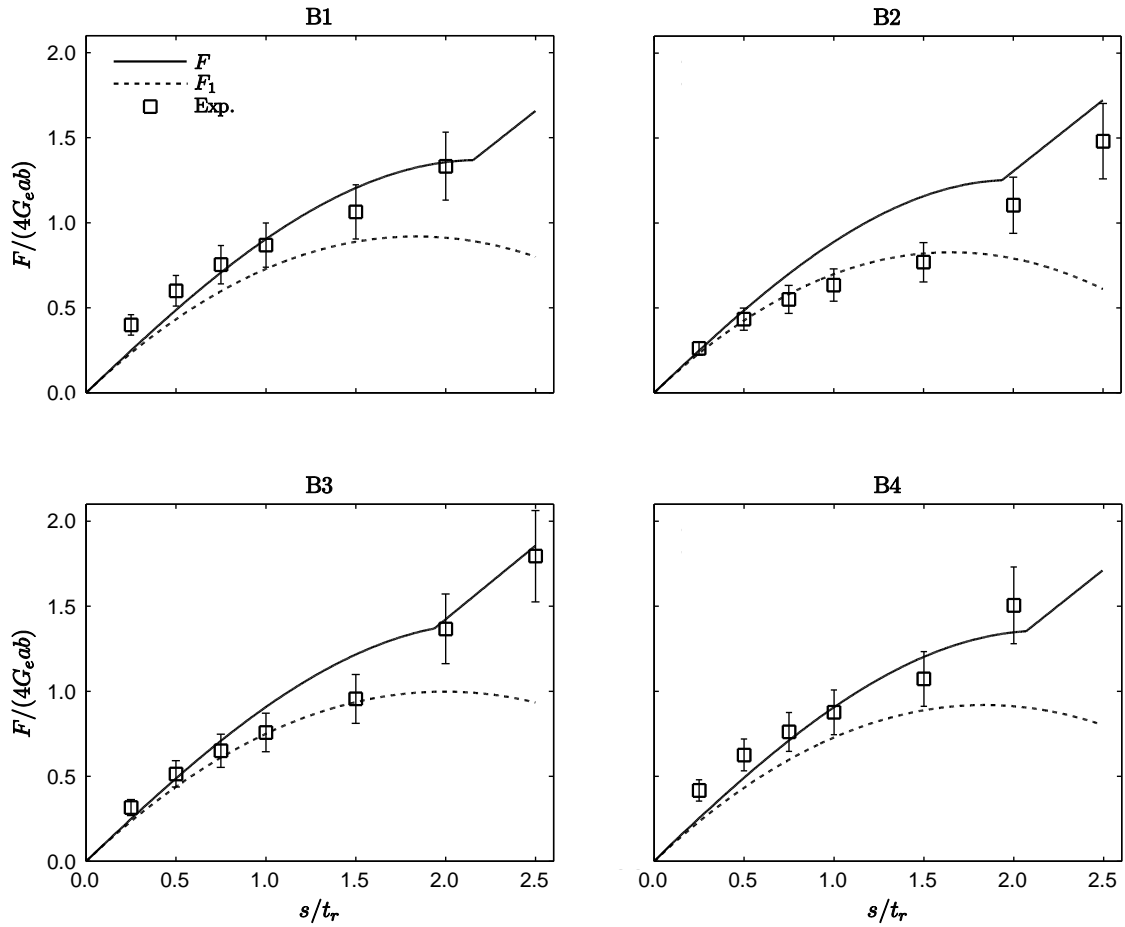


Figure 3-14: Normalized horizontal force as a function of displacement compared with experimental values with 15 % error bars

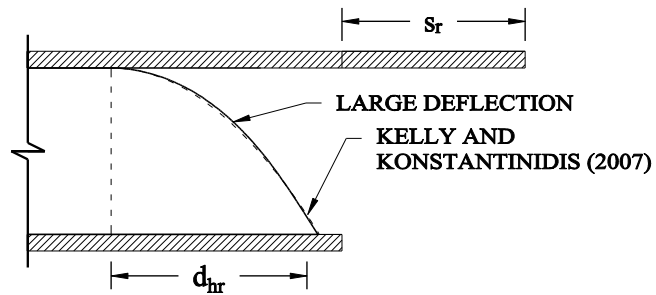


Figure 3-15: Comparison of the proposed model and theoretical full rollover deformed shape for isolators B1

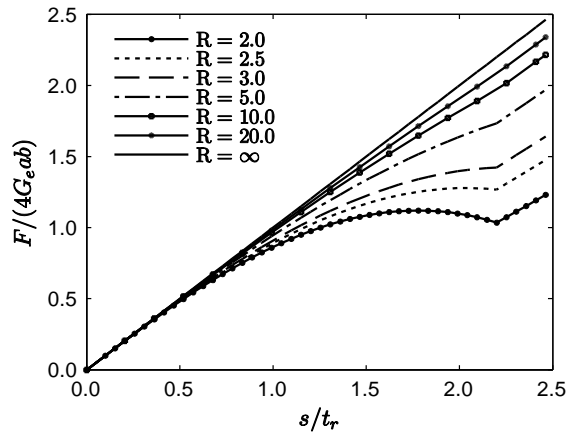


Figure 3-16: Normalized horizontal force as a function of displacement with various aspect ratios for isolator B1

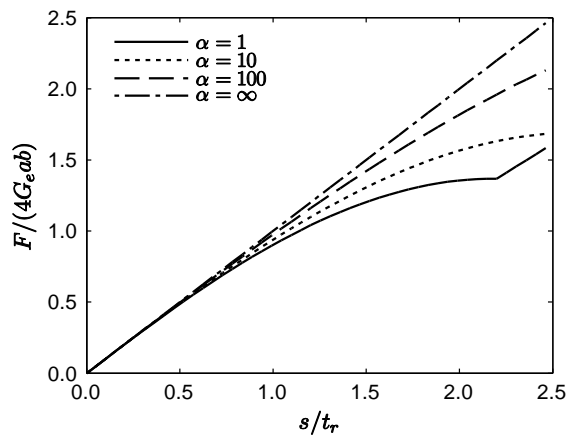


Figure 3-17: Normalized horizontal force as a function of displacement with various values of  $\alpha$  for isolator B1

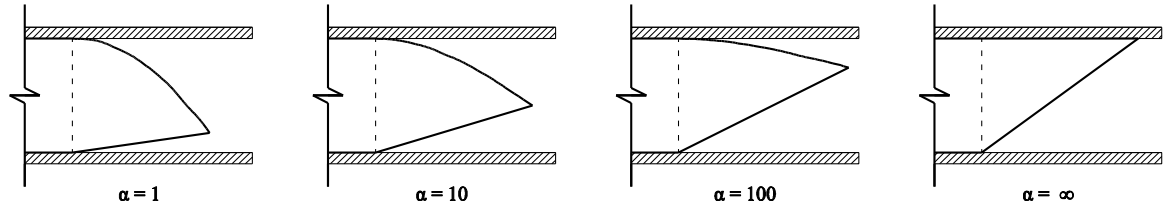


Figure 3-18: Deformed shape of the rollover sections with various values of  $\alpha$  at  $2.00 t_r$  for isolator B1

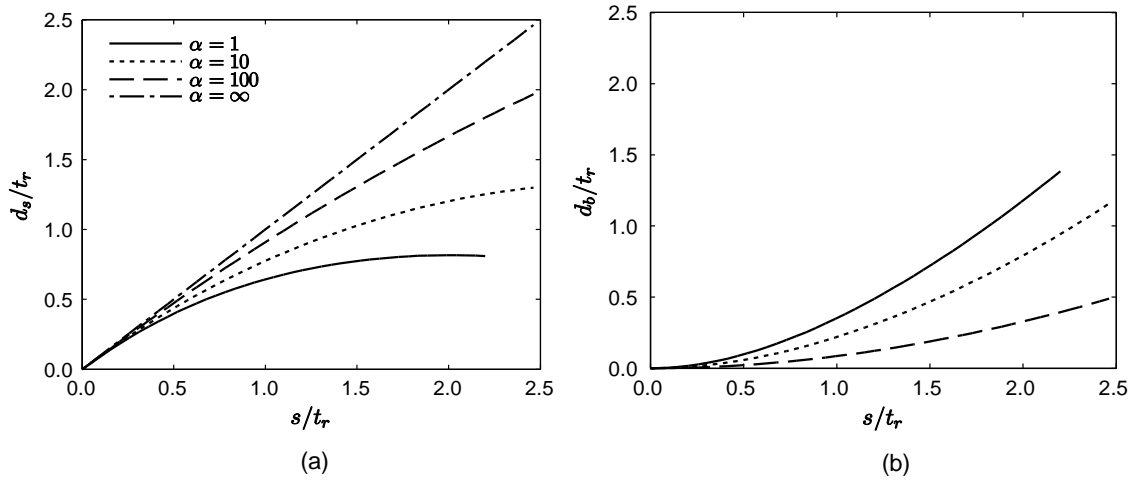


Figure 3-19: Normalized (a) shear displacement and (b) bending displacement of the rollover section as a function of horizontal displacement and various values of  $\alpha$  for isolator B1

## **4 Development of Design Code Orientated Formulas for Elastomeric Bearings Including Bulk Compressibility and Reinforcement Extensibility**

Reproduced with permission from ASCE.

Van Engelen NC, Tait MJ, Konstantinidis D. 2015. Development of Design Code Orientated Formulas for Elastomeric Bearings Including Bulk Compressibility and Reinforcement Extensibility. *Journal of Engineering Mechanics (ASCE)*.

### *Abstract*

The introduction of alternative reinforcement types for elastomeric bearings has rendered it necessary to consider the extensibility of the reinforcement as an additional design parameter. The extensibility of the reinforcement reduces the lateral restraint on the elastomer and, similar to the compressibility of the elastomer, reduces important design parameters such as the compression modulus and bending modulus. Neglecting the compressibility of the elastomer or the extensibility of the reinforcement may result in an unconservative overestimation of these design parameters. The existing analytical solutions, which have been developed based on the pressure solution, are usually not suitable for design purposes. In this study, the analytical solutions for infinite strip, circular, square and annular pad geometries are expanded and simplified to form geometry-specific approximations that account for reinforcement extensibility and bulk compressibility. The derived approximations closely and conservatively follow the analytical solutions over a large range of shape factors and values of the elastomer bulk modulus and reinforcement extensibility. A similar procedure used for the compression modulus and bending modulus is applied to approximate the maximum shear strain due to compression also including bulk compressibility and reinforcement extensibility. Generalized equations are proposed that can be adapted to the elastomeric pad geometries considered.

### *4.1 Introduction*

Fiber-reinforced elastomeric isolators (FREIs) were originally proposed as a potential low-cost alternative to conventional steel-reinforced elastomeric isolators (SREIs) (Kelly 1999). The concept was centered on the light-weight nature of the fiber reinforcement, which has comparable mechanical properties in tension to steel, and the ability to manufacture and cut FREIs to the desired size from larger pads. From an analytical perspective, the primary difference between FREIs and SREIs is that the assumption of rigid reinforcement is relaxed and the extensibility and lack of flexural resistance of the fiber reinforcement must be considered. Similar to the compressibility of

the elastomer, the extensibility of the reinforcement can play an important role in the design and performance of the isolator. From a design perspective, not including the compressibility of the elastomer and/or the extensibility of the reinforcement could seriously and unconservatively overestimate important properties, such as the compression modulus and bending modulus, or impose unwarranted design restrictions due to substantial errors in calculated values, such as the maximum shear strain due to compression.

The sensitivity of elastomeric isolators to the compressibility of the elastomer is well recognized (Kelly and Konstantinidis 2011). This sensitivity is demonstrated in Figure 4-1 as a function of the shape factor,  $S$ , for an infinite strip pad where the compression modulus,  $E_c$ , has been normalized by the compression modulus assuming an incompressible elastomer,  $E_c^\infty$ . The compressibility of the elastomer is represented by the ratio of the bulk modulus,  $K$ , to the shear modulus,  $G$ . Even for a relatively low shape factor of 10, the compressibility of the elastomer decreases  $E_c$  by 19 %. Similarly, elastomeric isolators are sensitive to the extensibility of the reinforcement as demonstrated a finite element investigation by Osgooei et al. (2014). Despite this, compressibility is often ignored, accounted for in a limited capacity, or erroneously corrected for in current design codes and standards (AASHTO 2014a,b, CSA 2014, ISO 2010). The development of generalized expressions for critical design parameters, such as the compression and bending modulus and the maximum shear strain due to compression, inclusive of the compressibility of the elastomer and extensibility of the reinforcement is valuable from a design perspective.

Analytical solutions for the compression modulus and bending modulus, which include the compressibility of the elastomer and extensibility of the reinforcement, are available for most simple elastomeric pad geometries. These analytical solutions are often complex and unsuitable for design purposes. Alternatively, Constantinou et al. (2011) presented simplified expressions for the maximum shear strain due to compression and rotation that include tabulated correction factors to account for the bearing geometry and elastomer bulk compressibility. Van Engelen and Kelly (2015) developed a generalized expression for the compression modulus and bending modulus that included bulk compressibility based on a Taylor series expansion and inversion of the analytical solutions. These studies assume rigid reinforcement and do not account for the extensibility of the reinforcement.

In this paper, the analytical solutions that include the extensibility of the reinforcement are expanded and truncated using the procedure from Van Engelen and Kelly (2015) to provide simplified generalized expressions more suitable for design codes. The simplified expressions are similar to the ad hoc approximation originally proposed by Gent and Lindley (1959) but include mathematically determined correction

factors to the terms representing the compressibility of the elastomer and extensibility of the reinforcement. The analytical solutions for the maximum shear strain due to compression, often omitted from the analytical derivations for the compression modulus, are presented, and a similar procedure is used to propose a generalized approximation which is subsequently compared to current code equations. The procedure is given in detail for the compression modulus of an infinite strip pad, while a condensed derivation is presented for the circular, square and annular pad geometries considered in this study.

## 4.2 Accounting for Compressibility

### 4.2.1 Compression Modulus and Bending Modulus

The compression modulus and bending modulus,  $E_b$ , of elastomeric bearings can be highly sensitive to the compressibility of the elastomer, especially for large shape factors, defined as the ratio of the loaded area to unloaded area of a single layer of elastomer (Kelly and Konstantinidis 2011). Prior to the development of analytical solutions based on the pressure solution, it was proposed that the effects of compressibility could be included by assuming incompressibility and correcting with the bulk modulus. The ad hoc approximation is (ISO 2010)

$$\frac{1}{E_c} = \frac{1}{E_c^\infty} + \frac{1}{K} \quad (4-1)$$

$$\frac{1}{E_b} = \frac{1}{E_b^\infty} + \frac{1}{K} \quad (4-2)$$

where  $E_b^\infty$  is the bending modulus assuming the elastomer is incompressible. This ad hoc approximation is intuitively based, capturing the correct limits, for a small  $S$ ,  $E_c \rightarrow E_c^\infty$  and as  $S \rightarrow \infty$ ,  $E_c \rightarrow K$  (Gent and Lindley 1959).

In Van Engelen and Kelly (2015), it was demonstrated that the ad hoc approximation may significantly and unconservatively overestimate  $E_c$  and  $E_b$  in comparison to the analytical solutions. The procedure originally presented in Chalhoub and Kelly (1991) based on the expansion and truncation of the analytical solution using a Taylor and binomial series, respectively, was applied to derive a correction factor to  $K$  dependent on the geometry of the pad. The inclusion of the correction factor provided a conservatively lower approximation relative to the analytical solution and generally reduced the magnitude of the error over the entire range of  $K$  and  $S$  considered.

In this study, the effect of the extensibility of the reinforcement is included by adding an additional term and geometry-specific correction factor in the form of

$$\frac{1}{E_c} = \frac{1}{E_c^\infty} + \kappa_c \frac{1}{K} + \kappa_{ec} \frac{t}{E_f t_f} \quad (4-3)$$

$$\frac{1}{E_b} = \frac{1}{E_b^\infty} + \kappa_b \frac{1}{K} + \kappa_{eb} \frac{t}{E_f t_f} \quad (4-4)$$

where  $t$  is the thickness of the elastomeric pad,  $t_f$  is the thickness of the extensible reinforcement,  $E_f$  is the elastic modulus of the extensible reinforcement, and  $\kappa_c$ ,  $\kappa_b$ ,  $\kappa_{ec}$  and  $\kappa_{eb}$  are the mathematically derived correction factors for the compression modulus, bending modulus, and reinforcement extensibility for compression and bending, respectively.

#### 4.2.2 Maximum Shear Strain due to Compression

Design codes, such as AASHTO (2014a,b) and CSA (2014) impose restrictions to limit the maximum shear demand resulting from compression, rotation, imposed lateral displacements and earthquake displacements, individually and/or in combination. These limitations are imposed to prevent failure, such as the delamination of the reinforcement from the elastomer. The maximum shear strain due to compression,  $\gamma_c$ , is given as (AASHTO 2014a,b, CSA 2014)

$$\gamma_c = \frac{D_c \sigma_c}{GS} \quad (4-5)$$

where  $\sigma_c$  is the average vertical stress due to compression, and  $D_c$  is a geometry dependent factor. If incompressibility and inextensibility are assumed, it can be shown that  $E_c \propto GS^2$  and  $\gamma_c \propto S\varepsilon_c$  based on the pressure solution (Kelly and Konstantinidis 2011). Thus, the derivation of Eq. (4-5) is relatively simple, although AASHTO (2014a,b) and CSA (2014) only provide values of  $D_c$  for circular and rectangular pad geometries. The value of  $D_c$  is recommended as 1.0 (AASHTO 2014b, CSA 2014) or 1.4 (AASHTO, 2014a) for a rectangular pad.

The commentary of AASHTO (2014a,b) allows  $D_c$  to be determined including the compressibility of the elastomer for a rectangular pad based on best-fit equations from Stanton et al. (2008). The best-fit equations recommended are

$$D_c = \max \left[ d_{a1}, (d_{a2} + d_{a3} L/W) \right] \quad (4-6)$$

with

$$d_{a1} = 1.06 + 0.210\lambda + 0.413\lambda^2 \quad (4-7)$$

$$d_{a2} = 1.506 - 0.071\lambda + 0.406\lambda^2 \quad (4-8)$$

$$d_{a3} = -0.315 + 0.195\lambda - 0.047\lambda^2 \quad (4-9)$$

and

$$\lambda = \sqrt{\frac{3GS^2}{K}} \quad (4-10)$$

where  $L$  is the plan dimension perpendicular to the axis of rotation and  $W$  is the plan dimension parallel to the axis of rotation. For a square pad with an incompressible elastomer  $L/W = 1$ ,  $\lambda \rightarrow 0$  and from Eq. (4-6),  $D_c = 1.19$ .

### 4.3 Analytical Solutions

The analytical solutions presented in this paper were derived based on the assumptions of the pressure solution. Solutions developed based on the assumptions of the pressure solution are often characterized as being appropriate for elastomeric pads with a shape factor of approximately 5 or greater (Kelly 1997). The accuracy of the analytical solutions for several pad geometries including the effects of compressibility has been verified in Constantinou et al. (2011), and in Osgooei et al. (2014) and Toopchi-Nezhad et al. (2012) including compressibility and the extensibility of the reinforcement using finite element analysis. The procedure for the pressure solution is outlined in this section, focusing on the derivation of the maximum shear strain due to compression.

An arbitrarily shaped elastomeric pad with a constant thickness and a rectangular Cartesian coordinate system  $(x, y, z)$  is presented in Figure 4-2. If a vertical load is applied in the  $z$  direction, the elastomeric pad will bulge laterally, restrained by the extensible reinforcement at the top and bottom of the pad. It is assumed that the lateral bulging of the elastomer follows a parabolic curve and horizontal planes remain plane and horizontal. Following these kinematic assumptions, the displacements in the elastomeric layer along the coordinate directions are (Kelly 1997)

$$\begin{aligned} u(x, y, z) &= u_0(x, y) \left( 1 - \frac{4z^2}{t^2} \right) + u_1(x, y) \\ v(x, y, z) &= v_0(x, y) \left( 1 - \frac{4z^2}{t^2} \right) + v_1(x, y) \\ w(x, y, z) &= w(z) \end{aligned} \quad (4-11)$$

where the functions  $u_0$  and  $v_0$  are related to the lateral bulging of the elastomer and  $u_1$  and  $v_1$  to the extension of the fiber reinforcement. Figure 4-3 shows the lateral bulging in the  $x$ - $z$  plane. The vertical deflection,  $\Delta$ , is accommodated by volumetric strain, determined by the compressibility of the elastomer, and by lateral displacement and bulging, determined by the extensibility of the reinforcement and shape factor.

The compressibility constraint gives

$$\varepsilon_{xx} + \varepsilon_{yy} + \varepsilon_{zz} = -\frac{p}{K} \quad (4-12)$$

where  $\varepsilon_{xx}$ ,  $\varepsilon_{yy}$ , and  $\varepsilon_{zz}$  are the normal strains, and  $p$  is the internal pressure (i.e. the hydrostatic portion of the stress tensor). Substitution of the respective strains, determined

from Eq. (4-11) into Eq. (4-12) and integrating through the thickness of the elastomeric layer gives

$$u_{o,x} + v_{o,y} + \frac{3}{2}(u_{1,x} + v_{1,y}) = \frac{3}{2}\varepsilon_c - \frac{3}{2}\frac{p}{K} \quad (4-13)$$

where  $\varepsilon_c = \Delta/t$  is the compression strain in the pad (with compression taken as positive), and the commas denote partial differentiation with respect to the indicated coordinate.

The pressure solution assumes that the stress state is dominated by the internal pressure such that  $\sigma_{xx} \approx \sigma_{yy} \approx \sigma_{zz} \approx -p$  and that  $\tau_{xy}$  is negligible compared to  $\tau_{xz}$  and  $\tau_{yz}$  (Kelly 1997). Applying these assumptions reduces the equations of equilibrium, under the assumption of no body forces, to

$$\tau_{xz,z} = -\sigma_{xx,x} = p_{,x} \quad (4-14)$$

$$\tau_{yz,z} = -\sigma_{yy,y} = p_{,y}$$

Assuming that the elastomer is linear elastic, the relationship between the shear stresses,  $\tau_{xz}$  and  $\tau_{yz}$ , and shear strains,  $\gamma_{xz} = u_{,z} + w_{,x}$  and  $\gamma_{yz} = v_{,z} + w_{,y}$ , yields

$$\tau_{xz} = -G \frac{8z}{t^2} u_0 \quad (4-15)$$

$$\tau_{yz} = -G \frac{8z}{t^2} v_0$$

With the equilibrium conditions, Eq. (4-14), and definition of the shear stress, Eq. (4-15), the relationship between the shear strain and pressure is

$$\gamma_{xz} = \frac{z}{G} p_{,x} \quad (4-16)$$

$$\gamma_{yz} = \frac{z}{G} p_{,y}$$

Lateral bulging causes shear strains to develop in the elastomer. Analytically, the maximum shear strain due to compression occurs at the free edge interface of the elastomer and extensible reinforcement where  $z = \pm t/2$  (see Figure 4-3). In reality, the maximum occurs just before this point, and the shear stresses rapidly drop to zero at the free surfaces: thus the analytical values can be considered as a slightly conservative estimate (Constantinou et al. 2011).

With the definition of the shear stress, Eq. (4-15), the equilibrium conditions, Eq. (4-14), become

$$p_{,x} = -G \frac{8}{t^2} u_0 \quad (4-17)$$

$$p_{,y} = -G \frac{8}{t^2} v_0$$

The complete system of equations is formed by considering the stress in the reinforcement, resulting in five equations, Eq. (4-13), Eq. (4-17), and

$$\begin{aligned} E_f t_f u_{1,xx} + \frac{8Gu_0}{t} &= 0 \\ E_f t_f v_{1,yy} + \frac{8Gv_0}{t} &= 0 \end{aligned} \quad (4-18)$$

for the five unknowns:  $u_0$ ,  $v_0$ ,  $u_1$ ,  $v_1$ , and  $p$ .

While solving, the solutions often define two dimensionless parameters,  $\alpha^2$  and  $\beta^2$ , which are functions of the extensibility of the reinforcement and compressibility of the elastomer, respectively. Often, the two parameters are summed as

$$\lambda^2 = \alpha^2 + \beta^2 \quad (4-19)$$

or

$$\lambda^2 = cGS^2 \left( \frac{1}{K} + e \frac{t}{E_f t_f} \right) \quad (4-20)$$

where the coefficients  $c$  and  $e$  depend on the pad geometry. The definitions used herein express  $\alpha^2$  and  $\beta^2$  as functions of the shape factor, which may differ from the definitions used in the analytical solution derivations presented elsewhere. For convenience, an equivalent parameter,  $K_e$ , which accounts for compressibility and extensibility is introduced

$$\frac{1}{K_e} = \frac{1}{K} + e \frac{t}{E_f t_f} \quad (4-21)$$

where the subscript represents the value of the coefficient  $e$ .

#### 4.4 Proposed Approximation Derivation

##### 4.4.1 Material and Geometric Properties

In addition to the geometric properties, the proposed approximations are dependent on three material properties; the shear and bulk modulus of the elastomer, and the elastic modulus of the extensible reinforcement. The results are presented over a range of shape factor values of  $5 \leq S \leq 50$  with the lower bound being determined due to the limitations of the pressure solution (Kelly 1997). The bulk modulus of elastomers can vary significantly and is several orders of magnitude larger than the shear modulus; estimates place it between 1000 MPa and 3500 MPa for natural rubber and Neoprene (Lindley

1978, Fuller et al. 1988, Burns 1990). In this paper, the bulk modulus was normalized by the shear modulus of the elastomer,  $G$ , and a range of  $1000 \leq K/G \leq 10000$  was considered.

Many different types of fibers have been investigated for the extensible reinforcement; accordingly,  $E_f$  can vary substantially depending on the type of extensible reinforcement selected. A range of  $3000 \leq E_f t_f / t G \leq 60000$  was considered in this study, which encompasses a large range due to dependency on the ratio of layer thickness,  $t_f / t$ . Note that  $E_f$  is designated to represent the elastic modulus of the extensible reinforcement as a composite, including the bonding agent, not as the elastic modulus of the fiber reinforcement alone. Thus,  $E_f$  can also change substantially depending on the density and weave of the fiber, in addition to the type of fiber material. It is essential that the value accurately represents the stiffness of the extensible reinforcement to avoid an overestimate of the lateral restraint provided by the reinforcement.

## 4.4.2 Infinite Strip Pad

### 4.4.2.1 Compression Modulus

The analytical solution for the compression modulus of an infinite strip pad, including the compressibility of the elastomer and extensibility of the reinforcement, is (Kelly and Takhirov 2002)

$$E_c = K_{e=1} \left( 1 - \frac{1}{\lambda} \tanh(\lambda) \right) \quad (4-22)$$

where

$$\alpha^2 = 12GS^2 \frac{t}{E_f t_f} \quad \beta^2 = 12GS^2 \frac{1}{K} \quad (4-23)$$

Note that Eq. (4-22) is identical to the analytical solution of an infinite strip pad assuming rigid reinforcement (Chalhoub and Kelly 1991) if  $E_f \rightarrow \infty$  (i.e.  $K_{e=1} = K$ ). As  $S \rightarrow \infty$  lateral bulging is largely restrained, implying that the vertical deflection is accommodated almost entirely by volumetric strain, dependent on  $K$ , and the uniform lateral extension due to the extensibility of the fiber reinforcement, dependent on  $E_f t_f / t$ .

Equation (4-22) can be expanded and simplified using the procedure from Chalhoub and Kelly (1991), and Van Engelen and Kelly (2015). The hyperbolic tangent function is expanded with a Taylor series for small values of  $\lambda$ , which yields

$$\tanh(\lambda) = \lambda - \frac{1}{3} \lambda^3 + \frac{2}{15} \lambda^5 - \frac{17}{315} \lambda^7 + O(\lambda^9) \quad (4-24)$$

Substituting the first three terms of the Taylor series into Eq. (4-22), and with the definition of  $\lambda$ , approximates  $E_c$  as

$$E_c = 4GS^2 \left( 1 - \frac{24GS^2}{5K_{e=1}} \right) \quad (4-25)$$

From Eq. (4-25) it can be observed that for small  $S$  or large  $K$  the bracketed term approaches unity and  $E_c \rightarrow 4GS^2$ , which is the analytical solution of an infinite strip pad assuming rigid reinforcement and incompressibility (Chalhoub and Kelly 1991). The volume of elastomer that laterally bulges in elastomeric pads with a small  $S$  is large in comparison to the volumetric strain or uniform lateral extension due to the extensible reinforcement. Consequently, for very small values of  $S$ , the elastomeric pad can be assumed incompressible.

Inverting Eq. (4-25) yields

$$\frac{1}{E_c} = \frac{1}{4GS^2} \left( 1 - \frac{24GS^2}{5K_{e=1}} \right)^{-1} \quad (4-26)$$

Applying a binomial series expansion in the form of

$$(1-x)^{-1} = 1 + x + O(x^2) \quad (4-27)$$

for the bracketed terms gives

$$\frac{1}{E_c} = \frac{1}{4GS^2} + \frac{6}{5} \frac{1}{K} + \frac{6}{5} \frac{t}{E_f t_f} \quad (4-28)$$

which is identical to the approximation from Chalhoub and Kelly (1991) and Van Engelen and Kelly (2015), with an additional term representing the extensibility of the reinforcement.

The compression modulus can be highly sensitive to the compressibility of the elastomer and extensibility of the reinforcement, as demonstrated in Figure 4-4. The results with  $\kappa_c = \kappa_{ec} = 6/5$  for the compression modulus of an infinite strip pad are shown in Figure 4-5. The compressibility of the elastomer and extensibility of the reinforcement in this derivation appear together in an inverted summation, which is equivalent to  $1/K_{e=1}$ . As such, it is convenient to show the percent error as a function of  $S$  and  $K_{e=1}$ . A range of  $500 \leq K_{e=1}/G \leq 10000$  is shown in Figure 4-5 which encompasses the range of approximately  $750 \leq K_{e=1}/G \leq 8500$  based on the selected ranges of  $K/G$  and  $E_f t_f / tG$ .

#### 4.4.2.2 Shear Strain due to Compression

The maximum shear strain due to compression which occurs at the interface of the elastomer and extensible reinforcement at the unloaded edge of the bearing, derived from the solution for  $E_c$  presented in Kelly and Takhirov (2002), is

$$\frac{\gamma_c}{\varepsilon_c} = 6S \frac{\tanh(\lambda)}{\lambda} \quad (4-29)$$

where  $\varepsilon_c = \sigma_c / E_c$  is the vertical compression strain. A similar procedure as with the compression modulus, based on a Taylor series expansion, truncation, inversion and application of the binomial series, is employed to develop a simplified expression for the strain ratio. This procedure yields

$$\frac{\gamma_c}{\varepsilon_c} = \left( \frac{1}{6S} + \frac{2}{3} \frac{GS}{K_{e=1}} \right)^{-1} \quad (4-30)$$

Unlike  $E_c$ , as  $S$  increases Eq. (4-30) diverges from the analytical solution and the error becomes large and unconservative. It is necessary to present a second approximation based on large values of  $S$ . Note that as  $\lambda$  increases, the hyperbolic tangent function rapidly approaches unity. Thus, the analytical solution, Eq. (4-29), for large  $S$  can be approximated as

$$\frac{\gamma_c}{\varepsilon_c} = \frac{6S}{\lambda} \quad (4-31)$$

Using the definition of  $\lambda$  from Eq. (4-19) and Eq. (4-23), Eq. (4-31) can equivalently be expressed as

$$\frac{\gamma_c}{\varepsilon_c} = \sqrt{3} \frac{K_{e=1}}{G} \quad (4-32)$$

which is independent of  $S$  and represents the horizontal asymptote that Eq. (4-29) approaches as  $S$  becomes infinitely large.

An example of the proposed approximations is shown in Figure 4-6. The approximation for small shape factors (Eq. (4-30)) reaches a maximum before diverging from the analytical solution. It is proposed that the transition between the approximation based on small shape factors (Eq. (4-30)) and large shape factors (Eq. (4-32)) occur when Eq. (4-30) reaches a maximum at

$$S = \sqrt{\frac{1}{4} \frac{K_{e=1}}{G}} \quad (4-33)$$

Up to this point, the error gradually increases with increasing  $S$ , after this point Eq. (4-30) will decrease and begin to diverge, rapidly increasing the error. Using this criterion, an example of the percent error is provided in Figure 4-7. The procedure to determine this criterion was applied to all pad geometries.

#### 4.4.2.3 Bending Modulus

The analytical solution for the bending modulus of an infinite strip pad, including the compressibility of the elastomer and extensibility of the reinforcement, is (Kelly and Takhirov 2002)

$$E_b = \frac{36GS^2}{\lambda^4} \left( 1 + \frac{\lambda^2}{3} - \lambda \coth(\lambda) \right) \quad (4-34)$$

where  $e = 1$  from Eq. (4-23).

Equation (4-34) is identical to the solution assuming rigid reinforcement (Kelly and Konstantinidis 2011) if  $E_f \rightarrow \infty$ . Following the expansion and truncation procedure, the bending modulus can be approximated as

$$\frac{1}{E_b} = \frac{1}{\frac{4}{5}GS^2} + \frac{10}{7} \frac{1}{K} + \frac{10}{7} \frac{t}{E_f t_f} \quad (4-35)$$

The results with  $\kappa_b = \kappa_{eb} = 10/7$  for the bending modulus of an infinite strip pad are compared in Figure 4-8.

### 4.4.3 Circular Pad

#### 4.4.3.1 Compression Modulus

It is assumed that the reinforcement in orthogonal directions acts as a uniaxial material with no interaction between the opposing directions (i.e. Poisson's ratio for the fiber reinforcement is zero). Including the compressibility of the elastomer and extensibility of the reinforcement, the compression modulus of a circular pad, is expressed as (Kelly and Calabrese 2013)

$$E_c = \frac{I_0(\lambda) - \frac{2}{\lambda} I_1(\lambda)}{2 \frac{t}{E_f t_f} \left[ I_0(\lambda) - \frac{1}{\lambda} I_1(\lambda) \right] + \frac{1}{K} I_0(\lambda)} \quad (4-36)$$

where  $I_0$ , and  $I_1$  are order 0 and 1 modified Bessel functions of the first kind, respectively, and for a circular pad

$$\alpha^2 = 48GS^2 \frac{t}{E_f t_f} \quad \beta^2 = 48GS^2 \frac{1}{K} \quad (4-37)$$

Expanding Eq. (4-36) in a Taylor series yields

$$E_c = 6GS^2 \left[ 1 - 8GS^2 \left( \frac{1}{K} + \frac{7}{4} \frac{t}{E_f t_f} \right) \right] \quad (4-38)$$

Inverting the expression and expanding with a binomial series gives

$$\frac{1}{E_c} = \frac{1}{6GS^2} + \frac{4}{3} \frac{1}{K} + \frac{7}{3} \frac{t}{E_f t_f} \quad (4-39)$$

The results with  $\kappa_c = 4/3$  and  $\kappa_{ec} = 7/3$  for the compression modulus of a circular pad are compared in Figure 4-9. Unlike the infinite strip isolator, where the compressibility and extensibility terms can be replaced with  $K_e$ , the circular pad is

necessarily compared against the selected ranges of  $K/G$  and  $E_f t_f / tG$  since these terms in Eq. (4-36) cannot be replaced by  $K_e$ .

#### 4.4.3.2 Shear Strain due to Compression

The maximum shear strain due to compression, derived from the solution for  $E_c$  presented in Kelly and Calabrese (2013), is

$$\frac{\gamma_c}{\varepsilon_c} = 6S \left\{ \frac{I_1(\lambda)}{\frac{\alpha^2}{\lambda} \left[ I_0(\lambda) - \frac{1}{\lambda} I_1(\lambda) \right] + \frac{\beta^2}{\lambda} \frac{1}{2} I_0(\lambda)} \right\} \quad (4-40)$$

Following the procedure used herein, Eq. (4-40) can be simplified to

$$\frac{\gamma_c}{\varepsilon_c} = \left( \frac{1}{6S} + \frac{GS}{K_{e=2}} \right)^{-1} \quad (4-41)$$

which reaches a maximum at

$$S = \sqrt{\frac{1}{6} \frac{K_{e=2}}{G}} \quad (4-42)$$

The limit of Eq. (4-40) as  $S \rightarrow \infty$  gives

$$\frac{\gamma_c}{\varepsilon_c} = \sqrt{3 \frac{G}{K_{e=1}} \frac{K_{e=2}}{G}} \quad (4-43)$$

Introducing the following approximation

$$\frac{K_{e=2}^2}{K_{e=1}} \approx K_{e=13/4} \quad (4-44)$$

which was determined by minimizing the squared residuals over the range of  $K/G$  and  $E_f t_f / tG$  considered, a similar expression as with the infinite strip pad is obtained

$$\frac{\gamma_c}{\varepsilon_c} = \sqrt{3 \frac{K_{e=13/4}}{G}} \quad (4-45)$$

The percent error from the proposed approximation is shown in Figure 4-10. Equation (4-41) is selected if  $S$  is less than Eq. (4-42), and Eq. (4-45) is selected if  $S$  is greater than Eq. (4-42).

### 4.4.4 Square Pad

#### 4.4.4.1 Compression Modulus

The compression modulus of a rectangular pad, including the compressibility of the elastomer and extensibility of the reinforcement, was first investigated by Angeli et al. (2013) using a double Fourier series solution. The method presented by Kelly and Van Engelen (2015), based on a single Fourier series, is selected since it converges rapidly and

conveniently simplifies to the analytical solutions of a square pad assuming rigid reinforcement and a compressible or an incompressible elastomer (Kelly 1997, Kelly and Konstantinidis 2011). The compression modulus of a square pad, a special case of the solution for a rectangular pad, including the compressibility of the elastomer and extensibility of the reinforcement is (Kelly and Van Engelen 2015)

$$E_c = 1536GS^2 \sum_{n=1,3,5,\dots}^{\infty} \frac{1}{n^4 \pi^4 \xi_n^2} \left( 1 - \frac{2}{n\pi\xi_n} \tanh\left(\frac{n\pi}{2} \xi_n\right) \right) \quad (4-46)$$

where

$$\xi_n = \sqrt{1 + \frac{192GS^2}{n^2 \pi^2 K_{e=2}}} \quad (4-47)$$

and  $e = 2$  is determined from the analytical solution.

Following the expansion and truncation procedure, the proposed approximation is

$$\frac{1}{E_c} = \frac{1}{6.748GS^2} + \frac{7}{5} \frac{1}{K} + \frac{14}{5} \frac{t}{E_f t_f} \quad (4-48)$$

The results with  $\kappa_c = 7/5$  and  $\kappa_{ec} = 14/5$  for the compression modulus of a square pad are compared in Figure 4-11.

#### 4.4.4.2 Shear Strain due to Compression

For a square pad, the maximum shear strain due to compression is (Kelly and Van Engelen 2015)

$$\frac{\gamma_c}{\varepsilon_c} = 96S \sum_{n=1,3,5,\dots}^{\infty} \frac{1}{n^2 \pi^2 \xi_n} \tanh\left(\frac{n\pi}{2} \xi_n\right) \sin\left(\frac{n\pi}{2}\right) \quad (4-49)$$

which can be approximated as

$$\frac{\gamma_c}{\varepsilon_c} = \left( \frac{1}{8.104S} + 0.945 \frac{GS}{K_{e=2}} \right)^{-1} \quad (4-50)$$

The maximum of Eq. (4-50) occurs at

$$S = \sqrt{\frac{1}{7.658} \frac{K_{e=2}}{G}} \quad (4-51)$$

Similar to the infinite strip pad, for large values of  $S$  the hyperbolic tangent function will approach unity and the expression becomes proportional to the inverse of  $\xi_n$ . Taking the limit as  $S \rightarrow \infty$  of Eq. (4-49) yields

$$\frac{\gamma_c}{\varepsilon_c} = \sum_{n=1,3,5,\dots}^{\infty} \frac{4}{n\pi} \sqrt{3 \frac{K_{e=2}}{G}} \sin\left(\frac{n\pi}{2}\right) \quad (4-52)$$

Summing the series gives approximately

$$\frac{\gamma_c}{\varepsilon_c} = \sqrt{3 \frac{K_{e=2}}{G}} \quad (4-53)$$

The percent error from the proposed approximation is shown in Figure 4-12. Equation (4-50) is selected if  $S$  is less than Eq. (4-51), and Eq. (4-53) is selected if  $S$  is greater than Eq. (4-51).

#### 4.4.4.3 Bending Modulus

The bending modulus of a square pad including the compressibility of the elastomer and extensibility of the reinforcement is (Angeli et al. 2013)

$$E_b = \frac{2304GS^2}{\pi^4} \sum_{n=1,2,3,\dots}^{\infty} \sum_{m=1,3,5,\dots}^{\infty} \frac{1}{n^2 m^2} \frac{1}{(n\pi)^2 + \left(\frac{m\pi}{2}\right)^2 + \alpha^2 + \beta^2}. \quad (4-54)$$

In Angeli et al. (2013), the thickness of the reinforcement layer was divided by two to represent the assumed bi-directional fiber reinforcement. Following the definition of  $E_f$  used herein, selected to represent the flexible reinforcement layer as a composite with the bonding agent, the definition of  $\alpha^2$  and  $\beta^2$  are

$$\alpha^2 = 96GS^2 \frac{t}{E_f t_f} \quad \beta^2 = 48GS^2 \frac{1}{K} \quad (4-55)$$

Following the expansion and truncation procedure, the proposed approximation is

$$\frac{1}{E_b} = \frac{1}{2.228GS^2} + \frac{8}{5} \frac{1}{K} + \frac{16}{5} \frac{t}{E_f t_f} \quad (4-56)$$

The results with  $\kappa_b = 8/5$  and  $\kappa_{eb} = 16/5$  for the bending modulus of a square pad are compared in Figure 4-13.

### 4.4.5 Annular Pad

#### 4.4.5.1 Compression Modulus

The compression modulus of an annular pad including the compressibility of the elastomer and extensibility of the reinforcement is (Pinarbasi and Okay 2011)

$$E_c = \frac{E_f t_f}{2t} \frac{\left\{ \begin{aligned} & \left[ (1-\eta^2) [I_0(\lambda) - A_1 K_0(\lambda)] - \right. \\ & \left. \frac{2}{\lambda} [I_1(\lambda) - \eta I_1(\eta\lambda) + A_1 [K_1(\lambda) - \eta K_1(\eta\lambda)]] \right] \end{aligned} \right\}}{A_2 - \eta^2 A_3 + (1-\eta^2) A_4} \quad (4-57)$$

where

$$\alpha^2 = 48GS^2 \frac{1}{K} \frac{1}{(1-\eta)^2} \quad \beta^2 = 48GS^2 \frac{t}{E_f t_f} \frac{1}{(1-\eta)^2} \quad (4-58)$$

$$A_1 = \frac{I_0(\lambda) - I_0(\eta\lambda)}{K_0(\lambda) - K_0(\eta\lambda)} \quad (4-59)$$

$$A_2 = I_0(\lambda) - A_1 K_0(\lambda) - \frac{I_1(\lambda) - A_1 K_1(\lambda)}{\lambda} \quad (4-60)$$

$$A_3 = I_0(\eta\lambda) - A_1 K_0(\eta\lambda) - \frac{I_1(\eta\lambda) - A_1 K_1(\eta\lambda)}{\eta\lambda} \quad (4-61)$$

$$A_4 = \frac{1}{2} \frac{E_f t_f}{Kt} [I_0(\lambda) - A_1 K_0(\lambda)] \quad (4-62)$$

and  $\eta$  is the ratio of the inner radius to the outer radius, and  $K_0$ ,  $K_1$  are order 0 and 1 modified Bessel functions of the second kind, respectively. Modified Bessel functions of the second kind cannot be expanded in a Taylor series, and this expression, as with the case assuming inextensible reinforcement, cannot be simplified with the procedure used herein (Van Engelen and Kelly 2015).

Alternatively, the following expression is proposed:

$$\frac{1}{E_c} = \frac{1}{6GS^2 \lambda_c} + \frac{6}{5} \frac{1}{K} + \frac{12}{5} \frac{t}{E_f t_f} \quad (4-63)$$

where (Constantinou et al. 1992)

$$\lambda_c = \frac{1 + \eta^2 - \frac{1 - \eta^2}{\ln(1/\eta)}}{(1 - \eta)^2} \quad (4-64)$$

Note that  $\lambda_c$ , which accounts for the presence of the hole, quickly converges to  $2/3$  and  $E_c^\infty \rightarrow 4GS^2$ , which is the solution for an infinite strip pad. Based on this observation, Van Engelen and Kelly (2015) proposed selecting  $\kappa_c = 6/5$  which was derived for an infinite strip pad. The correction factor of  $\kappa_{ec} = 12/5$  for the extensibility was selected based on the observation that for small values of  $\eta$ ,  $E_c$  approximately approaches  $K_{e=2}$  as  $S \rightarrow \infty$ . Note that, with the exception of the circular pad, which also converges to  $K_{e=2}$  as  $S \rightarrow \infty$ ,  $\kappa_{ec}/\kappa_c$  is equal to  $e$ . The result with  $\kappa_c = 6/5$  and  $\kappa_{ec} = 12/5$  for the compression modulus of an annular pad are compared in Figure 4-14 with  $\eta = 0.1$ . Due to the rapid convergence of the solution to an infinite strip pad, the error is not sensitivity to changes in  $\eta$ , increasing only slightly as  $\eta$  increases, as shown in Figure 4-15.

#### 4.4.5.2 Shear Strain due to Compression

The maximum shear strain due to compression occurs at the inner surface of an annular pad; however, the maximum value at the outer surface may also be of interest. The shear strain due to compression assuming an incompressible elastomer and inextensible reinforcement, derived from Kelly and Konstantinidis (2011), is

$$\frac{\gamma_c}{\varepsilon_c} = 6S |\lambda_s| \quad (4-65)$$

with

$$\lambda_s = \frac{b+a}{2r \ln(b/a)} - \frac{r}{b-a} \quad (4-66)$$

where  $a$  is the inner radius,  $b$  is the outer radius and  $r$  is the radius.

##### 4.4.5.2.1 Outer Surface ( $r = b$ )

The shear strain due to compression at the outer surface of an annular pad, including reinforcement extensibility and bulk compressibility, is (Pinarbasi and Okay 2011)

$$\frac{\gamma_c}{\varepsilon_c} = 6S \frac{\lambda}{\beta^2} (1+\eta) \frac{I_1(\lambda) + A_1 K_1(\lambda)}{A_2 - \eta^2 A_3 + (1-\eta^2) A_4} \quad (4-67)$$

All of the parameters for an annular bearing,  $\alpha^2$ ,  $\beta^2$  and  $\lambda^2$ , are equivalent to a circular isolator with the same outer radius since

$$S_c = \frac{S_a}{1-\eta} \quad (4-68)$$

where  $S_c$  and  $S_a$  are the shape factors for a circular and annular pad, respectively. Using this relationship, Eq. (4-67) can be expressed in terms of  $S_c$  as

$$\frac{\gamma_c}{\varepsilon_c} = 6S_c \frac{\lambda}{\beta^2} (1-\eta^2) \frac{I_1(\lambda) + A_1 K_1(\lambda)}{A_2 - \eta^2 A_3 + (1-\eta^2) A_4} \quad (4-69)$$

The shear strain at the outer surface is less in an annular pad than a circular pad with equal  $\varepsilon_c$  and equal outer radius. This occurs because the hole in an annular pad provides an additional free surface for lateral bulging which reduces the magnitude of lateral bulging at the outer surface. Due to these similarities, it is proposed that the expression for the maximum shear strain at the outer surface of an annular pad be expressed similar to the circular pad, Eq. (4-41) and Eq. (4-45). Furthermore, it can be shown that for small values of  $\eta$  that the limit of Eq. (4-67) as  $S \rightarrow \infty$  is approximately equal to the limit for a circular pad, Eq. (4-45). Therefore, the proposed approximation is

$$\frac{\gamma_c}{\varepsilon_c} = \left( \frac{1}{6|\lambda_s|S} + \frac{GS}{K_{e=2}} \right)^{-1} \quad (4-70)$$

which reaches a maximum at

$$S = \sqrt{\frac{1}{6|\lambda_s|} \frac{K_{e=2}}{G}} \quad (4-71)$$

The percent error from the proposed approximation is shown in Figure 4-16. Equation (4-70) is selected if  $S$  is less than Eq. (4-71), and Eq. (4-45) is selected if  $S$  is greater than Eq. (4-71). The percent error is not largely sensitive to changes in  $\eta$ .

#### 4.4.5.2.2 Inner Surface ( $r = a$ )

The shear strain due to compression at the inner surface is (Pinarbasi and Okay 2011)

$$\frac{\gamma_c}{\varepsilon_c} = 6S \frac{\lambda}{\beta^2} (1 + \eta) \frac{I_1(\eta\lambda) + A_1 K_1(\eta\lambda)}{A_2 - \eta^2 A_3 + (1 - \eta^2) A_4} \quad (4-72)$$

The general trend observed in the other pad geometries, where the strain ratio increases with  $S$  and approaches a horizontal asymptote (see Figure 4-6), does not occur. An example of the trend is provided in Figure 4-17 which shows that the shear strain ratio increases to a maximum. Although the horizontal asymptote is identical to the outer surface, the rate of convergence is slower and the asymptote is approached gradually from above with very large  $S$ . Note that Eq. (4-72) is governed by the incompressible and inextensible solution for small values of  $S$ . Therefore, the following expression is proposed

$$\frac{\gamma_c}{\varepsilon_c} = \left( \frac{1}{6|\lambda_s|S} + \lambda_a \frac{GS}{K_{e=7/4}} \right)^{-1} \quad (4-73)$$

where

$$\lambda_a = 0.1(\ln \eta + 5.25) \quad (4-74)$$

accounts for the increased sensitivity to the hole that occurs at the inner surface. The function  $\lambda_a$  and coefficient  $e$  were determined using an iterative least squares regression procedure over the selected range of  $S$ ,  $K/G$ ,  $E_f t_f / tG$  and  $0.02 \leq \eta \leq 0.4$ .

The maximum of Eq. (4-73) occurs at

$$S = \sqrt{\frac{1}{6|\lambda_s| \lambda_a} \frac{K_{e=7/4}}{G}} \quad (4-75)$$

Unlike the other pad geometries considered, the decrease that occurs after the maximum is beneficial as it follows the analytical solution. The analytical solution approaches Eq. (4-45) as  $S \rightarrow \infty$ , thus Eq. (4-45) is imposed as a lower limit if  $S$  exceeds Eq. (4-75). The percent error from the proposed approximation is shown in Figure 4-18 and an example of the sensitivity of the error to  $\eta$  is shown in Figure 4-19.

## 4.5 Discussion

### 4.5.1 Compression and Bending Modulus

The proposed approximation for the compression and bending modulus are especially useful for design since they build on the popular ad hoc approximation, Eq. (3-7), proposed by Gent and Lindley (1959) and used in design standards (ISO 2010). The proposed approximations introduce derived correction factors for various pad geometries that take into account both the elastomer compressibility and reinforcement extensibility. The coefficient to the incompressible analytical solution and correction factors of the compression and bending modulus are summarized in Table 3-1. Table 3-1 also includes the correction factor and coefficient for the bending modulus of a circular and annular pad in bending with

$$\lambda_b = \frac{(1+\eta)^2}{1+\eta^2} \quad (4-76)$$

which corrects the incompressible solution for the presence of the hole in bending (Van Engelen and Kelly 2015). Pressure solutions under pure bending including the compressibility of the elastomer and extensibility of the reinforcement are not available in the literature for circular and annular pads.

The proposed approximation, from Eq. (4-3), can alternatively be expressed as

$$\frac{1}{E_c} = \frac{1}{E_c^\infty} + \kappa_c \left( \frac{1}{K} + \frac{\kappa_{ec}}{\kappa_c} \frac{t}{E_f t_f} \right) \quad (4-77)$$

or as

$$\frac{1}{E_c} = \frac{1}{E_c^\infty} + \frac{\kappa_c}{K_e} \quad (4-78)$$

where  $e = \kappa_{ec}/\kappa_c$ . If  $K_e = K$  in Eq. (4-78), the expression is identical to the proposed approximation from Van Engelen and Kelly (2015) and many of the observations in that study apply when including reinforcement extensibility. This is the case for the infinite strip pad and square pad geometries. In Van Engelen and Kelly (2015), it was observed that the ad hoc approximation (Eq. (1)), assuming rigid reinforcement, captures the correct limits for small  $S$  or as  $S \rightarrow \infty$ , but otherwise may have a significant and unconservative error over the practical range of  $S$  for elastomeric bearings. The inclusion of the correction factor determines that  $E_c \rightarrow K/\kappa_c$  and the error approaches a maximum of  $(1-1/\kappa_c)$  as  $S \rightarrow \infty$ . Although the upper limit is not captured correctly, the inclusion of the correction factor results in an improved and conservative approximation for the range of  $S$  typical in elastomeric bearing design. The inclusion of the extensibility of the reinforcement implies  $E_c \rightarrow K_e/\kappa_c$  as  $S \rightarrow \infty$  (from Eq. (4-78)), and results in a

decreased lower bound of  $K_e$  in comparison to  $K$  (i.e. the minimum value of  $K_e/G$  is less than the minimum value of  $K/G$  considered). The error of the proposed approximation increases as  $K_e$  decreases. Consequently, the decrease in the lower bound of  $K_e$  increases the magnitude of the maximum percent error over the range considered. Regardless, the maximum percent error obtained as  $S \rightarrow \infty$  is unchanged. Identical observations can be made for the bending modulus.

For the analytical solutions to circular and annular pad geometries,  $\alpha^2$  and  $\beta^2$  appear individually, consequently the error was shown as a function of  $S$ ,  $K/G$ , and  $E_f t_f / tG$ . The error was only sensitive to small values of  $E_f t_f / tG$ . From a mathematical perspective, if  $E_f t_f / t$  is significantly greater than  $K$ , then  $K_e \approx K$  and both the analytical solution and the approximation will not be sensitive to small changes in  $E_f t_f / t$ . In a physical sense, this represents increased dependency on the bulk compressibility as the reinforcement becomes near-rigid. From Eq. (4-36), in the limit as  $S \rightarrow \infty$ ,  $E_c \rightarrow K_{e=2}$ . Thus the maximum error of the proposed approximation is  $(1-1/\kappa_c)$  if rigid reinforcement is assumed, or  $(1-e/\kappa_{ec})$ , where  $e=2$ , if the elastomer is incompressible and extensibility of the reinforcement is allowed.

#### 4.5.2 Shear Strain due to Compression

Two generalized approximations dependent on the elastomeric pad geometry can be used to determine the maximum shear strain due to compression. The approximations are

$$\frac{\gamma_c}{\varepsilon_c} = \begin{cases} \left( \frac{1}{\Gamma_1 S} + \Gamma_2 \frac{GS}{K_e} \right)^{-1}, & \text{if } S < \sqrt{\frac{1}{\Gamma_1 \Gamma_2} \frac{K_e}{G}} \\ \sqrt{3 \frac{K_e}{G}}, & \text{if } S \geq \sqrt{\frac{1}{\Gamma_1 \Gamma_2} \frac{K_e}{G}} \end{cases} \quad (4-79)$$

The factors,  $\Gamma_1$ ,  $\Gamma_2$ , and  $e$ , required to determine the shear strain due to compression are listed in Table 4-2. These proposed approximations are similarly easy to use and can be applied to multiple pad geometries.

The inverted expression obtained using a Taylor and binomial series expansion for small values of  $S$  contains  $S$  in the denominator of the first term, and in the numerator of the second term. The denominator of the first term is identical to  $\gamma_c/\varepsilon_c$  assuming an incompressible elastomer and inextensible reinforcement and, as with  $E_c$  and  $E_b$ , the second term corrects for these effects. However, the appearance of  $S$  in both terms determines that  $\gamma_c/\varepsilon_c \rightarrow 0$  as  $S \rightarrow \infty$ , thus the error increases substantially after the maximum of the approximation for small  $S$  is obtained. Comparable to  $E_c$  and  $E_b$ , this

approximation will always provide a lower estimate than the analytical solution, which with respect to the shear strain ratio is unconservative, although the magnitude of the error is small.

The criterion selected to determine which shear strain approximation should be selected minimized the error for small values of  $S$  to below 20 %, depending on the geometry of the pad. The shear strain ratio increases with increasing  $S$ , and approaches a horizontal asymptote, independent of  $S$ . This is analogous to  $E_c$  and  $E_b$  approaching  $K_e$  as  $S$  becomes infinitely large. By selecting this limit as the strain ratio for large values of  $S$ , the approximation will always provide a conservative estimate for larger values of  $S$ . Note that the shear strain ratio, unlike  $E_c$  and  $E_b$  and with the exception of the inner surface of an annular pad, rapidly converges to this limit within the range of  $S$  considered for typical elastomeric bearing design. Similar to the approximation for small values of  $S$ , the error was found to not exceed -20%, which is conservative for the shear strain ratio, decreasing in magnitude with increasing  $S$ .

### 4.5.3 Example

The maximum shear strain due to compression is investigated for a square pad with an average vertical stress of 7.0 MPa, corresponding to the maximum value allowed at the serviceability limit state (CSA 2014). Note that stability considerations and limitations on  $\gamma_c$  due to specific load cases are omitted from this example. Figure 4-20 compares  $\gamma_c$  determined by the analytical solution to the approximations in CSA (2014) (i.e. neglecting compressibility and extensibility), AASHTO (2014a,b) including compressibility, and the proposed approximation with  $G = 0.5$  and 1.0 MPa and various values of  $K_{e=2}$ . Note that the extensibility was included in AASHTO (2014a,b) by taking  $K = K_{e=2}$  in Eq. (4-10).

The value of  $\gamma_c$  is directly proportional to  $\varepsilon_c$ . For low values of  $S$ ,  $\varepsilon_c$ , and consequently  $\gamma_c$ , are large due to the low compression modulus. As  $S$  increases,  $E_c$  increases and  $\gamma_c$  decreases. Determining  $\varepsilon_c$  based on a value of  $E_c$  neglecting compressibility and extensibility may significantly under estimate the actual value, which will consequently result in large and unconservative errors in the calculated value of  $\gamma_c$ .

The sensitivity to the compressibility of the elastomer or the extensibility of the reinforcement increases as  $S$  increases. Deriving Eq. (4-5) from the pressure solution assuming an incompressible elastomer and inextensible reinforcement yields a coefficient of approximately  $D_c = 1.2$  for a square pad. In light of the recommend value of  $D_c = 1.0$ , the code approximation is unconservative before the effects of compressibility and extensibility are included. Neglecting compressibility and extensibility significantly and

unconservatively underestimates  $\gamma_c$ , as shown in Figure 4-21 over  $500 \text{ MPa} \leq K_{e=2} \leq 10000 \text{ MPa}$ .

The best-fit approximation presented by Stanton et al. (2008), and recommended in the commentary of AASHTO (2014a,b), fits the analytical solution well over much of the range considered, but diverges quickly for large values of  $S$  and low compressibility, which presumably exceeds the range considered. Despite the low error, the equations in AASHTO (2014a,b) are not as convenient for use as the proposed approximation and are exclusive to a single pad geometry (i.e. rectangular). The proposed approximation closely follows the analytical solution (see Figure 4-20) with minimal error, ranging between -20 % to 10 %, as shown in Figure 4-21. Furthermore, the proposed approximation can easily be adapted to other pad geometries by selecting the appropriate coefficients.

#### *4.6 Conclusion*

The introduction of alternative types of reinforcement, such as fiber, for elastomeric bearings has required that the extensibility of the reinforcement be considered as an additional design parameter. It was demonstrated that the often complex analytical solutions that include the compressibility of the elastomer and extensibility of the reinforcement could be expanded and truncated to simple approximations. The pad geometry is accounted for through the inclusion of correction factors; otherwise the proposed approximations take a similar form for all pad geometries considered.

The procedure was used to develop proposed approximations for the compression and bending modulus and maximum shear strain due to compression. Recognizing that design codes often remain technology neutral, it is recommended that these expressions be adapted as simple approximations for the compression modulus, bending modulus, and the maximum shear strain due to compression. If it is appropriate to assume an incompressible elastomer or rigid reinforcement, the appropriate terms of the proposed approximations can be eliminated and the expressions reduced.

#### *Acknowledgements*

Financial support for this study was provided by the McMaster University Centre for Effective Design of Structures (CEDS) funded through the Ontario Research and Development Challenge Fund (ORDCF) as well as an Early Researcher Award (ERA) grant, both of which are programs of the Ministry of Research and Innovation (MRI). The support of the Natural Sciences and Engineering Research Council of Canada and a Vanier Canada Graduate Scholarship is gratefully acknowledged.

#### *References*

Angeli P, Russo G, Paschini A. (2013). “Carbon Fiber-Reinforced Rectangular Isolators

- with Compressible Elastomer: Analytical Solution for Compression and Bending.” *Int. J. Solids Struct.*, 50(22): 3519-3527.
- AASHTO. (2014a). *AASHTO LRFD Bridge Design Specifications*. 7<sup>th</sup> Ed., American Association of State Highway and Transportation Officials, Washington, D.C.
- AASHTO. (2014b). *Guide Specifications for Seismic Isolation Design*. 4<sup>th</sup> Ed., American Association of State Highway and Transportation Officials, Washington, D.C.
- Burns, J., Dubbelday, P.S., and Ting, R.Y. (1990). “Dynamic bulk modulus of various elastomers.” *J. Polymer Sci. Part B Polymer Physics*, 28(7), 1187-1205.
- Chalhoub M.S., and Kelly, J.M. (1991). “Analysis of infinite-strip-shaped base isolator with elastomer bulk compression.” *J. Eng. Mech. ASCE*, 117(8), 1791-1805.
- Constantinou, M.C., Kalpakidis, I., Filiatrault, A., and Ecker Lay, R.A. (2011). “LRFD-based analysis and design procedures for bridge bearings and seismic isolators.” Rept. No, MCEER-11-0004.
- Constantinou, M.C., Kartoum, A., and Kelly, J.M. (1992). “Analysis of compression of hollow circular elastomeric bearings.” *Eng. Struct.*, 14(2), 103-111. MCEER, University at Buffalo, NY.
- CSA. (2014). *S6-14 Canadian Highway Bridge Design Code*. Canadian Standards Association, Canada.
- Fuller, K.N.G., Gregory, M.J., Harris, J.A., Muhr, A.H., Roberts, A.D., and Stevenson, A. (1988). “Engineering use of natural rubber.” *Natural Rubber Science and Technology*, A.D. Roberts, eds., Oxford University Press, New York.
- Gent, A.N. and Lindley, P.B. (1959). “Compression of bonded rubber blocks.” *Proc., Inst. Mech. Eng.*, 173(1), 111-122.
- ISO. (2010). “Elastomeric seismic-protection isolators.” ISO 22762, Geneva.
- Kelly, J.M. (1997). *Earthquake-resistant design with rubber*. Springer, London.
- Kelly, J.M. (1999). “Analysis of fiber-reinforced elastomeric isolators,” *J. Seismol. Earthq. Eng.*, 2(1), 19-34.
- Kelly, J.M. and Takhirov S.M. (2002). “Analytical and Experimental Study of Fiber-Reinforced Strip Isolators.” Rept. No, PEER 2002/11. Pacific Earthquake Engineering Research Center, University of California, Berkeley, CA.
- Kelly, J.M. and Calabrese, A. (2013). “Analysis of fiber-reinforced elastomeric isolators including stretching of reinforcement and compressibility of elastomer.” *Ingegneria Sismica*, 30(3), 5-16.
- Kelly, J.M. and Van Engelen, N.C. (2015). “Single Series Solution for the Rectangular Fiber-Reinforced Elastomeric Isolator Compression Modulus.” Rept. No, PEER 2015/03. Pacific Earthquake Engineering Research Center, University of California, Berkeley, CA.
- Kelly, J. M., and Konstantinidis, D. (2011). *Mechanics of rubber bearings for seismic and vibration isolation*. Wiley, Chichester, U.K.
- Lindley, P.B. (1978). *Engineering design with natural rubber*. Malaysian Rubber Producers’ Research Association, Brickendonbury, Hertford, England.
- Osgooei, P.M., Tait, M.J., and Konstantinidis, D. (2014). “Three-dimensional finite element analysis of circular fiber-reinforced elastomeric bearings under compression.” *Comp. Struct.*, 108(1): 191-204.

- Pinarbasi, S. and Okay, F. (2011). “Compression of hollow-circular fiber-reinforced rubber bearings.” *Struct Eng Mech*, 38(3): 361-384.
- Stanton, J.F., Roeder, C.W., Mackenzie-Helnwein, P., White, C., Kuester, C., and Craig, B. (2008). *NCHRP Report 596: Rotation Limits for Elastomeric Bearings*. TRB, National Research Council, Washington, D.C.
- Toopchi-Nezhad, H., Tait, M.J., and Drysdale, R.G. “Influence of thickness of individual elastomer layers (first shape factor) on the response of unbonded fiber-reinforced elastomeric bearings.” *J Comp Mater*, 47(27): 3433-3450.
- Van Engelen, N.C., and Kelly, J.M. (2015). “Correcting for the influence of bulk compressibility on the design properties of elastomeric bearings.” *J. Eng. Mech.-ASCE*, 141(6).

Table 4-1: Compression and bending modulus for an incompressible elastomeric pad and correction factors to take into account elastomer compressibility and reinforcement extensibility

Pad Geometry	$\frac{1}{E_c} = \frac{1}{E_c^\infty} + \kappa_c \frac{1}{K} + \kappa_{ec} \frac{t}{E_f t_f}$			$\frac{1}{E_b} = \frac{1}{E_b^\infty} + \kappa_b \frac{1}{K} + \kappa_{eb} \frac{t}{E_f t_f}$		
	$E_c^\infty / GS^2$	$\kappa_c$	$\kappa_{ec}$	$E_b^\infty / GS^2$	$\kappa_b$	$\kappa_{eb}$
Infinite Strip	4	6/5	6/5	4/5	10/7	10/7
Circular	6	4/3	7/3	2	3/2	-
Square	6.748	7/5	14/5	2.228	8/5	16/5
Annular	$6\lambda_c$	6/5	12/5	$2\lambda_b$	10/7	-

where  $\lambda_c$  is given by Eq. (4-64) and  $\lambda_b$  by Eq. (4-76)

Table 4-2: Factors for the proposed approximations for the maximum shear strain due to compression, Eq. (4-66)

Pad Geometry	$\Gamma_1$	$\Gamma_2$	$e$
Infinite Strip	6	2/3	1
Circular	6	1	2 (13/4)*
Square	8.104	0.945	2
Annular (Outer Surface)	$6 \lambda_s $	1	2 (13/4)*
Annular (Inner Surface)	$6 \lambda_s $	$\lambda_a$	7/4 (13/4)*

where  $\lambda_s$  is given by Eq. (4-65) and  $\lambda_a$  by Eq. (4-74)

\*For large shape factors

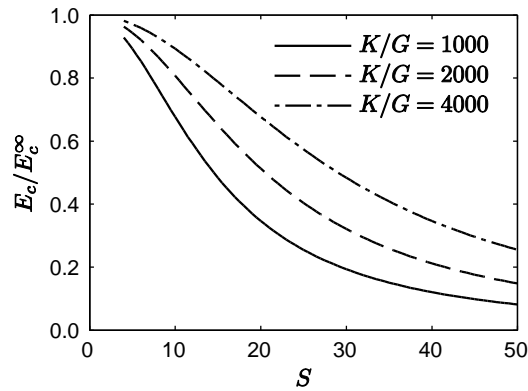


Figure 4-1: Compression modulus assuming a compressible elastomer normalized by the compression modulus assuming an incompressible elastomer as a function of shape factor for an infinite strip pad.

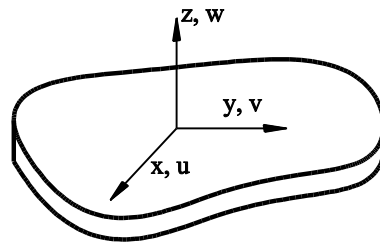


Figure 4-2: Arbitrarily shaped elastomeric pad with a Cartesian coordinate system and displacement field ( $u, v, w$ ).

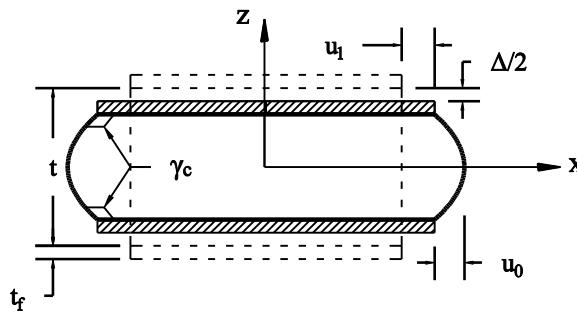


Figure 4-3: Lateral bulging of a constrained elastomeric pad under compression identifying the locations of the maximum shear strain due to compression.

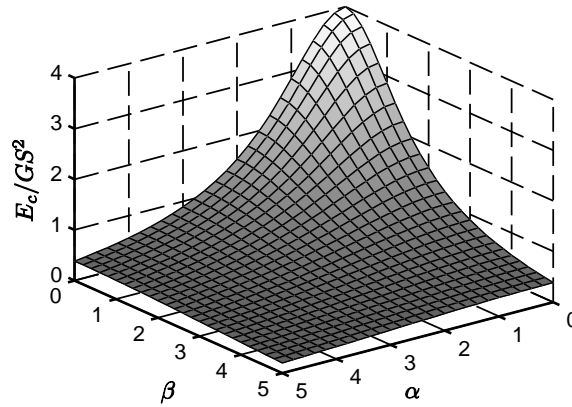


Figure 4-4: Normalized compression modulus as a function of  $\alpha$  and  $\beta$  for an infinite strip pad.

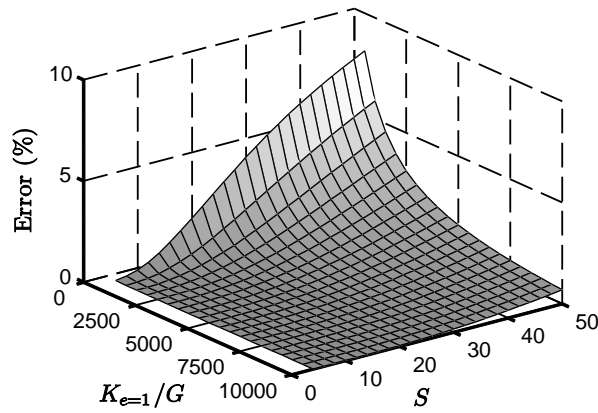


Figure 4-5: Percent error of  $E_c$  for an infinite strip pad.

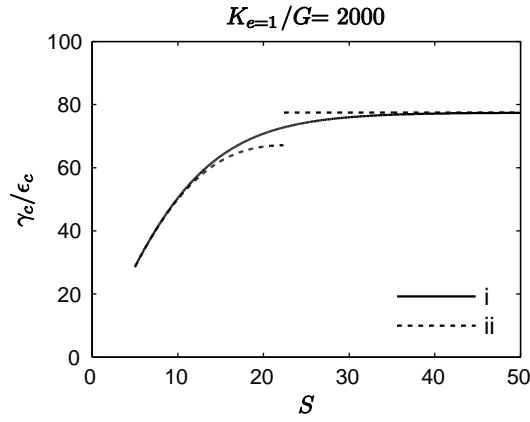


Figure 4-6: Example relationship of the maximum shear strain due to compression normalized by the compression strain of an infinite strip pad as a function of the shape factor for the i) analytical solution and ii) proposed approximation.

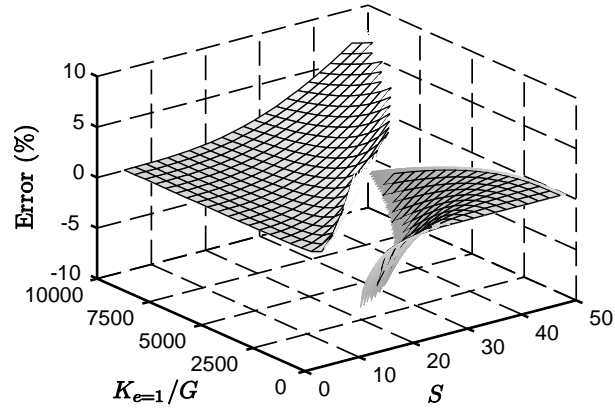


Figure 4-7: Percent error of  $\gamma_c/\epsilon_c$  for an infinite strip pad.

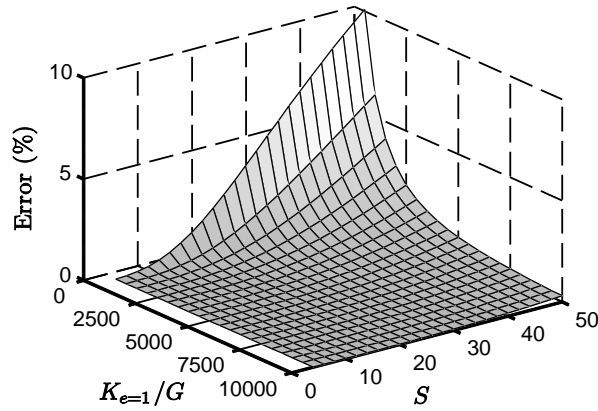


Figure 4-8: Percent error of  $E_b$  for an infinite strip pad.

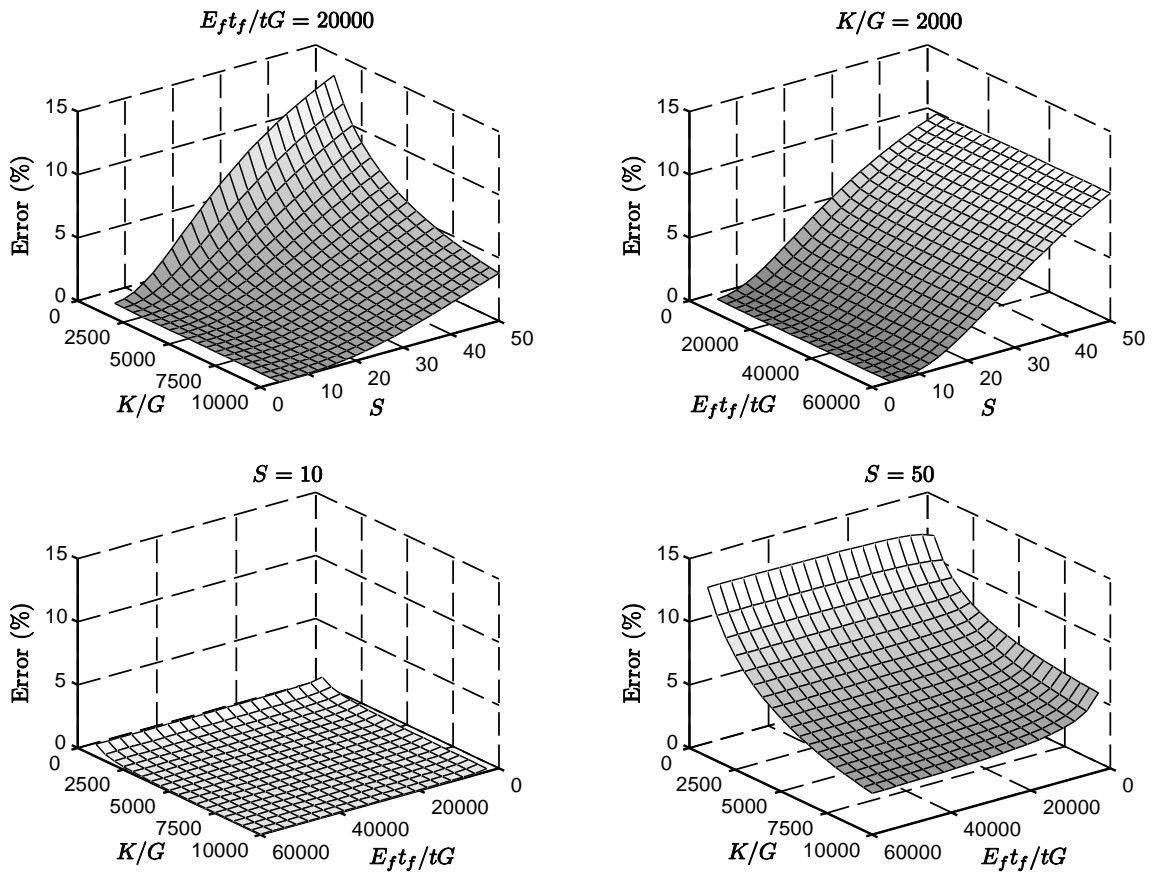


Figure 4-9: Percent error of  $E_c$  for a circular pad.

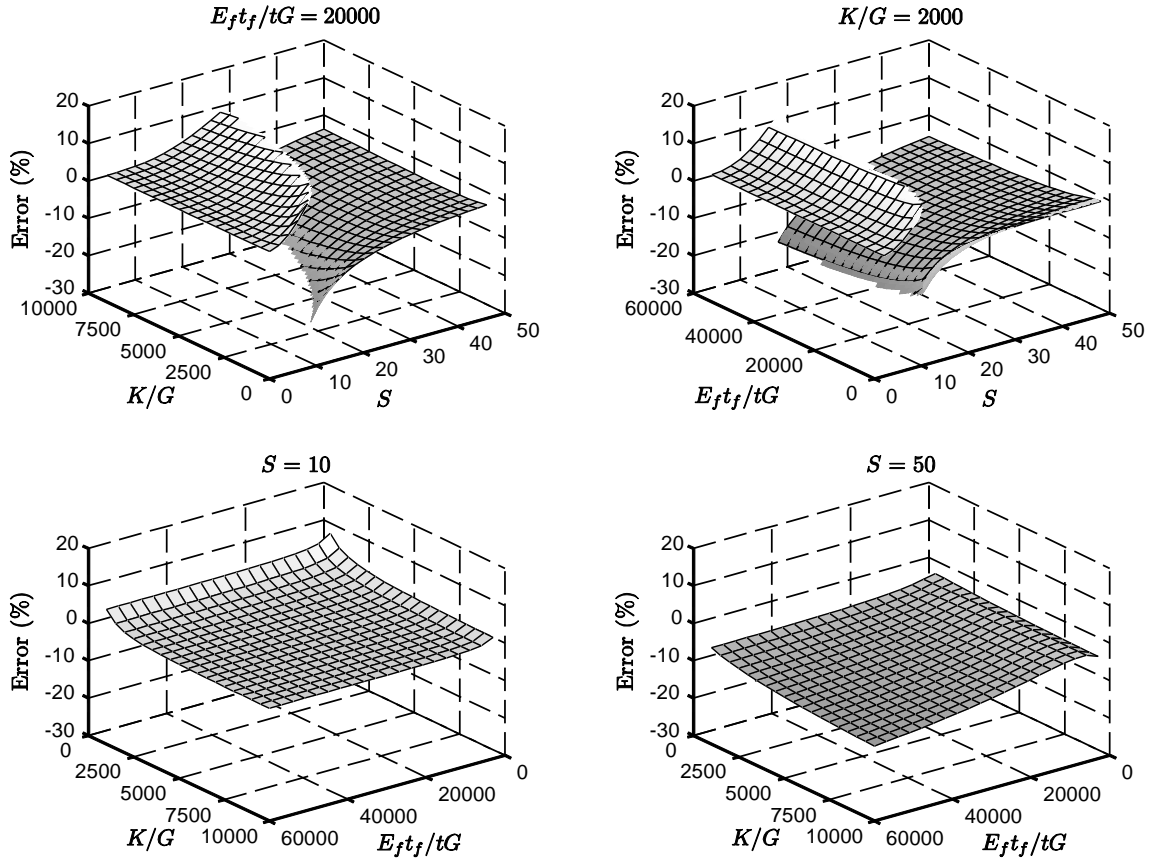


Figure 4-10: Percent error of  $\gamma_c/\epsilon_c$  for a circular pad.

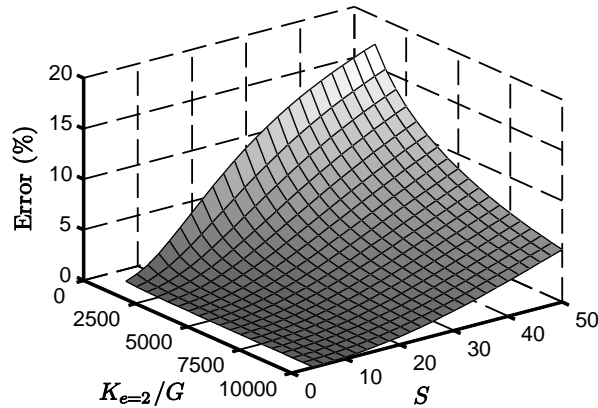


Figure 4-11: Percent error of  $E_c$  for a square pad.

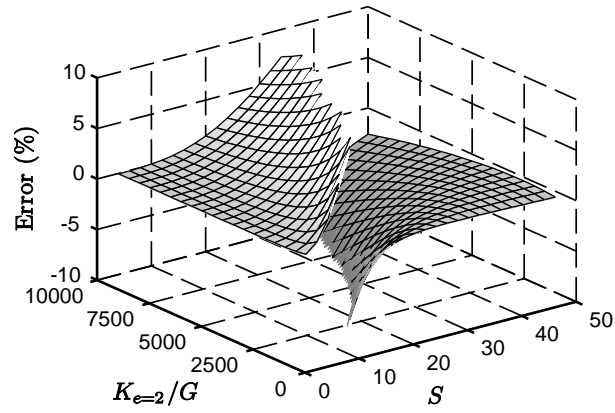


Figure 4-12: Percent error of  $\gamma_c/\epsilon_c$  for a square pad.

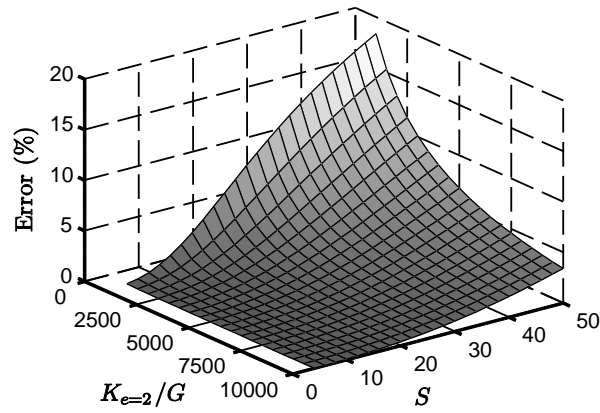


Figure 4-13: Percent error of  $E_b$  for a square pad.

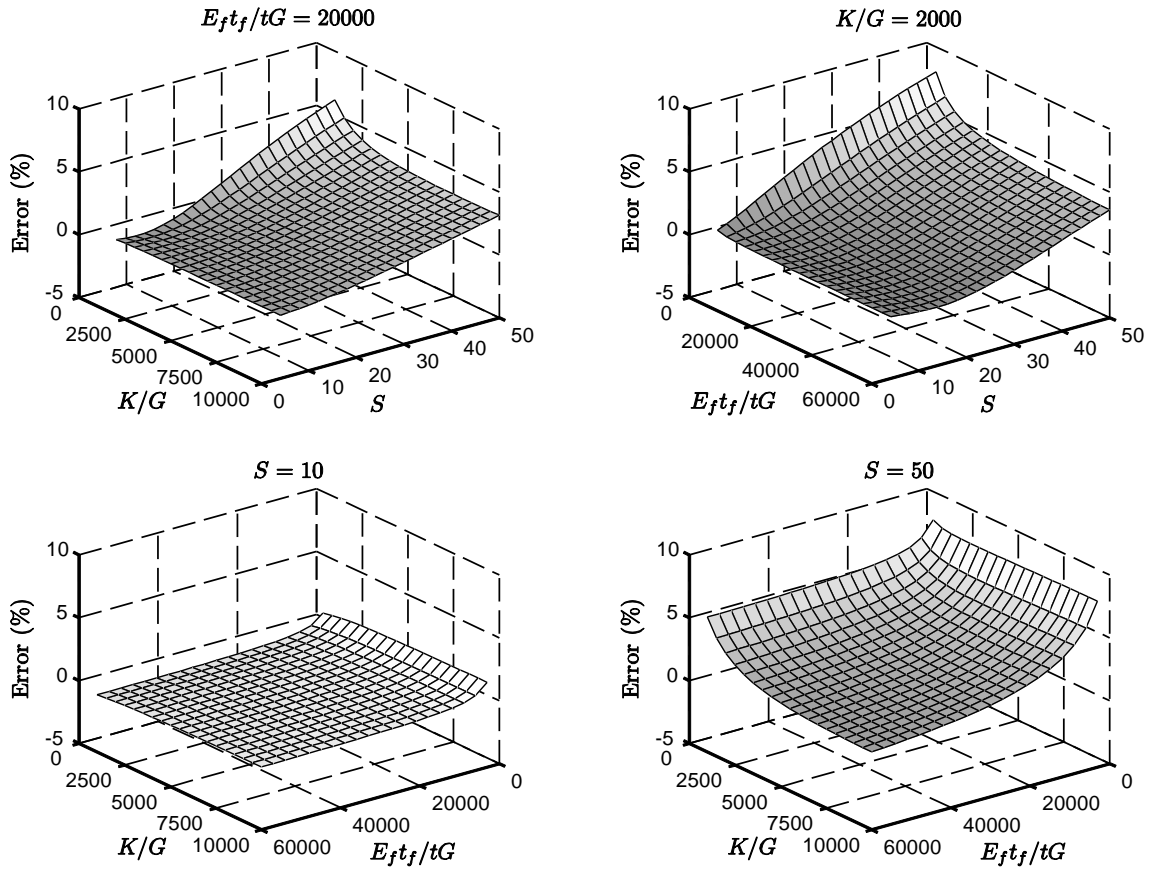


Figure 4-14: Percent error of  $E_c$  for an annular pad ( $\eta = 0.1$ ).

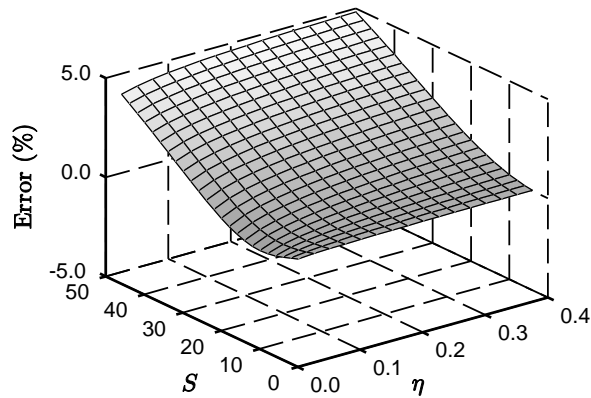


Figure 4-15: Sensitivity of the percent error for  $E_c$  of an annular pad to  $\eta$  ( $K/G = 2000$ ,  $E_f t_f / t G = 20000$ ).

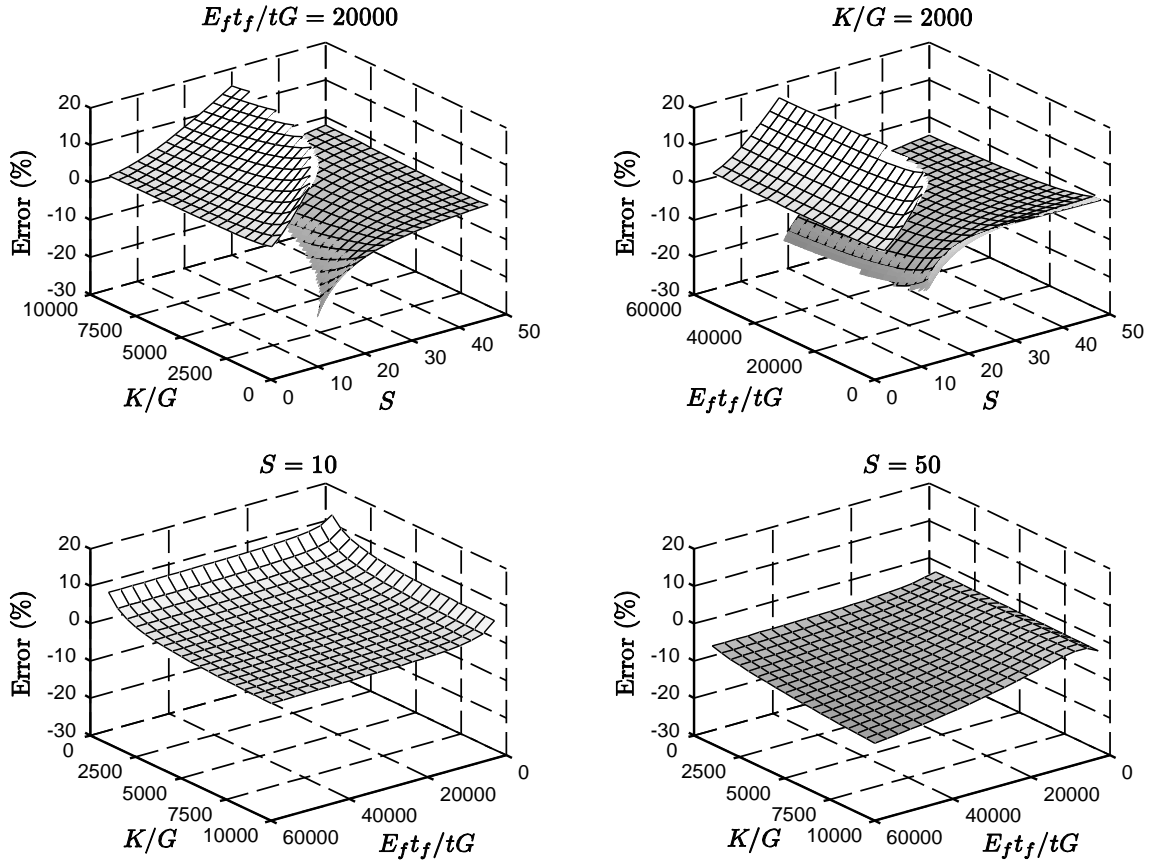


Figure 4-16: Percent error of  $\gamma_c/\epsilon_c$  for the outer surface of an annular pad ( $\eta = 0.1$ ).

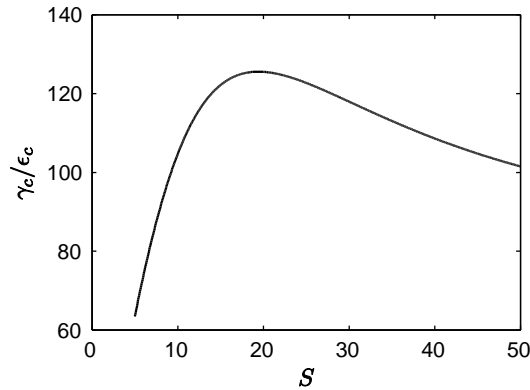


Figure 4-17: Example of  $\gamma_c/\epsilon_c$  as a function of  $S$  for the inner surface of an annular pad ( $\eta = 0.1$ ,  $K/G = 2000$ ,  $E_f t_f / t G = 20000$ ).

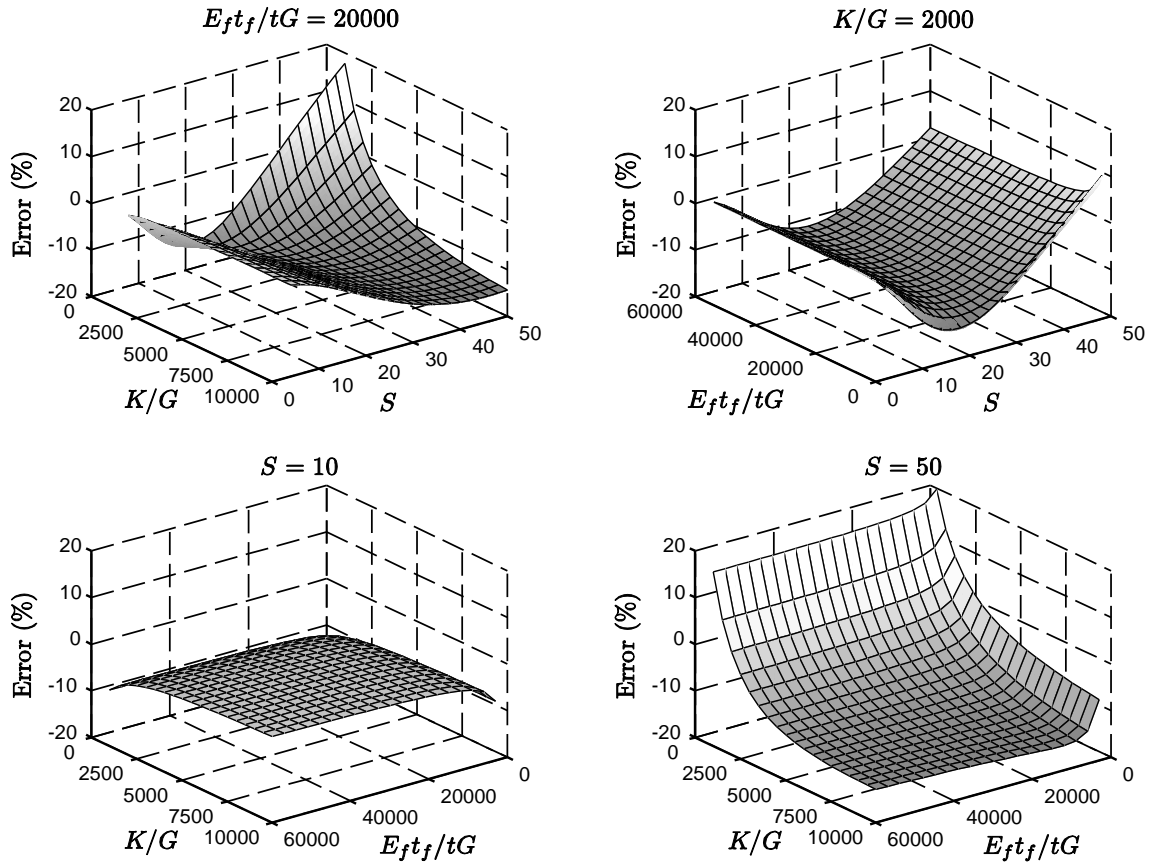


Figure 4-18: Percent error of  $\gamma_c/\epsilon_c$  for the outer surface of an annular pad ( $\eta = 0.1$ ).

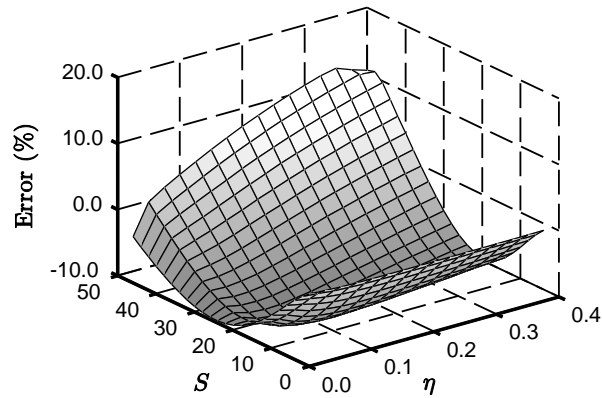


Figure 4-19: Sensitivity of the percent error for  $\gamma_c/\epsilon_c$  at the inner surface of an annular pad to  $\eta$  ( $K/G = 2000$ ,  $E_{ft_f}/tG = 20000$ ).

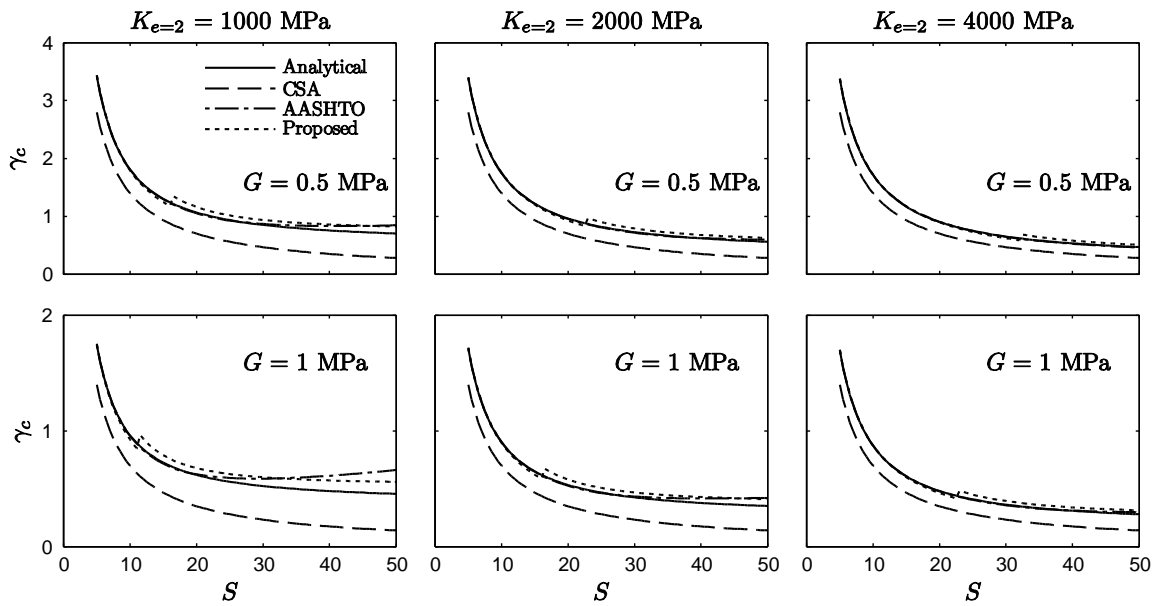


Figure 4-20: Maximum shear strain due to compression as a function of  $S$  for selected values of  $G$  and  $K_{e=2}$  ( $\sigma_c = 7.0$  MPa).

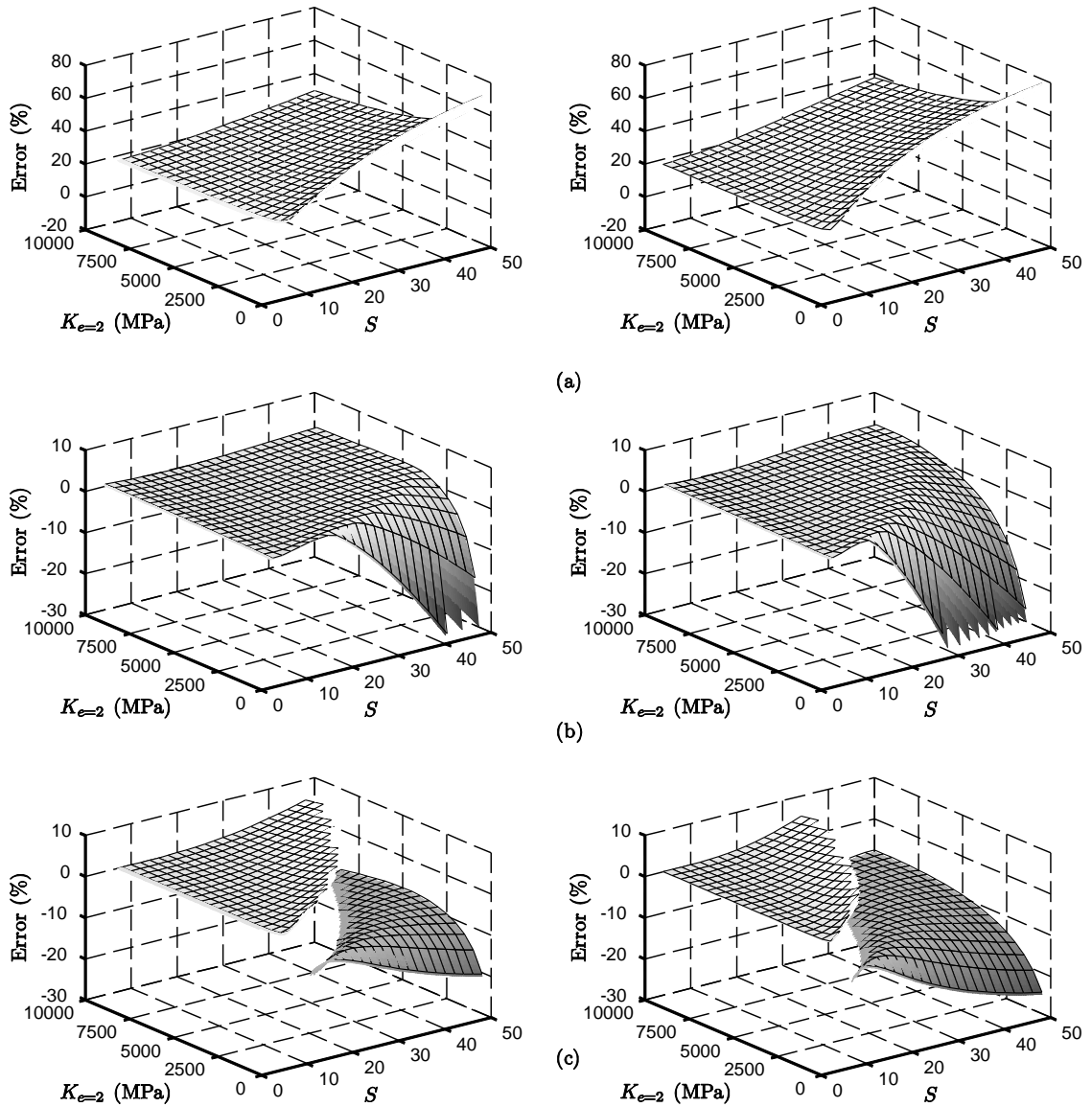


Figure 4-21: Percent error of (a) CSA (2014), (b) AASHTO (2014a,b) including compressibility and (c) the proposed approximation for a square pad with  $G = 0.5$  MPa (left) and  $G = 1.0$  MPa (right).

## 5 Shear Strain Demands in Elastomeric Bearings Subjected to Rotation

Van Engelen NC, Konstantinidis D, Tait MJ. 2015. Shear Strain Demands in Elastomeric Bearings Subjected to Rotation. To be submitted to the *Journal of Engineering Mechanics (ASCE)*.

### *Abstract*

Fiber reinforcement was initially proposed as a potential cost-saving alternative to conventional steel reinforcement in laminated bearings. Steel reinforcement is often assumed to be rigid, but the extensibility of the reinforcement serves as an additional design parameter that must be considered. Similar to the compressibility of the elastomer, the extensibility of the reinforcement has a pronounced effect on important design parameters such as the compression modulus, bending modulus and shear strains that develop due to compression or rotation. Analytical solutions for the compression modulus and bending modulus developed based on the pressure solution are available for most common pad geometries and can be used to derive the maximum shear strain due to rotation. These solutions are often complex and unsuitable for design purposes. In this study, the analytical solutions for an infinite strip, circular, square, rectangular and annular pad geometries are derived and simplified to form geometry-specific approximations for the maximum shear strain due to rotation. The simplified approximations account for the reinforcement extensibility and the compressibility of the elastomer. The derived approximations are evaluated based on the analytical solutions and provide accurate values over a wide range of shape factors and values of bulk compressibility and reinforcement extensibility.

### *5.1 Introduction*

Laminated elastomeric bearings have been used extensively as bridge bearings and, more recently, as seismic isolators. Conventional steel-reinforced elastomeric isolators (SREIs) are composed of alternating horizontal layers of steel and elastomer. The steel reinforcement restrains the lateral bulging of the elastomeric bearing under a compressive load, substantially increasing the vertical and rotational stiffness. The horizontal properties are relatively uninfluenced by the reinforcement and the elastomer enables the bearing to undergo large recoverable horizontal displacements.

Fiber-reinforced elastomeric isolators (FREIs), initially proposed as a potentially light-weight and low-cost alternative to SREIs, have been investigated for application as seismic base isolators (Kelly 1999, Kelly and Takhirov 2002, Toopchi-Nezhad et al. 2008). Fiber reinforcement, which is allowed in specific applications in design codes,

such as CSA S6-14 (CSA 2014), is attractive due to the light-weight, comparable tensile properties to that of steel, and the ability to manufacture and cut FREIs from a larger pad. Analytically, FREIs differ from SREIs primarily on the extensibility of the reinforcement. Steel shims are often assumed inflexible and inextensible, but the extensibility of the fiber reinforcement is included in the analysis. The extensibility of the reinforcement and compressibility of the elastomer can have a pronounced effect on critical design parameters (e.g. compression modulus), especially for moderate-to-large shape factors, defined as the ratio of the loaded area to the unloaded area of a single layer of elastomer (Osgooei et al. 2014).

Analytical solutions including the compressibility of the elastomer and extensibility of the reinforcement, for brevity hereinafter referred to as compressibility and extensibility, are available for the compression modulus and bending modulus of most simple elastomeric pad geometries. These solutions are often complex and not appropriate for use in design. Alternatively, approximations have been presented based on tabulated results (Constantinou et al. 2011) or best-fit approximations derived from analytical solutions (Stanton et al. 2008) to account for these effects. Van Engelen and Kelly (2015) proposed a generalized approximation for the compression modulus and bending modulus based on the pressure solution including compressibility. The proposed approximation takes the form of the ad hoc approximation originally proposed by Gent and Lindley (1959) that has been used in design standards (ISO 2010). The inclusion of a mathematically derived correction factor provided a more accurate and conservative approximation based on the analytical solution. In Van Engelen et al. (2015), the same procedure was extended to include the extensibility of the reinforcement and was applied to develop a generalized expression for the maximum shear strain due to compression.

In this paper, the procedure from Van Engelen and Kelly (2015) and Van Engelen et al. (2015) is extended to derive an approximation for the maximum shear strain due to rotation for an infinite strip, square and rectangular pad geometry including the effects of compressibility and extensibility. Approximations are also presented for circular and annular pad geometries that include the effects of compressibility. An example compares the proposed approximation and code equations (CSA 2014, AASHTO 2014a,b) to the analytical solution derived using the pressure solution.

## 5.2 *Rotations in Elastomeric Bearings*

### 5.2.1 **Code Considerations**

In addition to the shear strain due to imposed horizontal displacement and compression, shear strain due to rotation is an important parameter in the design of elastomeric bearings. The maximum shear strain due to compression,  $\gamma_c$ , and the

maximum shear strain due to rotation,  $\gamma_r$ , occur at the interface of the extensible reinforcement and elastomer near the edge of the bearing, illustrated in Figure 5-1. Design codes (CSA 2014, AASHTO 2014a,b) impose restrictions on the maximum shear strain due to compression, rotation, imposed lateral displacements and earthquake displacements, individually and/or in combination. For elastomeric bearings in isolation systems, CSA S6-14 (2014) imposes the following limitation

$$\gamma_c + \gamma_r + \gamma_d \leq 5.5 \quad (5-1)$$

where  $\gamma_d$  is the maximum shear strain due to imposed lateral displacements. Similarly, in AASHTO (2014b) the seismic shear strain combination is

$$\gamma_c + 0.5\gamma_r + \gamma_d \leq 5.5 \quad (5-2)$$

In AASHTO (2014b) it is indicated that the factor of 0.5 applied to  $\gamma_r$  is intended to differentiate between static and cyclic loading (i.e. static rotation is less damaging) which will both occur. Note that a similar expression in AASHTO (2014a) differentiates static and cyclic loading for non-seismic load combinations.

Some level of rotation will always occur due to tolerances in the construction process, or in some applications, notably in bridge bearings, rotations can be introduced due to the deflections of the structure due to traffic and other effects. The need to accommodate shear strains caused by compression and rotation becomes challenging due to opposing trends as a function of the shape factor. Increasing the shape factor vertically stiffens the bearing, reduces the vertical compression strain, which is proportional to  $\gamma_c$ ; however, it also increases the rotational stiffness, resulting in an increased value of  $\gamma_r$  for the same level of rotation. In unbonded applications, gaps may form between the bearing and the structure under large levels of rotation (Konstantinidis et al. 2008, Al-Anany and Tait 2015).

Despite being an important design consideration, rotation has received considerably less attention than shear or compression (Stanton et al. 2008). Studies involving rotation typical focus on stability (Gent 1964, Stanton et al. 1990, Nagarajaiah and Ferrel 1999, de Raaf et al. 2011), whereas the maximum shear strain due to rotation has been of lesser focus. Stanton et al. (2008) conducted a comprehensive study on the rotation of steel-reinforced elastomeric bearings including an experimental program, analytical and finite element analysis, and proposed design rules. Currently, considerations for  $\gamma_r$  in design codes (CSA 2014, AASHTO 2014a,b) primarily originate from this study.

According to CSA (2014) and AASHTO (2014a,b)  $\gamma_r$  may be determined as

$$\gamma_r = \frac{D_r B^2}{t_r T} \theta_t \quad (5-3)$$

where  $D_r$  is a geometry dependent factor,  $B$  is the plan dimension in the direction of loading (diameter for a circular bearing),  $\theta_i$  is the total rotation of the isolator,  $t_i$  is the thickness of the  $i$ th layer of elastomer, and  $T$  is the total thickness of the elastomer. Note that Eq. (5-3) does not include the compressibility of the elastomer. For a rectangular pad,  $D_r = 0.55$  or  $0.5$  in CSA (2014) and AASHTO (2014a,b), respectively, and for a circular pad,  $D_r = 0.375$  (CSA 2014, AASHTO 2014a,b).

AASHTO (2014a) allows  $D_r$  to be determined for a rectangular pad including the compressibility of the elastomer based on a best-fit approximation over a range of aspect ratios from Stanton et al. (2008). The recommended expression is:

$$D_r = \frac{1.552 - 0.627\lambda}{2.233 + 0.156\lambda + L/W} \leq 0.5 \quad (5-4)$$

where

$$\lambda = \sqrt{\frac{3GS^2}{K}} \quad (5-5)$$

and  $L$  is the plan dimension perpendicular to the axis of rotation,  $W$  is the plan dimension parallel to the axis of rotation,  $S$  is the shape factor,  $G$  is the shear modulus of the elastomer, and  $K$  is the bulk modulus of the elastomer.

### 5.2.2 Analytical Solutions

The pressure solution has been commonly applied to develop the analytical solution for the bending modulus of elastomeric pads, from which the maximum shear strain due to rotation can be derived. References to these analytical solutions are provided in the subsequent sections. The pressure solution notably assumes that the normal stresses within the elastomer are dominated by the internal pressure, that the elastomer is linearly elastic, that the lateral bulging of the elastomer follows a parabolic profile and that horizontal planes remain plane (Kelly 1997). The extensibility of the reinforcement has been included by the addition of a uniform displacement term to the assumed parabolic lateral bulging (Kelly 1999). Solutions developed based on the simplifying assumptions of the pressure solution are often characterized as being appropriate for elastomeric pads with a shape factor of approximately 5 or greater (Kelly 1997).

The derivation of the bending modulus, following the assumption of the pressure solution, produces two terms representative of the sensitivity of the solution to compressibility and extensibility. These two terms are often summed as

$$\lambda^2 = cGS^2 \left( \frac{1}{K} + e \frac{t}{E_f t_f} \right) \quad (5-6)$$

where  $c$  and  $e$  are constants dependent on the pad geometry,  $t$  is the thickness of the elastomeric pad,  $t_f$  is the thickness of a reinforcement layer, and  $E_f$  is the effective elastic

modulus of the reinforcement. Note that  $\lambda$  is often defined as a function of a geometric property (e.g. diameter or width) in lieu of the shape factor. Thus, the definition used herein may vary from the respective analytical derivations.

The extensibility of the reinforcement is represented by  $E_f$ , corrected by the ratio  $t_f/t$ . The direct summation of the inverted bulk modulus and reinforcement effective elastic modulus in Eq. (5-6) determines that the analytical solution is often equally sensitive to these parameters. In Van Engelen et al. (2015), the value in the parenthesis was represented by an equivalent parameter,  $K_e$ , defined as

$$\frac{1}{K_e} = \frac{1}{K} + e \frac{t}{E_f t_f} \quad (5-7)$$

where the subscript represents the magnitude of the coefficient  $e$ .

The analytical solutions in subsequent sections present the relationship between the shear stress and pressure distribution. The analytical solutions for the maximum shear strain due to rotation presented herein were derived from this relationship. According to the pressure solution, the maximum shear strain occurs exactly at the free surface, whereas in reality the maximum shear strain occurs very near to the free surface. Note that the location of the maximum shear stress was selected to provide a positive value in all cases.

### 5.3 Generalized Approximations

#### 5.3.1 Material and Geometric Properties

Previous studies (Van Engelen and Kelly 2015, Van Engelen et al. 2015) evaluated the proposed approximation against the analytical solutions over a selected range of  $S$ ,  $K/G$ , and  $E_f t_f / tG$ . Herein, the proposed approximations are compared against the analytical solutions as a function of the dimensionless parameter  $\lambda$ , as defined in Eq. (5-6). Using  $\lambda$  is convenient for evaluation of the proposed approximations since a single value of  $\lambda$  can represent infinite combinations of  $G$ ,  $S$ , and  $K_e$ . The range of  $\lambda$  differs depending on the pad geometry and can be determined from the ranges of  $S$ , and  $K_e/G$  considered. A range of  $5 \leq S \leq 50$  and  $500 \leq K_e/G \leq 10000$  was selected, as presented in Van Engelen et al. (2015).

The lower bound of the shape factor was determined by the limitations of the pressure solution (Kelly 1997). The range of  $K_e/G$  is intended to encompass achievable values of  $K/G$  and  $E_f t_f / tG$ . In absence of testing, AASHTO (2014a) allows a value of  $K = 3100$  MPa to be assumed. Comparatively, the extensibility of the reinforcement is easier to determine and to control. The variety of fiber reinforcement types, weaves, densities and thicknesses available allow the designer to have considerable flexibility over the reinforcement design. Note that  $E_f$  should be selected to represent the effective

elastic modulus of the extensible reinforcement as a composite within the bearing, and not the fiber reinforcement. An accurate value of  $E_f$  is necessary to avoid an over-estimate of the restraint on the elastomeric layers provided by the reinforcement.

The following sections develop approximate expressions for the maximum shear strain due to rotation in bearings with different geometries. Previously published closed-form solutions for the pressure distribution under pure rotation are used in conjunction with the assumptions that the magnitudes of the normal stresses are approximately equal to the pressure in the equilibrium equations, and that the in-plane shears are negligible, to recover closed-form solutions for the maximum shear stress in the elastomer. From the closed-form solution, the maximum shear strain is obtained under the assumption of linear elastic material.

### 5.3.2 Infinite Strip Pad

The analytical solution for the maximum shear strain due to rotation of an infinite strip pad, including the compressibility of the elastomer and extensibility of the reinforcement, can be derived from the pressure distribution provided in Kelly and Takhirov (2002) as

$$\frac{\gamma_r}{\theta} = \frac{6S^2}{\lambda^2} (\lambda \coth \lambda - 1) \quad (5-8)$$

where

$$\lambda^2 = \frac{12GS^2}{K_{e=1}} \quad (5-9)$$

Equation (5-8) is non-linear, but approaches a constant slope as  $S \rightarrow \infty$ . The rate at which Eq. (5-8) approaches the constant slope is governed by  $K_{e=1}/G$ , demonstrated in Figure 5-2.

The procedure from Chalhoub and Kelly (1991), which has subsequently been applied in Van Engelen and Kelly (2015) and Van Engelen et al. (2015), can be used to expand and simplify Eq. (5-8) to a generalized expression. The terms contained in the parenthesis are expanded with a Taylor series for small values of  $\lambda$

$$\lambda \coth \lambda - 1 = \frac{\lambda^2}{3} - \frac{\lambda^4}{45} + O(\lambda^6) \quad (5-10)$$

Truncating Eq. (5-10) and substituting the first two terms into Eq. (5-8) yields:

$$\frac{\gamma_r}{\theta} = 2S^2 \left( 1 - \frac{\lambda^2}{15} \right) \quad (5-11)$$

Inverting Eq. (5-11) and expanding with a binomial series gives

$$\frac{\gamma_r}{\theta} = \left( \frac{1}{2S^2} + \frac{2G}{5K_{e=1}} \right)^{-1} \quad (5-12)$$

The denominator of the first term in the parenthesis is the maximum shear strain due to rotation assuming an incompressible elastomer and inextensible reinforcement. As  $S$  becomes large, the first term of Eq. (5-12) becomes negligible and the maximum shear strain due to rotation approaches a horizontal asymptote equal to the inverse of the second term. Thus, Eq. (5-12) diverges from the analytical solution, which approaches a constant slope with increasing  $S$ , as described above, and demonstrated in Figure 5-3. Consequently it is necessary to determine a second approximation to correct for this divergence similar to the maximum shear strain due to compression as presented in Van Engelen et al. (2015).

Differentiating Eq. (5-8) with respect to  $S$  and taking the limit as  $S \rightarrow \infty$  yields

$$\lim_{S \rightarrow \infty} \frac{d}{dS} \frac{\gamma_r}{\theta} = \sqrt{3 \frac{K_{e=1}}{G}} \quad (5-13)$$

Ideally, the transition to the second approximation should occur when the slope of Eq. (5-12) and Eq. (5-13) are equal. However, differentiating the proposed approximation, Eq. (5-12), and equating it to Eq. (5-13) results in a quartic equation with no real roots. Alternatively, the transition shape factor,  $S_t$ , is established when the absolute difference of the first derivative of Eq. (5-12) and Eq. (5-13) is minimized (i.e. the point of inflection of Eq. (5-12)). The transition shape factor for an infinite strip pad is

$$S_t = \frac{\sqrt{15}}{6} \sqrt{\frac{K_{e=1}}{G}} \quad (5-14)$$

If  $S$  exceeds  $S_t$ , a linear approximation can be used defined by

$$\frac{\gamma_r}{\theta} = \left( \frac{\gamma_r}{\theta} \right)_t + \sqrt{3 \frac{K_{e=1}}{G}} (S - S_t) \quad (5-15)$$

where

$$\left( \frac{\gamma_r}{\theta} \right)_t = \left( \frac{1}{2S_t^2} + \frac{2G}{5K_{e=1}} \right)^{-1} \quad (5-16)$$

is the approximated maximum shear strain due to rotation at  $S_t$ .

It is convenient to analyze the proposed approximation in terms of  $\lambda$  in lieu of  $S$ ,  $G$  and  $K_e$ . Equivalently, the proposed approximation, Eq. (5-12), becomes

$$\frac{\gamma_r}{\theta} = 2S^2 \left( 1 + \frac{\lambda^2}{15} \right)^{-1} \quad (5-17)$$

with the transition from small values of  $\lambda$  to large values of  $\lambda$  determined by  $\lambda_t$  from Eq. (5-14)

$$\lambda_t = \sqrt{5} \quad (5-18)$$

For  $\lambda \geq \lambda_t$ , expressing Eq. (5-15) in terms of  $\lambda$ , the proposed approximation becomes:

$$\frac{\gamma_r}{\theta} = S^2 \left( \frac{6}{\lambda} + \frac{7.5 - 6\lambda_t}{\lambda^2} \right) \quad (5-19)$$

Figure 5-4 shows  $\gamma_r/(S^2\theta)$  and the associated percent error over a range of  $0 \leq \lambda \leq 7.75$ , which encompasses the considered range of  $K_{e=I}/G$  and  $S$ . The proposed approximation closely follows the analytical solution over the entire range of  $\lambda$  considered. The transition between approximations is visible in Figure 5-4 as the slope of the percent error instantaneously changes. In the case of the maximum shear strain due to rotation, a negative percent error is representative of a conservative over prediction. The magnitude of the error does not exceed 3.0 % over the range considered. Therefore, the proposed approximation and criterion for transition between approximations were considered acceptable. Figure 5-5 shows the percent error as a function of  $K_{e=I}/G$  and  $S$ .

### 5.3.3 Circular Pad

The analytical solution for the maximum shear strain due to rotation of a circular pad assuming rigid reinforcement and including the compressibility of the elastomer can be derived from the pressure distribution presented in Chalhoub and Kelly (1990) as

$$\frac{\gamma_r}{\theta} = \frac{48S^2}{\lambda^2} \left( \frac{\lambda}{2} \frac{I_0(\lambda)}{I_1(\lambda)} - 1 \right) \quad (5-20)$$

where

$$\lambda^2 = \frac{48GS^2}{K} \quad (5-21)$$

and  $I_0$  and  $I_1$  are order 0 and 1 modified Bessel functions of the first kind.

Following the expansion, truncation and inversion procedure yields

$$\frac{\gamma_r}{\theta} = 6S^2 \left( 1 + \frac{\lambda^2}{24} \right)^{-1} \quad (5-22)$$

where the factor before the parenthesis represents the maximum shear strain due to rotation assuming an incompressible elastomer.

If  $\lambda \geq \lambda_t$ , the following approximation is recommend

$$\frac{\gamma_r}{\theta} = S^2 \left( \frac{24}{\lambda} + \frac{36 - 24\lambda_t}{\lambda^2} \right) \quad (5-23)$$

where

$$\lambda_t = 2\sqrt{2} \quad (5-24)$$

for a circular pad. The analytical solution and proposed approximation are presented in Figure 5-6 with the percent error over  $0 \leq \lambda \leq 15.5$ . The proposed expression is highly accurate; the magnitude of the percent error is below 4 % over the range considered.

### 5.3.4 Square Pad

The analytical solution for the maximum shear strain due to rotation of a square pad including the compressibility of the elastomer, derived from the expression for shear strain presented in Angeli et al. (2013), is

$$\frac{\gamma_r}{\theta} = \frac{192S^2}{\pi} \sum_{n=1,2,3}^{\infty} \sum_{m=1,3,5}^{\infty} \frac{1}{m} \frac{(-1)^{\frac{m-1}{2}}}{(n\pi)^2 + \left(\frac{m\pi}{2}\right)^2 + \lambda^2} \quad (5-25)$$

where

$$\lambda^2 = \frac{48GS^2}{K_{e=2}} \quad (5-26)$$

Angeli et al. (2013) recommended that  $t_f$  be divided by two to represent the reinforcement weaved in perpendicular directions. The definition used herein assumes that  $E_f$  is selected appropriately to encompass the effective properties of the layer and the expression is based on the full thickness of  $t_f$ .

Following the expansion and truncation procedure yields

$$\frac{\gamma_r}{\theta} = 7.576S^2 (1 + 0.056\lambda^2)^{-1} \quad (5-27)$$

where the factor before the parenthesis represents the maximum shear strain due to rotation assuming an incompressible elastomer and inextensible reinforcement.

If  $\lambda \geq \lambda_t$ , the following approximation is recommend

$$\frac{\gamma_r}{\theta} = S^2 \left( \frac{24}{\lambda} + \frac{33.8 - 24\lambda_t}{\lambda^2} \right) \quad (5-28)$$

where

$$\lambda_t = 2.439 \quad (5-29)$$

for a square pad. The analytical solution and proposed approximation are presented in Figure 5-7 with the percent error over  $0 \leq \lambda \leq 15.5$ . The magnitude of the error of the proposed approximation is below 3 % over the range considered.

### 5.3.5 Rectangular Pad

The analytical solution for the maximum shear strain due to rotation of a rectangular pad including compressibility and extensibility, derived from the expression for shear strain due to rotation presented in Angeli et al. (2013), is

$$\frac{\gamma_r}{\theta} = \frac{48S^2}{\pi} (1 + \rho)^2 \sum_{n=1,2,3}^{\infty} \sum_{m=1,3,5}^{\infty} \frac{1}{m} \frac{\sin(m\pi/2)}{(\rho n\pi)^2 + \left(\frac{m\pi}{2}\right)^2 + \lambda^2 (1 + \rho)^2} \quad (5-30)$$

where

$$\lambda^2 = \frac{12GS^2}{K_{e=2}} \quad (5-31)$$

Following the expansion and truncation procedure yields

$$\frac{\gamma_r}{\theta} = 2\rho_r S^2 (1 + 0.05913\rho_r \lambda^2)^{-1} \quad (5-32)$$

where

$$\rho_r = \frac{2.92}{\rho} + 0.86 \quad (5-33)$$

and the factor before the parenthesis in Eq. (5-32) represents the maximum shear strain due to rotation assuming an incompressible elastomer and inextensible reinforcement and the function  $\rho_r$  corrects for the aspect ratio of the pad. The function  $\rho_r$  was determined by minimizing the least squares regression over  $0.5 \leq \rho \leq 10$ .

If  $\lambda \geq \lambda_t$ , the following approximation is proposed

$$\frac{\gamma_r}{\theta} = S^2 \left( \frac{m}{\lambda} + \frac{b - m\lambda_t}{\lambda^2} \right) \quad (5-34)$$

where

$$\lambda_t = 0.6912 \sqrt{\frac{12}{\rho_r}} \quad (5-35)$$

$$m = 6 \frac{1 + \rho}{\rho} \quad (5-36)$$

$$b = 2\rho_r \lambda_t^2 (1 + 0.05913\rho_r \lambda_t^2)^{-1} \quad (5-37)$$

for a rectangular pad. The percent error of the proposed approximation is shown in Figure 5-8 over  $0 \leq \lambda \leq 7.75$ . The magnitude of the error is below 10 % over the range of aspect ratio and  $\lambda$  considered.

### 5.3.6 Annular Pad

#### 5.3.6.1 Outer Surface

The maximum shear strain due to rotation of an annular pad with an incompressible elastomer and rigid reinforcement, derived from the pressure distribution presented in Chalhoub and Kelly (1990), is

$$\frac{\gamma_r}{\theta} = 6S^2 \lambda_r \quad (5-38)$$

where

$$\lambda_r = \frac{1 + \eta}{1 - \eta} \quad (5-39)$$

and  $\eta$  is the ratio of the inner diameter to the outer diameter. Note that Eq. (5-38) is valid at the inner surface and the outer surface of an annular pad.

The maximum shear strain due to rotation of an annular pad with a compressible elastomer and rigid reinforcement on the outer surface, derived from the pressure distribution presented in Kelly and Konstantinidis (2011), is

$$\frac{\gamma_r}{\theta} = \frac{24S^2}{\lambda} \frac{1}{(1-\eta)^2} \left( B_1 \left( I_0(\lambda) - \frac{I_1(\lambda)}{\lambda} \right) - B_2 \left( K_0(\lambda) + \frac{K_1(\lambda)}{\lambda} \right) - \frac{1}{\lambda} \right) \quad (5-40)$$

with

$$\begin{aligned} B_1 &= \frac{-K_1(\eta\lambda) + \eta K_1(\lambda)}{I_1(\eta\lambda) K_1(\lambda) - I_1(\lambda) K_1(\eta\lambda)} \\ B_2 &= \frac{I_1(\eta\lambda) - \eta I_1(\lambda)}{I_1(\eta\lambda) K_1(\lambda) - I_1(\lambda) K_1(\eta\lambda)} \\ \lambda^2 &= \frac{48GS^2}{K} \frac{1}{(1-\eta)^2} \end{aligned} \quad (5-41)$$

where  $K_0$ ,  $K_1$  are order 0 and 1 modified Bessel functions of the second kind, respectively. Modified Bessel functions of the second kind approach infinity as  $\lambda \rightarrow 0^+$  and cannot be expanded in a Taylor series.

The maximum shear strain due to rotation on the outer surface of an annular pad is, in comparison to the inner surface, less sensitive to  $\eta$ . The properties on the outer surface of an annular pad are similar to a circular pad with the same radius. The shape factors of an annular and circular pad can be related by  $S_c = S_a(1-\eta)$  where  $S_c$  and  $S_a$  are the shape factors for a circular and annular pad, respectively, with the same outer radius.

The general trend of the maximum shear strain due to rotation at the outer surface of an annular pad follows a similar trend as observed in the other pad geometries considered (see Figure 5-2). Thus, the proposed approximation is

$$\frac{\gamma_r}{\theta} = 6S^2 \lambda_r \left( 1 + \frac{1-\eta^2}{24} \lambda^2 \right)^{-1} \quad (5-42)$$

The coefficient before the parenthesis represents the incompressible solution, whereas the terms within the parenthesis were selected based on a circular pad and corrected for the presence of the hole.

Similar to a circular pad, it is necessary to establish an approximation for  $\lambda \geq \lambda_r$

$$\frac{\gamma_r}{\theta} = S^2 \left( \frac{m}{\lambda} + \frac{b - m\lambda_r}{\lambda^2} \right) \quad (5-43)$$

where

$$\lambda_r = \frac{2\sqrt{2}}{1-\eta^2} \quad (5-44)$$

$$m = \frac{24}{(1-\eta)^2} \quad (5-45)$$

$$b = 6\lambda_r \lambda_t^2 \left( 1 + \frac{1-\eta^2}{24} \lambda_t^2 \right)^{-1} \quad (5-46)$$

for the outer surface of an annular pad. The percent error of the proposed approximation is shown in Figure 5-9 over  $0 \leq \lambda \leq 17.2$  and  $0 \leq \lambda \leq 25.8$  for  $\eta = 0.1$  and  $\eta = 0.4$ , respectively.

### 5.3.6.2 Inner Surface

The maximum shear strain due to rotation of an annular pad with a compressible elastomer and rigid reinforcement on the inner surface, derived from the pressure distribution presented in Kelly and Konstantinidis (2011), is

$$\frac{\gamma_r}{\theta} = \frac{24S^2}{\lambda} \frac{1}{(1-\eta)^2} \left( \frac{1}{\lambda} - B_1 \left( I_0(\eta\lambda) - \frac{I_1(\eta\lambda)}{\eta\lambda} \right) + B_2 \left( K_0(\eta\lambda) + \frac{K_1(\eta\lambda)}{\eta\lambda} \right) \right) \quad (5-47)$$

Unlike the other pad geometries considered, the shear strain at the inner surface of an annular pad is unique due to a change in concavity that generally occurs within the range of interest. Initially the slope increases at an increasing rate and then decreases approaching a constant slope as  $S \rightarrow \infty$ , this general trend is demonstrated in Figure 5-10.

The following approximation is proposed

$$\frac{\gamma_r}{\theta} = 6S^2 \lambda_r \left( 1 + \frac{1-\eta^2}{8\lambda_t} \lambda^2 \right)^{-1} \quad (5-48)$$

where

$$\lambda_t = 5.5\eta + 1 \quad (5-49)$$

corrects for the sensitivity of the compressibility term to  $\eta$  at the inner surface. Equation (5-49) was determined by minimizing the squared residuals over the range considered.

Equation (5-48) accurately approximates the maximum shear strain due to rotation over much of the range considered; however, similar to the other pad geometries, it is necessary to correct the approximation for large values of  $\lambda$ . It is proposed that the transition to a corrected expression occurs at

$$\lambda_t = \frac{1.79}{(1-\eta)} \sqrt{\frac{48}{\lambda_r \lambda_t}} \quad (5-50)$$

The slope of the analytical solution, Eq. (5-40), as  $S \rightarrow \infty$  is approximately

$$\lim_{S \rightarrow \infty} \frac{d}{dS} \frac{\gamma_r}{\theta} \approx \eta (7.56\eta + 2.68) \sqrt{\frac{K}{G}} \quad (5-51)$$

determined through least squares regression analysis.

Thus, if  $\lambda > \lambda_t$ , by expressing Eq. (5-51) in terms of  $\lambda$ , the following approximation is proposed

$$\frac{\gamma_r}{\theta} = S^2 \left( \frac{m}{\lambda} + \frac{b - m\lambda_t}{\lambda^2} \right) \quad (5-52)$$

where

$$m = \frac{\sqrt{48\eta}(7.59\eta + 2.68)}{1 - \eta} \quad (5-53)$$

$$b = 6\lambda_r\lambda_t^2 \left( 1 + \frac{1 - \eta^2}{8\lambda_r} \lambda_t^2 \right)^{-1} \quad (5-54)$$

Figure 5-11 shows the percent error over  $0 \leq \lambda \leq 17.2$  and  $0 \leq \lambda \leq 25.8$  for  $\eta = 0.1$  and  $\eta = 0.4$ , respectively. The magnitude of the error is within 12 % over  $0.02 \leq \eta \leq 0.40$ .

## 5.4 Discussion

### 5.4.1 Generalized Approximation

The maximum shear strain due to rotation can be represented by generalized approximations dependent on the elastomeric pad geometry, as functions of  $G$ ,  $S$ , and  $K_e$ , or of a single dimensionless parameter,  $\lambda$ . Expressed as a function of  $\lambda$ , the proposed approximation is

$$\frac{\gamma_r}{\theta} = \begin{cases} \Gamma_1 S^2 (1 + \Gamma_2 \lambda^2)^{-1}, & \text{if } \lambda < \lambda_t \\ S^2 \left( \frac{\Gamma_3}{\lambda} + \frac{\Gamma_4}{\lambda^2} \right), & \text{if } \lambda \geq \lambda_t \end{cases} \quad (5-55)$$

The coefficients for each pad geometry are listed in Table 1.

The approximation for  $\lambda < \lambda_t$  obtained from the truncated Taylor and binomial series is accurate for all the pad geometries considered. With the exception of the annular and rectangular pad, the percent error for  $\lambda < \lambda_t$  is below 5 %. In the  $S$ ,  $G$ , and  $K_e$  space with  $\lambda > \lambda_t$ , the proposed approximation is a straight line parallel to the analytical solution (see Figure 5-2). Thus, the percent error decreases with increasing  $\lambda$  from a maximum at  $\lambda = \lambda_t$  as the magnitude of the difference between the analytical solution and proposed approximation remains nearly constant. The result is an accurate approximation that is adaptable to any pad geometry.

The analytical solutions for the bending modulus and the maximum shear strain due to rotation of an annular and circular pad including extensibility and compressibility have not been derived in the literature. Consequently, the value of  $e$  for these geometries is unknown. In Van Engelen et al. (2015), it was found that  $e \approx 2$  for the compression modulus and maximum shear strain due to compression with small values of  $S$ . It is

postulated that the value of  $e$  for the maximum shear strain due to rotation will likewise be approximately equal to 2. Validation of the proposed value of  $e$  is required either through derivation of the analytical solutions, or comprehensive numerical modelling.

#### 5.4.2 Example: Square Pad ( $\rho = 1$ )

For a square pad of equal side lengths,  $B$ , and expressing in terms of a single pad (i.e.  $\theta_i/T = \theta/t_i$ ), Eq. (5-3) becomes

$$\gamma_r = 8.8S^2\theta \quad (5-56)$$

$$\gamma_r = 8.0S^2\theta \quad (5-57)$$

based on the CSA (2014) and AASHTO (2014a,b) values of  $D_r$ , respectively. The coefficient of Eq. (5-56) and Eq. (5-57) are conservative in comparison to the analytical solution, which has a coefficient of 7.576 when assuming incompressibility and inextensibility (see Eq. (5-27)). For a square pad with an incompressible elastomer  $L/W = 1$ ,  $\lambda \rightarrow 0$  and from Eq. (5-4),  $D_r = 0.48$ , which yields a coefficient of 7.68, which is also conservative. Note that Eq. (5-56) and Eq. (5-57) are independent of the aspect ratio.

Figure 5-12 compares the predicted values of  $\gamma_r/\theta$  to the analytical solution based on CSA (Eq. (5-56)), AASHTO (2014b) (Eq. (5-3)) modified to include compressibility and extensibility, and the proposed approximation for a square pad as a function of  $S$  for various values of  $K_e/G$ . Note that extensibility was included in AASHTO (2014a) by taking  $K = K_{e=2}$  in Eq. (5-5). As  $S$  increases the pad becomes increasingly sensitive to rotations. The CSA (2014) approximation, which is similar to, but more conservative than, the analytical solution assuming incompressibility and inextensibility, rapidly diverges from the analytical solution including these effects. Although the CSA (2014) approximation is conservative, the magnitude of the error determines that the approximation is restricting, particularly for low values of  $K_{e=2}/G$  and large values of  $S$  (i.e. a large value of  $\lambda$ ). The AASHTO (2014a) approximation, based on the proposed approximation by Stanton et al. (2008), but modified to include compressibility and extensibility, accurately represents  $\gamma_r/\theta$  for small values of  $S$ , but rapidly diverges as  $S$  increases, presumably exceeding the best-fit range considered. The proposed approximation accurately predicts  $\gamma_r/\theta$  over the entire range considered. The percent error of the AASHTO (2014b) and proposed approximations are compared in Figure 5-13. Note that the large percent error for large values of  $S$  and small values of  $K_{e=2}/G$  (i.e. large values of  $\lambda$ ) based on AASHTO (2014b) has not been shown. Although both approximations have minimal error over the range considered, the proposed approximation has the advantage that it can easily be adapted to any pad geometry with a similar level of accuracy. The accuracy of AASHTO (2014b) suggests that extensibility could be included by replacing  $K$  with  $K_{e=2}$  in Eq. (5-4).

### 5.4.3 Example: Circular Pad

For a circular pad with a diameter,  $B$ , expressed as a single pad, Eq. (5-3) becomes

$$\gamma_r = 6S^2\theta \quad (5-58)$$

for CSA (2014) and AASHTO (2014a,b). Note that Eq. (5-58) is identical to the analytical solution assuming an incompressible elastomer and inextensible reinforcement (see Eq. (5-22)). Neither CSA (2014) nor AASHTO (2014a,b) provide a correction for compressibility or extensibility. Figure 5-14 compares the predicted values of  $\gamma_r/\theta$  determined by CSA (2014) or AASHTO (2014a,b), and the proposed approximation to the analytical solution. Similar to the square pad, the CSA (2014) and AASHTO (2014a,b) approximations are conservative, but the magnitude of the error becomes large and restricting from a design perspective as  $S$  increases. The proposed approximation closely follows the analytical solution over the entire range considered.

## 5.5 Conclusion

The complexity of analytical solutions developed based on the pressure solution inclusive of elastomer compressibility and reinforcement extensibility renders the expressions inappropriate for use in design codes. Design codes currently use equations derived by neglecting these effects, or include them in a limited capacity for specific pad geometries. Neglecting compressibility and/or extensibility severely limits the range over which these expressions are accurate, resulting in unacceptable large errors if applied to pads with moderate or large shape factors. It was demonstrated that the maximum shear strain due to rotation could be represented by a simple generalized approximation for infinite strip, circular, square, rectangular and annular pad geometries. The pad geometry is incorporated through the inclusion of geometry-specific correction factors. Both the compressibility of the elastomer and the extensibility of the reinforcement have a pronounced effect on the design properties of elastomeric bearings. It is recommended that these expressions be adopted in design codes as simple approximations for the maximum shear strain due to rotation.

### *Acknowledgements*

Financial support for this study was provided by the McMaster University Centre for Effective Design of Structures (CEDs) funded through the Ontario Research and Development Challenge Fund (ORDCF) as well as an Early Researcher Award (ERA) grant, both of which are programs of the Ministry of Research and Innovation (MRI). The support of the Natural Sciences and Engineering Research Council of Canada and a Vanier Canada Graduate Scholarship is gratefully acknowledged.

*References*

- Angeli P, Russo G, Paschini A. (2013). “Carbon Fiber-Reinforced Rectangular Isolators with Compressible Elastomer: Analytical Solution for Compression and Bending.” *Int. J. Solids Struct.*, 50(22): 3519-3527.
- AASHTO. (2014a). *AASHTO LRFD Bridge Design Specifications*. 7<sup>th</sup> Ed., American Association of State Highway and Transportation Officials, Washington, D.C.
- AASHTO. (2014b). *Guide Specifications for Seismic Isolation Design*. 4<sup>th</sup> Ed., American Association of State Highway and Transportation Officials, Washington, D.C.
- Al-Anany, Y.M. and Tait, M.J. (2015). “A numerical study on the compressive and rotational behavior of fiber reinforced elastomeric isolators (FREI).” *Composite Structures*, 133: 1249-1266.
- Chalhoub, M.S., and Kelly, J.M. (1990). “Effect of Bulk Compressibility on the Stiffness of Cylindrical Base Isolation Bearings.” *Int. J. Solids Struct.*, 26(7): 743-760.
- Chalhoub M.S., and Kelly, J.M. (1991). “Analysis of infinite-strip-shaped base isolator with elastomer bulk compression.” *J. Eng. Mech. ASCE*, 117(8), 1791-1805.
- Constantinou, M.C., Kalpakidis, I., Filiatrault, A., and Ecker Lay, R.A. (2011). “LRFD-based analysis and design procedures for bridge bearings and seismic isolators.” Rept. No, MCEER-11-0004.
- CSA. (2014). *S6-14 Canadian Highway Bridge Design Code*. Canadian Standards Association, Canada.
- De Raaf, M.G.P, Tait, M.J., and Toopchi-Nezhad, H. (2011). “Stability of Fiber-Reinforced Elastomeric Bearings in an Unbonded Application.” *J. Compos. Mater.*, 45: 1873-1884.
- Gent, A.N. (1964). “Elastic Stability of Rubber Compression Springs.” *J. Mech. Eng. Sci.*, 6(4): 318-326.
- Gent, A.N. and Lindley, P.B. (1959). “Compression of bonded rubber blocks.” *Proc., Inst. Mech. Eng.*, 173(1), 111-122.
- ISO. (2010). “Elastomeric seismic-protection isolators.” ISO 22762, Geneva.
- Kelly, J.M. (1997). *Earthquake-resistant design with rubber*. Springer, London.
- Kelly, JM. (1999). “Analysis of fiber-reinforced elastomeric isolators,” *J. Seismol. Earthq. Eng.*, 2(1), 19-34.
- Kelly, J.M. and Takhirov S.M. (2002). “Analytical and Experimental Study of Fiber-Reinforced Strip Isolators.” Rept. No, PEER 2002/11. Pacific Earthquake Engineering Research Center, University of California, Berkeley, CA.
- Kelly, J.M. and Van Engelen, N.C. (2015). “Single Series Solution for the Rectangular Fiber-Reinforced Elastomeric Isolator Compression Modulus.” Rept. No, PEER 2015/03. Pacific Earthquake Engineering Research Center, University of California, Berkeley, CA.
- Kelly, J. M., and Konstantinidis, D. (2011). *Mechanics of rubber bearings for seismic and vibration isolation*. Wiley, Chichester, U.K.
- Konstantinidis, D., Kelly, J.M, and Makris, N. (2008). “Experimental investigation on the seismic response of bridge bearings.” *Report EERC-2008/02*. Earthquake Engineering Research Center: University of California, Berkeley.

- Nagarajaiah, S., and Ferrell, K. (1999). “Stability of Elastomeric Seismic Isolation Bearings.” *J. Struct. Eng.-ASCE*, 125(9): 946-954.
- Osgooei, P.M., Tait, M.J., and Konstantinidis, D. (2014). “Three-dimensional finite element analysis of circular fiber-reinforced elastomeric bearings under compression.” *Comp. Struct.*, 108(1): 191-204.
- Stanton, J.F., Scroggins, G., Taylor, A.W., and Roeder, C.W. (1990). “Stability of Laminated Elastomeric Bearings.” *J. Eng. Mech-ASCE* 116(6): 1351-1371.
- Stanton, J.F., Roeder, C.W., Mackenzie-Helnwein, P., White, C., Kuester, C., and Craig, B. (2008). *NCHRP Report 596: Rotation Limits for Elastomeric Bearings*. TRB, National Research Council, Washington, D.C.
- Toopchi-Nezhad, H., Tait, M.J., and Drysdale, R.G. (2008). “Testing and Modeling of Square Carbon Fiber-reinforced Elastomeric Seismic Isolators.” *Struct. Control Hlth.*, 15: 876-900.
- Van Engelen, N.C., and Kelly, J.M. (2015). “Correcting for the influence of bulk compressibility on the design properties of elastomeric bearings.” *J. Eng. Mech.-ASCE*, 141(6).
- Van Engelen, N.C., Tait, M.J. and Konstantinidis, D. (2015). “Development of Code Oriented Formulas for Elastomeric Bearings Including Bulk Compressibility and Reinforcement Extensibility.” *J. Eng. Mech.-ASCE*. [in-press]

Table 5-1: Summary of the proposed approximate formulas for maximum shear strain due to rotation

Pad Geometry	$\Gamma_1$	$\Gamma_2$	$\Gamma_3$	$\Gamma_4$	$c$	$\lambda_r$
Infinite Strip	2	1/15	6	-5.92	12	$\sqrt{5}$
Circular	6	1/24	24	-31.9	48	$2\sqrt{2}$
Square	7.576	0.056	24	-24.7	48	2.439
Rectangle*	$2\rho_r$	0.05913	$m$	$b - m\lambda_r$	12	$0.6912\sqrt{\frac{12}{\rho_r}}$
Annular† (Outer)	$6\lambda_r$	$(1-\eta^2)/24$	$m_1$	$b_1 - m_1\lambda_r$	$48/(1-\eta)^2$	$\frac{2\sqrt{2}}{1-\eta^2}$
Annular‡ (Inner)	$6\lambda_r$	$(1-\eta^2)/8\lambda_r$	$m_2$	$b_2 - m_2\lambda_r$	$48/(1-\eta)^2$	$\frac{1.79}{(1-\eta)}\sqrt{\frac{48}{\lambda_r\lambda_r}}$

$$* \rho_r = \frac{2.92}{\rho} + 0.86$$

$$m = 6\frac{1+\rho}{\rho}$$

$$b = 2\rho_r\lambda_r^2(1+0.05913\rho_r\lambda_r^2)^{-1}$$

$$† \lambda_r = \frac{1+\eta}{1-\eta}$$

$$m_1 = \frac{24}{(1-\eta)^2}$$

$$b_1 = 6\lambda_r\lambda_r^2\left(1+\frac{1-\eta^2}{24}\lambda_r^2\right)^{-1}$$

$$‡ \lambda_r = \frac{1+\eta}{1-\eta}, \lambda_r = 5.5\eta + 1$$

$$m_2 = \frac{\sqrt{48}\eta(7.59\eta + 2.68)}{1-\eta}$$

$$b_2 = 6\lambda_r\lambda_r^2\left(1+\frac{1-\eta^2}{8\lambda_r}\lambda_r^2\right)^{-1}$$

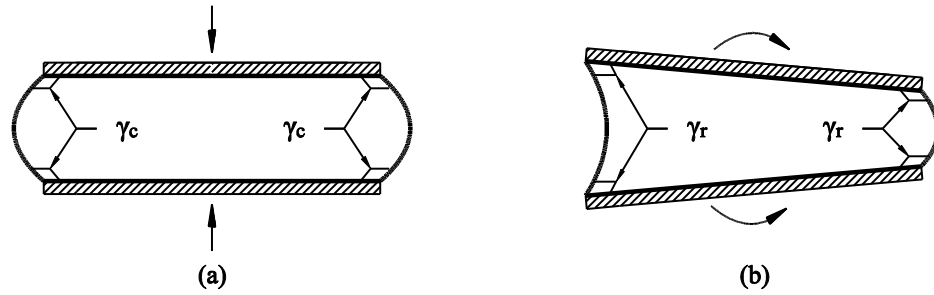


Figure 5-1: Location of the maximum shear strain due to (a) compression and (b) rotation.

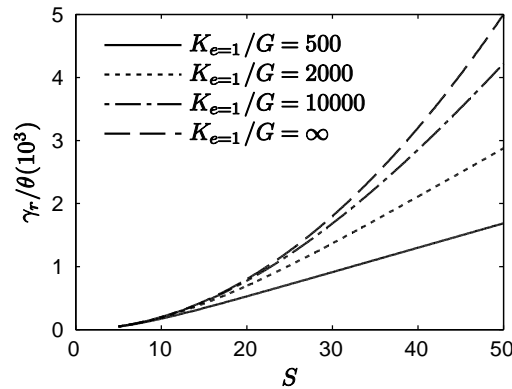


Figure 5-2: Normalized maximum shear strain due to rotation as a function of the shape factor for an infinite strip pad.

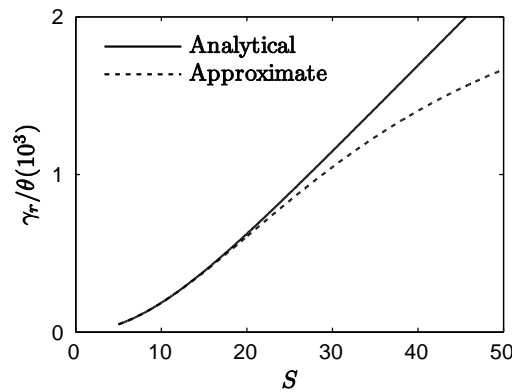


Figure 5-3: Example of the divergence of the analytical solution and proposed approximation for an infinite strip pad with  $K_{e=1}/G = 1000$ .

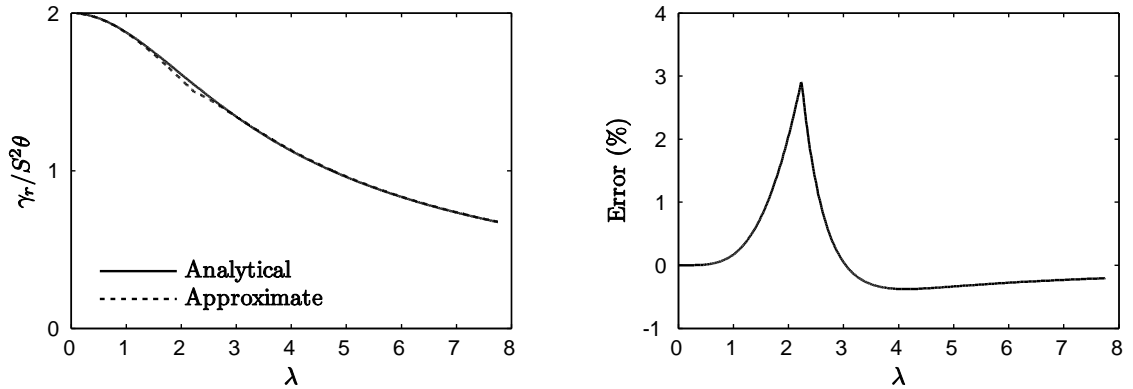


Figure 5-4: Comparison of the analytical solution and proposed approximation and percent error as a function of  $\lambda$  for an infinite strip pad.

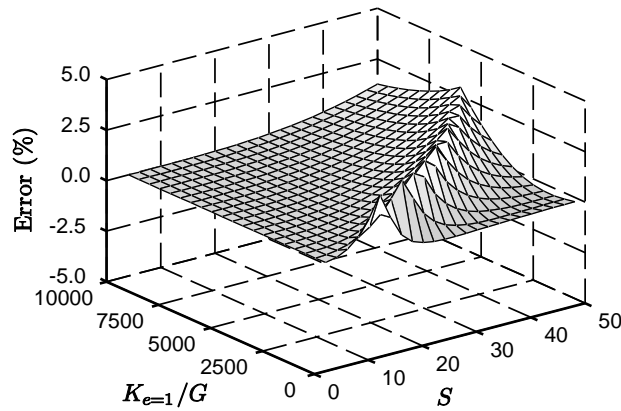


Figure 5-5: Percent error of  $\gamma_r/\theta$  for an infinite strip pad.

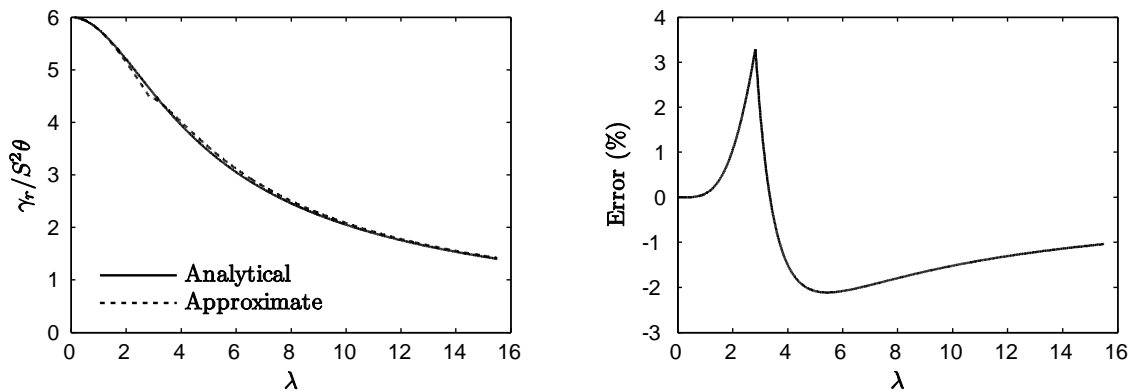


Figure 5-6: Comparison of the analytical solution and proposed approximation and percent error as a function of  $\lambda$  for a circular pad.

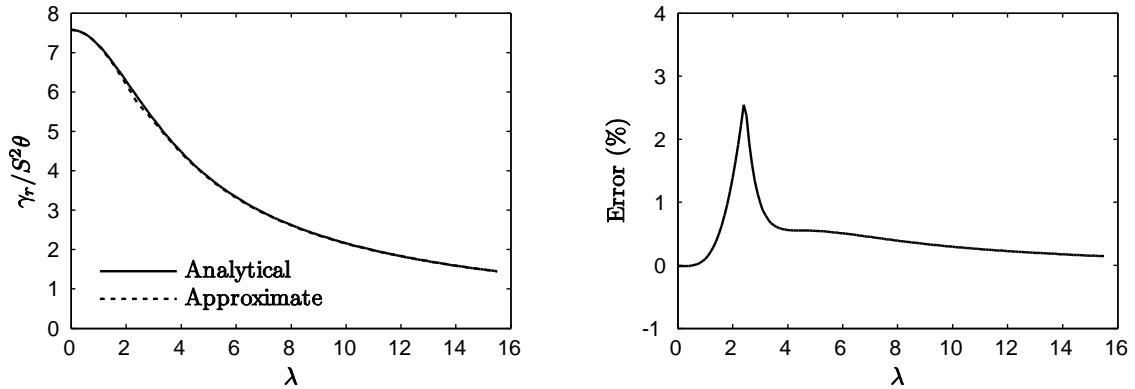


Figure 5-7: Comparison of the analytical solution and proposed approximation and percent error as a function of  $\lambda$  for a square pad.

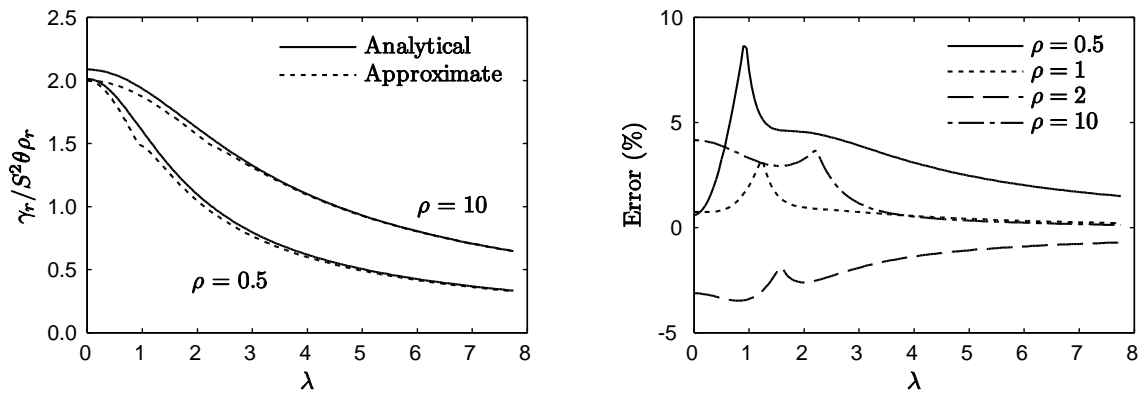


Figure 5-8: Comparison of the analytical solution and proposed approximation and percent error as a function of  $\lambda$  for a rectangular pad.

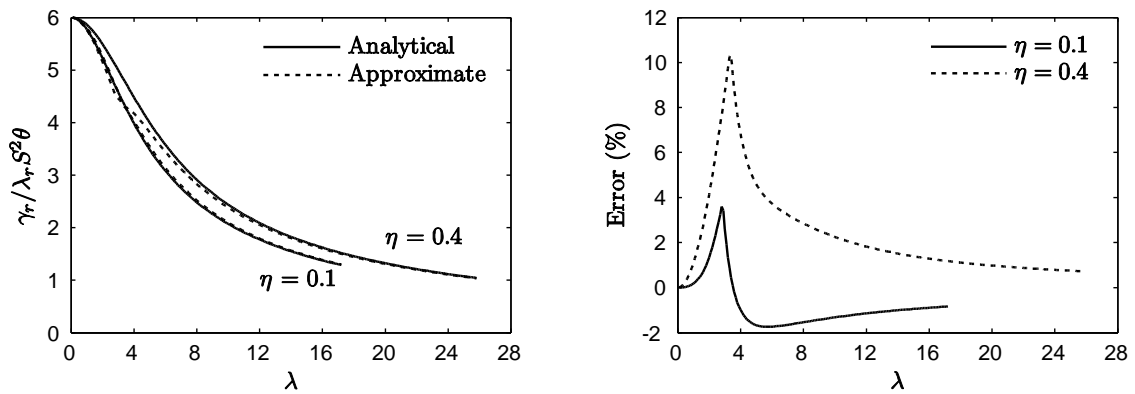


Figure 5-9: Comparison of the analytical solution and proposed approximation and percent error as a function of  $\lambda$  for the outer surface of an annular pad.

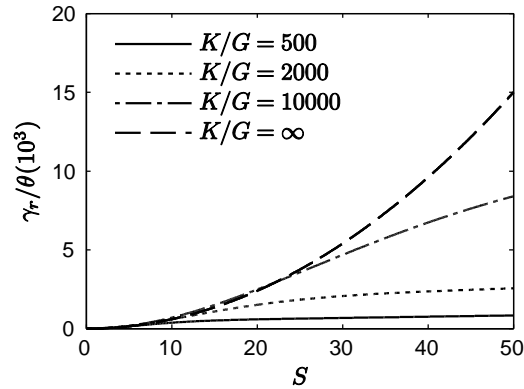


Figure 5-10: Normalized maximum shear strain due to rotation as a function of the shape factor for the inner surface of an annular pad ( $\eta = 0.1$ ).

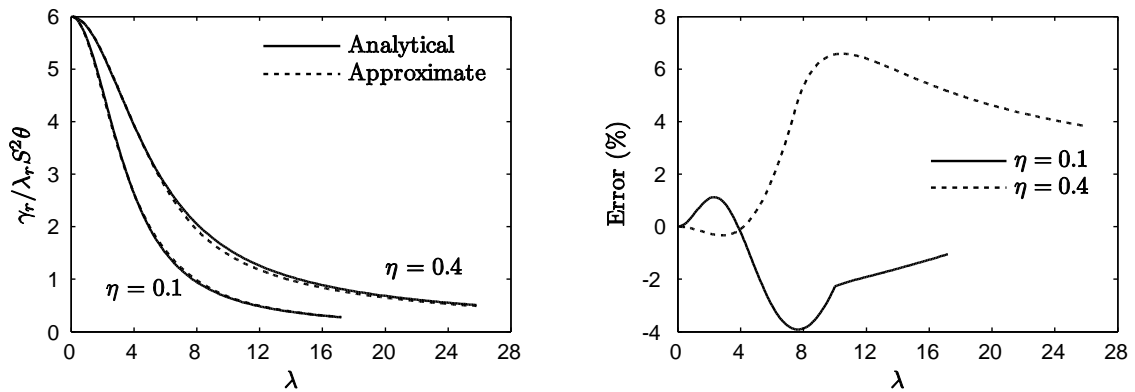


Figure 5-11: Comparison of the analytical solution and proposed approximation and percent error as a function of  $\lambda$  for the inner surface of an annular pad.

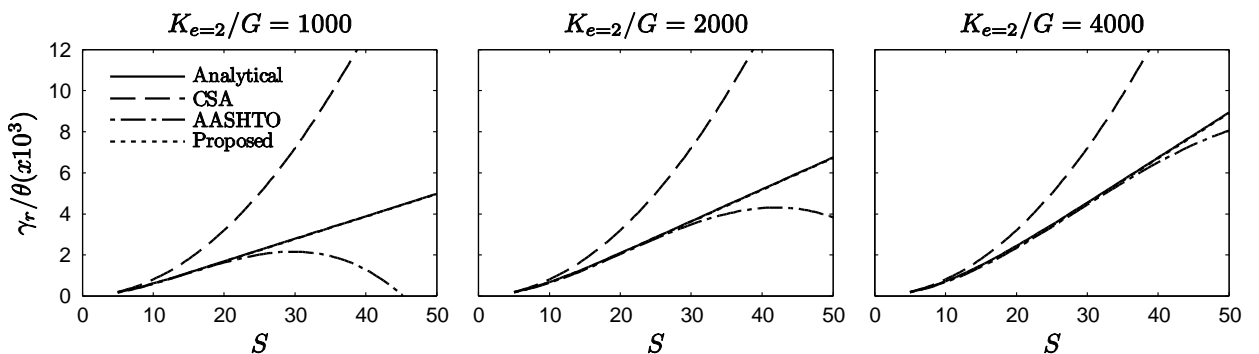


Figure 5-12: Comparison of the CSA (2014), AASHTO (2014b), and proposed approximations to the analytical solution.

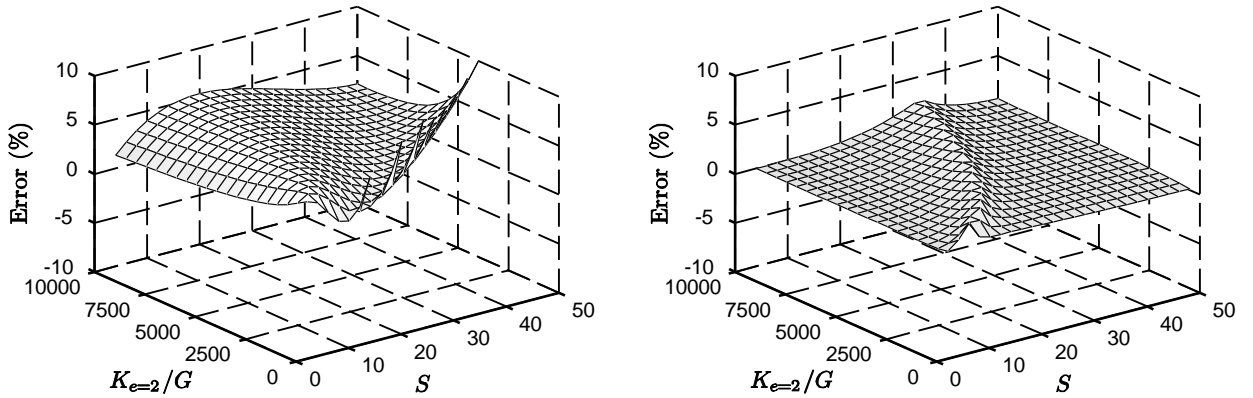


Figure 5-13: Percent error of (a) AASHTO (2014b) and (b) the proposed approximation.

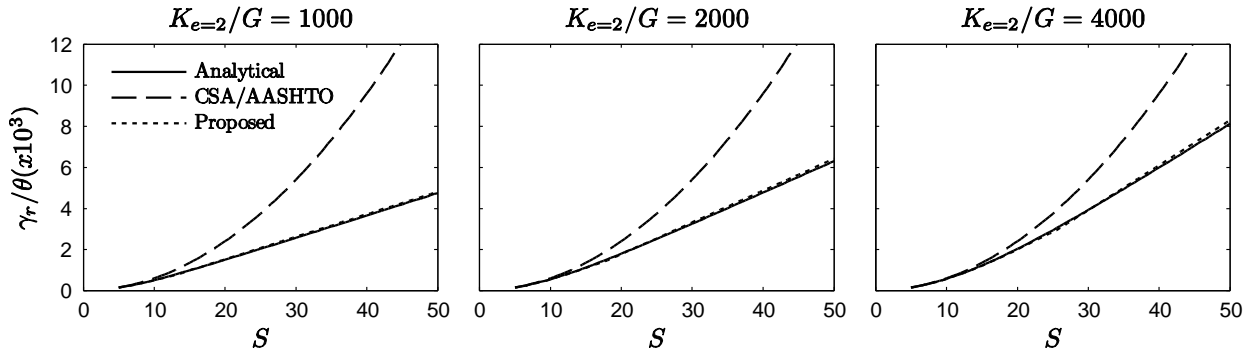


Figure 5-14: Comparison of the CSA (2014), AASHTO (2014a,b), and proposed approximations to the analytical solution.

## **6 Experimental and Finite Element Study on the Compression Properties of Modified Rectangular Fiber-Reinforced Elastomeric Isolators (MR-FREIs)**

Reproduced with permission from Elsevier.

Van Engelen NC, Osgooei PM, Tait MJ, Konstantinidis D. 2014. Experimental and Finite Element Study on the Compression Properties of Modified Rectangular Fiber-Reinforced Elastomeric Isolators (MR-FREIs). *Engineering Structures*, 74: 52-64, DOI: 10.1016/j.engstruct.2014.04.046.

### *Abstract*

This study investigates the compressive behaviour of Modified Rectangular Fiber-Reinforced Elastomeric Isolators (MR-FREIs). The geometric modifications are introduced to reduce the horizontal stiffness and increase the energy dissipation of the isolation system, allowing long rectangular isolators that provide uniform support along walls to be utilized. It is of critical importance that MR-FREIs maintain adequate vertical stiffness to satisfy the requirements for an isolation system. Experimental data from vertical tests of four rectangular FREIs with and without geometric modifications is used to evaluate a three-dimensional (3D) finite element (FE) model. The 3D FE model is then used to conduct a parametric study on two MR-FREI configurations with varying geometry. The parametric study investigates the effect of the geometric modifications on the vertical stiffness and compression modulus in addition to stress and strain distributions in the elastomer and fiber reinforcement. The study identifies that, similar to annular isolators, introducing a minor geometric modification to the interior of the isolator results in a significant decrease in vertical stiffness and compression modulus. This influence is considerably less for geometric modifications positioned on the exterior of the isolator.

### *6.1 Introduction*

Elastomeric isolators consist of alternating horizontal layers of elastomer and reinforcement. The reinforcement serves primarily to restrain the lateral bulging of the elastomeric layers under vertical compressive stresses. The restraint of the elastomer enhances the vertical stiffness of the isolator due to the near incompressibility of the elastomer, resulting in a vertical stiffness that is significantly greater than the horizontal stiffness. The horizontal stiffness is comparatively uninfluenced by the reinforcement. A high vertical stiffness is necessary for the suppression of a rocking mode which may be introduced by the isolation system. Historically, steel plates in the form of shims have been the reinforcement of choice; however, conventional Steel-Reinforced Elastomeric

Isolators (SREIs) are heavy and expensive. The weight is attributed to the steel shims and thick steel end plates used to mechanically fasten the isolator to the supports. The cost is in part due to the highly labour-intensive process required to prepare the steel for bonding to the elastomeric layers [1]. It was proposed by Kelly [2] that the steel reinforcement be replaced with lighter fiber reinforcement of similar mechanical tensile properties. The concept of Fiber-Reinforced Elastomeric Isolators (FREIs) has been investigated experimentally in numerous studies, including Kelly [2], Moon et al. [3, 4], and Toopchi-Nezhad et al. [5, 6], and shown to perform well with several distinct advantages, such as superior energy dissipation and, for unbonded FREIs with a sufficiently large width-to-height aspect ratio, a unique stable rollover behaviour.

The positioning of FREIs between the upper and lower supports can be in a bonded or unbonded application. In a bonded application, the isolator is bonded to two steel end plates that are mechanically fastened to the supports. In an unbonded application, the thick steel end plates are eliminated, and the isolator is placed between the upper and lower supports with no mechanical restraints. Stable unbonded FREIs exhibit unique stable rollover due to the unbonded application and the lack of flexural rigidity of the fiber reinforcement. In addition to stable rollover, this type of isolator has been shown, through finite element analysis, to have desirable advantages over identical bonded FREIs, such as lower tensile stress demand on the elastomeric layers and on the fiber reinforcement when displaced horizontally [7].

A significant advantage of FREIs is the ability to manufacture large pads and cut individual isolators from the pads to the desired size [2]. Individual FREIs manufactured using this technique have been utilized in numerous experimental studies such as Toopchi-Nezhad et al. [6] and de Raaf et al. [8]. In buildings with structural walls as the lateral-force-resisting system, conventional square or circular isolators are often orientated in a grid pattern and require the use of a structural system to adequately transfer the loads applied to the walls to the isolators. Long rectangular FREIs allow for uniform support to be provided along shear walls [2], which reduces the requirements of a load transfer system. This approach has the potential for significant cost savings in the construction process and is well suited to structures with concrete or masonry shear walls. A comparison of a base-isolated masonry wall using square or circular and rectangular isolators is illustrated in Figure 6-1.

The performance of a base isolation system is primarily a function of the horizontal stiffness. The horizontal stiffness should be sufficiently low in order to shift the fundamental period out of the high-energy range of a typical earthquake event and essentially decouple the structure from the ground motion. If long rectangular isolators are used, a relatively high horizontal stiffness is expected due to the large plan area of the isolator, thereby reducing the shift in the fundamental period and, thus, the overall

efficiency of the isolation system. In the interest of improving the design of the isolation system, the horizontal stiffness and energy dissipation characteristics can be adjusted through the introduction of geometric modifications to the plan loaded surface. This concept, denoted as Modified Rectangular Fiber-Reinforced Elastomeric Isolators (MR-FREIs), is demonstrated in Figure 6-2. Although intended to alter the horizontal performance, the geometric modifications also influence the vertical properties of the isolator relative to an unmodified isolator. It is critical that the rectangular geometry and high vertical stiffness necessary for isolation systems be maintained despite the modifications. Therefore, it is vital to understand how modifications to the plan loaded surface will simultaneously alter both the horizontal and vertical performance of the isolator, including increased stresses and changes in pressure distributions caused by the modifications.

In this paper the effect of modifications to the plan loaded surface on the vertical stiffness and compression modulus of MR-FREIs is investigated. A three-dimensional (3D) Finite Element (FE) model is developed and evaluated using experimental data from four isolators. The model is subsequently used to conduct a parametric study on the influence of the diameter of the circular modifications on the vertical stiffness and compression modulus for two different configurations. Furthermore, the FE model is used to examine the variations in the stress and strain distributions of the elastomeric layers and fiber reinforcement.

## 6.2 Background

### 6.2.1 MR-FREIs

Selecting an elastomer with a low shear modulus,  $G_e$ , alone often permits the targeted horizontal stiffness to be achieved; however, additional measures may be required for long rectangular isolators. The introduction of modifications will simultaneously decrease the plan loaded area, decrease the shape factor,  $S$ , defined as the ratio of the loaded area to the unloaded area of a single layer of elastomer, and modify the pressure distribution. A reduction in plan loaded area directly decreases both the horizontal and vertical stiffness, whereas changes in the shape factor and pressure distribution will also alter the horizontal and vertical behaviour of the isolator, as discussed in Van Engelen et al. [9].

It is common for shape factors greater than approximately 5 to assume that the stress within the elastomeric layers is dominated by the internal pressure, known as the pressure solution [10]. This assumption is often made in analytical solutions for rectangular and circular elastomeric isolators [2, 10-17], although analytical solutions exist that relax this assumption, such as Pinarbasi and Mengi [18] and Tsai [19, 20]. Modifications can significantly alter the pressure distribution depending on the

orientation, resulting in areas of higher stress concentrations. Therefore, changes in the pressure distribution as a result of the modifications are also expected to influence the horizontal and vertical properties.

Modifications will decrease the shape factor since the unloaded area increases and the plan loaded area decreases simultaneously, which both act to reduce the shape factor. It has been shown through analytical solutions that the vertical stiffness of rectangular FREIs [16] and horizontal stiffness of infinite strip FREIs [21, 22] are influenced by the shape factor. In a FE study, the compression modulus for unmodified unbonded FREIs was shown to have a greater rate of increase than the rate of increase of the shape factor, rendering the shape factor an important design parameter [23].

A preliminary study on the vertical stiffness and compression modulus of MR-FREIs was conducted by Van Engelen et al. [24]. The purely experimental study considered six specimens with three modification configurations and two modification diameters. The test results showed that a substantial drop in vertical stiffness occurred with minor modification, but that the decrease was dependent on the configuration of the modification. Similar trends observed with the vertical stiffness were noted with the compression modulus, but to a lesser degree, suggesting that the shape factor and pressure distribution are important considerations.

The effective horizontal stiffness and energy dissipation characteristics of four isolators presented in Van Engelen et al. [24] were experimentally examined in Van Engelen et al. [9] over a displacement range of  $0.25 t_r$  to  $2.50 t_r$ , where  $t_r$  is the total thickness of the elastomeric layers. The study, which only considered isolators with holes placed in the interior of the plan area, indicated that the effective horizontal stiffness and equivalent viscous damping, in comparison to the control specimen, were dependent on the horizontal displacement. With the exception of large displacements, i.e.,  $2.00 t_r$  to  $2.50 t_r$ , the decrease in effective horizontal stiffness was larger than the decrease in the plan loaded area of the specimen. The equivalent viscous damping was found to increase at all displacement amplitudes considered in comparison to the control specimen. The increase in damping was attributed to the decrease in effective horizontal stiffness and a decrease in the length of the fiber reinforcement. It was postulated in the study that the modifications allowed for an increase in inter-fiber movement causing an increase in the energy dissipation characteristics of the isolator.

In a FE study conducted by Dezfuli and Alam [25], it was shown that the vertical stiffness of FREIs reinforced with carbon fiber was more sensitive to changes in the shear modulus, thickness of the fiber reinforcement and number of elastomeric layers than the effective horizontal stiffness or equivalent viscous damping. In that study, the total height was held constant, thus the number of elastomeric layers is also representative of the shape factor since an increase in the number of layers requires a decrease in the layer

thickness resulting in a larger shape factor. Utilizing FE analysis, Toopchi-Nezhad et al. [23] identified that the compression modulus was highly sensitive to changes in the shape factor, while the horizontal stiffness was not. The preliminary findings in Van Engelen et al. [9, 24] suggest that the decrease in the vertical properties due to the modifications can be significant. Therefore, assessing the effect of various design parameters is critical to accurately characterizing the vertical behaviour of MR-FREIs.

### 6.2.2 Annular Isolators

Modifications have been investigated analytically for circular SREIs and FREIs in the form of annular isolators. Constantinou et al. [11] developed a factor to take into consideration the addition of a circular hole at the center of a circular SREI forming an annular isolator. Figure 6-3 shows the profile view of a section of a circular and annular isolator with an outer radius,  $R_1$ , and inner radius,  $R_2$ . The introduction of the modification creates an additional free surface where lateral bulging occurs. As the ratio of  $R_2/R_1$  for an annular isolator with an incompressible elastomer approaches unity, the compression modulus,  $E_c$ , initially that of a circular isolator,  $E_c = 6GS^2$ , converges to the solution of an infinite strip isolator,  $E_c = 4GS^2$ . The compression modulus drops abruptly at small values of  $R_2/R_1$  and quickly converges to the solution of an infinite strip isolator. Due to this rapid convergence, it has been indicated that regardless of the size of the central hole, the compression modulus for annular isolators should conservatively be taken as the solution for an infinite strip isolator,  $E_c = 4GS^2$  [14].

An analytical study conducted by Pinarbasi and Okay [17] investigated the performance of annular FREIs focusing on four key parameters: the reinforcement extensibility, modification diameter, shape factor and elastomer compressibility. The deformed shape was defined according to the assumptions of the pressure solution. An additional displacement term was included to capture the extensibility of the fiber reinforcement and the compressibility of the elastomer was also considered. The study concluded that  $E_c$  drops abruptly with the introduction of a minor modification for incompressible elastomers, similar to the analytical solution obtained for SREIs. The magnitude of the drop decreases with compressibility, especially for isolators with a high shape factor where the restraint effect is reduced due to the compressibility.

## 6.3 Experimental Testing

### 6.3.1 Isolator Design

The isolators considered in this study are of the same geometry and layer design as four of the isolators used in Van Engelen et al. [9, 24]. The isolators were manufactured in large pads and subsequently cut to the desired plan dimensions with a width,  $(2a)$ , of 76 mm and length,  $(2b)$ , of 52 mm, as illustrated in the plan and profile view in Figure

6-4. The quarter scale layer design is identical to the design described in Foster [26]. The isolators contained seven layers of Neoprene; the five interior layers of elastomer had a thickness of 3.18 mm, and the two exterior layers of elastomer had a thickness of 1.59 mm. Bidirectional plain weave carbon fiber reinforcement with a 0.25 mm thickness was bonded to the elastomer. After bonding, the reinforcement layer thickness was approximately 0.55 mm for a total thickness of elastomeric layers of 19.05 mm, and a total height,  $h$ , of 22.35 mm.

A plan view of the four specimens considered and the test specimens are shown in Figure 6-5. Two modification configurations and two diameters were considered. The geometric characteristics of the specimens considered are summarized in Table 6-1. The modifications were circular with a diameter,  $d$ , of 18 mm and 24 mm, or normalized by the length,  $d/2b = 0.35$  and  $0.46$ , respectively. The specimens are numbered C2 through to C4. If the specimen has been modified, a designation is included after the specimen number. The designation represents the normalized diameter of the modification,  $d/2b$ , expressed as a percent and placement of the modification as interior, I, or exterior, E. For example, C2-46I refers to specimen C2 with an interior modification of  $d/2b = 0.46$ . As shown in Figure 6-5b, Specimen C2-46I and C3-35I each had a single circular modification placed at the geometric center of the isolator, referred to as an interior modification. Specimen C4-46E and C5-35E had a half-circle modification removed from each side of the isolator at the center of the 76 mm width, referred to as an exterior modification. By placing modifications on the interior and exterior, isolators of identical loaded area but different shape factors can be analyzed. The modifications reduced the loaded area of the specimens by 6.4 % and 11.4 % for the  $d/2b = 0.35$  and  $0.46$  modifications, respectively.

### 6.3.2 Experimental Setup and Vertical Test Procedure

A photograph and schematic of the experimental test apparatus emphasising the components for vertical tests are shown in Figure 6-6. The setup was configured to conduct horizontal displacement controlled and vertical load-controlled tests. The vertical load was applied to a steel plate and distributed to three identical load cells. The specimen was situated between two steel plates, and the vertical displacement was measured at four locations between the upper and lower platen with laser displacement transducers. The lower platen was on linear bearings and connected to a horizontal actuator, a brace on the upper platen provided the reaction force to the horizontal actuator during horizontal tests. Each isolator was placed unbonded into the setup between two level steel plates.

The compressive force was selected assuming application of the isolators on a structure similar to those considered in experimental tests conducted by Foster [26] and Toopchi-Nezhad et al. [27]. In the test program, the load was held constant for all specimens to simulate the application of the isolators on an identical structure. The

loading was conducted according to procedures outlined in ISO-22762 [28]. Each specimen was monotonically loaded to a compressive force of 7.9 kN at zero horizontal displacement, which corresponds to an average vertical compressive stress of  $\bar{p} = 2.0$  MPa for the unmodified specimen plan area. Once the compressive load was achieved, it was fluctuated  $\pm 20\%$  over three sinusoidal cycles at a frequency of 0.2 Hz and then monotonically unloaded, as shown in Figure 6-7 for an unmodified isolator. Each specimen was initially tested unmodified and visually inspected for damage. The modifications were then introduced, and the specimens were re-tested following the same procedure at an average vertical stress of 1.0 MPa and 2.0 MPa according to the unmodified area and visually inspected for damage after each experiment.

The vertical tests in this study were all conducted at zero horizontal displacement, and the properties with horizontal deformation were not considered. The influence of horizontal displacement on low-damping rubber and lead-rubber bearings was experimentally investigated in Warn et al. [29]. The study concluded that the vertical stiffness of the bearings considered decreased with increasing horizontal displacement. A similar decrease in vertical stiffness is expected in MR-FREIs with increasing horizontal displacement.

### 6.3.3 Experimental Results

The vertical stiffness was determined by using the third cycle maximum and minimum force,  $P$ , and maximum and minimum displacement,  $\delta_v$ , observed over the cycle [28]. The vertical stiffness,  $k_v$ , is:

$$k_v = \frac{P_{max} - P_{min}}{\delta_{v,max} - \delta_{v,min}} \quad (6-1)$$

The compression modulus is determined by:

$$E_c = \frac{k_v t_r}{A} \quad (6-2)$$

where  $A$  is the plan loaded area.

Figure 6-8 presents the average vertical stress as a function of the vertical compressive strain for the unmodified isolator C2. The slope of the dashed line is representative of the compression modulus of 108 MPa obtained for the third cycle using Eq. (6-1) and (6-2). All isolators considered displayed some degree of run-in prior to developing the vertical stiffness. The level of run-in is a function of the development of stresses within the fiber reinforcement which may not be initially taut [6, 12] and potential strain sensitivity of the elastomer. Table 6-2 shows the vertical stiffness and compression modulus values, where  $E$  is the elastic modulus of the elastomer, for the unmodified and modified specimens. The unmodified isolator performance was consistent for the four isolators considered and overall good agreement was obtained with a mean,  $\mu$ , of 101 MPa, standard deviation,  $\sigma$ , of 5 MPa, and coefficient of variation,  $c_v$ , of 0.05.

## 6.4 Finite Element Modeling

### 6.4.1 Model Development

The 3D FE analysis was conducted using MSC Marc [30], a general purpose commercially available FE software. Both the elastomeric and fiber reinforcement layers were modeled using eight-node linear full integration isoparametric hexahedron elements. The compressible *Neo-Hookean* model used in this study was used to describe the elastomer. This material model is characterized by the shear and bulk moduli of the elastomer. The fiber reinforcement materials were modeled using a linear-elastic isotropic material model. Table 6-3 gives the material properties used in the FE analysis where  $K_e$  is the bulk modulus of the elastomer and  $E_f$  and  $\nu_f$  are the elastic modulus and Poisson's ratio of the fiber reinforcement. A bulk modulus of  $K_e = 2000$  MPa was selected for the Neoprene elastomer. The shear modulus of the Neoprene used in the FE analysis was based on the experimental test results of the unmodified isolators.

The top and bottom supports were modeled using rigid surface elements. A *glue* contact was defined between the rigid surfaces and the top and bottom elastomer layers to prevent any slip along the interface. The hexahedron elements used to model elastomeric layers use a mixed formulation to overcome the numerical difficulties associated with the near incompressibility of the elastomeric material [30]. Figure 6-9 shows the FE model of C4-46E highlighting the element size.

### 6.4.2 Model Evaluation

Figure 6-10 shows a cross section of the deformed shape of C2-35I obtained from FE analysis. Similar to the experimental program, the FE analysis was conducted using a constant load determined from  $\bar{p}$  based on the unmodified plan area and the vertical stiffness was calculated using Eq. (6-1). Table 6-4 compares the experimental and FE analysis ratios of the modified-to-unmodified vertical stiffness. The Neoprene used in these isolators was found to be nonlinear, with a stiffening behaviour observed under larger vertical compressive stresses that occur due to the reduced plan area. The 8.6 % average error between the FE predictions and test results can partially be attributed to this nonlinear behaviour. A more sophisticated constitutive model than the compressible Neo-Hookean constitutive model is required for the elastomeric material in order to capture this stiffening behaviour in the FE analysis. However, the 13.3 % maximum error between the FE analysis and experimental results was deemed acceptable given the limitations of the material model.

The average compression modulus of the unmodified isolators from the experimental tests was  $E_c = 101$  MPa. The closed form solution derived by Tsai and Kelly [16] was used to estimate the compression modulus of the unmodified isolator. From Tsai and Kelly [16], with the material properties given in Table 6-3, the compression modulus

of the elastomer pads with thicknesses of 3.18 mm and 1.59 mm were calculated as  $E_c = 90$  MPa and  $E_c = 347$  MPa, respectively. The closed form solution derives the compression modulus using a single elastomeric layer that is assumed to be perfectly bonded to flexible reinforcement. In reality, the isolator is composed of a finite number of elastomeric layers and the contact of the elastomer and the end supports, which are usually assumed to be rigid in comparison to the flexible reinforcement, will affect the vertical response of the isolator. Neglecting the effects of the rigid end boundary condition of the supports on the vertical response of the isolator, the total compression modulus of the isolator can be calculated by treating the elastomeric layers as springs in series. Using this approach, it was calculated that  $E_c = 103$  MPa, which is 2.0 % higher than the FE analysis result. It should be noted that considering the bulk compressibility of the elastomer would reduce the predicted value of vertical stiffness. Also, considering the rigid end condition would increase the predicted vertical stiffness value. Osgooei et al. [31] showed that neglecting the rigid end condition in a circular isolator with  $S = 5$  can reduce the vertical stiffness value by 8.5 %. Therefore, the results obtained from FE are considered to be in good agreement with the experimental results and analytical solution, and the FE model was deemed appropriate for proceeding with the parametric study.

### 6.5 Parametric Study

A parametric study was conducted to determine the influence of modifications on the vertical stiffness, compression modulus, and stress and strain distributions. The study considered isolators with interior and exterior circular modifications with diameters ranging between  $d/2b = 0$  and  $d/2b = 0.58$ .

#### 6.5.1 Vertical Stiffness

Figure 6-11 shows the vertical stiffness of the modified isolators normalized by the unmodified isolator vertical stiffness,  $k_{vo}$ , as a function of  $d/2b$  and  $S/S_o$ , where  $S_o$  is the unmodified shape factor. Figure 6-11a includes the vertical stiffness of an isolator that is directly proportional to the area removed (P). It can be seen that both interior (I) and exterior (E) modifications result in a larger decrease in normalized stiffness than can be attributed to the reduction in area alone. The interior modification results in a significant decrease even at low values of  $d/2b$ . For example, at  $d/2b = 0.12$  an interior modification has  $k_v/k_{vo} = 0.84$ , in comparison to the exterior modification for which  $k_v/k_{vo} = 0.97$ . The exterior modification normalized stiffness is comparable to the proportional area normalized stiffness of  $k_v/k_{vo} = 0.99$ . The interior modification trend is concave upwards while the exterior modification trend is concave downwards. The contrasting behaviour results in a maximum difference in normalized stiffness of 0.27 at  $d/2b = 0.35$  and reduces to 0.17 at the maximum considered normalized diameter of  $d/2b = 0.58$ . The minimum normalized stiffness was 0.42, 0.59 and 0.82 over the range considered for the

interior, exterior and proportional representations, respectively. Figure 6-11b shows  $k_v/k_{v0}$  as a function of  $S/S_o$ . The change in  $S$  for interior modifications is larger than that of exterior modification with the same diameter. Consequently, the difference between interior and exterior modifications is reduced and begins to converge as  $S/S_o$  decreases.

### 6.5.2 Compression Modulus

Similar to the vertical stiffness, the introduction of an interior modification results in an abrupt decrease in normalized compression modulus,  $E_c/E_{co}$ , as shown in Figure 6-12, where  $E_{co}$  is the unmodified isolator compression modulus. The magnitude  $E_c/E_{co}$  is larger than the respective normalized stiffness values with equal diameters, indicating that the compression modulus is less sensitive to the modifications. The minimum relative compression modulus was 0.51 and 0.71 for interior and exterior modifications, respectively. It is interesting to note that the relative compression modulus of 0.85 for an interior diameter of  $d/2b = 0.12$  is not surpassed until a diameter of  $d/2b = 0.46$  for an exterior modification. This demonstrates that the diameter of the exterior modification can be several times larger than an interior modification and still achieve a comparable compression modulus. Similar to the vertical stiffness, the compression modulus of the interior and exterior modifications begins to converge as the diameter is increased. In the limit, as  $d/2b$  approaches unity, the isolator approaches two individual isolators and the influence of the modification configuration diminishes.

The shape factor initially decreases at a larger rate for interior modifications than exterior modifications, as illustrated in Figure 6-13. The shape factor for interior modifications is nearly inversely proportional to the diameter. Initially, exterior modifications result in a small change in the shape factor. An exterior modification removes a portion of the unloaded area equal to  $2dt$ , where  $t$  is the thickness of the elastomeric layer, but increases the unloaded area by  $\pi dt$  for a total increase of  $dt(\pi-2)$ . In comparison, an interior modification adds an unloaded area of  $\pi dt$  without removing any of the existing unloaded area. Therefore, with equal diameters, the change in the interior modification shape factor is more aggressive due to the larger unloaded area. The lower shape factor is representative of a reduction in the restraint of the elastomer by the fiber reinforcement and is believed to be in part responsible for the larger sensitivity of the interior modifications.

### 6.5.3 Vertical Strain

Figure 6-14a and b plot FE results of the vertical strain,  $\epsilon_{zz}$ , at the center of the mid-height elastomer layer with interior modifications where 0 represents the center of the isolator and 1 the respective edge. It can be seen that for the unmodified isolator, with the exception of the edges where lateral bulging occurs, the vertical strain is nearly constant across segments AA and BB. This is in conformance with the assumption in the pressure

solution that horizontal planes remain horizontal. Furthermore, the strain in the modified specimens also remains nearly constant. The interior modification caused an increase in the normalized vertical strain in the elastomeric layer. As the diameter increases, the rate of increase in the vertical strain also increases, which is primarily attributed to the increasing rate of area removed.

Figure 6-14c and d compare  $\varepsilon_{zz}$  in the mid-height elastomer layer for exterior modifications. Similar to interior modifications, as the diameter increases, the rate of increase in  $\varepsilon_{zz}$  increases. The magnitude of the strain for exterior modifications is significantly less than interior modifications. Introducing a  $d/2b = 0.12$  exterior modification results in a 4 % increase in the average  $\varepsilon_{zz}$ , which is notably lower than the 36 % increase in  $\varepsilon_{zz}$  observed in the isolator with an equal diameter interior modification. Figure 6-15 shows the average  $\varepsilon_{zz}$ , ignoring the lateral bulging at the edges, as a function of the percent of area removed. It can be seen that the average  $\varepsilon_{zz}$  is nearly a linear function of the area removed, with the exception of interior modifications, where an abrupt increase in strain magnitude occurs with a minor amount of area removed.

#### 6.5.4 Vertical Stress

Figure 6-16a and b compare the normalized vertical stress distribution,  $S_{zz}/\bar{p}$ , where  $S_{zz}$  is the vertical stress at the center of the mid-height elastomer layer, for isolators with interior modifications. Introducing the interior modification alters the vertical stress distribution significantly along both segments. An overall decrease in the magnitude of  $S_{zz}/\bar{p}$  was observed along both segments at a diameter of  $d/2b = 0.12$ . As the diameter increases,  $S_{zz}/\bar{p}$  along segment AA increases, exceeding the peak  $S_{zz}/\bar{p}$  of the unmodified isolator at a diameter of  $d/2b = 0.46$ . Along segment BB, however, the magnitude of the peak  $S_{zz}/\bar{p}$  continues to decrease with increasing diameter. As the diameter increases, the width of the two portions of the isolator that segment BB crosses become small. As a consequence, the distance to a free edge is reduced, reducing the restraint effect of the reinforcement. Due to the loss of restraint in these regions the primary vertical load resistance is supplied by the ends of the isolator on either side of segment BB.

Figure 6-16c and d show the  $S_{zz}/\bar{p}$  distribution at the center of the mid-height elastomer layers for isolators with exterior modifications. Initially, the introduction of exterior modifications has little influence over the vertical stress distribution with only a modest increase in peak  $S_{zz}/\bar{p}$  along both segments up to a diameter of  $d/2b = 0.35$ . At a diameter of  $d/2b = 0.46$ , two peaks of equal magnitude occur along segment CC. The emergence of these two peaks is representative of the response of the isolator approaching two individual isolators. Along segment DD, it can be seen that the small diameter modifications cause a slight increase in the peak  $S_{zz}/\bar{p}$ , but a minor decrease along the majority of the segment. As the diameter increases, a substantial drop in vertical stress is

observed along the entire segment, indicative of reduced restraint in the center of the isolator and the response approaching two individual isolators.

### 6.5.5 Shear Stress

Figure 6-17 and Figure 6-18 show the  $S_{xz}$  shear stress contours normalized by  $\bar{p}$  at the interface of the center elastomer layer and fiber reinforcement for isolators with interior and exterior modifications, respectively. A peak  $S_{xz}/\bar{p}$  value of 0.17 was observed in the unmodified isolator. As described earlier, the modifications create an additional free surface that allows additional lateral bulging and increased shear stresses to develop in the vicinity of the modification. For interior modifications, the peak  $S_{xz}/\bar{p}$  value occurs near the edge of the modification, whereas for exterior modifications the peak  $S_{xz}/\bar{p}$  value occurs at either end of the isolator, similar to an unmodified isolator. Large  $S_{xz}/\bar{p}$  values are also observed near the edges of the modifications. With a modification diameter of  $d/2b = 0.23$ , the peak  $S_{xz}/\bar{p}$  value increased by 92.6 % for interior modifications (Figure 6-17) in comparison to a 13.2 % increase for exterior modifications (Figure 6-18). At the maximum considered modification diameter of  $d/2b = 0.58$ , the peak  $S_{xz}/\bar{p}$  value increased by 149.8 % and 76.6 % for interior and exterior modifications, respectively. A peak  $S_{xz}/\bar{p}$  value of 0.42 was observed for the interior modification  $d/2b = 0.58$ .

The normalized  $S_{yz}$  shear stress contours are shown in Figure 6-19 and Figure 6-20 for interior and exterior modifications, respectively. Similar to the  $S_{xz}/\bar{p}$  contours, significant shear stresses develop in the vicinity of the modifications. A peak  $S_{yz}/\bar{p}$  value of 0.19 was observed in the unmodified isolator. The peak  $S_{yz}/\bar{p}$  value occurs near the edge of the modification for  $d/2b = 0.23$  and  $0.35$ , and near the outer edge of the isolator for the largest considered interior modification,  $d/2b = 0.58$ . For the exterior modification, the peak  $S_{yz}/\bar{p}$  value occurs near the modification. A modification diameter of  $d/2b = 0.23$  resulted in a similar increase in peak  $S_{yz}/\bar{p}$  value of 40.2 % and 41.1 % for interior and exterior modifications, respectively. A maximum increase of 64.4 % and 78.8 % was observed for interior and exterior modifications, respectively. A peak  $S_{yz}/\bar{p}$  value of 0.34 was observed for the exterior modification at  $d/2b = 0.58$ .

In all modification diameters considered, the overall peak shear stress was observed in  $S_{xz}$  for interior modifications and in  $S_{yz}$  for exterior modifications. The peak shear stress was larger for all diameters considered for the interior modification in  $S_{xz}$  and the exterior modification in  $S_{yz}$ . The magnitude of the peak stress in both directions,  $S_{xz}$  and  $S_{yz}$ , was larger for interior modifications at all diameters considered. Therefore, the shear stresses in the isolators considered in this study with interior modification are more sensitive to the modifications, although significant increases occurred in both geometries.

### 6.5.6 Fiber Reinforcement Von Mises Stress

Figure 6-21 and Figure 6-22 show the Von Mises stress contours normalized by the average vertical pressure,  $\sigma_v/\bar{p}$ , in the center fiber reinforcement layers in the isolators with interior and exterior modifications, respectively. It can be seen that, similar to the observations made with the vertical stress distribution, introducing an interior modification causes a minor decrease in the peak value of  $\sigma_v/\bar{p}$ . As the diameter increases the peak value of  $\sigma_v/\bar{p}$  also increases, exceeding the peak value of an unmodified isolator. For exterior modifications, a minor increase is immediately observed. This increase in  $\sigma_v/\bar{p}$  continues until two peaks begin to form as seen with a diameter of  $d/2b = 0.58$ . The peak value of  $\sigma_v/\bar{p}$  in the center fiber reinforcement layers is 10.5 % and 11.1 % greater than the unmodified isolator at a diameter of  $d/2b = 0.58$  for exterior and interior modifications, respectively.

## 6.6 Conclusions

This paper investigated the vertical behaviour of unbonded Modified Rectangular Fiber-Reinforced Elastomeric Isolators (MR-FREIs). Experimental results were used to evaluate a three-dimensional finite element model. A parametric study was conducted on interior and exterior geometric modifications. It was found that both the vertical stiffness and compression modulus were highly sensitive to interior modifications and, to a lesser extent, exterior modifications. Similarly, the peak shear stress was also greater in isolators with interior modifications, and the peak shear stress usually occurred in the vicinity of the modification. The modifications generally increased the vertical stress and Von Mises stress distribution in the fiber reinforcement. As the diameter of the modification increased, the isolator began to behave as two individual isolators.

The primary purpose of MR-FREIs is to reduce the potentially high horizontal stiffness; consequently the horizontal behaviour of MR-FREIs requires further investigation. An ongoing study by the authors indicates that the influence of modifications on the horizontal properties is displacement dependent, but a favourable decrease in horizontal stiffness and an increase in energy dissipation capability have been observed. Furthermore, the performance of a structure utilizing MR-FREIs, which has a direction-dependent horizontal stiffness, has yet to be investigated. It is expected that the modifications will provide designers with an additional parameter to optimize unbonded FREI design.

### *Acknowledgements*

Financial support for this study was provided by the McMaster University Centre for Effective Design of Structures (CEDs) funded through the Ontario Research and Development Challenge Fund (ORDCF) as well as an Early Researcher Award (ERA)

grant, both are programs of the Ministry of Research and Innovation (MRI). Support was also provided through the Natural Sciences and Engineering Research Council (NSERC) of Canada. The support of a Vanier Canada Graduate Scholarship is gratefully acknowledged.

### *References*

- [1] Kelly JM, Konstantinidis D. Low-cost seismic isolators for housing in highly-seismic developing countries. In: ASSISI 10<sup>th</sup> World Conference on Seismic Isolation, Energy Dissipation and Active Vibrations Control of Structures, Istanbul, Turkey; May 28-31, 2007.
- [2] Kelly JM. Analysis of fiber-reinforced elastomeric isolators. *J Seismol Earthq Eng* 1999; 2(1):19-34.
- [3] Moon BY, Kang GJ, Kang BS, Kelly JM. Design and manufacturing of fiber reinforced elastomeric isolator for seismic isolation. *J Mater Process Technol* 2002;130-131:145-50.
- [4] Moon BY, Kang GJ, Kang BS, Kelly JM. Mechanical properties of seismic isolation system with fiber-reinforced bearing of strip type. *Int Appl Mech* 2003; 39(10):1231-9.
- [5] Toopchi-Nezhad H, Tait MJ, Drysdale, RG. Testing and modeling of square carbon fiber-reinforced elastomeric seismic isolators. *Struct Control Health Monitor* 2008; 15:876-900.
- [6] Toopchi-Nezhad H, Tait MJ, Drysdale, RG. Lateral response evaluation of fiber-reinforced Neoprene seismic isolators utilized in an unbonded application. *J Struct Eng ASCE* 2008; 134(10):1627-37.
- [7] Toopchi-Nezhad H, Tait MJ, Drysdale, RG. Bonded versus unbonded strip fiber reinforced elastomeric isolators: finite element analysis. *Compos Struct* 2011; 93:850-859.
- [8] de Raaf MGP, Tait MJ, Toopchi-Nezhad H. Stability of fiber-reinforced elastomeric bearings in an unbonded application. *J Comp Mat* 2011; 45(18):1873-84.
- [9] Van Engelen NC, Tait MJ, Konstantinidis D. Horizontal behaviour of stable unbonded fiber reinforced elastomeric isolators (SU-FREIs) with holes. In: *Proceedings of the 15<sup>th</sup> World Conference on Earthquake Engineering*, Lisbon, Portugal; September 24-28, 2012.
- [10] Kelly JM. *Earthquake resistant design with rubber*. 2nd ed. London: Springer; 1997.
- [11] Constantinou MC, Kartoum A, Kelly JM. Analysis of compression of hollow circular elastomeric bearings. *Eng Struct* 1992; 14(2):103-111.
- [12] Kelly JM. Analysis of the run-in effect in fiber-reinforced isolators under vertical load. *J Mech Mater Struct* 2008; 3(7):1383-401.
- [13] Kelly JM, Konstantinidis, D. Effect of friction on unbonded elastomeric bearings. *J Eng Mech* 2009; 135(9):953-960.
- [14] Kelly JM, Konstantinidis D. *Mechanics of Rubber Bearings for Seismic and Vibration Isolation*. Chichester: John Wiley & Sons; 2011.

- [15] Konstantinidis D, Kelly JM, Makris, N. Experimental investigation of the seismic response of bridge bearings. Report EERC-2008/02. Earthquake Engineering Research Center, University of California Berkeley: 2008.
- [16] Tsai HC, Kelly JM. Stiffness analysis of fiber-reinforced rectangular seismic isolators. *J Eng Mech* 2002; 128(4):462-470.
- [17] Pinarbasi S, Okay F. Compression of hollow-circular fiber-reinforced rubber bearings. *Struct Eng Mech* 2011; 38(3):361-384.
- [18] Pinarbasi S, Mengi Y. Elastic layers bonded to flexible reinforcements. *Int J Solids Struct* 2008; 45:794-820.
- [19] Tsai HC. Compression stiffness of infinite-strip bearings of laminated elastic material interleaving with flexible reinforcements. *Int J Solids Struct* 2004; 41(24):6647–60.
- [20] Tsai HC. Compression stiffness of circular bearings of laminated elastic material interleaving with flexible reinforcements. *Int J Solids Struct* 2006; 43(11):3484–97.
- [21] Tsai HC, Kelly JM. Buckling of short beams with warping effect included. *Int J Solids Struct* 2005; 42:239-53.
- [22] Tsai HC, Kelly JM. Buckling load of seismic isolators affected by flexibility of reinforcement. *Int J Solids Struct* 2005; 42:255-69.
- [23] Toopchi-Nezhad H, Tait MJ, Drysdale RG. Influence of thickness of individual elastomer layers (first shape factor) on the response of unbonded fiber-reinforced elastomeric bearings. *J Comp Mat* 2013; 47(27): 3433-50.
- [24] Van Engelen NC, Tait MJ, Konstantinidis D. Vertical response behaviour of stable unbonded fiber reinforced elastomeric isolators (SU-FREIs) with holes in the loaded surface. In: Canadian Society for Civil Engineering Annual General Conference. Edmonton, Canada; June 6-9, 2012.
- [25] Dezfuli FH, Alam, MS. Multi-criteria optimization and seismic performance assessment of carbon FRP-based elastomeric isolator. *Eng Struct* 2013; 49:525-40.
- [26] Foster BAD. Base isolation using stable unbonded fibre reinforced elastomeric isolators (SU-FREI): Master's thesis. Hamilton: McMaster University, 2011.
- [27] Toopchi-Nezhad H, Tait MJ, Drysdale RG. Shake table study on an ordinary low-rise building seismically isolated with SU-FREIs (stable unbonded-fiber reinforced elastomeric isolators). *Earthq Eng Struct Dyn* 2009;38:1335-57.
- [28] International Organization for Standardization. Elastomeric seismic-protection isolators, ISO 22762. Geneva: International Organization for Standardization, 2010.
- [29] Warn GP, Whittaker AS, Constantinou MC. Vertical stiffness of elastomeric lead-rubber seismic isolation bearings. *J Struct Eng* 2007;133(9):1227-36.
- [30] MSC Marc. Theory and user information, vol. A. Santa Ana: MSC Software Corporation, 2011.
- [31] Osgooei PM, Tait MJ, Konstantinidis D. Three-dimensional finite element analysis of circular fiber-reinforced elastomeric bearings under compression. *Comp Struct* 2014; 108:191-204.

Table 6-1: Specimen geometric characteristics.

Specimen	Area (mm <sup>2</sup> )	<i>S</i>		<i>d/2b</i>	Area Removed (%)
		<i>Interior</i>	<i>Exterior</i>		
Unmodified	3952	4.9	9.7	-	-
C2-46I	3500	3.3	6.7	0.46	11.4
C3-35I	3698	3.7	7.5	0.35	6.4
C4-46E	3500	3.9	7.8	0.46	11.4
C5-35E	3698	4.2	8.4	0.35	6.4

Table 6-2: Experimental results.

Property		C2	C3	C4	C5	$\mu$	$\sigma$	$c_v$
$(k_{v,t_r}) / (4Eab)$	Unmodified	67	58	61	61	62	4	0.06
	Modified	37	39	51	52	-		
$E_c$ (MPa)	Unmodified	108	98	97	102	101	5	0.05
	Modified	67	69	91	93	-		

Table 6-3: Material properties.

Elastomer	Reinforcement
$G_e = 0.6$ MPa	$E_f = 23$ GPa
$K_e = 2000$ MPa	$\nu_f = 0.2$

Table 6-4: Comparison of the experimental and FE analysis ratios of modified to unmodified vertical stiffness.

Specimen	Experimental	FE	Error (%)
C2-46I	0.55	0.50	9.1
C3-35I	0.66	0.59	10.6
C4-46E	0.83	0.72	13.3
C5-35E	0.85	0.86	1.2

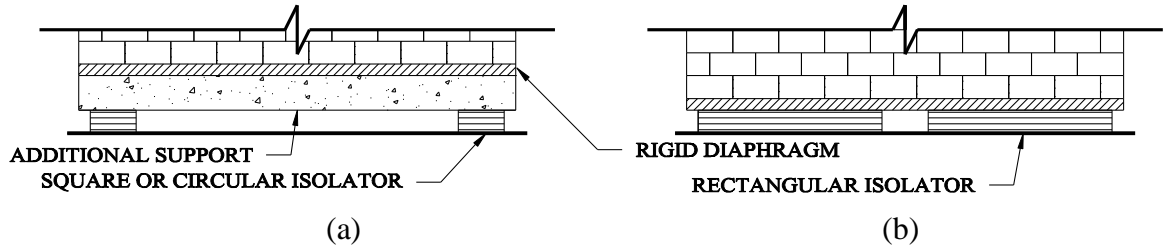


Figure 6-1: Isolation system supporting a masonry wall with (a) localized square or circular isolators and (b) large rectangular isolators that provide uniform support.

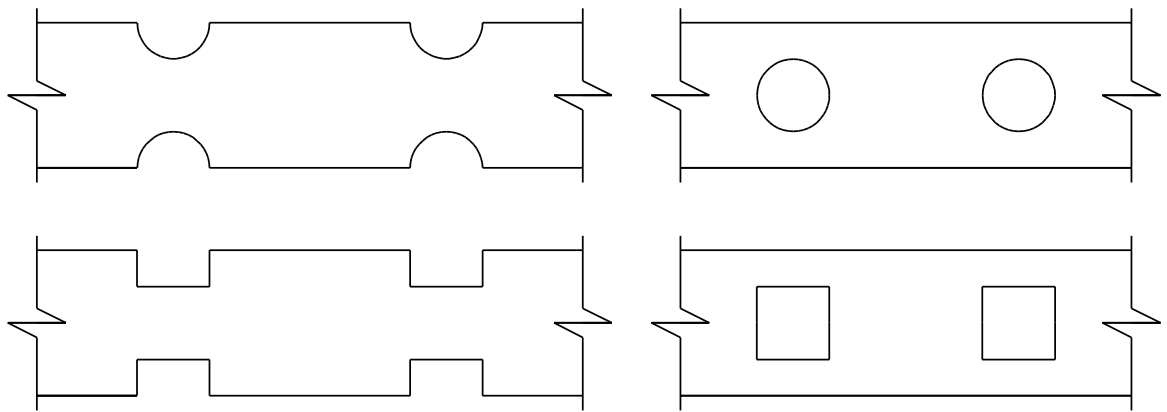


Figure 6-2: Plan view of potential MR-FREI designs.

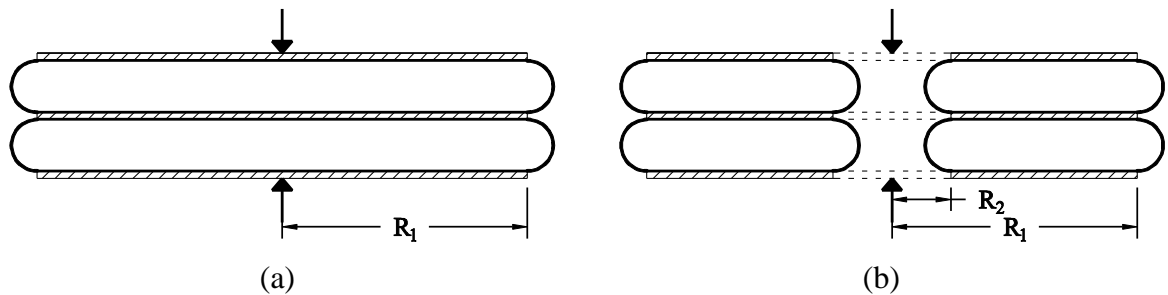


Figure 6-3: Profile view of the lateral bulging of (a) a circular isolator and (b) an annular isolator.

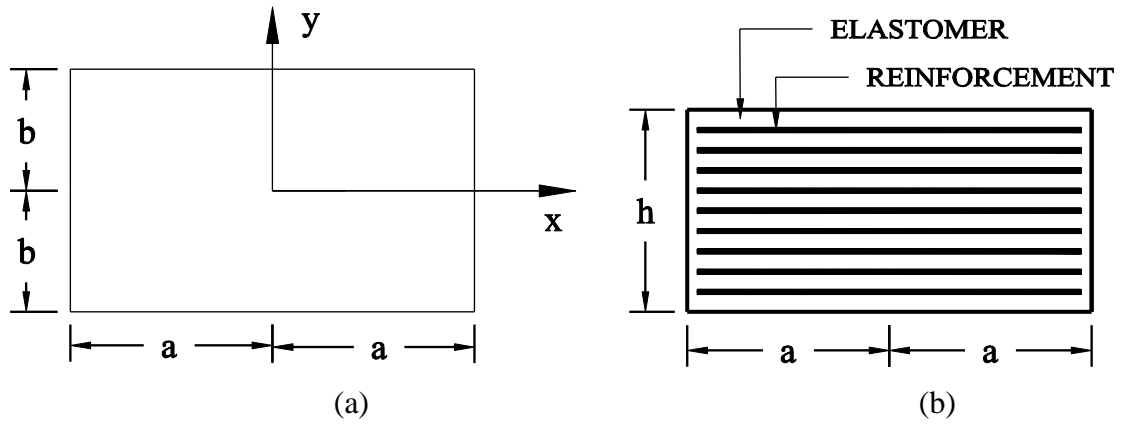


Figure 6-4: (a) Plan and (b) profile view of a FREI.

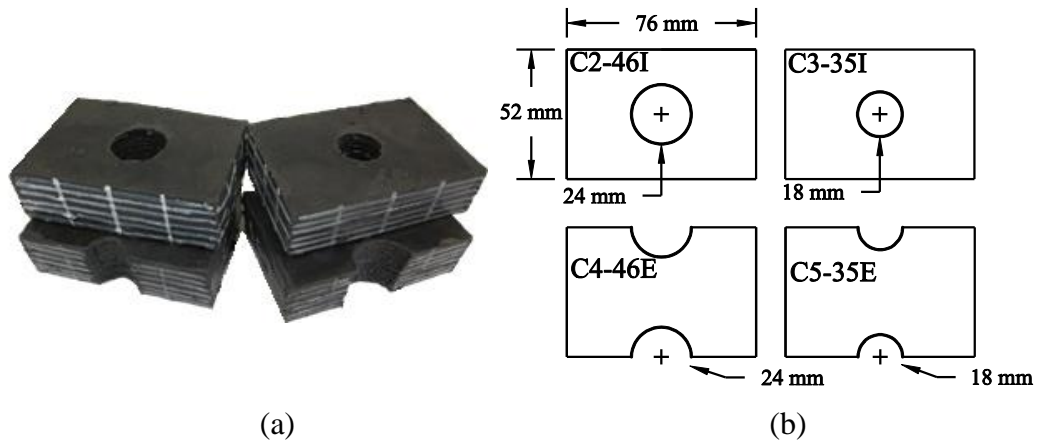


Figure 6-5: (a) Photograph and (b) plan view of the specimens.

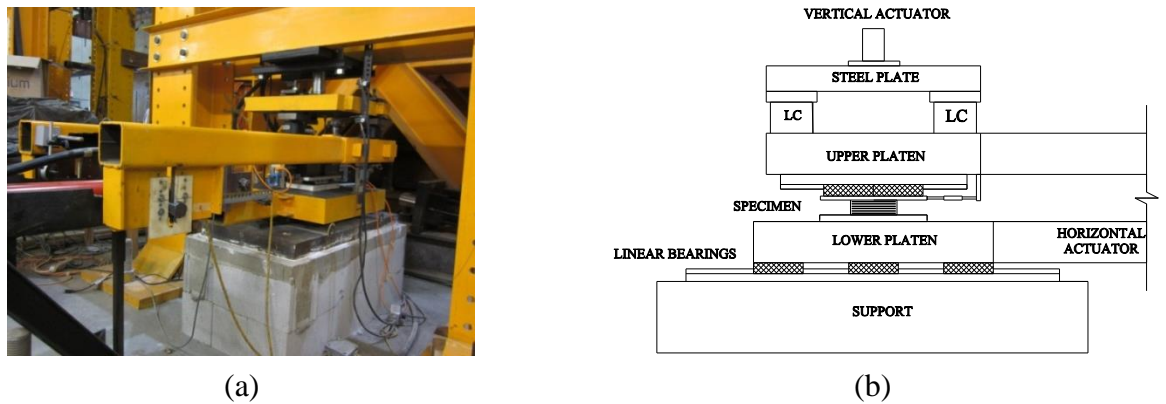


Figure 6-6: (a) Photograph of the test apparatus and (b) schematic.

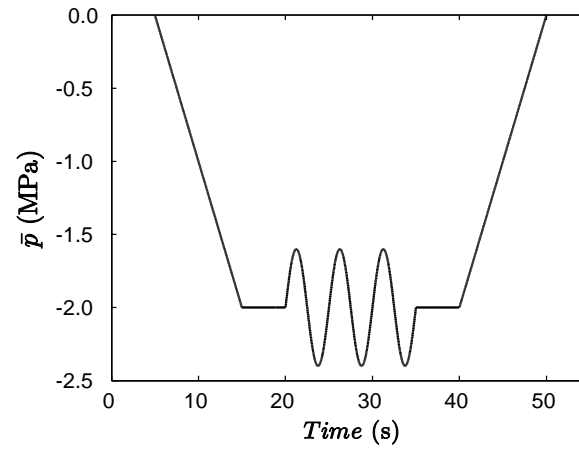


Figure 6-7: Compression test time history for an unmodified isolator.

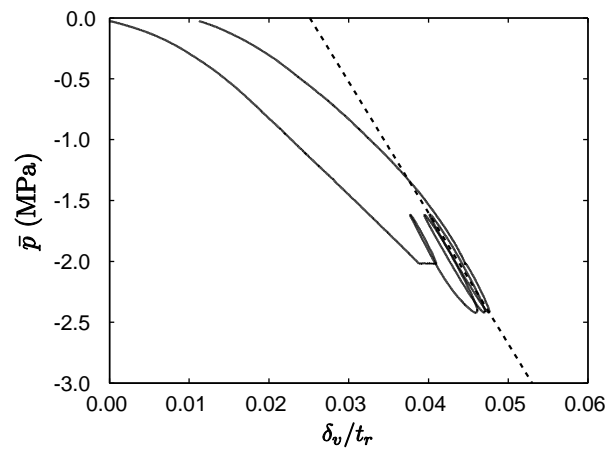


Figure 6-8: Unmodified specimen C2 experimental results showing the compression modulus determined from the third cycle.

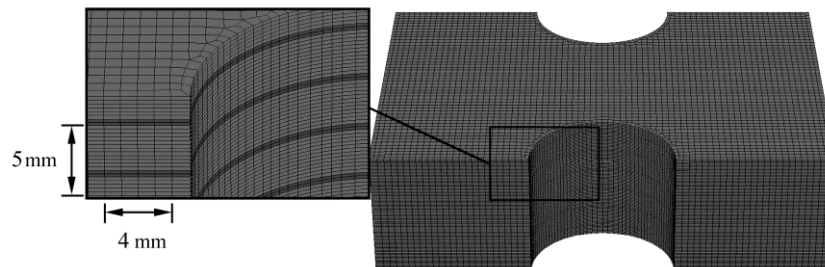


Figure 6-9: FE model of C4-46E.

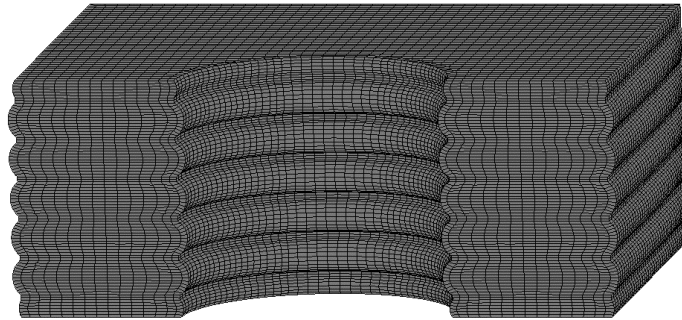


Figure 6-10: Deformed shape cross section of C2-35C at the design load.

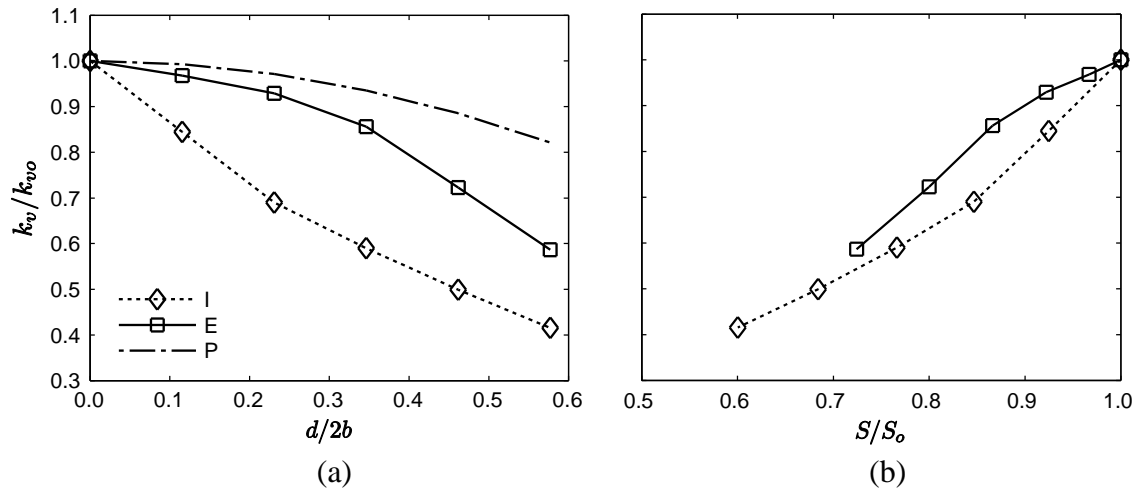


Figure 6-11: Normalized vertical stiffness as a function of (a) diameter and (b) shape factor.

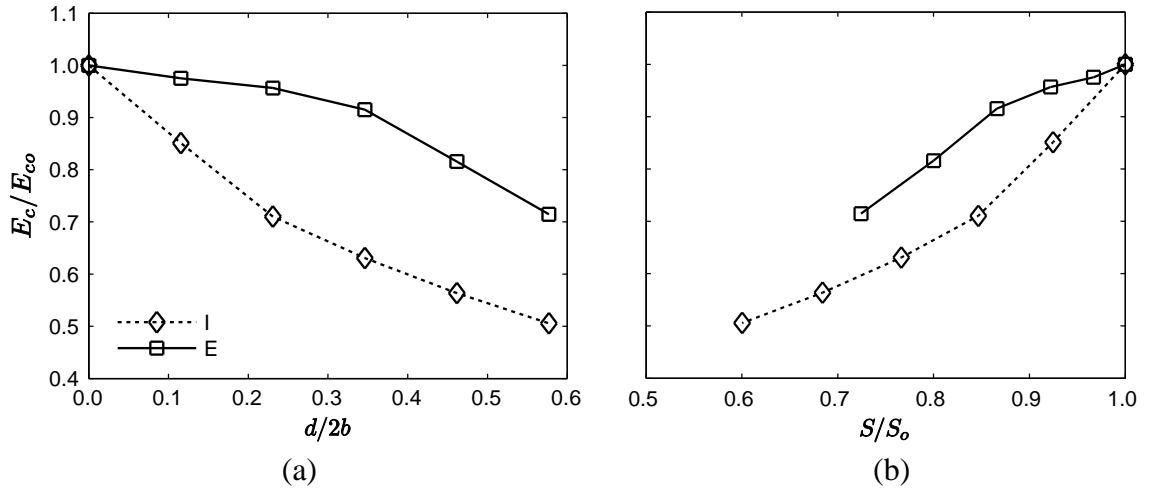


Figure 6-12: Normalized compression modulus as a function of (a) normalized diameter and (b) normalized shape factor.

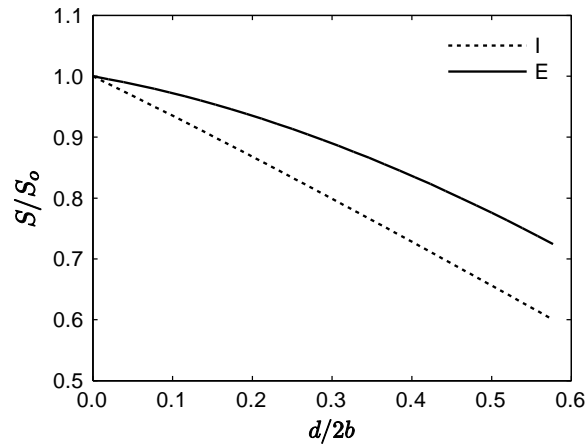


Figure 6-13: Normalized shape factor as a function of normalized diameter.

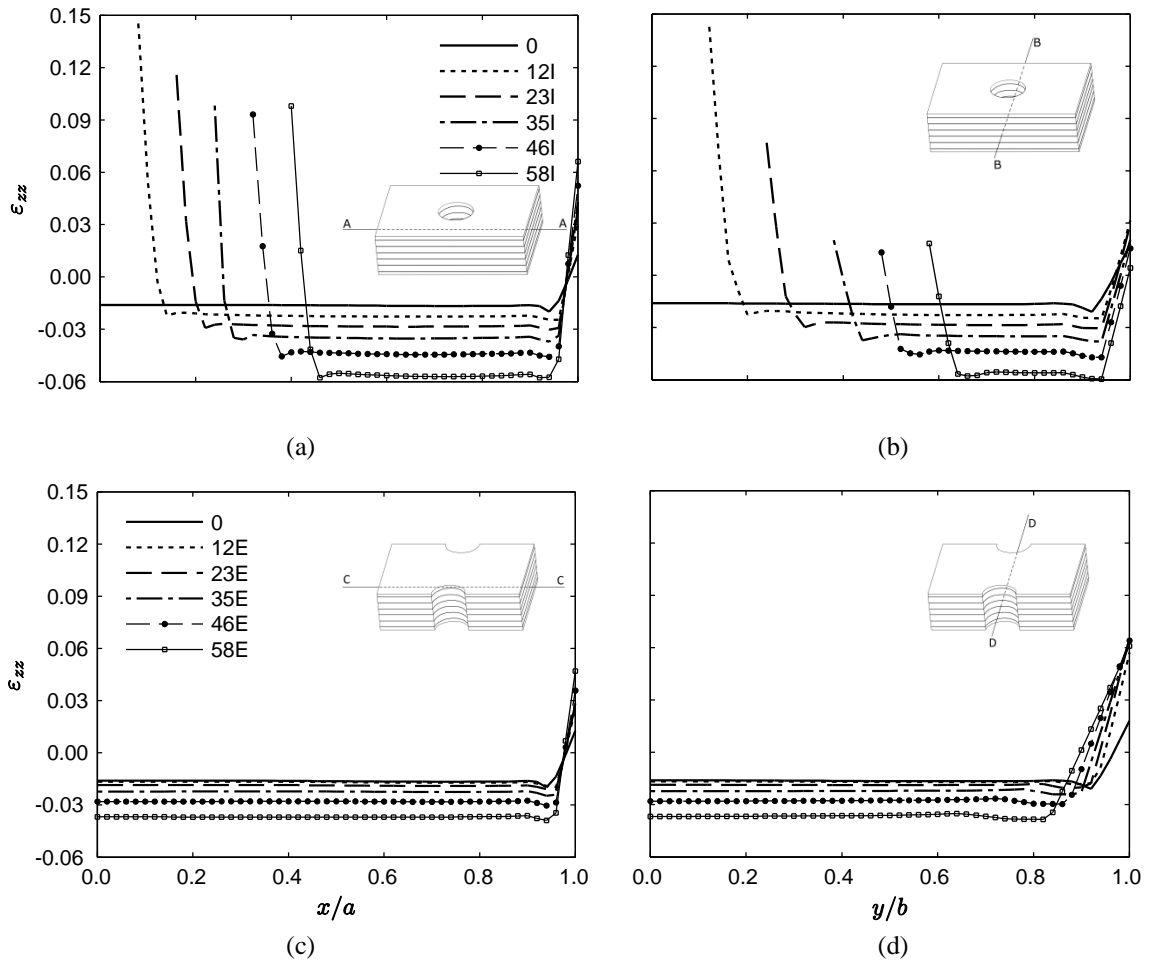


Figure 6-14: Vertical strain distribution along the respective segments at the center of the mid-height elastomer layer.

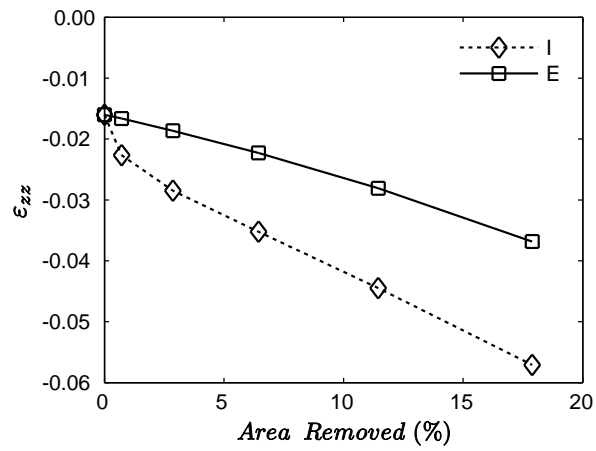


Figure 6-15: Average vertical strain as a function of area removed.

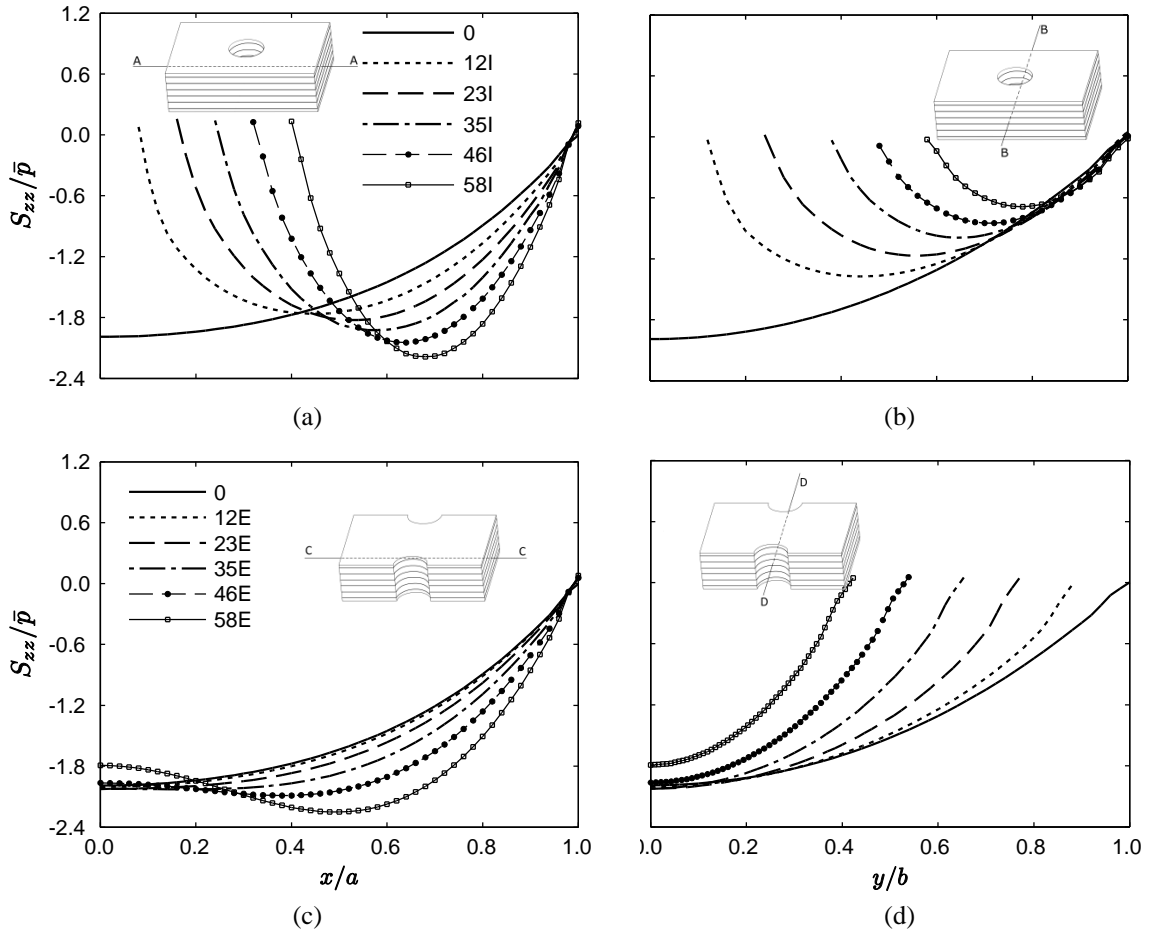


Figure 6-16: Normalized vertical stress distribution along the respective segments at the center of the mid-height elastomer layer.

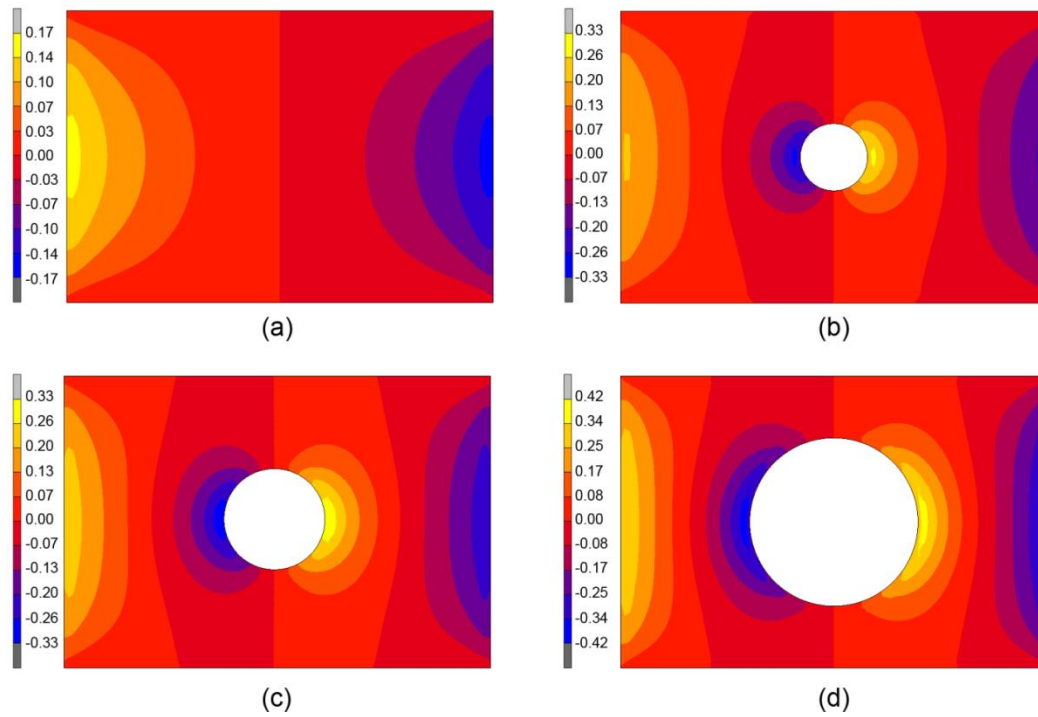


Figure 6-17: Normalized  $S_{xz}$  shear stress contours at the interface of the center elastomeric layer and fiber reinforcement for isolators with interior modification diameter  $d/2b =$  a) 0 , b) 0.23, c) 0.35 and d) 0.58.

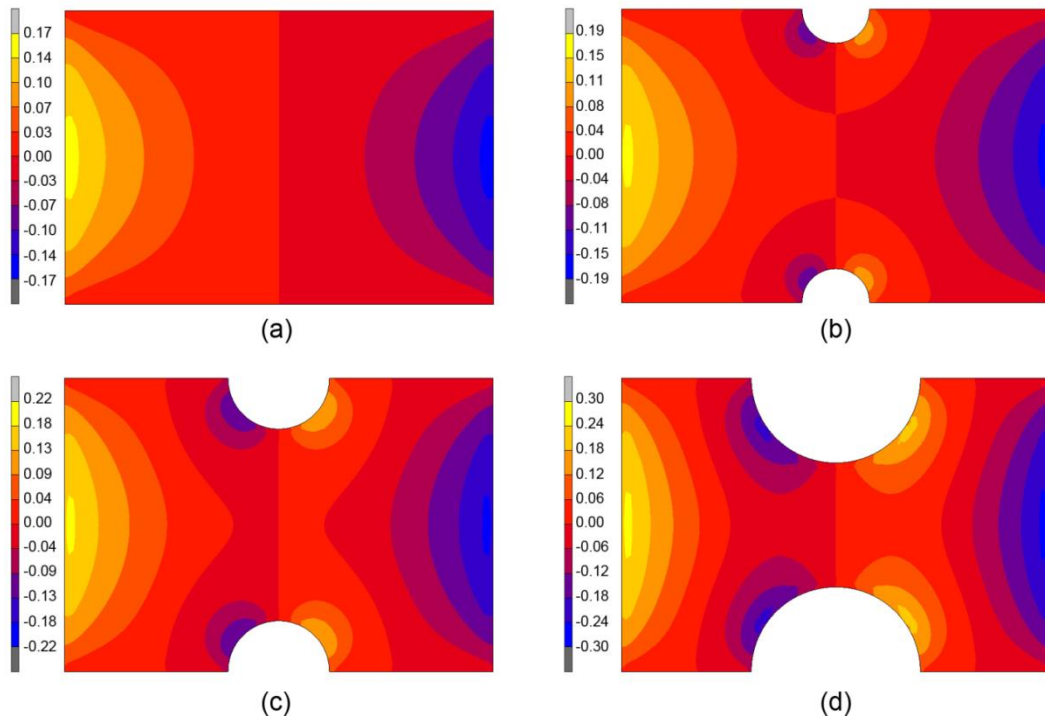


Figure 6-18: Normalized  $S_{xz}$  shear stress contours at the interface of the center elastomeric layer and fiber reinforcement for isolators with exterior modification diameter  $d/2b =$  a) 0 , b) 0.23, c) 0.35 and d) 0.58.

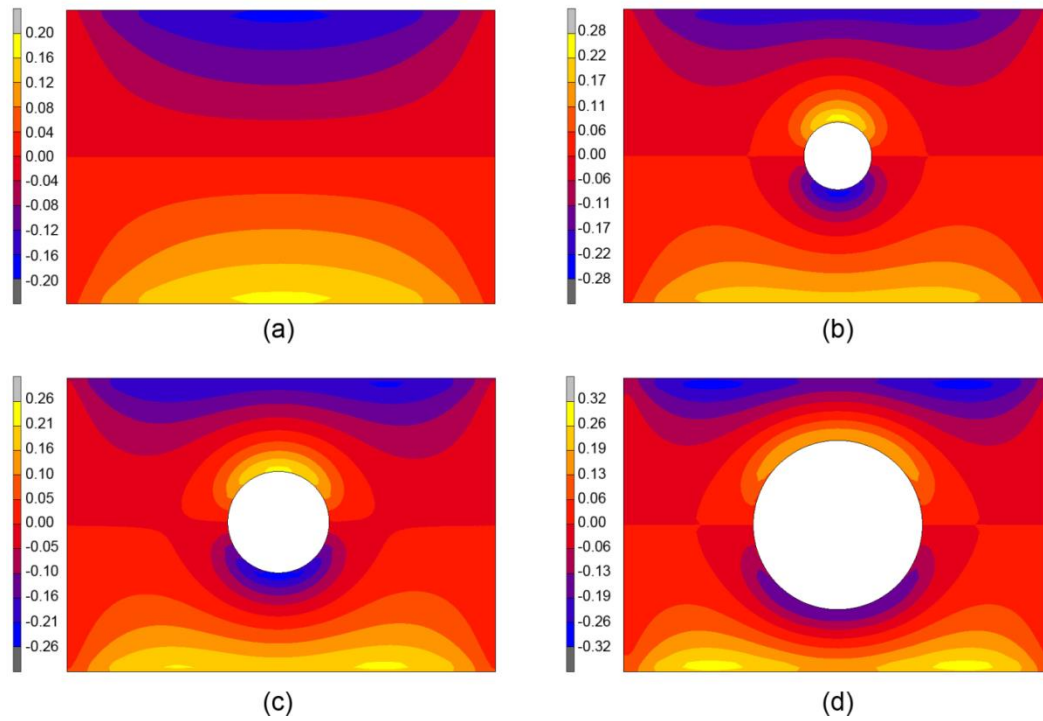


Figure 6-19: Normalized  $S_{yz}$  shear stress contours at the interface of the center elastomeric layer and fiber reinforcement for isolators with interior modification diameter  $d/2b =$  a) 0, b) 0.23, c) 0.35 and d) 0.58.

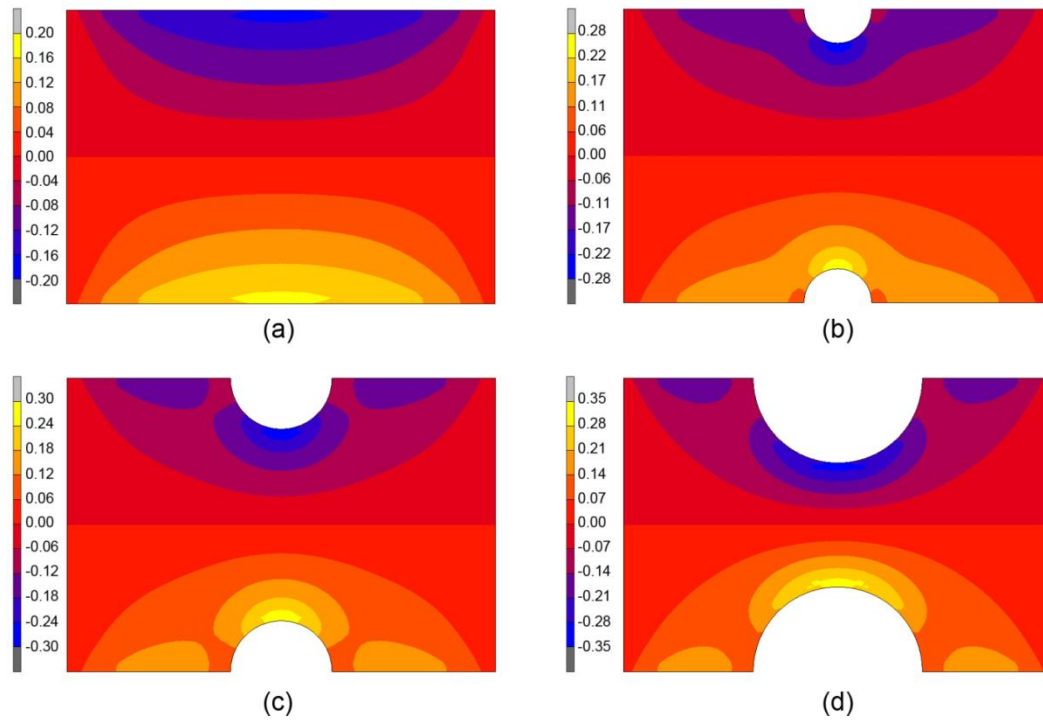


Figure 6-20: Normalized  $S_{yz}$  shear stress contours at the interface of the center elastomeric layer and fiber reinforcement for isolators with exterior modification diameter  $d/2b =$  a) 0 , b) 0.23, c) 0.35 and d) 0.58.

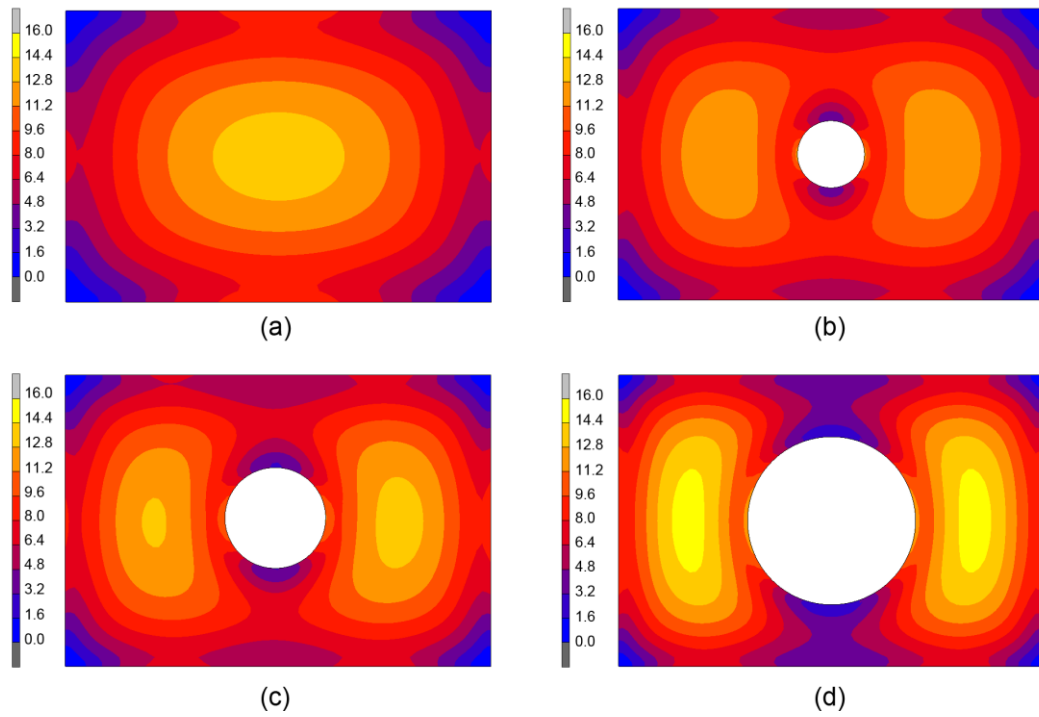


Figure 6-21: Normalized Von Mises stress contours in center fiber reinforcement layers for isolators with interior modification diameter of  $d/2b =$  a) 0 , b) 0.23, c) 0.35 and d) 0.58.

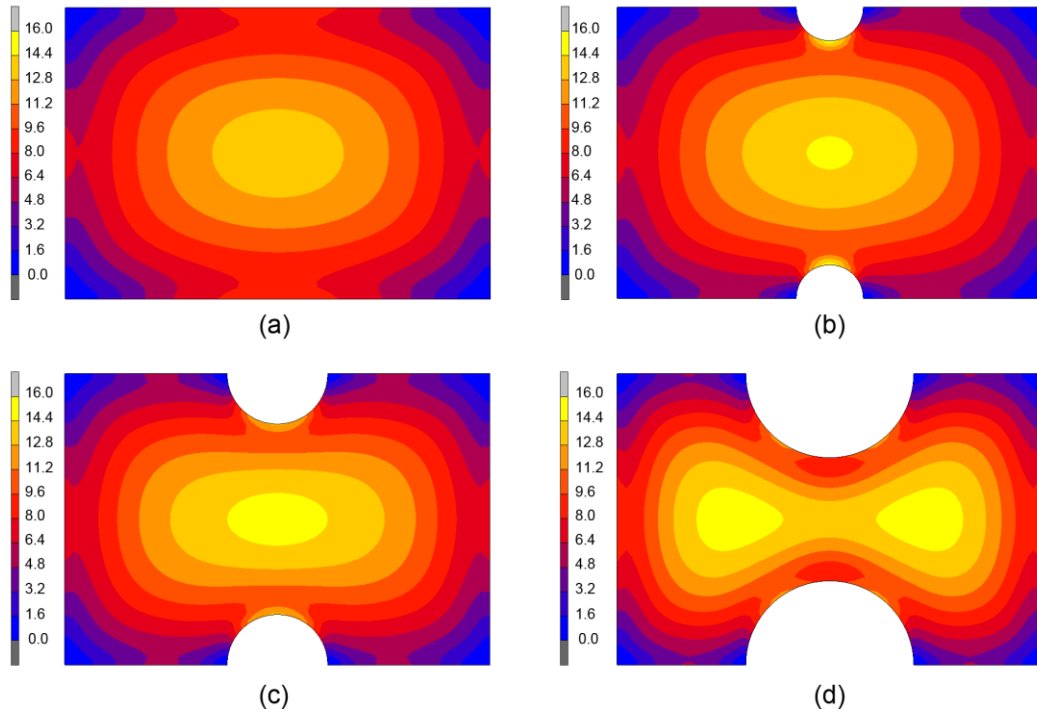


Figure 6-22: Normalized Von Mises stress contours in center fiber reinforcement layers for isolators with exterior modification diameter of  $d/2b =$  a) 0 , b) 0.23, c) 0.35 and d) 0.58.

## **7 Structural and non-structural performance of a seismically isolated building using stable unbonded fiber-reinforced elastomeric isolators**

Reproduced with permission from Elsevier.

Van Engelen NC, Konstantinidis D, Tait MJ. 2015. Structural and non-structural performance of a seismically isolated building using stable unbonded fiber-reinforced elastomeric isolators. *Earthquake Engineering and Structural Dynamics*.

### *Summary*

Stable unbonded fiber-reinforced elastomeric isolators (SU-FREIs) exhibit a characteristic horizontal softening and stiffening response, similar to other adaptive devices such as the triple friction pendulum and sliding systems with variable curvature. The transition between the softening and stiffening occurs at a displacement corresponding to a unique deformation known as *full rollover*. In this paper, the full rollover displacement of SU-FREIs is altered by using modified support geometry (MSG), a geometric modification of the upper and lower supports applied to tailor the hysteresis loops of the isolator. Experimental results are used to calibrate a numerical model of a base isolated structure. The model demonstrates that the stiffening regime provides minimal restraint against displacements during events that meet or exceed the maximum considered earthquake. A parametric study revealed that the level of stiffening required to restrain displacements during large events is significant. This increase in stiffness is reflected in an increase in the response of the structure and light non-structural components. Full rollover and MSG is considered advantageous to maintain horizontal stability and provide control over the stiffening of SU-FREIs.

### *7.1 Introduction*

Fiber-reinforced elastomeric isolators (FREIs) have been introduced as a potential low-cost alternative to conventional steel-reinforced elastomeric isolators (SREIs) [1]. Low-cost isolation systems are pertinent to the seismic protection of structures in developing countries where the devastation due to earthquakes is often more severe; but, are also desirable to encourage economical widespread base isolation application in developed countries. The concept of FREIs is based on the premise that the steel reinforcement, which requires a costly manufacturing process and produces a heavy bearing, can be replaced with lighter fiber reinforcement that has similar mechanical properties in tension, thereby retaining a large vertical stiffness.

A key component of the low-cost concept is the positioning of the bearing unbonded between the upper and lower supports. SREIs often require thick steel end

plates to mechanically fasten the bearing to the upper and lower supports. The removal of these plates further reduces the cost and weight of the bearing. The unbonded application has also been found to reduce the stress demand on the elastomer and fiber reinforcement in comparison to an identical bonded FREI through finite element analysis [2]. In a bonded isolator, large horizontal displacements develop an unbalanced moment that is equilibrated by the development of tensile stresses in the triangular end sections protruding beyond the overlap of the top and bottom supports, as illustrated in Figure 7-1a. In an unbonded application, the triangular sections of the bearing lose contact with the supports, as illustrated in Figure 7-1b, mitigating the development of large tensile stresses. In this case, the unbalanced moment is equilibrated by a resisting couple caused by the offset of the vertical force resultants on the top and bottom surfaces [3].

The unbonded application, combined with certain FREI designs, results in a nonlinear horizontal force-displacement relationship characterized by a softening regime and a subsequent stiffening regime [4]. Unbonded FREIs that maintain a positive tangential stiffness throughout all levels of imposed displacement are horizontally stable and denoted as *stable-unbonded* FREIs (SU-FREIs) [5]. Similar adaptive characteristics can be achieved with rubber isolators with strain induced crystallization [6], the triple friction pendulum [7-9] and sliding systems with variable curvature [10, 11]. The softening regime increases the efficiency of the isolation system by shifting the fundamental period further out of the critical high-energy range of a typical earthquake event; whereas, the stiffening regime is believed to behave as a self-restraint against excessive displacements at events that meet or exceed the maximum considered earthquake (MCE) [6, 7, 10, 12, 13].

Quantification of the non-structural components and systems (NCS) response has not received as much attention as the isolation system or structure. The effect of different seismic isolation systems on the performance of attached equipment that behaves like viscously damped linear oscillators has been studied at various levels in [6, 14-21]. Recently, full-scale physical testing programs were undertaken to investigate the system-level performance of NCS in base-isolated buildings. Shake table tests of a full-scale, four-story, base-isolated reinforced-concrete specimen representing a medical facility housing a wide variety of NCS, including furniture and medical equipment, were carried out by the Nakashima group [22-24]. Furukawa et al. [23] studied the effects of vertical motion on the structure and its contents, while Shi et al. [24] focused on the seismic performance of the contents.

In this paper, the sensitivity of a base isolated structure and the NCS to modified support geometry (MSG) is investigated. MSG uses the surrounding support conditions, in lieu of modifying the isolator, to tailor the shape of the hysteresis loops. MSG can be used to accelerate or delay the stiffening regime of SU-FREIs without affecting the

softening regime. An element was developed in OpenSees [25] and calibrated to the experimental results of a SU-FREI with MSG. A set of 14 ground motions was considered and scaled to hazard levels that fall between the service level earthquake (SLE) and hazard levels that exceed the MCE to investigate the effect of the softening and stiffening regimes. The performance was evaluated based on the response of the structure, as well as the NCS, represented by light attached equipment and unanchored equipment vulnerable to sliding.

## 7.2 *SU-FREIS and MSG*

The softening and stiffening characteristics of SU-FREIs occur due to the lack of flexural rigidity of the fiber reinforcement and the unbonded application. As relative displacement occurs between the upper and lower supports, the ends of the isolator lose contact with the supports through a unique deformation denoted as *rollover*. This process continues until *full rollover*, when the initially vertical faces become horizontal and contact the supports. It is convenient to analyze an unbonded FREI in three sections: a central section and two equivalent rollover sections (see Figure 7-1b). The size of the rollover section is proportional to the horizontal displacement [26], while the horizontal resistance of the rollover section is less than an equivalent volume in simple shear [27]. Consequently, as the horizontal displacement increases, the size of the rollover sections increases and the central section decreases; horizontally softening the isolator. Full rollover restricts additional rollover and causes the horizontal response to stiffen. The retention of a positive tangential stiffness (i.e. horizontal stability) has been determined analytically and demonstrated experimentally to be dependent on the width-to-total height aspect ratio. Horizontal stability can be achieved at a width-to-total height aspect ratio of about 2.5 and greater, depending on the layer design [4, 27-29]. The full rollover displacement has analytically been shown to be a function of the layer design of the bearing and independent of the width-to-total height aspect ratio [26, 27]. Thus, full rollover and the concept of MSG are largely dependent on geometric properties, which can be controlled to a high accuracy.

Tait et al. [30] first proposed that the stiffening regime of a SU-FREI could be modified by either altering the geometry of the bearing rollover surfaces, or by modifying the contact surfaces of the supports. A proof-of-concept experimental study [30] identified that the latter approach could be used to accelerate or delay full rollover, effectively shifting the stiffening regime without altering the softening regime up to full rollover. Notably, the study demonstrated that the softening regime could be extended while still maintaining horizontal stability. It was suggested that MSG could be used as an additional design parameter to configure the stiffening regime based on the geometric

characteristics of the isolator and the upper and lower supports. Figure 7-2 illustrates MSG that will accelerate or delay full rollover.

### 7.3 Predicting Full Rollover

Kelly and Konstantinidis [26] analytically predicted the full rollover displacement of unbonded steel-reinforced elastomeric bridge bearings. Van Engelen et al. [27] developed an analytical model to predict full rollover and the horizontal force-displacement relationship including rollover and full rollover based on large deflection theory. The procedure used by Kelly and Konstantinidis [26] is expanded herein to determine an approximation of the full rollover displacement for SU-FREIs with MSG independent of the material properties. It is assumed that the elastomer is incompressible, the reinforcement is completely flexible, and the length of the curved arc of the rollover section is equal to the horizontal displacement,  $u$ . Initially the thickness of the reinforcement is neglected, and the bearing is assumed to have a unit height. The curved free surface of the rollover section is assumed to follow a parabolic arc:

$$y = 1 - \frac{x^2}{a^2} \quad (7-1)$$

where  $a$  is the length of the horizontal surface at  $y = 0$  and  $x$  and  $y$  are the Cartesian coordinates of the respective surface, illustrated in Figure 7-3. The MSG is assumed as a linear surface:

$$y = m_c x \quad (7-2)$$

where  $m_c$  is the slope of the MSG. For small values,  $m_c$  is approximately equal to the angle of the MSG with the horizontal plane.

The area enclosed within the rollover section,  $A_r$ , is:

$$A_r = \int_0^{a_o} \left( 1 - \frac{x^2}{a^2} - m_c x \right) dx = a_o - \frac{m_c a_o^2}{2} - \frac{a_o^3}{3a^2} \quad (7-3)$$

where  $a_o$  is the  $x$  coordinate of the point of intersection of the parabolic curve and the MSG (see Figure 7-3). Equation (7-1) and (7-2) evaluated at  $x = a_o$  give:

$$a_o = \frac{a^2}{2} \left( -m_c + \sqrt{m_c^2 + \frac{4}{a^2}} \right) \quad (7-4)$$

The curved arc length, which is equal to the horizontal displacement, is:

$$u = \int_0^{a_o} \sqrt{1 + \left( \frac{2x}{a^2} \right)^2} dx \quad (7-5)$$

Following Kelly and Konstantinidis [26], a change of variables is introduced,  $s = 2x/a^2$  :

$$u = \frac{a^2}{2} \int_0^{2a_o/a^2} \sqrt{1 + s^2} ds \quad (7-6)$$

and again with  $s = \sinh t$ :

$$u = \frac{a^2}{2} \int_0^{\sinh^{-1}(2a_o/a^2)} \cosh^2 t dt \quad (7-7)$$

Evaluating the integral yields:

$$u = \frac{a^2}{4} \left[ \frac{2a_o}{a^2} \sqrt{1 + \left(\frac{2a_o}{a^2}\right)^2} + \sinh^{-1}\left(\frac{2a_o}{a^2}\right) \right] \quad (7-8)$$

The condition of incompressibility requires  $A_r = u/2$ ; therefore,  $a$  can be solved using Eq. (7-3) and Eq. (7-8). Figure 7-4 shows  $u$ ,  $a$ , and  $a_o$  over the range of  $-0.3 \leq m_c \leq 0.3$ . Over this range of  $m_c$ , the value of  $u$  varies between 2.12 and 1.31, while for unmodified supports (i.e.,  $m_c = 0$ )  $u = 1.67$ . To correct for the thickness of the reinforcement,  $u$  is increased by the ratio of the total height to the total thickness of the elastomeric layers. The maximum level of MSG that accelerates full rollover is limited to prevent impact of the upper and lower supports, whereas MSG that delays full rollover is limited by the requirement of horizontal stability, which was not considered in this derivation.

#### 7.4 Experimental Program

A SU-FREI bearing with MSG that accelerates (A-MSG), delays (D-MSG) or leaves rollover unaltered (i.e., unmodified support geometry (USG)) was considered. The quarter-scale specimen was comprised of seven layers of Neoprene with a shear modulus of  $G = 0.43$  MPa and reinforced with plain weave bi-directional carbon fiber. The total height of the specimen was 22.35 mm and the total thickness of the elastomeric layers,  $t_r$ , was 19.05 mm. The specimen was cut from a larger pad to a length of 52 mm and a width of 76 mm and had a shape factor of 4.9.

In order to mitigate the influence of the Mullins effect and to provide a more direct comparison between the different levels of MSG, the specimen was initially cycled horizontally before conducting the experiments for this study. The experimental tests were conducted with horizontal displacement control and vertical load control. A schematic of the experimental apparatus is shown in Figure 7-5. The vertical load was measured with three load cells, and the vertical displacement was measured with four laser transducers. The horizontal load was measured directly with a single load cell, and the displacement was measured with a string potentiometer. The specimen was placed unbonded between two level steel plates and monotonically loaded to an average vertical compressive stress of 2.0 MPa. Three sinusoidal cycles were conducted at each of the seven horizontal displacement amplitudes in ascending order: 0.25, 0.50, 0.75, 1.00, 1.50, 2.00 and 2.50  $t_r$ . The specimen was then monotonically unloaded, removed from the apparatus and visually inspected for damage.

The MSG was constructed using steel plates that were machined to the desired slope of  $m_c = \pm 0.2$ , corresponding to an expected full rollover displacement of 1.67, 1.96 and 2.30  $t_r$  for A-MSG, USG and D-MSG, respectively. Note that these values have been corrected for the thickness of the reinforcement. The MSG plates were bolted to the upper and lower steel plate supports; for USG, additional steel plates were not required. The use of steel plates to create the MSG was convenient for adaptability of the experimental apparatus; although, in other applications, the MSG could be built on site by concrete formwork or by other means.

The effective horizontal stiffness,  $k_{eff}$ , was calculated as:

$$k_{eff} = \frac{F_{max} - F_{min}}{u_{max} - u_{min}} \quad (7-9)$$

where  $F_{max}$ ,  $F_{min}$  and  $u_{max}$ ,  $u_{min}$  are the maximum and minimum force and displacement over each cycle, respectively. The equivalent viscous damping,  $\zeta_{eff}$ , was calculated as:

$$\zeta_{eff} = \frac{W_d}{2\pi k_{eff} u_{ave}^2} \quad (7-10)$$

where  $W_d$  is the area contained within the hysteresis loops and  $u_{ave} = (u_{max} + |u_{min}|)/2$ .

The normalized force-displacement hysteresis loops from the third cycle for the three levels of MSG are compared in Figure 7-6; the horizontal restoring force,  $F$ , has been normalized by  $G$  and the plan area,  $A$ . The associated values of  $k_{eff}$  and  $\zeta_{eff}$  are provided in Table 7-1. The hysteresis loops were consistent at smaller amplitudes since the MSG only affects full rollover and has no influence on the softening regime. The deformed shape of the isolator at 1.50, 2.00 and 2.50  $t_r$  with various levels of MSG is shown in Figure 7-7. Note that D-MSG was created with a recession in the steel plate which is not visible in the figure. Over the 1.50  $t_r$  cycle, the A-MSG began to stiffen in comparison to the USG and D-MSG, and significant stiffening was observed over the 2.00  $t_r$  cycle. Stiffening began over the 2.00  $t_r$  cycle and 2.50  $t_r$  cycle for the USG and D-MSG, respectively (see Table 7-1). The observed stiffening corresponds well with the predicted full rollover displacements, 1.67, 1.96 and 2.30  $t_r$ . Note that the exact full rollover displacement cannot be determined from the hysteresis loops due to the desirable smooth transition that occurs between the softening and stiffening regimes. The ratios of the effective horizontal stiffness,  $k_{eff}$ , at both the 2.00 and 2.50  $t_r$  cycles were approximately  $k_{eff}^{A-MSG} / k_{eff}^{USG} = 1.34$  and  $k_{eff}^{D-MSG} / k_{eff}^{USG} = 0.75$ , indicating that the effective horizontal stiffness was more sensitive to A-MSG. The equivalent viscous damping generally decreased with increasing displacement amplitude and remained above 10 % with the exception of the A-MSG and USG cases at the 2.00  $t_r$  and 2.50  $t_r$  cycles.

## 7.5 Model and Methodology

### 7.5.1 Structure and Equipment

The analysis was conducted using OpenSees [25] in two dimensions. The single bay, two storey prototype planar frame was selected from a previous experimental investigation on unbonded FREIs [32]. The total weight of the planar frame, illustrated schematically in Figure 7-8, was distributed equally over the six nodes, including the isolation layer. The beams and columns were represented using elastic beam column elements and were assumed to be axially rigid. The inherent equivalent viscous damping of the structure was assumed to be 2 % and was applied to the structure using initial stiffness proportional damping. Initial stiffness proportional damping, rather than the commonly applied Rayleigh damping, avoided exaggerated damping in the low frequency first mode [33, 34]. The fixed-base fundamental period of the full scale model was determined to be 0.21 s. As the experimental tests were conducted under constant vertical load with level plates and no rotation, the rotation and vertical degrees of freedom at the isolators were held fixed and these effects were not considered in the model. The analysis was conducted in quarter scale consistent with the experimental results and planar frame; the results are presented in full scale.

The sliding and attached equipment was assumed to be light, and, under this assumption, the dynamic interaction between the structure and the equipment was neglected [35, 36]. Light sliding and attached equipment was positioned at level three of the structure. The sliding equipment was modelled using a Flat Slider Bearing Element, presented in Schellenberg et al. [37], with a Coulomb friction model having a coefficient of friction of  $\mu = 0.025, 0.05$  and  $0.1$ . The response of light attached equipment was evaluated on the basis of the mean floor spectral accelerations with frequencies greater than 2.00 Hz considered to be the primary range of interest [6].

### 7.5.2 SU-FREIs

Love et al. [38] numerically modelled a base isolated structure with SU-FREIs and a tuned liquid damper calibrated from experimental results. The SU-FREIs were represented by adapting the Bouc-Wen model from Chen and Ahmadi [39] with a fifth order polynomial to better represent the softening and stiffening regimes. In the model, the horizontal restoring force was proportional to a higher order of the hysteretic parameter,  $z$ , and both hysteretic and viscous damping were included.

The model used herein is derived from the traditional Bouc-Wen model, based on an initial,  $k_i$ , and post-yield stiffness. The horizontal restoring force is:

$$F = \alpha k_i u + (1 - \alpha) u_y k_y z \quad (7-11)$$

where  $u_y$  is the yield displacement, and  $\alpha$  is the ratio of the post-yield stiffness to initial stiffness. The hysteretic parameter is determined from the differential equation:

$$\dot{z} = \frac{\dot{u}}{u_y} \{A - [\beta \text{sgn}(z\dot{u}) + \gamma] |z|^n\} \quad (7-12)$$

where  $A$ ,  $\beta$ ,  $\gamma$  and  $n$  are dimensionless quantities that control the shape of the hysteresis and  $\text{sgn}$  is the sign function.

Adapting this model with the inclusion of a fifth order polynomial results in the loss of the physical interpretations associated with the yield and post-yield stiffness (i.e. the relationship between  $k_i$ ,  $\alpha$ ,  $u_y$  is lost). Accordingly, the restoring force becomes:

$$F = a_1 u + a_2 |u|u + a_3 u^3 + a_4 |u|u^3 + a_5 u^5 + Bz \quad (7-13)$$

with

$$\dot{z} = \frac{\dot{u}}{Y} \{A - [\beta \text{sgn}(z\dot{u}) + \gamma] |z|^n\} \quad (7-14)$$

where  $Y$  replaces  $u_y$  and  $B$  absorbs the coefficients of  $z$  in Eq. (7-11). It should be noted that the model used herein assumes only hysteretic damping; although, viscous damping could also be included.

A comprehensive model for SU-FREIs including damping, rollover, full rollover, MSG and other effects, has not been developed; thus, the model needs to be calibrated based on experimental results. A best-fit procedure minimizing the squared residuals over the third cycle of the experimental results was used to determine the model parameters for each level of MSG (e.g., A-MSG, USG, and D-MSG). Note that the isolator softens over successive cycles due to the Mullins effect, thus the model calibration should be considered a lower-bound. An upper-bound analysis taking into account aging effects in the Neoprene is beyond the scope of this study. The Bouc-Wen model and experimental third cycle hysteresis loops are compared in Figure 7-9, and Table 7-2 compares the ratio of the model and experimental effective horizontal stiffness,  $k_{eff}$ , and equivalent viscous damping,  $\zeta_{eff}$ , over each cycle. The model properties are in almost all cases within 10 % of the experimental results with the notable exceptions of the lowest displacement amplitude,  $0.25 t_r$ , and largest displacement amplitude,  $2.50 t_r$ . By calibrating the model to all cycle amplitudes, the necessity for an iterative procedure that has been used in other numerical SU-FREI studies [32, 40] was avoided. Since shear displacement demands on an isolation system are generally substantially larger than  $0.25 t_r$ , even at the SLE hazard level, and that the peak values are of primary interest, the Bouc-Wen model was deemed appropriate to capture the performance of SU-FREIs with MSG for this study. Although, it was noted that the peak displacement may be increased in comparison to what would be expected from experimental results due to the lower modelled damping over the  $2.50 t_r$  cycle.

### 7.5.3 Earthquakes and Scaling

The response of the structure was investigated based on a set of 14 fault-normal broadband ground motions. The ground motions were selected at random from the

standardized set of broadband ground motions on rock provided in Baker et al. [41]. The ground motion records were scaled to a design spectrum [42] for Victoria City Hall, Canada, assuming all site class factors of unity, and a 2% probability of exceedance over 50 years [43]. The scaling was conducted to minimize the squared residuals over the period range of  $0.5T_M$  to  $1.25T_M$  for each record, where  $T_M = 1.74$  s is the effective period at the MCE hazard level determined according to ASCE 7-10 [42] for a base isolated structure. This period corresponds to an isolator displacement of  $u/t_r = 1.82$ . The values of  $k_{eff}$  and  $\zeta_{eff}$  were selected from the third cycle of the USG experimental values with linear interpolation between displacement amplitudes. The selected records are listed in Table 7-3 and the displacement,  $D$ , and pseudo-acceleration,  $S_a$ , response spectra are provided in Figure 7-10. In order to provide a direct comparison, the scaling was not changed between different levels of MSG. The SLE and design basis earthquake (DBE) hazard levels were determined as 1/3 MCE and 2/3 MCE, respectively. The MCE level was used as the baseline, and the records were further scaled from 0.4 MCE to 1.2 MCE in increments of 0.2 MCE to investigate the softening and stiffening regimes of the response.

## 7.6 Results

### 7.6.1 Structure

The normalized mean peak isolator displacement,  $u/t_r$ , and base shear through the isolation layer,  $V_b$ , normalized by the total weight of the base isolated structure,  $W$ , as a function of the hazard level are shown in Figure 7-11. The peak isolator displacement increases nearly linearly with increasing hazard level. The hysteresis loops of the USG and two types of MSG primarily deviate beginning at  $1.50 t_r$ , which is approached at 0.8 MCE and exceeded at the MCE level and greater. At low hazard levels, below the DBE, the systems performed consistently with respect to the mean peak values of  $u/t_r$  and  $V_b/W$  with little variation. At hazard levels exceeding the DBE, the systems deviate with respect to the mean peak  $V_b/W$  values. It was found that the stiffening provided minimal restraint to the isolation system displacements. At 1.2 MCE, the mean peak  $u/t_r$  values were 1.87, 1.89 and 1.89 for A-MSG, USG and D-MSG, respectively; however, the mean peak values of  $V_b/W$  was 0.24, 0.19 and 0.15. Note that  $u^{A-MSG}/u^{USG} = 0.99$ , while  $V_b^{A-MSG}/V_b^{USG} = 1.27$ . Similarly, D-MSG had no appreciable difference to USG with respect to mean peak  $u/t_r$ , but  $V_b^{D-MSG}/V_b^{USG}$  reduced to 0.80. The change in  $V_b$  relative to the USG case corresponded well with the experimentally obtained ratios of the effective horizontal stiffness at 2.00 and 2.50  $t_r$  of approximately 1.34 and 0.75 for A-MSG and D-MSG, respectively.

The mean peak inter-storey drift ratio (IDR) for the first (IDR<sub>12</sub>) and second (IDR<sub>23</sub>) story and mean peak absolute floor acceleration (PFA) at level three of the structure, PFA<sub>3</sub>, are shown in Figure 7-12 and Figure 7-13, respectively. Similar observations can be made as with  $V_b$ . Namely, at higher hazard levels, the A-MSG amplified the response, and the D-MSG reduced the response relative to the USG. At the DBE level, the PFA<sub>3</sub> was 0.15, 0.14, and 0.13 g with A-MSG, USG and D-MSG, respectively. Increasing the hazard level to 1.2 MCE (1.8 DBE) increased, respectively, the PFA<sub>3</sub> to 0.27, 0.21 and 0.17 g, corresponding to an 81, 52 and 30 % increase, respectively. The IDR was low over both storeys of the structure, representative of the structure moving in near rigid motion on-top of the isolation system. Regardless of the low values of the IDR, over the first and second levels of the structure at the 1.2 MCE hazard level  $IDR^{D-MSG}/IDR^{USG} = 0.80$  and  $IDR^{A-MSG}/IDR^{USG} = 1.27$ .

### 7.6.2 Light Equipment

The mean floor pseudo-acceleration response spectra at level 3 for light attached equipment are shown in Figure 7-14. Two dominant peaks can be observed at all hazard levels considered. Note that the range of interest for attached equipment was considered to be frequencies greater than 2.00 Hz. At the SLE, the isolation systems were nearly identical; the two peaks occurred at approximately 0.81 Hz and 7.77 Hz. These frequencies correspond closely to the first and second mode of the base isolated structure determined by initial-stiffness eigenvalue analysis. As the hazard increases to DBE, the PFA increases and there is a slight leftward shift in the first mode (left) peak; representative of the softening in the isolation layer. This leftward shift continues as the hazard level increases and at 1.2 MCE, the largest peak occurred at a frequency of 0.66, 0.65 and 0.63 Hz for the A-MSG, USG and D-MSG, respectively. Within the frequency range of interest for light attached equipment, the peak occurred at approximately 7.69 Hz independent of the MSG. At this frequency, the different levels of MSG amplified the floor acceleration by a factor of 2.15, 2.24 and 2.40 for A-MSG, USG and D-MSG, respectively. These observations suggest that light attached equipment is sensitive to the increase in peak floor acceleration, but is otherwise relatively uninfluenced by the changes in the stiffening regime of the isolator hysteresis due to MSG. This is because, unlike the first mode peak, the second mode peak in a base isolated structure is primarily governed by the superstructure, which in this study was assumed elastic.

The response of the unanchored equipment vulnerable to sliding was evaluated based on mean peak displacement demand,  $U$ , over the different levels of MSG; compared in Figure 7-15. A similar sliding response was observed between the different levels of MSG. An increase in the coefficient of friction, as expected, reduced  $U$ . With  $\mu = 0.1$ , sliding only occurred at hazard levels exceeding 0.6 MCE due to the low floor

accelerations. As the hazard level increased to 1.2 MCE,  $U$  increased to a maximum of 141 mm, 104 mm and 59 mm for the A-MSG, USG and D-MSG, respectively. The increased floor accelerations that developed due to the stiffening regime resulted in an increased duration of sliding, which is related to the peak displacement demand. With  $\mu = 0.025$  and  $\mu = 0.05$ , the low coefficients of friction caused approximately equal durations of sliding, independent of the isolation system, and thus achieved a similar response.

### 7.7 Effect of Stiffening

A parametric study was conducted to investigate the sensitivity of the structure and NCS to changes in the stiffening regime; notably the magnitude of stiffening required to act as an effective displacement restraint. The hysteretic parameters for USG were considered and the changes in the stiffening regime were introduced by modifying the fifth order polynomial coefficients. The model by Van Engelen et al. [27] was used to determine the full rollover displacement and force-displacement relationship prior to full rollover. The post-full rollover force-displacement relationship was selected to provide an effective period of  $T = 0.5, 1.0$  and  $1.5$  s at a displacement of  $2.50 t_r$ , assuming a single degree of freedom system, designated as  $k-1, k-2$ , and  $k-3$ , respectively. Figure 7-16 shows the fifth-order polynomials selected for each case. A total of nine were considered, corresponding to the three stiffness levels and three levels of MSG. A smooth transition, as observed in experimental testing, was allowed between the softening and stiffening regimes. The post-full rollover tangential stiffness of the A-MSG and D-MSG with  $m_c = \pm 0.2$  was selected to equal the USG tangential stiffness. The resulting effective periods at  $u/t_r = 2.50$  are listed in Table 7-4. The primary focus of the parametric study was to investigate the stiffening regime, and only the SLE and hazards greater than 0.6 MCE were considered. The structure, NCS and selected earthquake ground motions were otherwise identical to those previously discussed.

The hysteretic responses obtained for this parametric study do not necessarily reflect achievable SU-FREI designs. Furthermore, the substantial increase in stiffness required to meet the selected effective periods significantly reduces the equivalent viscous damping over the large amplitude cycles. By only modifying the fifth order polynomial, a direct comparison between the stiffness levels can be achieved. The area contained within the loops, represented by the hysteretic parameters of the Bouc-Wen model, is independent of the polynomial if the displacement time history and remaining model parameters are identical.

#### 7.7.1 Structure

The increased post-full rollover stiffness provided minimal displacement restraint, as shown in Figure 7-17. The mean peak isolator displacements at 1.2 MCE are provided in Table 7-5. As the post-full rollover stiffness increases, or full rollover displacement

decreases (accelerated full rollover), the mean peak displacement decreases. At the  $k$ -2 and  $k$ -3 stiffness level, the mean peak displacements were all within 2.1 % of the mean. At the  $k$ -1 stiffness level, accelerating full rollover decreased the mean peak displacement by 3.4 %, whereas delaying full rollover resulted in a 4.4 % increase over the USG case. The difference between the  $k$ -1 A-MSG case and the  $k$ -3 D-MSG case was  $0.20 t_r$ . These decreases in displacement were achieved by a considerable increase in the mean peak  $V_b/W$ ,  $PFA_3$ , and  $IDR_{12}$  (see Figure 7-17). Accelerating full rollover or increasing the post-full rollover stiffness increased the response of the structure. For  $k$ -1 A-MSG at 1.2 MCE,  $V_b/W = 0.94$ ,  $PFA_3 = 1.26$  g and  $IDR_{12} = 0.26$  %. These values represent an increase of 53, 53 and 54 %, respectively, over the  $k$ -1 USG case at the same hazard level.

### 7.7.2 Light Equipment

For attached light equipment, similar observations as previously discussed can be made with respect to the mean floor pseudo-acceleration response spectra, shown in Figure 7-18, for  $k$ -1 at level 3 of the structure. Note that the scale has been increased from Figure 7-14. As previously observed, at the MCE and 1.2 MCE hazard levels the accelerated and delayed full rollover causes a shift in the lowest frequency peak. The peak within the range of interest for light attached equipment remains relatively unaffected by the changes at the isolation layer since it is associated with the stiffness of the superstructure, which was assumed to remain linear elastic. Several additional peaks emerge, most notable in the A-MSG case. At 1.2 MCE, three dominant peaks occur with A-MSG; the third significant peak occurs at 3.31 Hz. The frequency corresponding to the tangential stiffness of  $k$ -1 post-full rollover was 4.17 Hz and a smooth transition was allowed between the softening and stiffening regime. The development of this peak demonstrated that the system response became sensitive to, and operated within, the stiffening regime. The amplification of the peak floor acceleration at approximately 7.81 Hz was 1.88, 2.21 and 2.15 for A-MSG, USG and D-MSG, respectively, showing increased sensitivity to MSG, but overall comparable magnification as the previously discussed results.

The mean peak displacement demand on unanchored light equipment is compared in Figure 7-19 for the three stiffness levels and the three coefficients of friction considered. A reduction in  $U$ , as previously observed, can be achieved by an increase in  $\mu$ . The increase in  $\mu$  also increases the sensitivity to the different levels of MSG, represented by a larger spread between A-MSG and D-MSG. At 1.2 MCE, with  $k$ -1 and  $\mu = 0.025$ , the coefficient of variation of 0.11 increased to 0.28 when  $\mu = 0.1$ . The overall maximum  $U$  occurred with  $k$ -1 and  $\mu = 0.025$  and was 467, 429, and 378 mm for A-MSG, USG and D-MSG, respectively. Reducing the magnitude of the stiffening and increasing  $\mu$  reduced the response, respectively, to 27, 26 and 26 % of the maximum  $U$  for the three levels of MSG. The decrease in response achieved by increasing the coefficient of friction

was greater than the changes due to the post-full rollover stiffness. Similar to changes in the level of MSG, an increase in  $\mu$  also increased the sensitivity to the post-full rollover stiffness. At 1.2 MCE with  $\mu = 0.025$ , changing the stiffness level from  $k-1$  to  $k-3$  decreased  $U$  by a mean of 13 % across the different levels of MSG, and by 56 % with  $\mu = 0.1$ .

### 7.8 Discussion

If the structure is idealized as a single degree of freedom system, the fundamental period, determined from the experimental  $k_{eff}$  of the USG isolation system, is 1.75 s and 1.58 s at  $2.00 t_r$  and  $2.50 t_r$ , respectively. By applying MSG, the fundamental period can vary between 1.37 and 2.02 s at displacements exceeding full rollover, depending on the displacement amplitude and level of MSG. A distinct change occurs in the mean displacement response spectrum at about 1.2 s (see Figure 7-10). Over the range of 1.37 s to 2.02 s, the spectral displacement is relatively constant. Consequently, the isolator displacement increases near-linearly with increasing hazard regardless of the different levels of stiffening generated by the MSG. At the SLE, the mean peak value of  $u/t_r$  was approximately 0.50, which corresponds to a fundamental period of about 1.3 s, depending on the level of MSG. The softening due to rollover from  $0.50 t_r$  to  $2.50 t_r$  similarly did not result in a significant shift in the fundamental period with respect to spectral displacement.

Accelerating full rollover and increasing the full rollover stiffness did reduce the displacements, the parametric study concluded that the magnitude of stiffening required to provide significant displacement restraint was substantial. Note that at large displacements, a large increase in the restoring force is required to substantially increase  $k_{eff}$  and adequately decrease the fundamental period. Consequently, the decrease in displacement was achieved at the expense of a substantial increase in the structure and NCS response, proportional to the change in the post-full rollover stiffness. The structure and NCS response should be carefully reviewed if significant stiffening is introduced. This becomes an impact problem if the tangential stiffness of the stiffening regime becomes very large, analogous to pounding against the seismic gap wall [44, 45]. As is expected, the performance of an adaptive device is dependent on the ground motion characteristics and the ability of the device to shift the fundamental period.

A numerical investigation by Kromodromos [46] considered the application of elastomeric bumpers to provide a smooth transition between the isolation stiffness and the post-impact stiffness. Comparing three cases, an upper and lower seismic gap wall limit, and elastomeric bumpers between the upper and lower seismic gap wall limits (i.e., collision with the elastomeric bumper occurs at the lower limit), it was found that the inclusion of the elastomeric bumper reduced the peak responses compared to the other

two cases. Although this was considered a favourable result, it was noted that a building without bumpers may avoid impact, but by including bumpers, which reduces the seismic gap, impact may occur that otherwise would have been avoided. In this respect, the stiffening regime may also serve to mitigate pounding against the seismic gap wall. If the stiffening regime is sufficient to provide the desirable smooth transition prior to impact, then the bumpers could be reduced or eliminated entirely. An experimental program conducted by Foster [32] included horizontal tests on SU-FREIs up to  $u/t_r = 4.00$ . The tests identified a favourable increase in damping characteristics over these large amplitude cycles that exceeded full rollover. These damping characteristics are also anticipated to favourably reduce the peak response of the structure; although they were not considered in the parametric study.

The stiffening regime is necessary to maintain horizontal stability, which is a requirement for isolation systems [42]. It is postulated that the stiffening regime could be used in conjunction with bumpers to mitigate the pounding of the structure against the seismic gap wall in extreme events by providing a smoother transition between the isolation stiffness and impact stiffness. Furthermore, the reduction in mean peak horizontal displacement obtained could be critical if it prevents impact from occurring.

It is postulated that by accelerating full rollover with A-MSG, the reduction in the softening regime would allow isolators with width-to-total height aspect ratios less than 2.5 to be horizontally stable. This could be used to reduce the size of the isolators, softening the isolation layer and resulting in a larger shift in the fundamental period. Applying D-MSG can also be used to increase the softening regime and reduce the magnitude of the stiffening, reducing the response of the key performance parameters at lower displacements.

## 7.9 Conclusions

This paper numerically investigated modifying the stiffening regime of SU-FREIs with MSG. Experimental results were used to model an elastic base isolated structure with MSG over a range of hazard levels. The stiffening regime has often been considered to act as a self-restraint mechanism against excessive displacements at events that meet or exceed the MCE hazard level. The findings, which are limited to the scope of this study and selected earthquake records, indicate that the stiffening regime for the isolators considered provided minimal displacement restraint. This is primarily contributed to the characteristics of the selected earthquake records, in particular the constant mean spectral displacements exhibited over the period range of interest. The parametric study demonstrated that the level of stiffening required to significantly restrain displacements is substantial and results in amplification of the response of the structure and light equipment.

The stiffening regime caused by full rollover in SU-FREIs and MSG are important and advantageous features. Full rollover is critical for maintaining horizontal stability by preventing further softening and could potentially be used in conjunction with bumpers to mitigate pounding against seismic gap walls. It is recommended that similar studies be conducted considering more complex structures, ground motions with different characteristics, and with other isolation systems that exhibit adaptive characteristics, such as rubber isolators with strain induced crystallization, the triple friction pendulum and sliding systems with variable curvature.

### *Acknowledgements*

Financial support for this study was provided by the McMaster University Centre for Effective Design of Structures (CEDs) funded through the Ontario Research and Development Challenge Fund (ORDCF) as well as an Early Researcher Award (ERA) grant, both of which are programs of the Ministry of Research and Innovation (MRI). Support was also provided through the Natural Sciences and Engineering Research Council (NSERC) of Canada. The support of a Vanier Canada Graduate Scholarship is gratefully acknowledged.

### *References*

- [1] Kelly JM. Analysis of fiber-reinforced elastomeric isolators. *Journal of Seismology and Earthquake Engineering* 1999; **2**(1):19-34.
- [2] Toopchi-Nezhad H, Tait MJ, Drysdale RG. Bonded versus Unbonded Strip Fiber Reinforced Elastomeric Isolators: Finite Element Analysis. *Composite Structures* 2011; **93**(2):850-859.
- [3] Kelly JM, Konstantinidis D. *Mechanics of Rubber Bearings for Seismic and Vibration Isolation*. Wiley: Chichester, UK, 2011.
- [4] Toopchi-Nezhad H, Tait MJ, Drysdale RG. Testing and Modeling of Square Carbon Fiber-reinforced Elastomeric Seismic Isolators. *Structural Control and Health Monitoring* 2008; **15**(6):876-900.
- [5] Toopchi-Nezhad H, Drysdale RG, Tait MJ. Parametric Study on the Response of Stable Unbonded-Fiber Reinforced Elastomeric Isolators (SU-FREIs). *Journal of Composite Materials* 2009; **43**:1569-1587.
- [6] Yang TY, Konstantinidis D, Kelly JM. The Influence of Isolator Hysteresis on Equipment Performance in Seismic Isolated Buildings. *Earthquake Spectra* 2010; **26**(1):275-293.
- [7] Fenz D, Constantinou MC. Spherical Sliding Isolation Bearings with Adaptive Behaviour: Theory. *Earthquake Engineering and Structural Dynamics* 2008; **37**(2):163-183.
- [8] Becker TC, Mahin SA. Experimental and analytical study of the bi-directional behavior of the triple friction pendulum isolator. *Earthquake Engineering and Structural Dynamics* 2012; **41**(3):355-373.

- [9] Dao ND, Ryan KL, Sato E, Sasaki T. Predicting the displacement of triple pendulum™ bearings in a full-scale shaking experiment using a three-dimensional element. *Earthquake Engineering and Structural Dynamics* 2013; **42**(11):1677-1695.
- [10] Lu LY, Lee TY, Yeh SW. Theory and experimental study for sliding isolators with variable curvature. *Earthquake Engineering and Structural Dynamics* 2011; **40**(14):1609-1627.
- [11] Tsai CS, Chiang TC, Chen BJ. Finite element formulations and theoretical study for variable curvature friction pendulum system. *Engineering Structures* 2003; **25**(14): 1719-1730.
- [12] Toopchi-Nezhad H, Tait MJ, Drysdale, RG. Lateral response evaluation of fiber-reinforced Neoprene seismic isolators utilized in an unbonded application. *Journal of Structural Engineering (ASCE)* 2008; **134**(10):1627-1637.
- [13] Sarlis AA, Constantinou MC, Reinhorn AM. Shake table testing of triple friction pendulum isolators under extreme conditions, *Multidisciplinary Center for Earthquake Engineering Research*, Buffalo, New York. Report MCEER-13-0011.
- [14] Kelly JM, Tsai HC. Seismic response of light internal equipment in base-isolated structures. *Earthquake Engineering and Structural Dynamics* 1985; **13**(6):711–732.
- [15] Juhn G, Manolis GD, Constantinou MC, Reinhorn AM. Experimental study of secondary systems in base-isolated structure. *Journal of Structural Engineering (ASCE)* 1992; **118**(8):2204–2221.
- [16] Kelly JM. The role of damping in seismic isolation. *Earthquake Engineering and Structural Dynamics* 1999; **28**(1):3–20.
- [17] Politopoulos I. A review of adverse effects of damping in seismic isolation. *Earthquake Engineering and Structural Dynamics* 2008; **37**(3):447–465.
- [18] Isakovic T, Zevnik J, Fischinger M. Floor response spectra in isolated structures subjected to earthquakes weaker than the design earthquake—Part I: Isolation with high-damping rubber bearings. *Structural Control and Health Monitoring* 2011; **18**(6):635–659.
- [19] Becker TC, Mahin SA. Approximating peak responses in seismically isolated buildings using generalized modal analysis. *Earthquake Engineering and Structural Dynamics* 2013; **42**(12):1807–1825.
- [20] Wolff ED, Ipek C, Constantinou MC, Tapan M. Effect of viscous damping devices on the response of seismically isolated structures. *Earthquake Engineering and Structural Dynamics*, 2015; **44**:185-198.
- [21] Wolff ED, Constantinou MC. Experimental study of seismic isolation systems with emphasis on secondary system response and verification of accuracy of dynamic response history analysis methods, *Multidisciplinary Center for Earthquake Engineering Research*, Buffalo, New York. Report MCEER-04-0001.
- [22] Sato E, Furukawa S, Kakehi A, Nakashima M. Full-scale shaking table test for examination of safety and functionality of base-isolated medical facilities. *Earthquake Engineering and Structural Dynamics* 2011; **40**(13):1435–1453.

- [23] Furukawa S, Sato E, Shi Y, Becker T, Nakashima M. Full-scale shaking table test of a base-isolated medical facility subjected to vertical motions. *Earthquake Engineering and Structural Dynamics* 2013; **42**(13):1931–1949.
- [24] Shi Y, Kurata M, Nakashima M. Disorder and damage of base-isolated medical facilities when subjected to near-fault and long-period ground motions. *Earthquake Engineering and Structural Dynamics* 2014; **43**(11):1683–1701.
- [25] OpenSees. Open System for Earthquake Engineering Simulation. Pacific Earthquake Engineering Research Center, University of California, Berkeley, CA.
- [26] Kelly JM, Konstantinidis D. Low-cost seismic isolators for housing in highly-seismic developing countries. *ASSISI 10th World Conference on Seismic Isolation, Energy Dissipation and Active Vibrations Control of Structures*, 2007.
- [27] Van Engelen NC, Tait MJ, Konstantinidis D. Model of the shear behavior of unbonded fiber-reinforced elastomeric isolators. *Journal of Structural Engineering ASCE* 2014.
- [28] Toopchi-Nezhad H. Horizontal stiffness solutions for unbonded fiber reinforced elastomeric bearings. *Structural Engineering and Mechanics* 2014; **49**(3):395-410.
- [29] Osgooei PM, Tait MJ, Konstantinidis D. Finite element analysis of unbonded square fiber-reinforced elastomeric isolators (FREIs) under lateral loading in different directions. *Composite Structures* 2014; **113**:164-173.
- [30] Tait MJ, Toopchi-Nezhad H, Drysdale RG. Influence of end geometry on fiber reinforced elastomeric isolator bearings. *14<sup>th</sup> World Conference on Earthquake Engineering*, 2008.
- [31] Van Engelen NC, Tait MJ, Konstantinidis D. Experimental investigation of unbonded fiber reinforced elastomeric isolators with modified support geometry. *10<sup>th</sup> National Conference on Earthquake Engineering*, 2014.
- [32] Foster BAD. Base Isolation using Stable Unbonded Fibre Reinforced Elastomeric Isolators (SU-FREIs). *M.A.Sc. thesis*, McMaster University, Hamilton, Canada, 2011.
- [33] Ryan KL, Polanco J. Problems with Rayleigh damping in base-isolated buildings. *Journal of Structural Engineering ASCE* 2008; **134**(11):1780-1784.
- [34] Pant DR, Wijeyewickrema AC, ElGawady MA. Appropriate viscous damping for nonlinear time-history analysis of base-isolated reinforced concrete buildings. *Earthquake Engineering and Structural Dynamics* 2013; **42**:2321-2339.
- [35] Konstantinidis D, Makris, N. Experimental and analytical studies on the response of free standing laboratory equipment to earthquake shaking. *Earthquake Engineering and Structural Dynamics* 2009; **38**(6):827-848.
- [36] Konstantinidis D, Nikfar F. Seismic response of sliding equipment and contents in base-isolated buildings subjected to broadband ground motions. *Earthquake Engineering and Structural Dynamics* 2014.
- [37] Schellenberg A, Maffei J, Talleen K, Ward R. Structural analysis and application of wind loads to solar arrays. *Journal of Wind Engineering and Industrial Aerodynamics* 2013; **123**(A): 261-272.

- [38] Love JS, Tait MJ, Toopchi-Nezhad H. A hybrid structural control system using a tuned liquid damper to reduce the wind induced motion of a base isolated structure. *Engineering Structures* 2011; **33**(1):738-746.
- [39] Chen Y, Ahmadi G. Wind effects on base-isolated structures. *Journal of Engineering Mechanics ASCE* 1992; **118**(8):1708-1727.
- [40] Toopchi-Nezhad H, Tait MJ, Drysdale RG. Simplified analysis of a low-rise building seismically isolated with stable unbonded fiber reinforced elastomeric isolators. *Canadian Journal of Civil Engineering* 2009; **36**(7):1182-1194.
- [41] Baker JW, Lin T, Shahi SK, Jayaram N. New ground motion selection procedures and selected motions for the PEER transportation research program. *Pacific Earthquake Engineering Research Center*, Berkeley, California, 2011. Report 2011-03.
- [42] ASCE 7-10. *Minimum Design Loads for Buildings and other Structures*, ASCE/SEI 7-10. American Society of Civil Engineers: New York, 2010.
- [43] NBCC 2010. *National Building Code of Canada 2010*. Institute for Research in Construction, National Research Council of Canada: Ottawa, 2010.
- [44] Masroor A, Mosqueda G. Experimental simulation of base-isolated buildings pounding against moat wall and effects on superstructure response. *Earthquake Engineering and Structural Dynamics*, 2012; **41**:2093-2109.
- [45] Masroor A, Mosqueda G. Impact model for simulation of base isolated buildings impacting flexible moat walls. *Earthquake Engineering and Structural Dynamics* 2013; **42**:357-376.
- [46] Komodromos P. Simulation of the earthquake-induced pounding of seismically isolated buildings. *Computers and Structures* 2008; **86**(7):618-626.

Table 7-1: Experimentally determined effective horizontal stiffness and equivalent viscous damping.

$u/t_r$	A-MSG		USG		D-MSG	
	$k_{eff}t_r/GA$	$\zeta_{eff}(\%)$	$k_{eff}t_r/GA$	$\zeta_{eff}(\%)$	$k_{eff}t_r/GA$	$\zeta_{eff}(\%)$
0.25	1.11	12.6	1.08	12.6	1.13	16.4
0.50	0.87	11.8	0.83	12.1	0.80	14.8
0.75	0.72	11.4	0.67	11.7	0.64	13.8
1.00	0.62	11.0	0.57	11.5	0.55	12.9
1.50	0.52	10.1	0.46	11.0	0.43	12.4
2.00	0.63	7.4	0.47	9.1	0.36	12.4
2.50	0.75	6.2	0.56	7.7	0.42	10.0

Table 7-2: Ratio of the model to experimental effective horizontal stiffness and equivalent viscous damping.

$u/t_r$	A-MSG		USG		D-MSG	
	$k_{eff}$	$\zeta_{eff}$	$k_{eff}$	$\zeta_{eff}$	$k_{eff}$	$\zeta_{eff}$
0.25	0.87	0.76	0.84	0.74	0.86	0.69
0.50	0.96	0.96	0.98	0.94	0.98	0.93
0.75	1.01	1.04	1.04	1.01	1.04	1.02
1.00	1.03	1.10	1.06	1.06	1.04	1.05
1.50	1.09	1.07	1.05	1.10	1.04	1.07
2.00	0.98	1.09	0.98	1.11	1.00	1.05
2.50	1.03	0.88	1.05	0.87	1.05	0.86

Table 7-3: Selected broadband fault normal records and scale factors.

Earthquake	Station	Scale Factor
San Fernando - 1971	Lake Hughes #4	4.21
Loma Prieta - 1989	Gilroy Array #6	1.76
Northridge-01 - 1994	LA - Wonderland Ave	2.74
Hector Mine - 1999	Hector	0.83
Hector Mine - 1999	Heart Bar State Park	6.55
Coyote Lake - 1979	Gilroy Array #6	0.80
Northridge-01 - 1994	Pacoima Dam (downstr)	1.32
Denali, Alaska - 2002	Carlo (temp)	2.53
Chi-Chi, Taiwan - 1999	WNT	0.71
Victoria, Mexico - 1980	Cerro Prieto	0.69
Loma Prieta - 1989	Gilroy Array #1	1.64
Northridge-01 - 1994	LA Dam	0.47
Northridge-01 - 1994	LA - Chalon Rd	2.28
Chi-Chi, Taiwan - 1999	TCU129	0.63

Table 7-4: Effective period at  $u/t_r = 2.50$ .

	$T$ (s)		
	$k-1$	$k-2$	$k-3$
A-MSG	0.42	0.88	1.39
USG	0.50	1.00	1.50
D-MSG	0.62	1.20	1.66

Table 7-5: Mean peak displacement.

	$u/t_r$		
	$k-1$	$k-2$	$k-3$
A-MSG	1.68	1.81	1.86
USG	1.74	1.84	1.86
D-MSG	1.81	1.86	1.88

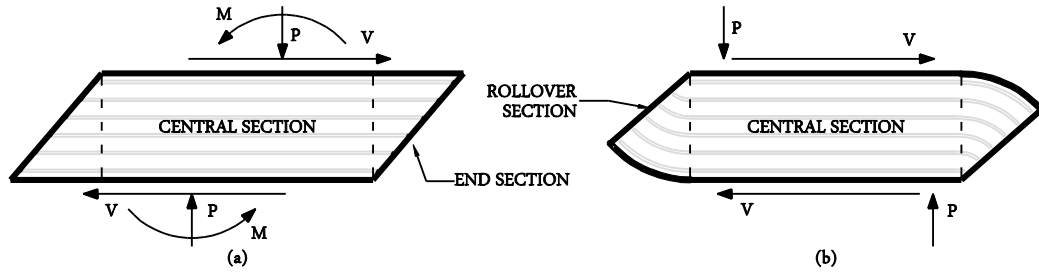


Figure 7-1: Idealized division of a (a) bonded and (b) unbonded FREI.

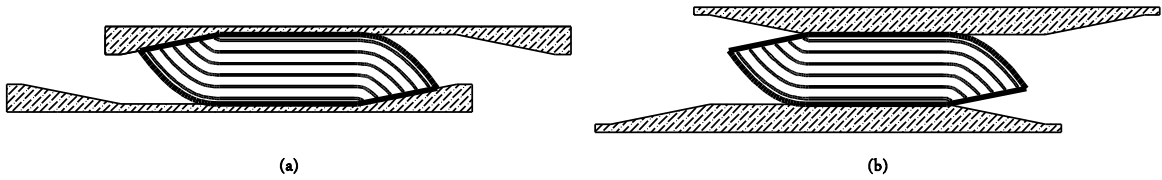


Figure 7-2: MSG that (a) accelerates full rollover, and (b) delays full rollover.

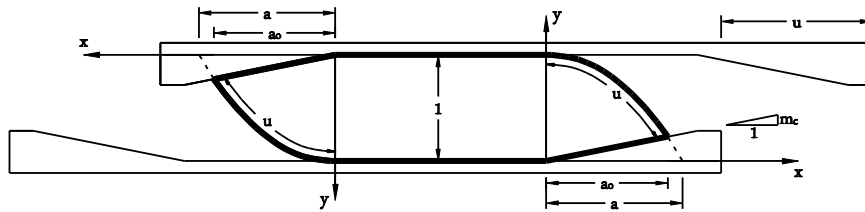


Figure 7-3: Cartesian coordinate system and deformed shape of the isolator with A-MSG at full rollover.

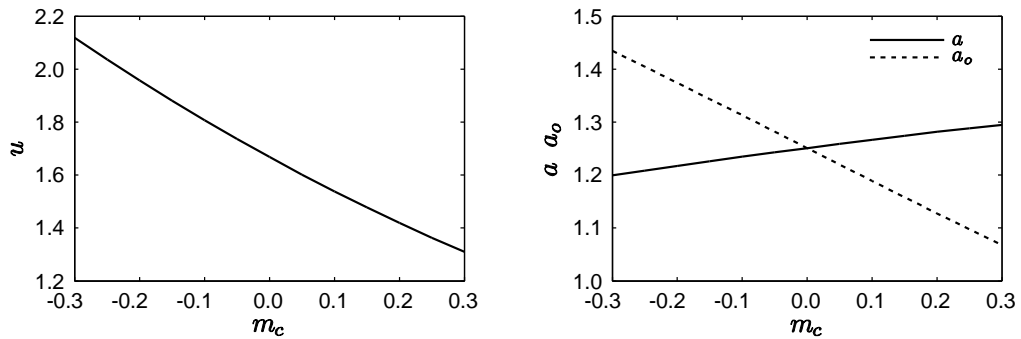


Figure 7-4: (a) Full rollover displacement and (b) corresponding parameters  $a$  and  $a_o$  for an isolator with unit height, neglecting the thickness of the reinforcement.

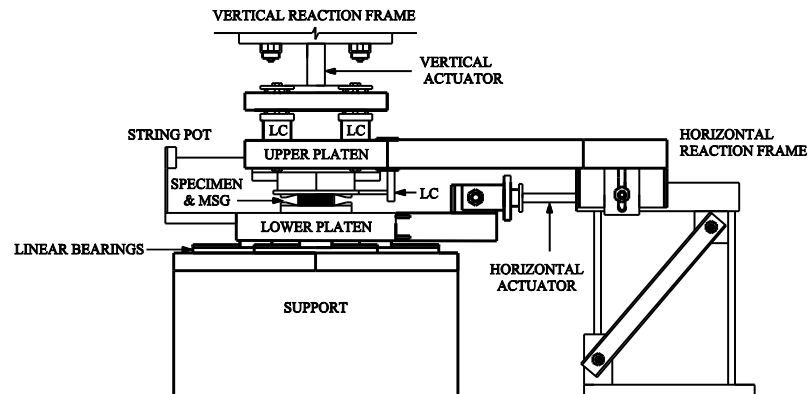


Figure 7-5: Schematic of the experimental setup.

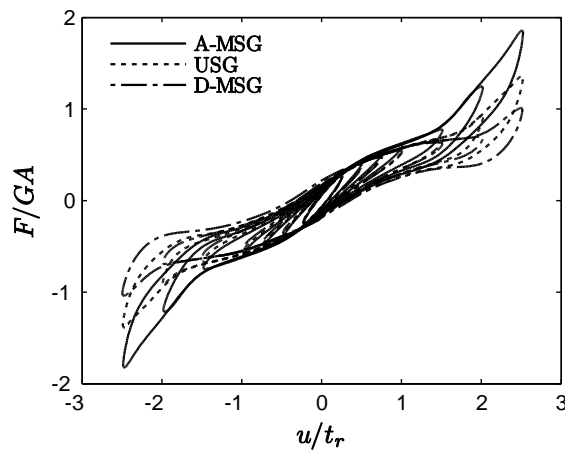


Figure 7-6: Normalized force-displacement experimental hysteresis loops for different levels of MSG.

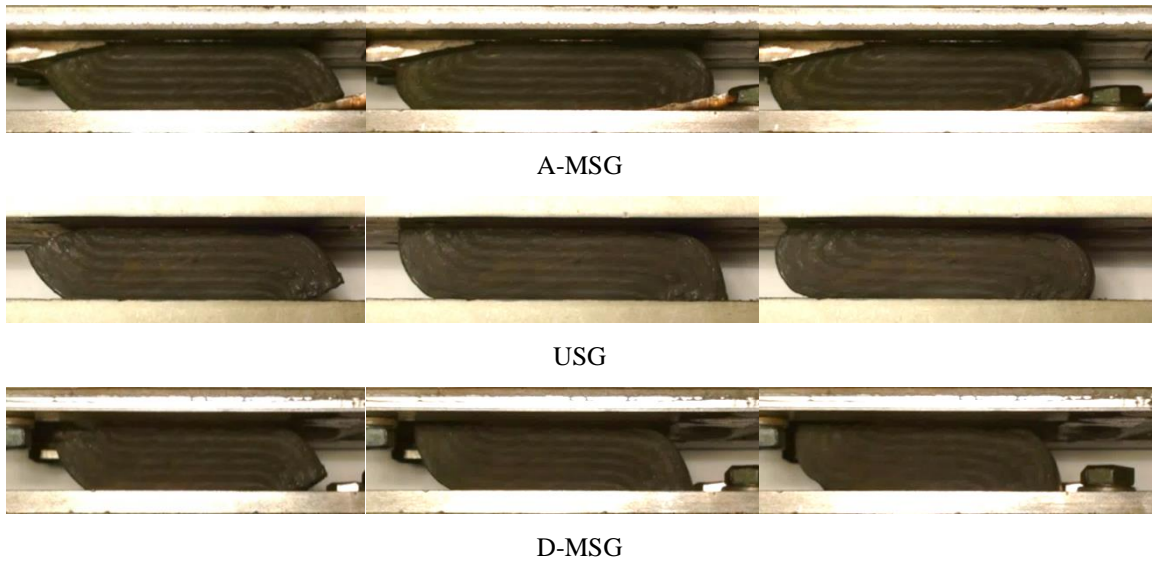


Figure 7-7: Isolator deformed shape at  $u/t_r = 1.50$  (left),  $2.00$  (center) and  $2.50$  (right).

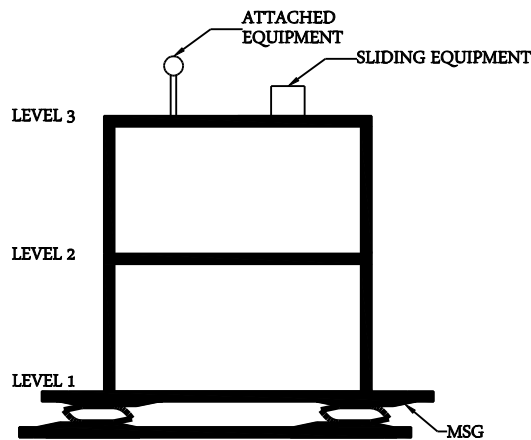


Figure 7-8: Idealized prototype structure and light equipment.

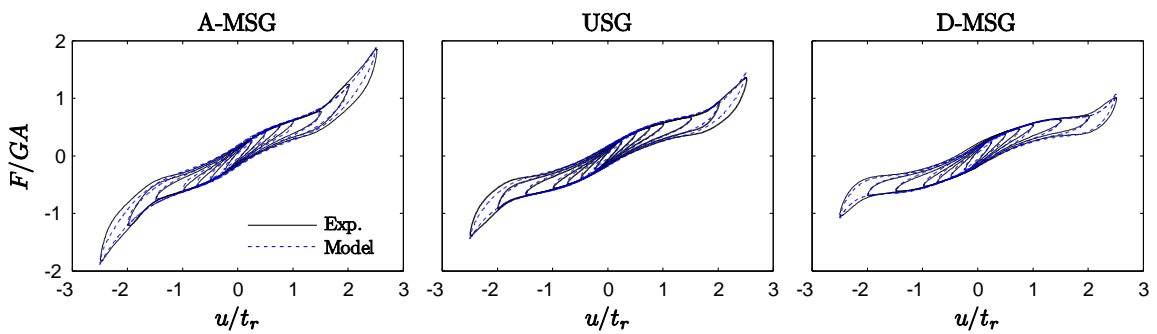


Figure 7-9: Comparison of the normalized experimental and model hysteresis loops.

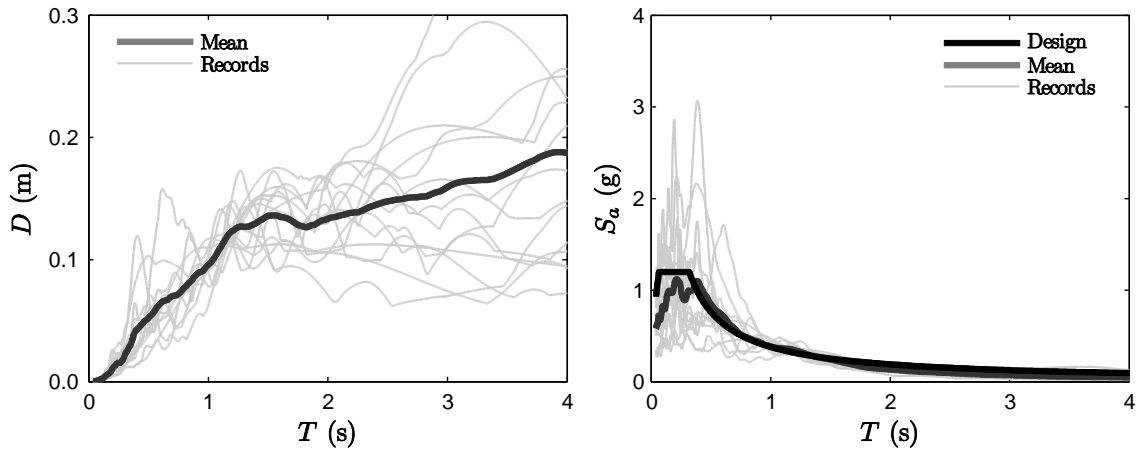


Figure 7-10: Scaled displacement and pseudo-acceleration response spectra showing the mean spectrum of the 14 ground motions and the design spectrum at Victoria City Hall, Canada.

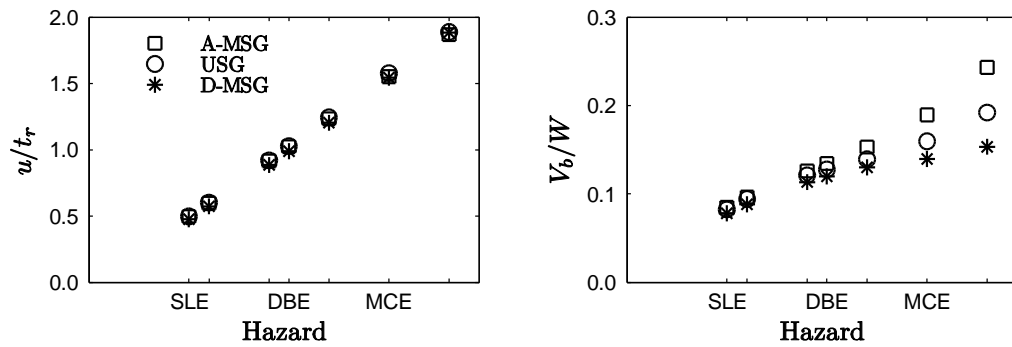


Figure 7-11: Normalized mean peak isolator displacement and normalized base shear as a function of the earthquake hazard level.

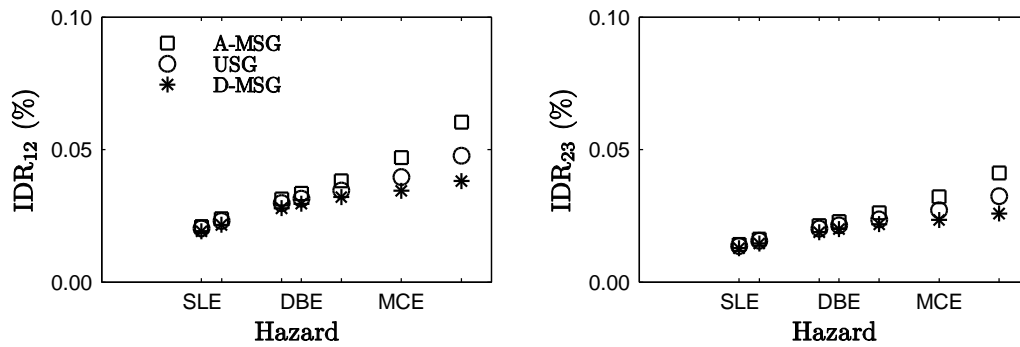


Figure 7-12: Mean peak IDR as a function of the earthquake hazard level.

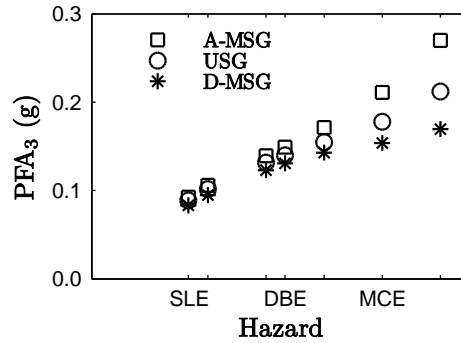


Figure 7-13: Mean peak floor absolute acceleration at level 3 of the structure as a function of the earthquake hazard level.

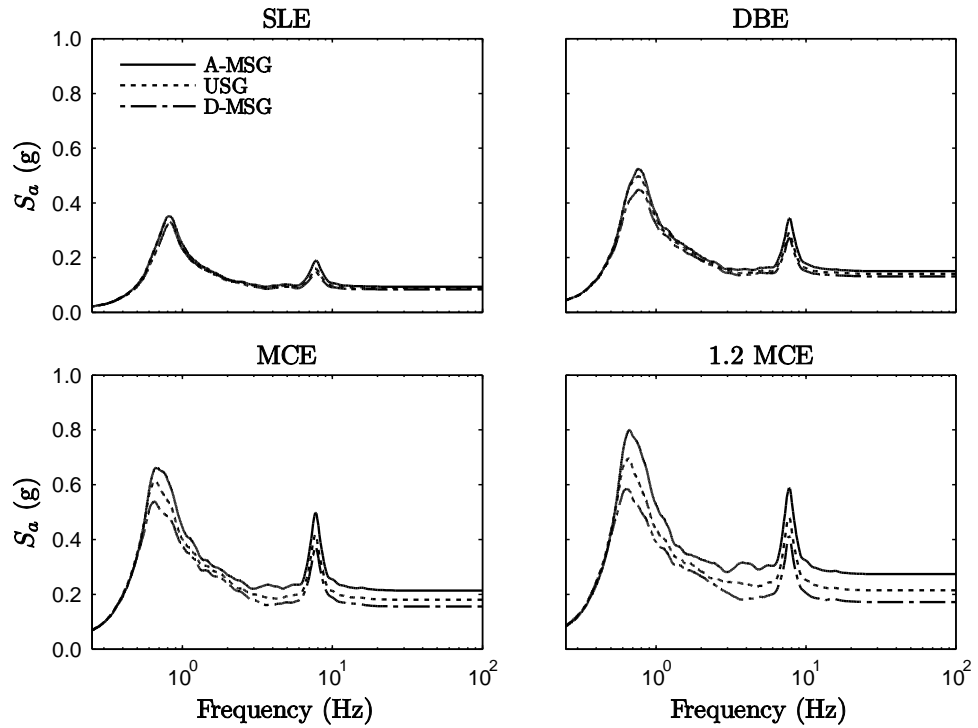


Figure 7-14: Mean floor pseudo-acceleration response spectra (Level 3).

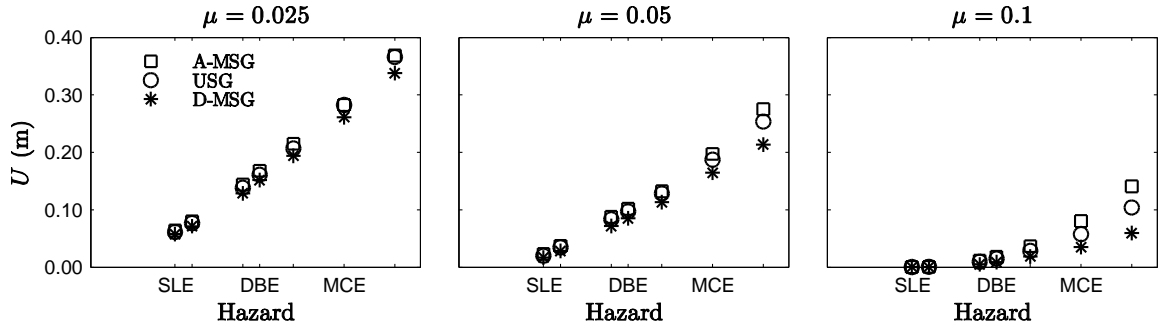


Figure 7-15: Mean displacement of sliding equipment as a function of hazard level (Level 3).

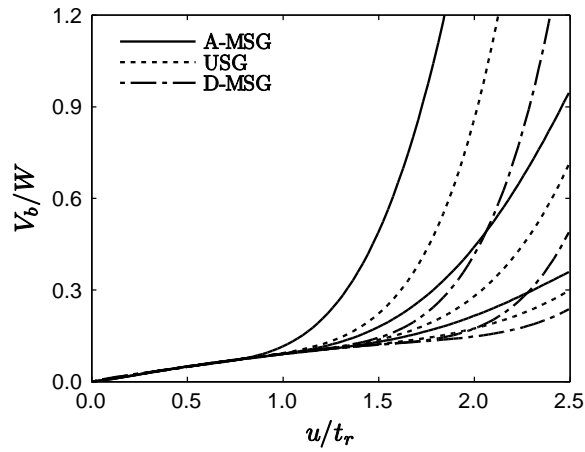


Figure 7-16: Fifth order polynomials used in the parametric study displaying the three stiffening levels for each MSG.

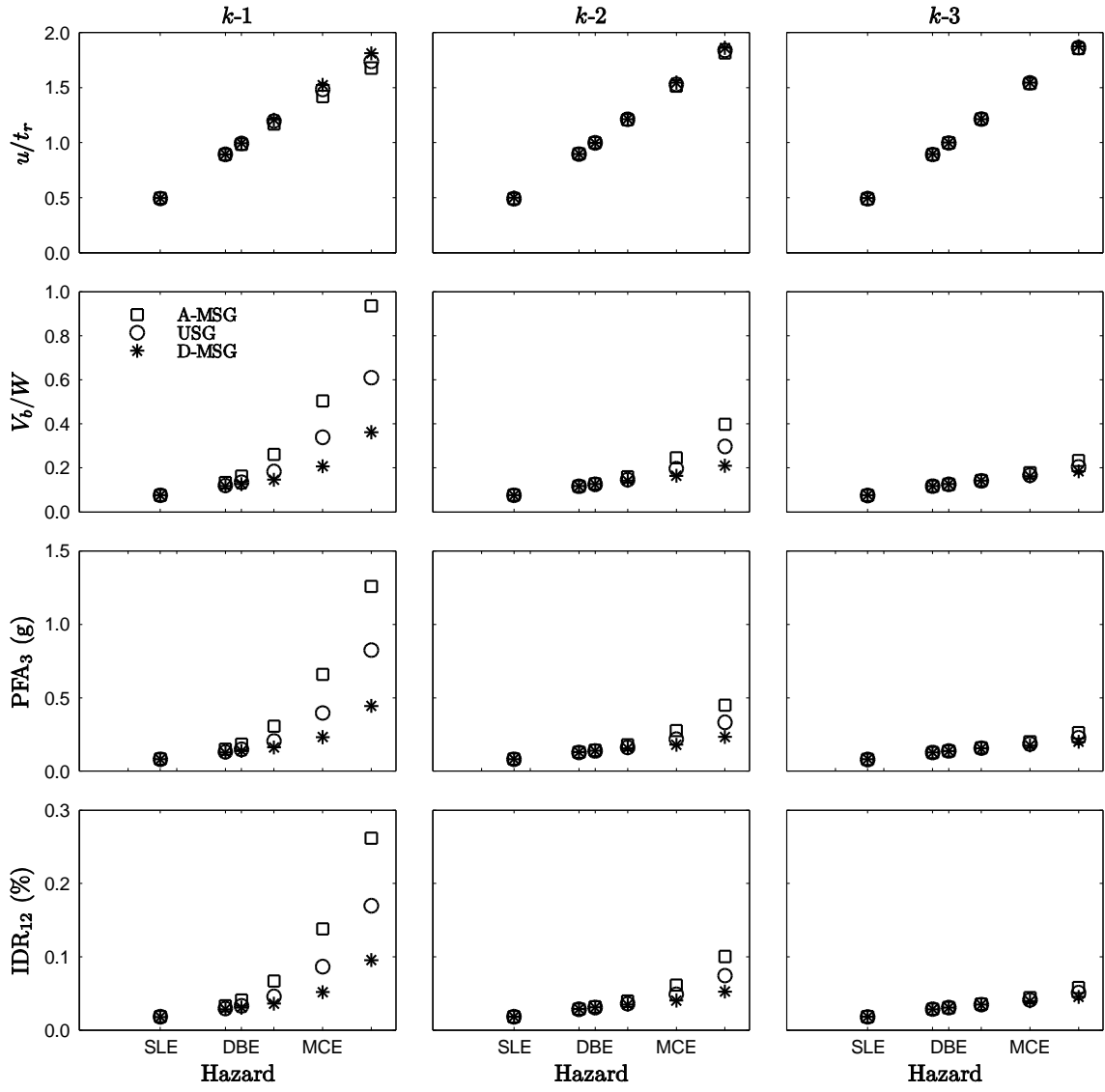


Figure 7-17: Mean response of key performance indicators as a function of earthquake hazard level.

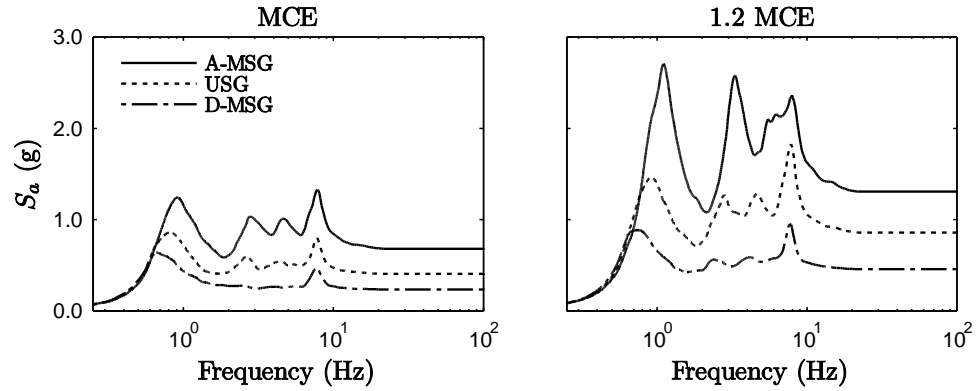


Figure 7-18: Mean floor pseudo-acceleration response spectra ( $k-1$ ).

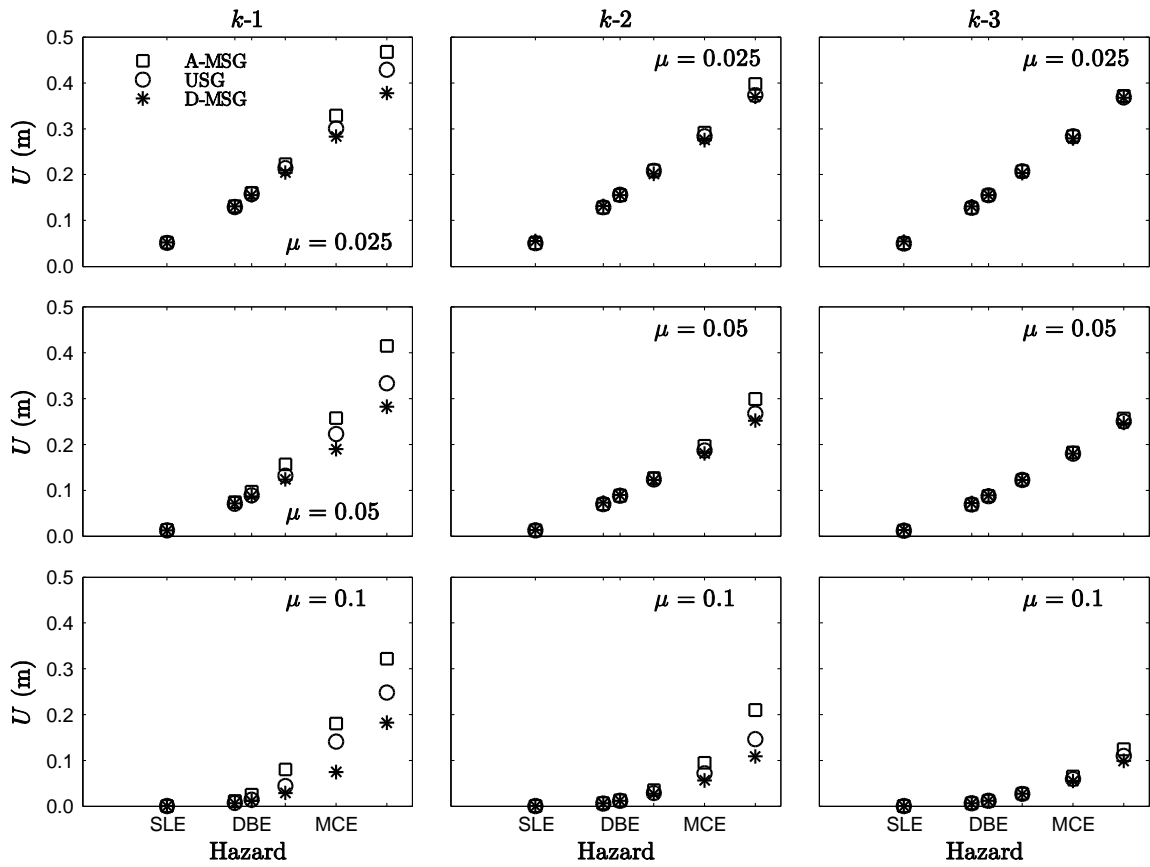


Figure 7-19: Sliding equipment mean displacement demand.

## 8 Partially Bonded Fiber-Reinforced Elastomeric Isolators (PB-FREIs)

Reproduced with permission from Elsevier.

Van Engelen NC, Osgooei PM, Tait MJ, Konstantinidis D. 2014. Partially Bonded Fiber-Reinforced Elastomeric Isolators (PB-FREIs). *Structural Control and Health Monitoring*, 22(3): 417-432, DOI: 10.1002/stc.1682.

### *Summary*

Although stable unbonded fiber-reinforced elastomeric isolators (SU-FREIs) have desirable characteristics for seismic isolation, the unbonded application also introduces limitations in comparison to bonded elastomeric isolators. SU-FREIs are not capable of resisting tensile forces, making SU-FREIs unsuited for situations where overturning is of concern or where large vertical accelerations are anticipated. Furthermore, as SU-FREIs rely on friction to transfer horizontal forces, the isolator could potentially slip under certain loading conditions, resulting in permanent displacements. This paper proposes that concerns over the transfer of tensile forces and potential slip can be addressed by partially bonding the SU-FREI to the upper and lower supports. In this way, Partially Bonded FREIs (PB-FREIs) retain the beneficial characteristics of an unbonded FREI, but also inherit characteristics of a bonded isolator; notably tensile and horizontal forces can be transferred through the partial bond. Experimental results from isolators tested unbonded and partially bonded under vertical compression are used to evaluate a finite element model. The experimental data and finite element analysis demonstrate that portions of a FREI can be bonded without substantially altering the rollover characteristics of the isolator within the range of average vertical compressive and tensile stresses considered. Despite an unconventional deformed shape under tensile vertical stress, the horizontal force-displacement relationship exhibits negligible deviation from a conventional unbonded SU-FREI under a compressive vertical stress. It is postulated that with further development PB-FREIs can retain the beneficial characteristics of unbonded FREIs while addressing concerns over tensile forces and slip.

### *Key Words*

partially bonded; base isolation; fiber-reinforced; elastomeric isolator; finite element analysis

### *8.1 Introduction*

The concept of fiber-reinforced elastomeric isolators (FREIs) was initially proposed to reduce the high cost and weight associated with conventional Steel Reinforced Elastomeric Isolators (SREIs) [1]. Experimental testing of FREIs revealed that similar

performance to SREIs could be obtained with the benefit of additional damping attributed to the inter-fiber movement of the reinforcement [1, 2]. In addition to replacing the steel reinforcement, the design and installation of FREIs can be further simplified by installing the isolator unbonded between the upper and lower supports. Placing the isolator unbonded between the supports eliminates the high tensile stress regions that develop in a bonded isolator when it is displaced horizontally [3]. Unlike the nearly rigid steel reinforcement, fiber reinforcement is extensible and provides no appreciable resistance in bending. The lack of bending rigidity, combined with the unbonded installation, results in a unique rollover deformation in the end sections that would otherwise be in tension, as illustrated in Figure 3-1. As the horizontal displacement increases, and the size of the rollover section of the isolator increases, the effective horizontal stiffness decreases. Toopchi-Nezhad et al. [4] demonstrated experimentally that the reduction in effective horizontal stiffness can result in instability if the tangential stiffness becomes negative. It was identified that the instability could be prevented by increasing the width-to-total height aspect ratio. An increase in horizontal stiffness occurred as the rollover sections contacted the upper and lower supports, completing *full rollover*. Unbonded FREIs exhibiting this type of behaviour were denoted as Stable Unbonded FREIs (SU-FREIs) [5]. The stiffening of the isolator is deemed to be an advantageous characteristic to protect against instability and to limit excessive displacements during beyond design basis events [4].

Despite the potentially advantageous softening and stiffening characteristics of the unbonded application there are two limitations associated with unbonded FREIs. Firstly, the unbonded application prevents the transfer of tensile forces through the isolator, making this type of isolator inappropriate for situations with a tensile minimum vertical design load. A tensile vertical design load may occur in near fault applications where high vertical ground accelerations are expected or in situations where overturning is of concern. Secondly, the horizontal force is transferred by friction only, rendering unbonded FREIs susceptible to slip under certain loading conditions resulting in permanent displacements. The frictional resistance of the contact interface between the unbonded FREI and the upper and lower supports is proportional to the compressive force. If the compressive force on an unbonded isolator approaches zero during an earthquake event the likelihood that the shear force will exceed the friction resistance is increased.

It is proposed that the above limitations related to unbonded FREIs can be addressed by partially bonding a portion of the isolator to steel end plates. Partially bonded fiber-reinforced elastomeric isolators (PB-FREIs) require the reintroduction of steel end plates, which can be mechanically fastened to the upper and lower supports, but addresses limitations over the transfer of tensile forces and slip under certain loading

conditions. The resulting isolator inherits advantageous characteristics from both unbonded and bonded isolators. This paper introduces the concept of PB-FREIs through finite element analysis (FEA) and an experimental program that compares PB-FREIs and unbonded FREIs.

## 8.2 *Background*

### 8.2.1 **Isolation Systems in Tension**

It is possible for the minimum vertical design load to be tensile as a result of the geometry of the structure, or the proximity of the structure to a geographical region with a high expected vertical acceleration component. Provisions for tensile testing are often provided and required in design codes and standards [6, 7]. In general, experimental testing of elastomeric isolators subjected to tension is limited due to difficulties in simultaneously applying a tensile load while displacing the isolator horizontally [8]. Theoretical analysis of SREIs has identified [9], and FEA has confirmed [10], that the isolator may also buckle in tension, therefore, as the tensile load increases, the horizontal stiffness of a bonded SREI will decrease. In practice, the tensile buckling load cannot be achieved due to cavitation of the elastomer [10]. Cavitation in multilayer elastomeric isolators has been a concern in the seismic isolation community. However, although the elastomer is susceptible to cavitation at very low tensile strains under the state of triaxial stress generated by pure tension, under the combined action of tension and shear the isolator can avoid this damaging effect [10].

As described earlier, unbonded isolators are limited to situations where the minimum vertical design load is compressive. Partially bonding the isolator allows vertical tensile forces to be resisted. The performance of FREIs in tension is a unique problem due to the load dependent nature of the fiber reinforcement. As a vertical compressive load is applied, the elastomeric layers bulge outwards, restrained by the reinforcement. The restraint of the elastomeric layers introduces a horizontal tensile stress in the reinforcement. As a vertical tensile load is applied, an opposite type of response is expected to occur. The near incompressibility of the elastomer develops a horizontal compressive stress in the reinforcement as the elastomer is restrained from bulging inwards. When loaded along its plane as a homogeneous material, fiber reinforcement provides no appreciable resistance in compression; however, the performance of fiber reinforcement in compression as a composite with an elastomer, such as with bonded FREIs under a vertical tensile stress, has not been investigated.

### 8.2.2 **Friction and Slip**

An experimental investigation and literature review on neoprene-concrete friction characteristics was conducted by Magliulo et al. [11]. A comparison between code

equations, results from existing studies in the literature and the experimental data presented in the study demonstrated substantial variation in the friction coefficient as a function of vertical compressive stress. Magliulo et al. [11] contributed the variation in part to differences in the roughness of the concrete surface. It was stated that in many of the reviewed studies the quality and finish of the concrete surface was not specified or discussed. This variation contributes to uncertainties of the horizontal force transfer capacity of unbonded elastomeric isolators.

Kelly and Konstantinidis [12] analytically investigated the effect of friction at the contact interface between an unbonded SREI and the supports on the compressive behaviour. It was found that the vertical behaviour can be highly sensitive to the friction developed and level of slip depending on the layer design of the isolator. In an experimental study investigating the seismic response of unbonded elastomeric bridge bearings, slip between the bearing and the concrete supports was observed at a shear strain of about 2.25 [13]. Monotonic and cyclic testing on unbonded elastomeric bridge bearings conducted by Steelman et al. [14] observed slip at shear strains between 1.25 and 2.50 depending on the interface roughness, compressive load and magnitude of the velocity.

While conducting an experimental shake table program on a scaled base isolated structure with unbonded SU-FREIs, Foster [15] identified that permanent displacement occurred in a scaled earthquake record where the seismic demand significantly exceeded the design basis of the isolation system. The permanent displacement was observed when the peak displacement of the isolation layer reached  $3.11 t_r$ , where  $t_r$  is the total thickness of the elastomeric layers. This peak displacement was far in excess of the target design displacement of approximately  $2.00 t_r$  for the isolators considered in the study. The level of permanent displacement was reduced by 66 % when grit paper was introduced to increase the friction between the elastomer and the steel and aluminum support surfaces. The introduction of grit paper was found to have negligible influence on the response of the structure; however, it resulted in a substantial decrease in the level of permanent displacement. Russo and Pauletta [16] experimentally investigated the friction properties of unbonded FREIs on concrete surfaces with varying vertical compressive stress. In the experimental program, it was observed that at the end of a single horizontal displacement cycle that the contact surface of the isolator had some level of permanent displacement. The magnitude of the permanent displacement was found to be a function of the vertical compressive stress and the location along the surface of the isolator, attributed to the rollover deformation. Moment equilibrium in unbonded FREIs is maintained by a change in the vertical stress distribution; areas of the contact surface with high vertical stress concentrations displayed less residual deformation than areas with lower vertical stress.

These studies demonstrate that properties of unbonded elastomeric isolators can be strongly influenced by the friction between the elastomer and the supports. In some cases, the slip observed in the experimental studies [13, 14] occurred at shear strains that can be expected in a seismic event. Therefore, the friction properties of unbonded FREIs are an important consideration for design and an area that requires further investigation. The decreased size of the unbonded portion provided by partially bonding the isolator is postulated to decrease the sensitivity to friction.

### 8.2.3 Partially Bonded Region

The limiting shear strain of an unbonded SREI with thin steel reinforcing plates was investigated by Kelly and Konstantinidis [10, 17]. The limiting shear strain was defined as the strain at which full rollover occurs. Assuming incompressibility in the elastomer, that the reinforcement was perfectly flexible, and that the length of the free surface of the rollover section was equal to the horizontal displacement of the isolator, the limiting shear strain,  $\gamma_c$ , was determined as:

$$\gamma_c = \frac{5}{3} \frac{h}{t_r} \quad (8-1)$$

where  $h$  is the total height of the isolator.

Utilizing the limiting shear strain, a bond length,  $B$ , which does not enter the rollover section, can be established and is denoted as  $B_{max}$ . The bond length is expressed as a percentage of the total width of the isolator for square and rectangular designs, or as a percentage of the diameter for circular isolators. It is desirable to have the rollover sections of the isolator unbonded such that the rollover section is not influenced by the presence of the bond. To achieve this, from Equation (8-1), the bond must be located a distance of  $5/3 h$  from the free edge of the isolator. The maximum percentage of the isolator that can be bonded without entering the rollover region,  $B_{max}$ , can be expressed as:

$$B_{max} = \left(1 - \frac{10}{3R}\right) \times 100 \quad (8-2)$$

where  $R$  is the width-to-total height aspect ratio. By equating Equation (8-2) to zero, the minimum theoretical aspect ratio required such that a bonded portion can be introduced that does not enter the rollover section is  $R = 10/3 \approx 3.3$ . For isolators with aspect ratios  $R < 3.3$ , Equation (8-2) will be negative, implying that any level of bonding will enter the rollover section. The concept of a PB-FREI with a bonded region that has no influence over the rollover is well suited for isolators with aspect ratios  $R > 3.3$ . A comparison of an isolator of aspect ratio  $R = 2.5$  and 4.0 demonstrating  $B_{max}$  and an isolator where the entire width loses contact is illustrated in Figure 8-2. Russo et al. [18] proposed an analytical model for unbonded FREIs that included the vertical deflection of the isolator. The model recognized that the vertical deflection would delay the loss of contact between the

supports and the rollover section of the isolator as demonstrated in Figure 8-3. Consequently, it is anticipated that the bond could also be extended into the rollover section without influencing the rollover deformation. The estimate presented here is considered a lower bound.

### 8.3 *Experimental testing*

#### 8.3.1 **Isolator Design**

Two scaled isolator designs, denoted as type E1 and type E2, were considered in this study. Figure 8-4 shows the two isolator design types considered with the bond identified. Both designs were reinforced with plain weave bidirectional carbon fiber. The isolators were initially manufactured in large pads and subsequently cut to the desired size. Four specimens, two of each type, were considered. Type E1 isolators have a layer design matching the isolators investigated by Foster [15] and type E2 have a layer design matching the isolators described in de Raaf [19]. Type E1 isolators were cut to an aspect ratio of  $R = 3.5$  and type E2 isolators were cut to an aspect ratio of  $R = 5.0$ . Isolator E1-1 was tested unbonded while isolator E1-2, as illustrated in Figure 8-4(a), was bonded such that the bond enters the rollover section at a horizontal displacement of  $1.0 t_r$  or  $B = 50\%$  ( $B_{max} = 5\%$ ). Isolator E2-1, was tested unbonded and isolator E2-2, as shown in Figure 8-4(b), was bonded such that the bond does not enter the rollover section of the isolator, or  $B = B_{max} = 33\%$ . Isolators E1-2 and E2-2 were bonded to the steel plates using a cold vulcanization agent. The total height,  $h$ , was 22.4 mm and 24.0 mm for type E1 and type E2 isolators, respectively, while the total thickness of elastomeric layers,  $t_r$ , was 19.1 mm.

#### 8.3.2 **Experimental Setup and Horizontal Test Procedure**

The experimental apparatus used in this study was configured to conduct testing under vertical load control and horizontal displacement control. The horizontal load was measured directly with a single load cell and the horizontal displacement was measured with a string potentiometer. The vertical load was measured with three load cells and the vertical displacement was measured with four laser transducers. Each unbonded isolator was placed between two level steel plates, whereas the partially bonded isolators were mechanically fastened to the two level steel plates through the steel end plates that were bonded to the isolator.

Each isolator was tested under an average vertical stress,  $\bar{p}$ , of 2.0 MPa. Figure 8-5 shows the horizontal test displacement history where the horizontal displacement,  $u$ , has been normalized by  $t_r$ . Each isolator was subjected to eight displacement amplitudes at three cycles each. The displacement amplitude,  $0.10 t_r$ , was conducted at a constant rate of 30 mm/s and the remaining cycles, ranging from  $0.25 t_r$  to  $2.00 t_r$ , were conducted at a constant rate of 76.2 mm/s. Each isolator was monotonically loaded to the design

compressive stress before beginning the cycles and monotonically unloaded after the cycles were complete.

### 8.3.3 Experimental Results

Table 3-1 presents the ratio of the respective partially bonded values to the unbonded values for the effective horizontal stiffness,  $k_{eff}$ , and equivalent viscous damping ratio,  $\zeta_{eq}$ , for displacement amplitudes from  $0.25 t_r$  to  $2.00 t_r$ . For type E1 isolators, in all instances isolator E1-2 had a larger effective horizontal stiffness than isolator E1-1 with the largest ratio of 1.20 occurring at  $0.50 t_r$ . As the displacement amplitude increases that the ratio of E1-2 to E1-1 decreases and approaches unity. The largest ratio of 1.20 occurring at  $0.50 t_r$  was unexpected since the influence of the partially bonded region is not anticipated to influence the results for displacements below  $1.00 t_r$ . The ratio for E2-2 to E2-1 remained relatively constant with minor fluctuations from the average of 0.96. The ratio of equivalent viscous damping for E1-2 to E1-1 is, with the exception of  $0.50 t_r$ , approximately unity. The minimum ratio was 0.82, suggesting a decrease due to the partial bond, however, this may be in part due to the effective horizontal stiffness ratio of 1.20 observed at that displacement amplitude. Similar to the effective horizontal stiffness, the equivalent viscous damping ratio for E2-2 to E2-1 is near unity at all displacement amplitudes considered with the largest ratio of 1.08 occurring at  $0.50 t_r$ .

Figure 8-6 shows the normalized hysteresis loops for the partially bonded and unbonded isolators for both designs considered where the horizontal force,  $F$ , has been normalized by the shear modulus of the elastomer,  $G$ , and plan loaded area of the isolator at zero horizontal displacement,  $A$ . All isolators displayed the characteristic softening and subsequent stiffening associated with stable rollover of SU-FREIs. The softening and stiffening is less pronounced for type E2 isolators due to the larger aspect ratio, which mitigates the effect of the rollover. Figure 8-6(a) shows that, although the bond enters the rollover section at  $1.00 t_r$  for isolator E1-2, no appreciable change in the shape of the loop occurs; both the area contained within the loops and the peak normalized force remain consistent with isolator E1-1. Similarly, Figure 8-6(b) shows that the response of isolator E2-2 is nearly indistinguishable from that of isolator E2-1.

Although no significant deviation in the hysteretic loops of the isolator was noted, the deformed shape of the rollover section of the isolator is altered by the introduction of a partial bond as demonstrated in Figure 8-7, which compares the deformed shape of E1-1 and E1-2. Prior to  $1.00 t_r$  the bond has not entered the rollover section, and the deformed shape of the rollover section between isolator E1-1 and E1-2 is comparable. As the displacement increases to  $1.50 t_r$  only a minor difference in deformed shape is noted. Although the bond is now in the rollover section, the vertical deflection of the isolator delays the loss of contact between the isolator and the supports. As a consequence,

although the bond is in the rollover section, the influence is minimized. At a displacement of  $2.00 t_r$  the bonded portion is visible and results in localized deformations representative of the tensile stresses introduced in this portion by the bond. Despite the localized deformation, based on the experimental results, the global impact on the performance of the isolator has been shown to be negligible. Isolator E1-2 was visually inspected after the test program. The integrity of the elastomer-to-fiber and the elastomer-to-steel bond was not compromised. No delamination or other forms of damage were visually observed.

#### 8.4 Finite element analysis

##### 8.4.1 Model Description

Previous studies have been conducted that utilize FEA to compare unbonded and fully bonded FREIs [3, 20] and square unbonded FREIs with different aspect ratios and orientations [21]. In this study, the FEA was conducted using MSC Marc [22], a commercially available finite element software package. A three dimensional analysis was performed using an updated Lagrangian framework. In this framework, the reference configuration is updated, and the discrete equations are formulated in the current configuration. Eight-node hexahedron isoparametric elements were used to model the elastomeric layers. The fiber reinforcement layers were modeled using four-node quadrilateral membrane elements with no flexural rigidity. The nonlinear behaviour of the elastomeric materials was modeled using a hyperelastic material model. Unlike linear elastic materials where the stress-strain relationship is described using a constant factor, in the hyperelastic materials the stress-strain relationship is derived from a strain energy density function. In this study, the hyperelastic material law used for the rubber materials was compressible Neo-Hookean, with the following strain energy density function:

$$W = C_{10}(\bar{I}_1 - 3) + \frac{K}{2}(J_3 - 1)^2 \quad (8-3)$$

where  $C_{10}$  is the coefficient of the Neo-Hookean material model,  $K$  is the bulk modulus of the elastomeric material,  $\bar{I}_1$  is the first deviatoric strain invariant and  $J_3$  is the total volume ratio. The coefficient of the Neo-Hookean material model is related to the shear modulus of the elastomeric material by  $C_{10} = G/2$ . The first deviatoric strain invariant is expressed as:

$$\bar{I}_1 = \bar{\lambda}_1^2 + \bar{\lambda}_2^2 + \bar{\lambda}_3^2 \quad (8-4)$$

where  $\bar{\lambda}_i$  is the deviatoric stretches and is given by

$$\bar{\lambda}_i = J_3^{-\frac{1}{3}} \lambda_i \quad (8-5)$$

and  $\lambda_i$  is the principal stretches with  $J_3 = \lambda_1 \lambda_2 \lambda_3$ . Strain dependence of the shear modulus was not taken into consideration in this study. Constant values of  $G = 0.4$  MPa and  $0.7$  MPa were selected for E1 and E2, respectively, determined from experimental horizontal cyclic tests. The bulk modulus was selected as  $K = 1900$  MPa.

The FEA was conducted under the plane strain assumption, representing infinitely long strip isolators. The isolators were modeled with a unit length and restrained from lateral deformation perpendicular to the plane of the isolator in the direction of loading. A specific contact was defined between the isolators and the contact surfaces to allow the unbonded portions of the isolators to detach from the contact surfaces as the compressive contact stress approaches zero. The contact between the bonded regions of the FREIs and the contact surfaces was defined such that no separation or slip was allowed. Figure 8-8 shows the FEA model of isolator type E1 along with the mesh size that was used.

Figure 8-9 shows experimental results for E1-1 and E2-1 isolators compared to the FEA results of the respective isolator with  $B = 0\%$  normalized by  $GA$ . It can be observed that the FEA prediction is in good agreement with experimental results for displacements exceeding  $0.50 t_r$  and  $0.75 t_r$  for E1-1 and E2-1, respectively. The FEA prediction is lower than the experimental results for low displacement amplitudes; this is primarily attributed to the assumed constant value of  $G$ , which ignores the nonlinearity of the elastomer at low strains. According to Equation (8-1), full rollover occurs at  $1.96 t_r$  and  $2.10 t_r$  for E1-1 and E2-1, respectively. Therefore it is expected that E1-1 will display substantial stiffening as a result of full rollover before E2-1, which is observed in Figure 8-9(a) before  $2.00 t_r$ . This is in reasonable agreement with the full rollover prediction from Equation (8-1) and also matches well with the stiffening observed in the experimental results. Therefore the FEA model was considered to perform well in comparison to the experimental results and expected full rollover from theory and, as such, was considered suitable for this study.

#### 8.4.2 Vertical Modulus

Isolator type E1 with  $B = 50\%$  was investigated through FEA under a 1.0 MPa average compressive vertical stress and 0.4 MPa average tensile vertical stress determined by the total plan area. Figure 8-10 shows that a nearly linear local vertical stress,  $\sigma_{33}$ , and vertical strain,  $\varepsilon_{33}$ , relationship is obtained from the FEA. The vertical tensile modulus was determined to be 39.4 MPa, which is significantly lower than the compression modulus of 208 MPa. Figure 8-11 shows the normalized stress,  $S_{33} = \sigma_{33}/|\bar{p}|$ , contours for both vertical loading cases. As anticipated, in the compression case the magnitude of the stress increases approaching the center of the isolator from the edge, rendering the entire isolator effective in resisting the compressive load. As friction develops between the unbonded sections and the supports, slip is prevented and increases the restraint of the lateral bulging.

In the tensile case, only the bonded portion is largely effective in resisting the load while the unbonded sections exhibit minor tensile and compressive stresses. These unbonded sections have a unique deformed shape as the sections lose contact with the supports. The result is a reduced effective area of the isolator, the size of which is a

function of the bond length. As a consequence of the reduced size of the effective isolator, the magnitude of the normalized stresses observed is greater than that of the compression case which distributes the stresses over the entire width of the isolator. It should be noted that the system must be properly designed such that the expected tensile loads do not cause cavitation or delamination of the elastomer-fiber bonds.

#### 8.4.3 Horizontal Behaviour (Under Compression): $B < B_{max}$

The FEA force-displacement relationship, where the force is normalized by  $GA$ , with a maximum considered displacement of  $2.00 t_r$  for  $B = 0 \%$  and  $B = B_{max} = 5 \%$  is compared in Figure 8-12 for isolator type E1. As anticipated, the force-displacement relationship for  $B = 0 \%$  and  $B = B_{max}$  are indistinguishable from each other at all levels of displacement considered. Similar results were obtained for isolator type E2. The deformed shape at  $2.00 t_r$  is shown in Figure 8-13 for isolator type E1 and comparing the unbonded,  $B = 0 \%$ , and bonded,  $B = B_{max}$ , cases. It is evident that for both isolators, as with the experimental results, the deformed shape was also indistinguishable between the two cases. Furthermore, the stress contours of the normalized local stresses  $S_{33}$ , which are initially in the vertical direction, are shown. Results indicate that the bonded region does not introduce any stress concentrations, nor is any substantial alteration in the contours noted. In addition, the central section of the isolator that remains in contact is dominated by a compressive stress, whereas the rollover sections display a low tensile stress. Based on these observations it is postulated that any length of bond,  $0 \% < B < B_{max}$  will have negligible influence on the horizontal force-displacement relationship under vertical compressive stress.

#### 8.4.4 Horizontal Behaviour (Under Compression): $B > B_{max}$

The influence of bond length for  $B > B_{max}$  is considered in increments of 25 % from  $B_{max}$  to a fully bonded FREI with  $B = 25 \%$ , 50 %, 75 % and 100%. The FEA force-displacement relationships, where the force is normalized by  $GA$ , are compared in Figure 8-14. For the type E1 isolator, similar to the  $B = 0 \%$  and  $B = B_{max} = 5 \%$  case, there is negligible difference between  $B = 5 \%$  and  $B = 25 \%$ . As  $B$  is increased to 50 % an increase in the horizontal force is observed at approximately  $1.25 t_r$ . This slight increase is observed until full rollover occurs at approximately  $1.90 t_r$  where the cases of  $B = 5 \%$ , 25 % and 50 % once again become indistinguishable. The maximum increase over this range was 15 %. In the experimental program no appreciable difference was noted in the hysteresis between E1-1 and E1-2.

The deformed shape of  $B = 50 \%$  at  $2.00 t_r$  is shown in Figure 8-15 where, similar to the experimental results, localized deformations in the bonded rollover section occur. This localized deformation is associated with the minor increase in horizontal force observed in the  $1.25 t_r$  to  $2.00 t_r$  range. The rollover section is otherwise relatively

uninfluenced by the bond and completes full rollover, although delayed due to the bond. As a consequence of the bond, an increase in tensile stress is observed in the bonded rollover section. The central section also experiences an increase in compressive stress to accommodate the introduction of tensile stresses in the bonded rollover section.

Five distinct sections of the isolator are now observed: the central section, dominated by compressive stresses; two bonded rollover sections, which are a consequence of the bonded portion and are dominated by tensile stresses; and two conventional rollover sections, which are restrained by the bonded rollover section. These sections are illustrated schematically in Figure 8-16.

As the bond was increased to  $B = 75\%$  further softening was prevented at approximately  $0.75 t_r$  (see Figure 8-14). Despite the unbonded portion of the rollover section being approximately  $0.50 t_r$  in length, the influence of the partial bond was not observed until  $0.75 t_r$ . This is once again attributed to the vertical deflection of the isolator as described above. As the horizontal displacement increased, the size of the rollover section remained constant as additional rollover was restricted. As a consequence, the force-displacement relationship of the isolator becomes similar to that of a bonded isolator with a length equal to the bonded portion. Due to the increase in bond length, the size of the bonded rollover section was increased at the expense of the rollover section, as illustrated in Figure 8-17 at a displacement of  $2.00 t_r$ . The additional tensile stress that develops in the bonded rollover section, similar to a fully bonded isolator, was accommodated by an additional increase in compressive stress in the central section in comparison to the unbonded case (see Figure 8-13). In lieu of bulging outwards, the elastomeric layers bulged inwards and an increased amount of deformation was noted in the fiber reinforcement and elastomer at the interface of the rollover and bonded rollover sections. At this level of bonding, full rollover and the contact of the initially vertical face of the isolator with the supports was entirely prevented. Therefore, in this case, the stiffening observed is attributed to the bond and not to the occurrence of full rollover. The ratio of the horizontal force of  $B = 75\%$  in comparison to a fully bonded isolator,  $B = 100\%$ , at  $2.00 t_r$  was  $91\%$ . Since the ratio is larger than the bond length of  $B = 75\%$  this suggests that the rollover sections still contributes significantly to the horizontal force resistance capacity and that the horizontal force-displacement relationship of the isolator is not entirely dominated by the bonded portion.

Similar to type E1 isolators, the horizontal force-displacement relationship for type E2 isolators was indistinguishable for bond lengths slightly larger than  $B_{max}$ , and no appreciable difference was noted between  $B = B_{max} = 33\%$  and  $B = 50\%$ . As the length of the bond was increased to  $B = 75\%$  it was observed that further softening was prevented at approximately  $1.00 t_r$ . Review of the FEA results revealed that the bonded portion became effective at approximately  $1.00 t_r$ , thus preventing further rollover. The

deformed shape at  $2.00 t_r$  is shown in Figure 8-18. In both cases full rollover was prevented and the initially vertical face did not contact the supports. It was determined that the ratio of the horizontal force between  $B = 75 \%$  and a fully bonded isolator,  $B = 100 \%$ , at  $2.00 t_r$  was  $88 \%$ . As with type E1 isolators, it can be concluded that the restrained rollover section continues to provide substantial horizontal force resistance.

It is important to note that despite having identical bond lengths of  $B = 75 \%$  that the horizontal force-displacement relationship for type E1 and type E2 isolators diverged at different horizontal displacements,  $0.75 t_r$  and  $1.00 t_r$ , respectively. In this respect, the bond length,  $B$ , alone is not sufficient to give an accurate indication of the influence of the bond on the horizontal force-displacement relationship of the isolator. It has been demonstrated that the bond length can be significantly extended beyond  $B_{max}$  without notable change to the force-displacement relationship in comparison to an unbonded isolator. It is postulated that the level that the bond can be extended without notable influence is dependent on the level of vertical deflection of the isolator as previously discussed. It was observed that further softening was prevented when the bond prevented the loss of contact of the rollover section and the support.

#### 8.4.5 Horizontal Behaviour (Under Tension): $B > B_{max}$

A key component of the concept of PB-FREIs is the ability to provide tensile resistance. Accordingly, the horizontal properties under a vertical tensile load are important performance characteristics to investigate. FEA was used to investigate isolator type E1 with  $B = 50 \%$  under tension. The isolator was monotonically loaded to an average tensile stress of  $0.2 \text{ MPa}$ , based on the total plan area, before being displaced horizontally to a maximum displacement of  $2.00 t_r$ . Figure 8-19 compares the normalized force and stiffness of the tensile stress case to the reference unbonded case, conducted under a compressive stress of  $2.0 \text{ MPa}$ . It can be observed in Figure 8-19(a) that despite the tensile stress, the isolator exhibits the softening and stiffening response associated with SU-FREIs. While the response is similar to that of the reference case, the isolator under tension is initially softer and the stiffening at larger displacements is less than the reference case, as shown in Figure 8-19(b). Due to the tensile load, the unbonded portions of the isolator do not remain in contact with the supports. Subsequently, negligible shear forces are transferred through the unbonded portions at small displacements and the response of the isolator is dominated by the bonded portion.

As the horizontal displacement increases, the unbonded portions move in a near-rigid-body mode until contacting the supports, as shown in Figure 8-20(a). The normalized stress  $S_{33}$  contours are in essence the opposite of those previously observed for a partially bonded isolator under compression. The central section of the isolator is now dominated by a tensile stress whereas the rollover regions are largely in compression. Similar to full rollover of a SU-FREI, this contact is associated with an

increase in horizontal resistance. As the horizontal displacement increases the unbonded sections are forced into the supports resulting in a contact compressive stress. The development of this compressive stress allows for horizontal forces to be transferred through the contact regions. In addition, conventional rollover occurs as the initially vertical faces become horizontal and contact the supports. The deformed shape of the isolator at a displacement of  $1.50 t_r$  is shown in Figure 8-20(b). At this displacement the isolator begins to stiffen and the horizontal force begins to exceed the horizontal force of the unbonded reference case. Similar to the previously discussed partially bonded cases under compression, the partial bond restrains additional rollover, which prevents further softening. It can be seen that the portion of the isolator where the upper and lower bond overlap are dominated by tension. The remainder of the central section displays both minor tensile and compressive stresses. The contact that occurs due to the secondary rollover develops a moment equilibrating compressive stress.

The tangential stiffness for displacements between  $1.50 t_r$  and  $2.00 t_r$  is approximately constant (see Figure 8-19(a)). Despite the large horizontal displacement the isolator does not complete full rollover as regions of the initially vertical face of the isolator do not contact the horizontal supports. The unique deformed shape at  $2.00 t_r$  is shown in Figure 8-20(c). Throughout the levels of imposed horizontal displacement a gap develops between the bonded region and the rollover sections. The bonded region of the isolator is entirely in tension. Portions of the rollover section remain in contact with the supports but the overall level of compressive stress is significantly reduced. For isolators displaced horizontally under compression, the horizontal force and vertical compressive stress act together to increase the moment on the isolator that must be equilibrated. Conversely, the moments generated by the vertical tensile force and horizontal force counteract each other, reducing or eliminating the development of an equilibrating moment through changes in the vertical pressure distribution. Therefore, as the horizontal force increases, it reduces the compressive stress necessary to maintain moment equilibrium and consequently the compressive stresses generated due to contact of the rollover sections were reduced.

Regardless of the unique deformation and reduced contact area, the tangential stiffness remains positive over all levels of imposed displacement, maintaining stability. Furthermore, the overall force-displacement relationship remains comparable to the reference case of an unbonded FREI under compression. These findings suggest that PB-FREIs have the potential to provide tensile resistance without significantly altering the horizontal properties and performance of the isolator.

#### **8.4.6 Influence of Vertical Load**

It has been shown experimentally that the horizontal stiffness of unbonded FREIs decreases as the vertical compressive load increases [23]. Similarly, in bonded SREIs

analytical and FEM results demonstrate that the horizontal stiffness decreases with increasing vertical tensile load [9, 10]. It is postulated that PB-FREIs are likewise influenced by the vertical load; softening as the magnitude of the load increases. The findings of this study have indicated that the properties of PB-FREIs with vertical tensile load are sensitive to the length of the bonded section. Accordingly, it is expected that the sensitivity to the bonded section will also apply to the influence of the vertical tensile load. Conversely, under compression the length of the bond did not significantly change the horizontal properties for bond lengths substantially exceeding  $B_{max}$ . Therefore, the influence of the vertical compression load is expected to be comparable to an unbonded FREI of identical design for bond lengths lower than  $B_{max}$ .

### 8.5 Conclusion

In this paper partially bonded fiber-reinforced elastomeric isolators (PB-FREIs) were proposed to allow the transfer of tensile forces and to address concerns over permanent displacement due to slip under certain loading conditions in unbonded FREIs. By bonding an interior portion of the isolator it is postulated that adequate tensile resistance can be introduced and permanent displacement may be prevented without compromising the advantages associated with rollover of the isolator. Preliminary experimental and finite element analysis demonstrated that large portions of the isolator could be bonded without notably influencing the rollover characteristics of the isolator. From the experimental study and finite element analysis conducted, the main observations are:

1. For isolators with an aspect ratio  $R > 3.3$  a portion of the isolator does not rollover. FEA showed that bonding this portion of the isolator had negligible effect on the force-displacement response, deformed shape and local stress distribution.
2. Under pure tensile loading a reduced effective isolator develops based on the bond length. Due to the reduced area under tensile loads, the vertical modulus of a PB-FREI was found to be lower in tension than compression.
3. It was observed that further softening was prevented when the bonded portion prohibited further loss of contact and prevented additional rollover. The bond length that could be provided before a change in the horizontal force-displacement response was observed could be substantially larger than the maximum bond length determined from theory. It was postulated that this was a consequence of the vertical deflection of the isolator which prevented loss of contact between the isolator and the supports in the rollover section.
4. Under tension, the isolator can retain a positive incremental force-displacement relationship. The response of the isolator was characterized by a central section that formed around the bonded portion and two rollover sections. The rollover sections demonstrated two levels of rollover; one

similar to a conventional isolator and a secondary rollover that occurred as the unbonded regions contacted the supports.

The concept of PB-FREIs requires experimental investigation under pure tension and combined shear-tension to assess any possible vulnerability of the isolators to cavitation in the elastomer or failure of the elastomer-to-fiber or elastomer-to-steel bonds. It is suggested that with further development PB-FREIs can be used to address concerns over the transfer of tensile forces and slip under certain loading conditions while still retaining the desirable characteristics of unbonded FREIs.

### *Acknowledgements*

Financial support for this study was provided by the McMaster University Centre for Effective Design of Structures (CEDs) funded through the Ontario Research and Development Challenge Fund (ORDCF) as well as an Early Researcher Award (ERA) grant, both are programs of the Ministry of Research and Innovation (MRI). Support was also provided through the Natural Sciences and Engineering Research Council (NSERC) of Canada. The support of a Vanier Canada Graduate Scholarship is gratefully acknowledged.

### *References*

- [1] Kelly JM. Analysis of fiber-reinforced elastomeric isolators. *Journal of Seismology and Earthquake Engineering* 1999; **2**:19-34.
- [2] Moon BY, Kang GJ, Kang BS, Kelly JM. Design and manufacturing of fiber reinforced elastomeric isolator for seismic isolation. *Journal of Materials Processing Technology* 2002; **130-131**:145-150.
- [3] Toopchi-Nezhad H, Tait MJ, Drysdale, RG. Bonded versus unbonded strip fiber reinforced elastomeric isolators: Finite element analysis. *Composite Structures* 2011; **93**:850-859.
- [4] Toopchi-Nezhad H, Tait MJ, Drysdale, RG. Testing and modeling of square carbon fiber-reinforced elastomeric seismic isolators. *Structural Control and Health Monitoring* 2008; **15**:876-900.
- [5] Toopchi-Nezhad H, Drysdale RG, Tait MJ. Parametric Study on the Response of Stable Unbonded-Fiber Reinforced Elastomeric Isolators (SU-FREIs). *Journal of Composite Structures* 2009; **43**(15):1569-1587.
- [6] International Organization for Standardization. Elastomeric seismic-protection isolators, ISO 22762. International Organization for Standardization, 2010.
- [7] American Society of Civil Engineers. Minimum design loads for buildings and other structures, ASCE/SEI 7-10. American Society of Civil Engineers, 2010.
- [8] Naeim F, Kelly JM. *Design of Seismic Isolated Structures: From Theory to Practice*. Wiley: New York, 1999.
- [9] Kelly JM. Tension buckling in multilayer elastomeric bearings. *Journal of Engineering Mechanics ASCE* 2003; **129**(12):1363-1368.

- [10] Kelly JM, Konstantinidis D. *Mechanics of Rubber Bearings for Seismic and Vibration Isolation*. Wiley: Chichester, 2011.
- [11] Magliulo G, Capozzi V, Fabbrocino G, Manfredi G. Neoprene–concrete friction relationships for seismic assessment of existing precast buildings. *Engineering Structures* 2011; **33**(2): 532-538.
- [12] Kelly JM, Konstantinidis D. Effect of friction on unbonded elastomeric bearings. *Journal of Engineering Mechanics ASCE* 2009; **135**(9):953-960.
- [13] Konstantinidis D, Kelly JM, Makris, N. *Experimental investigation on the seismic response of bridge bearings*. Report EERC-2008/02. Earthquake Engineering Research Center: University of California, Berkeley, 2008.
- [14] Steelman JS, Fahnstock LA et al. Shear and friction response of non-seismic laminated elastomeric bridge bearings subject to seismic demands. *Journal of Bridge Engineering ASCE* 2013; **18**(7): 612-623.
- [15] Foster BAD. *Base isolation using Stable Unbonded Fibre Reinforced Elastomeric Isolators (SU-FREI)*. M.A.Sc. thesis. McMaster University: Hamilton, 2011.
- [16] Russo G, Pauletta M. Sliding instability of fiber-reinforced elastomeric isolators in unbonded applications. *Engineering Structures* 2013; **48**:70-80
- [17] Kelly JM, Konstantinidis D. Low-cost seismic isolators for housing in highly-seismic developing countries. ASSISI 10<sup>th</sup> World Conference on Seismic Isolation, Energy Dissipation and Active Vibrations Control of Structures, Turkey, 2007.
- [18] Russo G, Pauletta M, Cortesia A. A study on experimental shear behavior of fiber-reinforced elastomeric isolators with various fiber layouts, elastomers and aging conditions. *Engineering Structures* 2013; **52**:422-433.
- [19] de Raaf M. *Experimental Study of Unbonded Fiber Reinforced Elastomeric Bearings*. M.A.Sc. thesis. McMaster University: Hamilton, 2009.
- [20] Mordini A, Strauss A. An innovative earthquake isolation system using fibre reinforced rubber bearings. *Engineering Structures* 2008; **30**:2739-2751.
- [21] Osgooei PM, Tait MJ, Konstantinidis D. Finite element analysis of unbonded square fiber-reinforced elastomeric isolators (FREIs) under lateral loading in different directions. *Composite Structures* 2014; **113**:164-173.
- [22] MSC Marc. Theory and user information, vol. A. MSC Software Corporation: Santa Ana, 2011.
- [23] de Raaf MGP, Tait MJ, Toopchi-Nezhad H. Stability of fiber reinforced elastomeric bearings in an unbonded application. *Journal of Composite Materials* 2011; **45**(18):1873-1884.

Table 8-1: Comparison of the ratio of partially bonded to unbonded experimental results.

Disp. ( $t_r$ )	$k_{eff}$		$\zeta_{eq}$	
	E1-2/E1-1	E2-2/E2-1	E1-2/E1-1	E2-2/E2-1
0.25	1.05	0.94	0.99	1.02
0.50	1.20	0.96	0.82	1.08
0.75	1.10	0.95	0.99	1.02
1.00	1.06	0.95	0.97	1.01
1.50	1.04	0.96	0.95	1.00
2.00	1.01	0.97	0.94	0.95

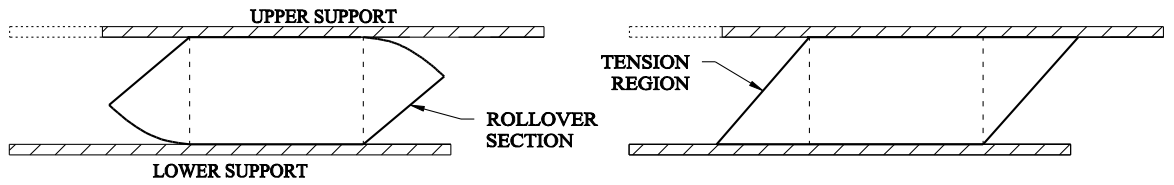


Figure 8-1: Deformed shape of (a) an unbonded FREI and (b) a bonded isolator

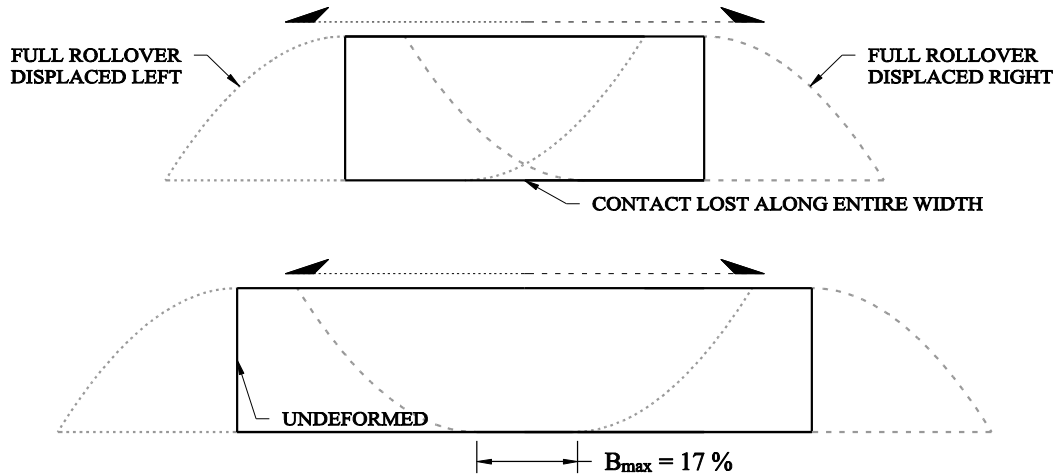


Figure 8-2: Deformed shape of an isolator with  $R = 2.5$  and  $R = 4.0$  at full rollover, showing the portion of the width that remains in contact with the supports

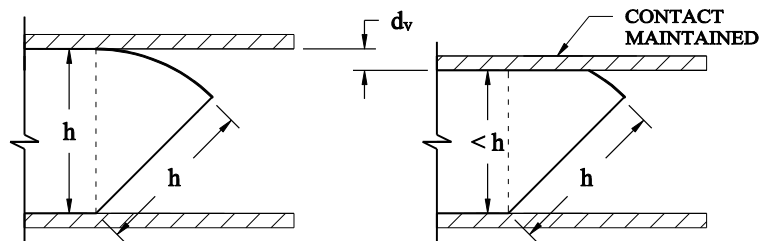


Figure 8-3: Exaggerated delayed loss of contact due to vertical deflection,  $d_v$

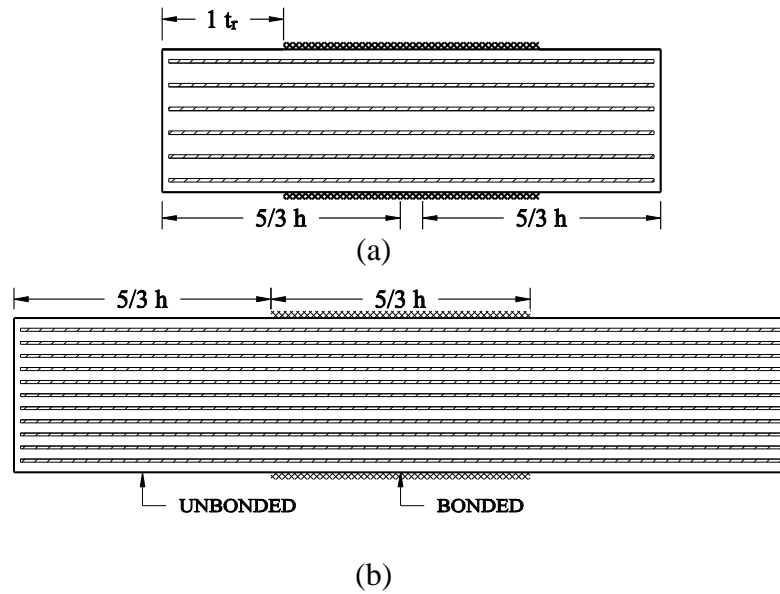


Figure 8-4: Profile view identifying bonded and unbonded regions of (a) isolator E1-2 ( $B = 50\%$ ) and (b) isolator E2-2, ( $B = 33\%$ )

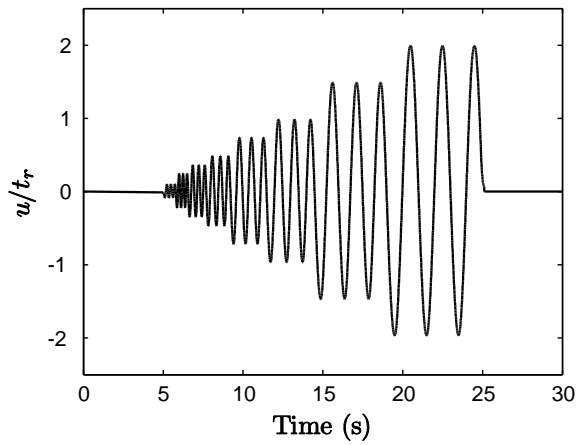


Figure 8-5: Horizontal experimental displacement history

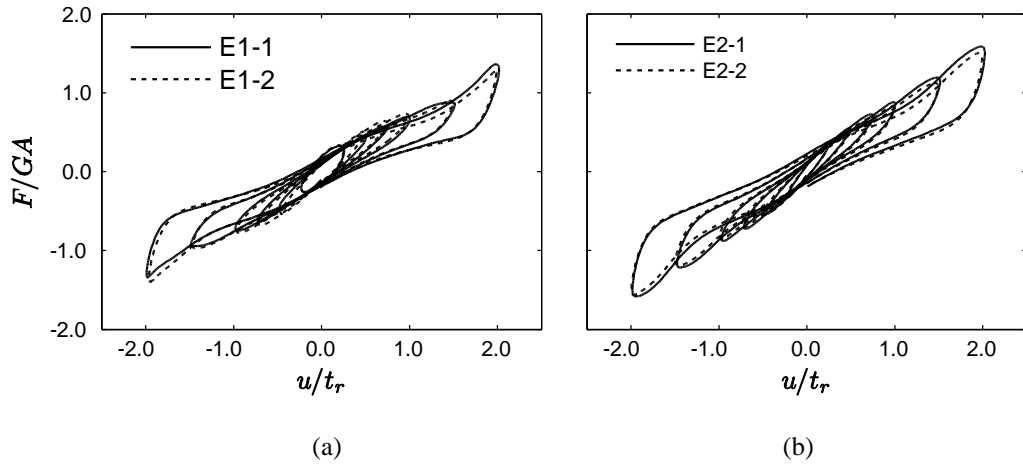


Figure 8-6: Normalized experimental force-displacement hysteresis loops for (a) isolator E1-1 and E1-2, and (b) isolator E2-1 and E2-2

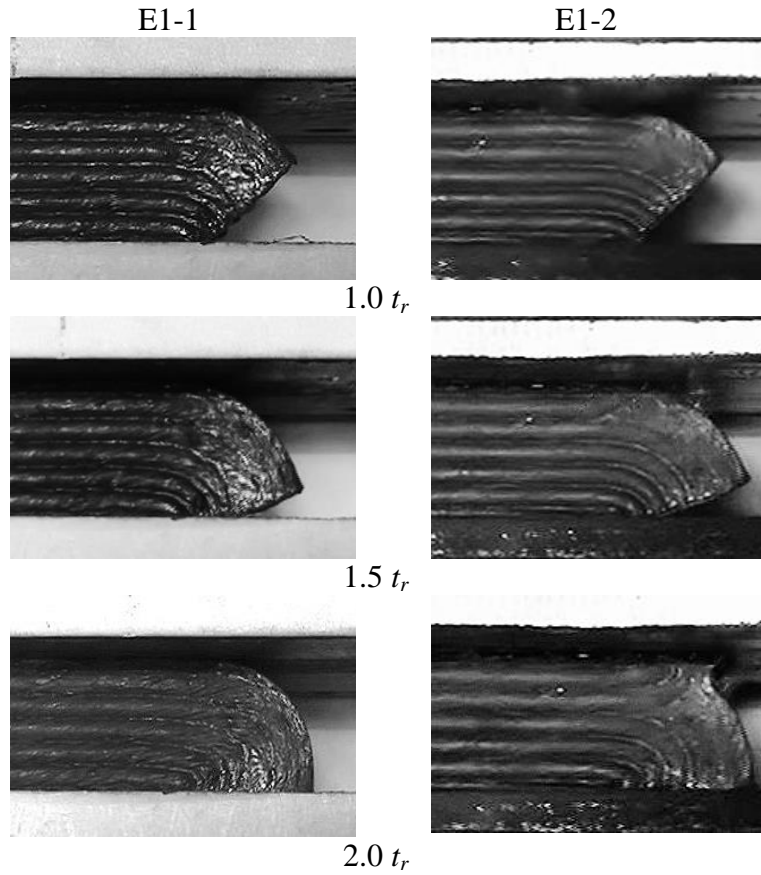


Figure 8-7: Comparison of the deformed shape of the rollover of E1-1 and E1-2

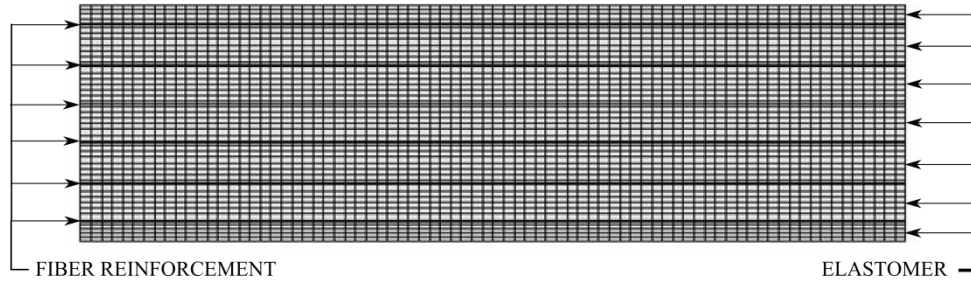


Figure 8-8: FEA model of isolator E1

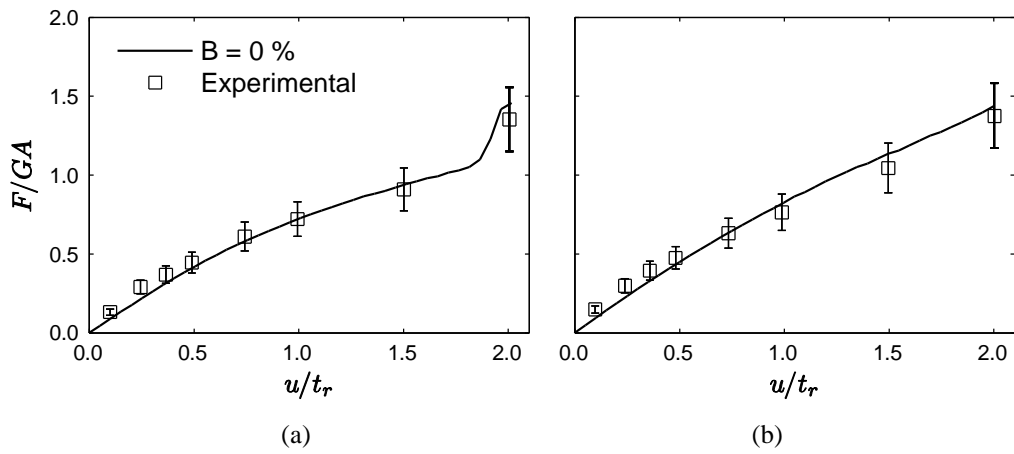


Figure 8-9: Comparison of FEA and experimental results with 15 % error bars for (a) E1-1 and (b) E2-1

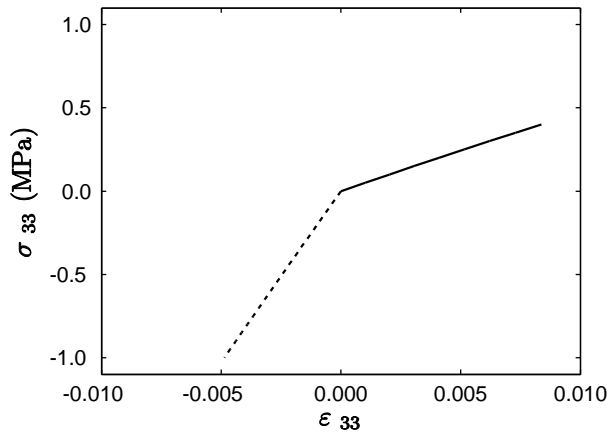


Figure 8-10: Vertical stress strain relationship for isolator type E1 from FEA under tension and compression

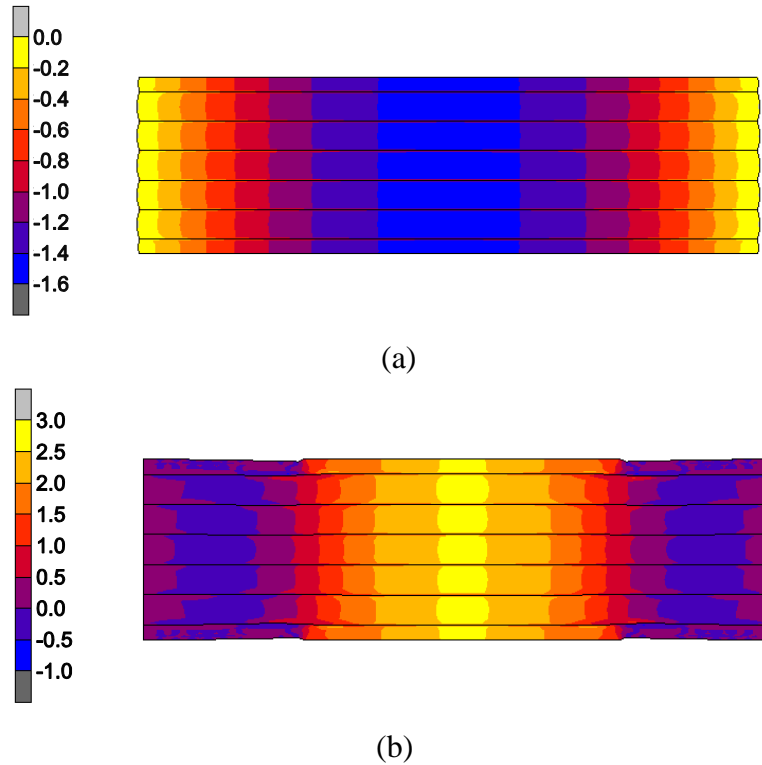


Figure 8-11: Normalized local stress  $S_{33}$  contours for isolator type E1 with  $B = 50\%$  under (a) 1.0 MPa compressive and (b) 0.4 MPa tensile stress

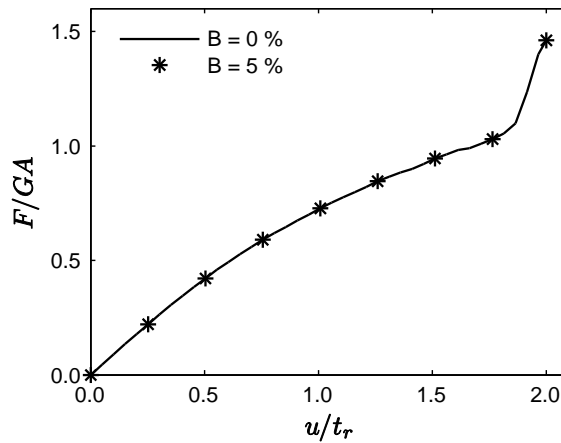


Figure 8-12: Comparison of  $B = 0\%$  and  $B = B_{max} = 5\%$  results for isolator type E1 showing negligible difference between the bonded and unbonded case

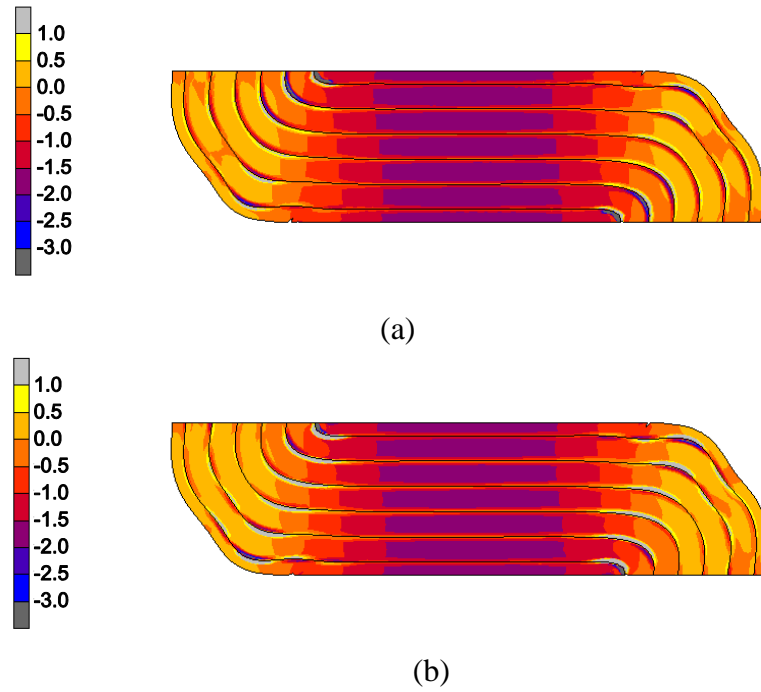


Figure 8-13: Normalized local stress  $S_{33}$  contours for isolator type E1 with (a)  $B = 0\%$  and (b)  $B = B_{max}$  at  $2.00 t_r$ .

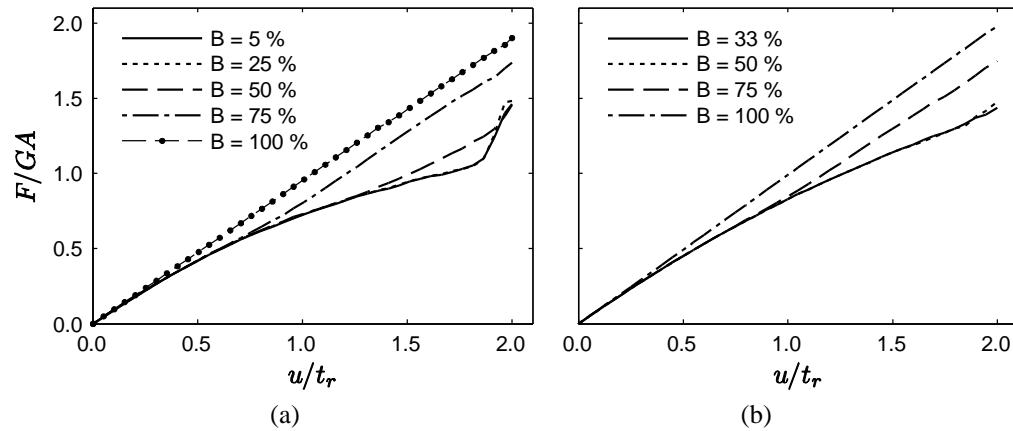


Figure 8-14: Normalized force-displacement relationship with  $B > B_{max}$  for (a) isolator type E1 and (b) isolator type E2

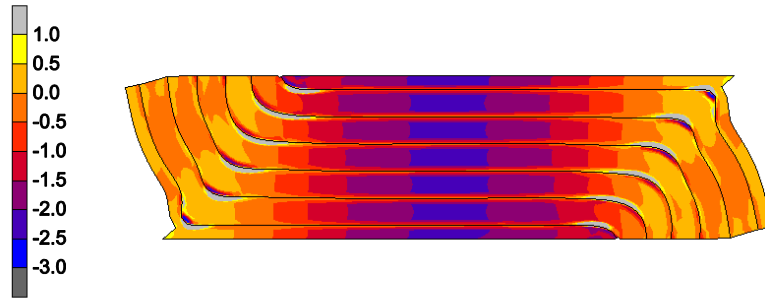


Figure 8-15: Normalized local stress  $S_{33}$  of isolator type E1 with  $B = 50 \%$  at  $2.00 t_r$ .

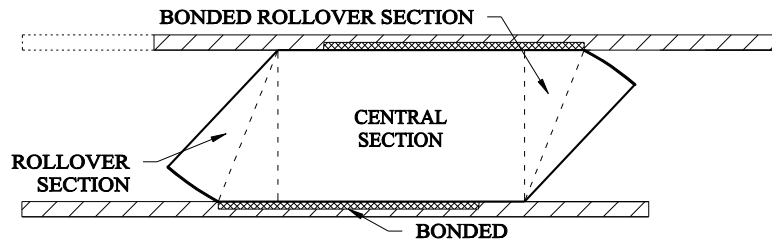


Figure 8-16: Idealized division of a PB-FREI into five sections.

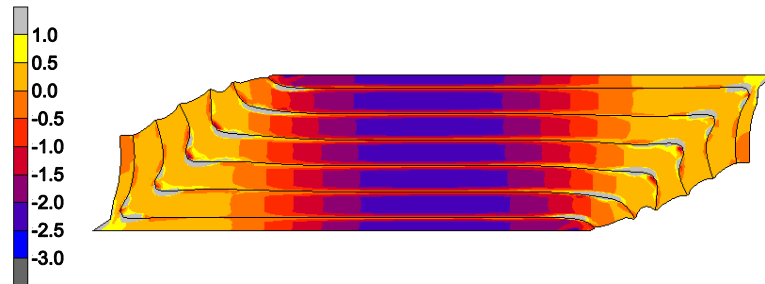


Figure 8-17: Normalized local stress  $S_{33}$  of isolator type E1 with  $B = 75 \%$  at  $2.00 t_r$ .

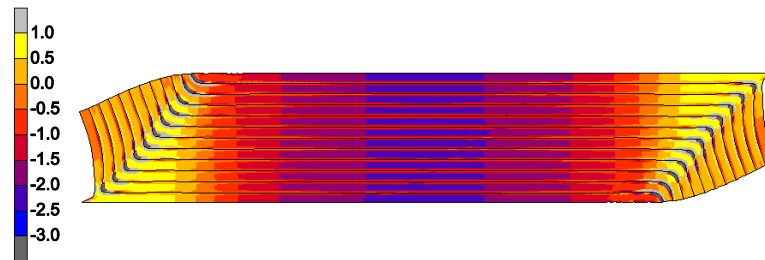


Figure 8-18: Normalized local stress  $S_{33}$  of isolator type E2 with  $B = 75 \%$  at  $2.00 t_r$ .

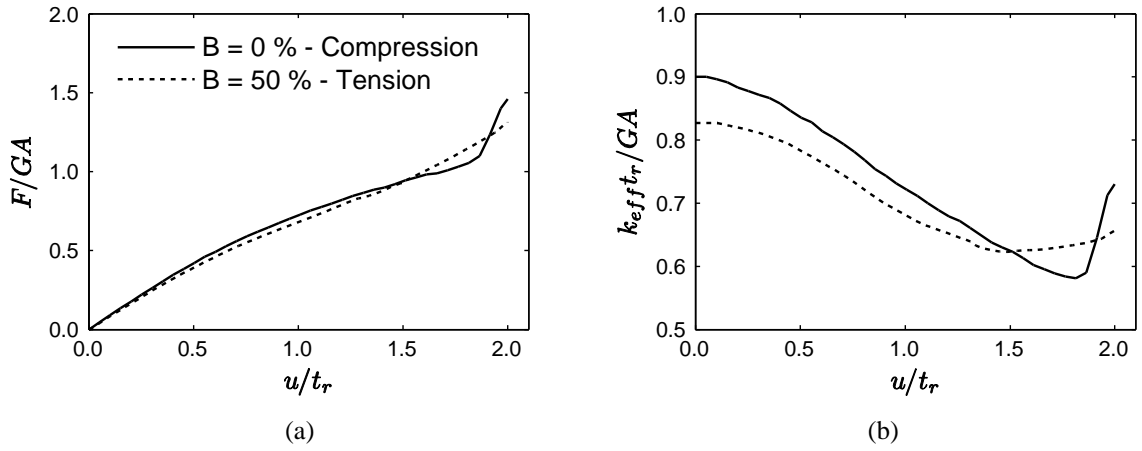


Figure 8-19: Normalized (a) force and (b) stiffness as a function of displacement for isolator type E1 with  $B = 0\%$  and a 2.0 MPa average vertical compressive stress and  $B = 50\%$  with a 0.2 MPa average vertical tensile stress

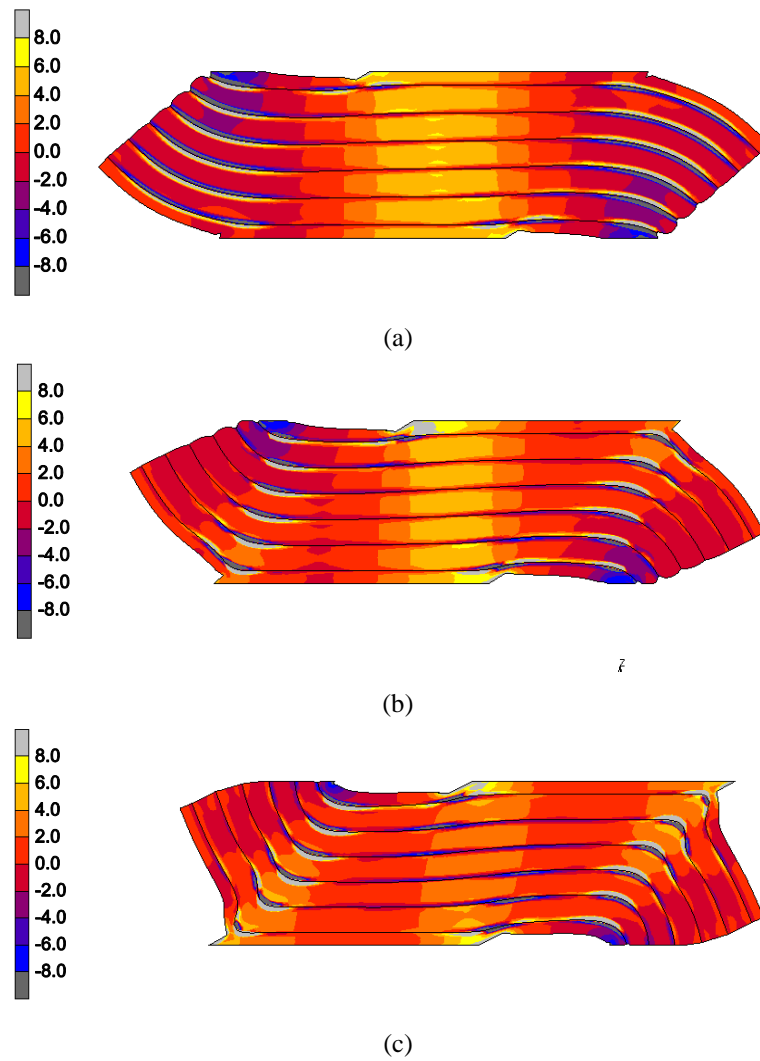


Figure 8-20: Normalized local stress  $S_{33}$  of isolator type E2 with  $B = 50\%$  and 0.2 MPa average vertical tensile stress at (a)  $1.00 t_r$ , (b)  $1.50 t_r$ , and (c)  $2.00 t_r$

## 9 Conclusions and Recommendations

### 9.1 Summary

Earthquakes pose a significant risk to many densely populated areas in Canada and around the world. The application of base isolation technology has the potential to improve on life safety performance objectives, and to extend protection to the structure and non-structural components and systems. In this respect, SU-FREIs have been proposed as a potential low-cost isolation system with adaptive characteristics appropriate for application in developed and developing countries. The research conducted in this thesis expands the understanding of SU-FREIs by identifying and addressing potential limitations and proposing variations to modify the horizontal hysteresis loops and performance characteristics. Chapter 2 presented a literature review of existing investigations into elastomeric isolators. The chapter included a discussion on the different materials available and how FREIs vary from conventional SREIs. Chapter 3 proposed an analytical model on the horizontal force-displacement relationship of a SU-FREI that included full rollover and the deformed shape. Chapter 4 and Chapter 5 proposed general formulas for the compression modulus, bending modulus, maximum shear strain due to compression, and maximum shear strain due to rotation for use in design. The formulas were derived from the analytical solutions and could be adapted to different pad geometries by selecting appropriate correction factors from a table. Chapter 6 and Chapter 7 demonstrated how the geometry of the isolator or the supports could be modified to alter the vertical and horizontal properties of the isolator. Chapter 8 proposed partially bonding the isolator to form a hybrid between a SU-FREI and fully bonded FREI in order to address concerns over permanent displacement in extreme loading conditions and the transfer of vertical tensile forces. Major conclusions for these chapters are presented in the subsequent sections.

#### 9.1.1 Model of the Shear Behavior of Unbonded Fiber-Reinforced Elastomeric Isolators

The rollover deformation that occurs in unbonded FREIs is a complex response resulting from the flexibility of the fiber reinforcement and the unbonded application. Most simple analytical models of unbonded FREIs neglect the rollover deformation of the isolator. An analytical model was developed to determine the horizontal force-displacement relationship using a cantilever representation of the rollover sections and large deflection theory. The model accounted for the reinforcement flexibility and captured the deformed shape of the rollover section, which was subsequently used to predict full rollover. After full rollover, the model was adjusted to predict the post-full rollover response of the isolator. The model was used to conduct a parametric study on the width-to-total height aspect ratio and reinforcement flexibility. It was found that the

transition between a horizontally unstable and stable isolator occurred at a width-to-total height aspect ratio of approximately 2.5. Furthermore, by an aspect ratio of about 10.0, the amount of softening was minimal and could be neglected. Increasing the bending modulus of the flexible reinforcement was found to delay full rollover and reduced the softening characteristics of the isolator.

### **9.1.2 Development of Design Orientated Formulas for Elastomeric Bearings**

Design codes often remain technology neutral; however, the assumption of rigid reinforcement (i.e. steel reinforcement) is typical in codes and standards related to elastomeric bearings. In order to include the effects of reinforcement extensibility and elastomer bulk compressibility, which can influence the isolator properties, generalized expressions were proposed for the compression modulus, bending modulus, maximum shear strain due to compression and maximum shear strain due to rotation. These generalized expressions are simple to use in comparison to the often complex analytical solutions and can easily be adapted to the specific geometry of the bearing. It was demonstrated that the error of the proposed approximations was generally low and conservative when compared to the analytical solution. It was recommended that the generalized expressions be adopted in design codes in lieu of the often complex analytical solutions and current approximations that neglect these critical effects. The development of technology neutral code equations is anticipated to remove barriers to the application of FREIs.

### **9.1.3 Experimental and Finite Element Study on the Compression Properties of Modified Rectangular Fiber-Reinforced Elastomeric Isolators**

MR-FREIs were proposed as a method of reducing the potentially high horizontal stiffness of long rectangular FREIs. Large rectangular isolators are able to provide uniform support along walls, reducing the requirements of structural systems to transfer loads to smaller isolators. The vertical properties of rectangular FREIs with modifications to the exterior and interior portions of the loaded surface were investigated experimentally and numerically. It was found that both the vertical stiffness and compression modulus were highly sensitive to interior modifications and, to a lesser extent, exterior modifications. The maximum shear strain was also greater in isolators with an interior modification. The primary purpose of MR-FREIs is to reduce the potentially high horizontal stiffness; consequently, the horizontal behaviour of MR-FREIs requires further investigation. A subsequent study by the authors indicated that the influence of modifications on the horizontal properties is displacement dependent, but a favourable decrease in horizontal stiffness and an increase in energy dissipation capability have been observed.

#### **9.1.4 Structural and Non-structural Performance of a Seismically Isolated Building using Stable Unbonded Fiber-Reinforced Elastomeric Isolators**

The stiffening that occurs in isolators that exhibit adaptive characteristics (e.g. the TFP and SU-FREIs) has often been considered to act as a self-restraint against excessive displacements in events that meet or exceed the maximum considered earthquake. The findings of this study indicated that this claim may not be accurate in all circumstances. The stiffening regime of SU-FREIs was effectively altered by applying MSG, which could accelerate or delay full rollover. It was demonstrated that, for the earthquake records considered, the stiffening regime provided minimal displacement restraint. Furthermore, the stiffening was proportionally reflected in the response of the structure and the NCS. Despite the minimal displacement restraint provided for the earthquake records considered, it was noted that the stiffening regime was still advantageous and necessary to maintain horizontal stability. Furthermore, it was postulated that the stiffening could be used in conjunction with elastomeric bumpers to mitigate pounding against seismic gap walls.

#### **9.1.5 Partially Bonded Fiber-Reinforced Elastomeric Isolators**

The unbonded application, in combination with the flexibility of the fiber reinforcement, allows for the desirable rollover deformation observed in unbonded FREIs to occur. However, it is simultaneously the source of perceived limitations, such as the potential for permanent displacements due to slip and the inability to transfer vertical tensile forces. It was proposed that these concerns could be eliminated by partially bonding the isolator to the upper and lower supports to form a hybrid of an unbonded FREI and a fully bonded FREI. In this way, the isolator retains the beneficial rollover deformation, but also resists slip and provides some level of tensile resistance through the partial bond. The investigation analytically derived that isolators with a width-to-total height aspect ratio of 3.3 and greater would have a region that does not enter into the rollover sections.

Finite element analysis determined that a partial bond that enters the rollover section could potentially prohibit further softening and delay or prevent full rollover. The length of the partial bond that could be introduced before altering the horizontal force-displacement relationship was substantial. The numerical investigation also investigated the horizontal force-displacement relationship of a PB-FREI under tension. It demonstrated that horizontal stability could be maintained with a vertical tensile load and had a similar overall relationship as observed in compression; however, this portion of the study lacked experimental verification.

## 9.2 *Recommendations for Future Study*

The following details recommendations for future research on SU-FREIs and other variations of FREIs:

- FREIs are often described as a potentially low-cost alternative to SREIs; however, a detailed cost analysis to verify this claim has not been conducted. Although FREIs and SREIs have been compared directly experimentally and numerically using finite element analysis, to fully verify the potential cost saving, a detailed study considering the manufacturing costs, installation, constructability, life-cycle costs, and performance objectives must be conducted. Such a study would be instrumental in validating the low-cost claim made in numerous studies on FREIs and promoting the use of low-cost base isolation systems.
- A numerical study presented herein identified that the stiffening regime for the SU-FREI considered did not provide substantial displacement restraint for the selected earthquakes. This was contrary to the claims made in many studies on adaptive devices with similar softening and stiffening characteristics. It was noted in the study that the findings were limited to the specific ground motions and isolator type and design considered. Therefore, a similar investigation should be conducted considering other adaptive devices and a broader range of ground motions with different characteristics. Furthermore, to avoid an iterative procedure, a single calibration was used to model the SU-FREI considered over the entire displacement range. It was noted that this approach did not accurately capture the damping characteristics as the equivalent viscous damping increases over larger amplitude cycles (i.e.  $2.50 t_r$ ). It is anticipated that the damping characteristics will play a greater part in preventing excessive displacements, warranting further investigation and potential revision to the calibrated element. While the stiffening characteristics may not provide substantial displacement restraint, it was postulated that the stiffening could be used in conjunction with elastomeric bumpers to mitigate moat-wall pounding. A numerical investigation should be conducted to further investigate this potential benefit.
- Studies that compare SREIs and FREIs directly have been conflicting; notably, these studies have provided differing conclusions on the damping characteristics of FREIs. Some studies have claimed that the damping characteristics of FREIs derive entirely from the elastomer, whereas other studies attribute additional damping to the inter-fiber movement of the fiber reinforcement. These conflicting conclusions alone suggest that additional investigation is required. These conclusions could be verified by comparing FREIs with different types of fiber reinforcement (i.e. different material, density, weaves, etc.) while using the same elastomer. It should be noted that a direct comparison between SREIs and FREIs

is difficult since the thickness of the fiber reinforcement is often much less than the steel reinforcement, resulting in different geometric properties.

- It is well established through theoretical analysis and experimental studies that the vertical force reduces the horizontal stiffness in SREIs. An experimental study demonstrated that a similar relationship exists for unbonded FREIs. However, theoretical analysis that includes the rollover sections has not been conducted. This is a critical component of a comprehensive model to predict the horizontal force-displacement relationship of unbonded FREIs.
- The aging of elastomers and of SREIs has been investigated in numerous studies. Only studies using accelerated aging methods have been conducted for FREIs and no investigation with natural aging has yet been conducted. The verification of long-term performance is a necessity. Although these characteristics are largely dependent on the elastomer, it is unclear if the introduction of fiber reinforcement will have any consequence or benefit. Furthermore, the performance of FREIs in colder climates should also be investigated. This is critical to determine the applicability of SU-FREIs in a Canadian climate and to establish the necessary temperature conditions of the isolation layer, if any.

## Appendix A: Generalized Approximations for a Rectangular Pad

### Preamble

Proposed approximations for the compression modulus, bending modulus and maximum shear strain due to compression are derived in this section. Approximations for these critical properties were omitted from Van Engelen and Kelly [1] and Van Engelen et al. [2]. The procedure used herein is identical to Van Engelen et al. [2].

### Compression Modulus

The compression modulus of a rectangular pad, including compressibility and extensibility, is given in Kelly and Van Engelen [3] as

$$E_c = 96GS^2 \frac{(1+\rho)^2}{\rho^2} \sum_{n=1,3,5,\dots}^{\infty} \frac{1}{\xi_n^2 n^2 \pi^2} \left( 1 - \frac{\tanh(\xi_n)}{\xi_n} \right) \quad (A1)$$

where

$$\lambda^2 = \frac{12GS^2}{K_{e=2}} \quad (A2)$$

$$\xi_n^2 = \frac{\lambda^2 (1+\rho)^2 + n^2 \pi^2 / 4}{\rho^2}$$

$E_c$  is the compression modulus,  $G$  is the shear modulus,  $S$  is the shape factor,  $\rho$  is the aspect ratio, and  $K_e$  is an equivalent parameter accounting for the compressibility of the elastomer and extensibility of the reinforcement.

The following approximation is proposed

$$\frac{1}{E_c} = \frac{1}{4\rho_c GS^2} + \frac{7}{5} \frac{1}{K} + \frac{14}{5} \frac{t}{E_f t_f} \quad (A3)$$

where

$$\rho_c = \frac{2.96\rho^2 + 4.01\rho + 0.47}{2.97\rho^2 - 0.14\rho + 1.59} \quad (A4)$$

$K$  is the bulk modulus of the elastomer,  $t$  is the thickness of an elastomeric layer, and  $t_f$  is the thickness of a reinforcement layer.

The values of  $\kappa_c = 7/5$  and  $\kappa_{ec} = 14/5$  (i.e. the coefficients to the compressibility and extensibility terms in Eq. (A3), respectively) were selected from Van Engelen et al. [2] based on a square pad geometry. It was observed that only the first term of Eq. (A3) (i.e. the incompressible and inextensible solution) was significantly sensitive to changes  $\rho$ . The function  $\rho_c$  was developed based on least squares regression over  $1 \leq \rho \leq 10$  to correct for the influence of the aspect ratio. Figure A1 shows the percent error with  $\rho = 2$

and Figure A2 shows the sensitivity of the error to  $\rho$ . The form and magnitude of the error is similar to the approximation for a square pad, as presented in Van Engelen et al. [2].

### *Maximum Shear Strain due to Compression*

The maximum shear strain due to compression,  $\gamma_c$ , normalized by the compression strain,  $\varepsilon_c$ , for a rectangular pad is [3]

$$\frac{\gamma_c}{\varepsilon_c} = 24S \frac{(1+\rho)}{\rho} \sum_{n=1,3,5,\dots}^{\infty} \frac{1}{\xi_n n \pi} \tanh(\xi_n) \sin\left(\frac{n\pi}{2}\right) \quad (\text{A5})$$

The following approximation is proposed

$$\frac{\gamma_c}{\varepsilon_c} = \left( \frac{1}{6\rho_s S} + 0.945 \frac{GS}{K_{e=2}} \right)^{-1} \quad (\text{A6})$$

where

$$\rho_s = \frac{1.42\rho^2 + 0.78\rho + 1.64}{1.43\rho^2 - 0.77\rho + 2.18} \quad (\text{A7})$$

The function  $\rho_s$  was developed based on least squares regression over  $1 \leq \rho \leq 10$  to correct the incompressible solution for the influence of the aspect ratio, and the approximation is otherwise identical to a square pad, presented in Van Engelen et al. [2].

Equation (A6) is selected if the following criterion is satisfied

$$S < \sqrt{\frac{1}{7.658} \frac{K_{e=2}}{G}} \quad (\text{A8})$$

If the criterion in Eq. (A8) is not satisfied, the following approximation is selected

$$\frac{\gamma_c}{\varepsilon_c} = \sqrt{3 \frac{K_{e=2}}{G}} \quad (\text{A9})$$

Figure A3 shows the percent error with  $\rho = 2$ ; the percent error is not largely sensitive to  $\rho$  and remains within  $\pm 14\%$  over  $1 \leq \rho \leq 10$ .

### *Bending Modulus*

The analytical solution for the bending modulus,  $E_b$ , of a rectangular pad including the compressibility of the elastomer and extensibility of the reinforcement is [4]

$$E_b = \frac{576GS^2}{\pi^4} (1+\rho)^2 \sum_{n=1,2,3}^{\infty} \sum_{m=1,3,5}^{\infty} \frac{1}{m^2 n^2} \frac{1}{(\rho n \pi)^2 + \left(\frac{m\pi}{2}\right)^2 + \lambda^2 (1+\rho)^2} \quad (\text{A10})$$

where

$$\lambda^2 = \frac{12GS^2}{K_{e=2}} \quad (\text{A11})$$

The following approximation is proposed

$$\frac{1}{E_b} = \frac{1}{\frac{4}{5}\rho_b GS^2} + \frac{8}{5} \frac{1}{K} + \frac{16}{5} \frac{t}{E_f t_f} \quad (\text{A12})$$

where

$$\rho_b = \frac{1.16\rho^2 + 1.49\rho + 2.44}{1.10\rho^2 + 0.23\rho + 0.49} \quad (\text{A13})$$

The function  $\rho_b$  was developed based on least squares regression over  $0.5 \leq \rho \leq 10$  to correct the incompressible solution for the influence of the aspect ratio, and the approximation is otherwise identical to a square pad from Van Engelen et al. [2]. Note that  $\rho < 1$  is representative of bending about the strong axis. The percent error of the proposed approximation is shown in Figure A4 with  $\rho = 2$ . The percent error is not largely sensitive to  $\rho$  if  $\rho > 1$ ; if  $\rho < 1$  the maximum error approaches 30 %, although the general trend remains the same.

### References

- [1] Van Engelen NC, Kelly JM. 2015. Correcting for the Influence of Bulk Compressibility on the Design Properties of Elastomeric Bearings. *J. Eng. Mech.-ASCE*, 141(6).
- [2] Van Engelen NC, Tait MJ, Konstantinidis D. 2015. Development of Code Oriented Formulas for Elastomeric Bearings Including Bulk Compressibility and Reinforcement Extensibility. *J. Eng. Mech.-ASCE*. [in-press]
- [3] Kelly JM, Van Engelen NC. 2015. Single Series Solution for the Rectangular Fiber-Reinforced Elastomeric Isolator Compression Modulus. Rept. No, PEER 2015/03. Pacific Earthquake Engineering Research Center, University of California, Berkeley, CA.
- [4] Angeli P, Russo G, Paschini A. 2013. Carbon Fiber-Reinforced Rectangular Isolators with Compressible Elastomer: Analytical Solution for Compression and Bending. *Int. J. Solids Struct.*, 50(22): 3519-3527.

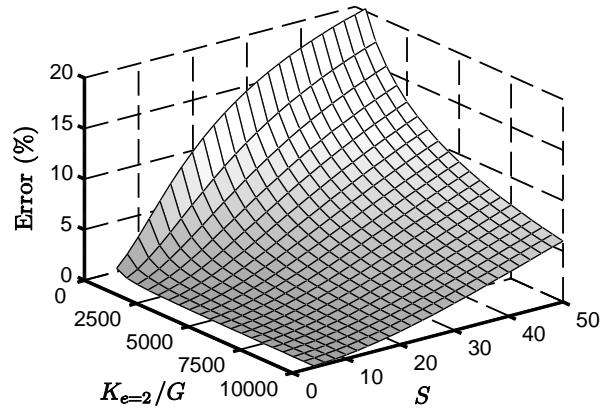


Figure A1: Percent error of  $E_c$  for a rectangular pad ( $\rho = 2$ ).

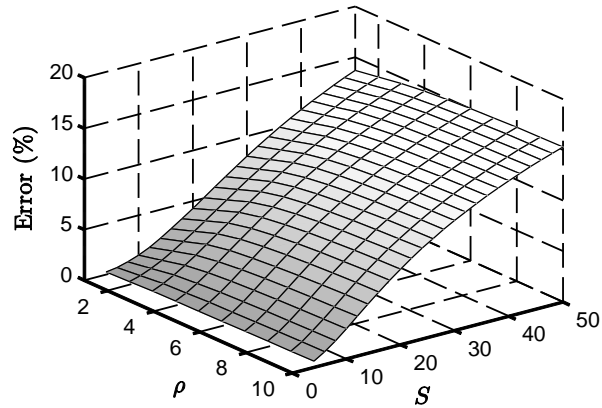


Figure A2: Sensitivity of the percent error for  $E_c$  of a rectangular pad to  $\rho$  ( $K_{e=2}/G = 2000$ ).

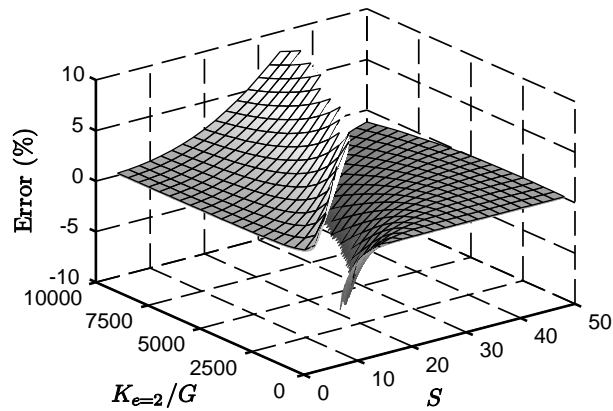


Figure A3: Percent error of  $\gamma/\epsilon_c$  for a rectangular pad ( $\rho = 2$ ).

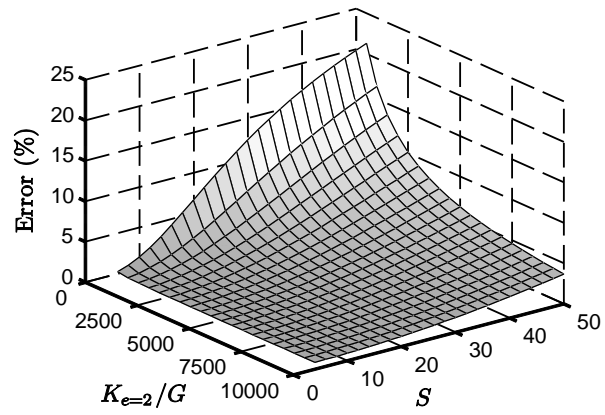


Figure A4: Percent error of  $E_b$  for a rectangular pad ( $\rho = 2$ ).